UNDERSTANDING DEFECTS AND EXCITED-STATE PROPERTIES IN PEROVSKITES FROM MANY-BODY PERTURBATION THEORY

MANISH KUMAR

DEPARTMENT OF PHYSICS
INDIAN INSTITUTE OF TECHNOLOGY DELHI
JULY 2022

UNDERSTANDING DEFECTS AND EXCITED-STATE PROPERTIES IN PEROVSKITES FROM MANY-BODY PERTURBATION THEORY

by

MANISH KUMAR

Department of Physics

Submitted

in fulfillment of the requirements of the degree of Doctor of Philosophy

to the

INDIAN INSTITUTE OF TECHNOLOGY DELHI

JULY 2022

Dedicated to my parents

Certificate

This is to certify that the thesis entitled "**Understanding Defects and Excited-State Properties in Perovskites from Many-Body Perturbation Theory**" being submitted by **Manish Kumar**, to the Indian Institute of Technology Delhi, for the award of the degree of **Doctor of Philosophy** in Physics is a record of bonafide research work carried out by him under my supervision and guidance. He has fulfilled the requirements for the submission of the thesis, which to the best of my knowledge has reached the required standard. The material contained in the thesis has not been submitted in part or full to any other University or Institute for the award of any degree or diploma.

Prof. Saswata Bhattacharya
Thesis Supervisor
Department of Physics,
Indian Institute of Technology Delhi,
Hauz Khas, New Delhi 110016, India.
Date:....................
Place: New Delhi

Acknowledgments

I would like to express my deepest gratitude and sincere appreciation to my thesis supervisor Prof. Saswata Bhattacharya for his inspiring and ever-encouraging guidance. His scientific temperament, logical thinking, scientist intuition, passion for physics, expertise and enthusiasm has been of great value to me and will have a bearing for the rest of my life. His invaluable advises, comments, new ideas and research guidance has been the cornerstone of my growth as a student and an independent research scholar. I would like to recognize his invaluable assistance in improving my presentation and scientific writing skills. I am extremely grateful to him for his relentless support during my PhD journey from day one. His immense patience and willingness to help everyone in any regard have had a profound effect on me.

I would like to thank all my colleagues and collaborators from our vibrant research group DISCERE (DISCovering Electronic CorRElation): Dr. Shikha Saini, Dr. Pooja Basera, Dr. Ekta Arora, Arunima Singh, Deepika Gill, Manjari Jain, Preeti Bhumla, Sajjan Sheoran and Ankita Phutela for their constant help and support. Their constant motivation, love and affection helped me to improve a lot and reach this stage. A very special thanks to Dr. Pooja Basera for several fruitful discussions and assistance throughout the whole period of my research work.

I would also like to thank my other collaborators: Prof. Venkat Krishnan, Prof. G. Vijay Prakash, Prof. Ritu Gupta, Prof. M. Ali Haider, Dr. Ashish Kumar, Dr. Sonit Balyan and Kshetra Mohan Dehury for useful discussions and collaborations.

I am deeply grateful to the Indian Institute of Technology Delhi (IIT Delhi) for providing me all the facilities to carry out my research work and providing the travel grant for participating in conferences. I am thankful to Council for Scientific and Industrial Research (CSIR) for funding my research and travel for conferences.

I would like to take this opportunity to thank my student research committee members: Prof. Sankalpa Ghosh, Prof. B. K. Mani and Prof. Hemant K. Kashyap for their evaluation of my

research work from time to time. Their intriguing questions and invaluable comments have guided me to look deeper into the problems. I would like to extend my sincere thanks to Prof. Amrita Bhattacharya for insightful discussions.

A word of sincere appreciation and deep gratitude for all my teachers for their blessings, encouragement and motivation that helped me to get this far. I sincerely thank all my friends here at IIT Delhi, especially Sandeep, Arvind, Sajjan, Hemant, Chandan, Aditya and Sooryansh for making my tenure at the campus all the more memorable and outside the campus, especially Nishant, Vishnu and Prerna for their consistent encouragement. I apologize for my failure to mention everyone by name.

Most importantly, I would like to thank my family. This thesis would not be possible without the unconditional love, support and encouragement of my parents. I appreciate all of the struggles and sacrifices that they have made for me. I am so blessed to have them in my life.

Manish Kumar

Abstract

Oxide perovskites such as $SrTiO_3$ and $CaTiO_3$ are the potential candidates to be used as a photocatalyst due to their exceptional electronic structure, high chemical stability, non-toxicity, and low cost. They exhibit suitable conduction and valence band-edge positions for reduction and oxidation of water to produce hydrogen and oxygen. Therefore, they can be exploited to generate hydrogen via water splitting, which is a clean, sustainable, and abundant source of energy. However, owing to their wide band gap, they absorb only UV irradiation (which consists $\sim$4% of the solar spectrum). Hence, several works are dedicated to expand optical response toward the visible region by reducing the band gap through doping with metals, nonmetals, or the combination of different elements. Despite significant amount of research is done, both experimentally and theoretically on these systems, it is still an open question concerning the kind of dopants or codopants, that could reduce the band gap while retaining the photocatalytic efficiency. In view of this, we systematically study the role of monodoping as well as codoping of a metal and nonmetal in $SrTiO_3$ in enhancing the photocatalytic efficiency for water splitting. Moreover, we investigate the effects of intrinsic defect (viz. O-vacancy) in $CaTiO_3$ to disentangle the role of O-vacancy for water splitting and N_2 fixation reaction.

On the other hand, lead halide perovskites have emerged as an efficient compound semiconductor alternative to conventional materials used in photovoltaics. This class of materials has suitable optical band gap, long carrier diffusion length, high charge carrier mobility and low manufacturing cost. However, the concerns regarding toxicity of lead and phase instability restricts their usage on large scale. In an attempt to deal with toxicity and instability, lead-free halide double perovskites such as $Cs_2M(I)M(III)X_6$ (M = metal, X = halogen) and chalcogenide perovskites ABX_3 (A, B = metals, X = chalcogen) have emerged. In this work, we aim to design lead-free halide double perovskites with improved optoelectronic properties since they have not shown the efficiency as that of lead halide perovskites. Furthermore, the excitonic and polaronic effects are unraveled in the case of chalcogenide perovskites.

We employ a robust methodological approach that integrates various levels of theories combined into one multi-scale simulation to address the optical properties such as dielectric function, absorption spectra, exciton binding energy and polaronic effects in perovskites. In this thesis work, the state-of-the-art methodologies that are used to obtain the desired objectives are: (i) density functional theory (DFT) for ground-state properties, (ii) *ab initio* atomistic thermodynamics to predict the stability, (iii) many-body perturbation theory (GW, BSE and model-BSE) for excited-state properties, (iv) Wannier-Mott approach to determine the exciton binding energy and exciton lifetime, and (v) density functional perturbation theory (DFPT) for including ionic contribution to dielectric function and to capture the electron-phonon coupling.

सार

ऑक्साइड पैरोव्स्काइट्स जैसे कि $SrTiO_3$ और $CaTiO_3$ सामर्थ्यवान उम्मीदवार हैं जिन्हें उनकी असाधारण इलेक्ट्रॉनिक संरचना, उच्च रासायनिक स्थिरता, गैर-विषाक्तता और कम लागत के कारण फोटोकैटलिस्ट के रूप में उपयोग किया जा सकता है। वे हाइड्रोजन और ऑक्सीजन का उत्पादन करने के लिए पानी का अपचयन और ऑक्सीकरण के लिए उपयुक्त चालन और संयोजकता बैंड-एज स्थिति प्रदर्शित करते हैं। इसलिए, पानी के विभाजन के माध्यम से हाइड्रोजन उत्पन्न करने के लिए उनका दोहन किया जा सकता है, जो ऊर्जा का एक स्वच्छ, टिकाऊ और प्रचुर स्रोत है। हालांकि, उनके व्यापक बैंड अंतराल के कारण, वे केवल यूवी विकिरण (जो सौर स्पेक्ट्रम का लगभग 4% होता है) को अवशोषित करते हैं। इसलिए, धातुओं, अधातुओं या विभिन्न तत्वों के संयोजन के साथ मादन (डोपिंग) के माध्यम से बैंड अंतराल को कम करके दृश्य क्षेत्र की ओर ऑप्टिकल प्रतिक्रिया का विस्तार करने के लिए कई कार्य समर्पित हैं। इन प्रणालियों पर प्रायोगिक और सैद्धांतिक दोनों तरह से विस्तृत मात्रा में शोध किए जाने के बावजूद, यह अभी भी एक खुला प्रश्न है कि किस तरह के अपमिश्रक (डोपेंट) या कोडोपेंट हैं, जो फोटोकैटलिटिक दक्षता को बनाए रखते हुए बैंड अंतराल को कम कर सकते हैं। इसे ध्यान में रखते हुए, हम पानी के विभाजन के लिए फोटोकैटलिटिक दक्षता को बढ़ाने में $SrTiO_3$ में मोनोडोपिंग के साथ-साथ धातु और अधातु के कोडोपिंग की भूमिका का व्यवस्थित रूप से अध्ययन करते हैं। इसके अलावा, हम पानी के विभाजन और N_2 निर्धारण प्रतिक्रिया के लिए O-रिक्ति की भूमिका को सुलझाने के लिए $CaTiO_3$ में आंतरिक दोष (अर्थात O-रिक्ति) के प्रभावों की जांच करते हैं।

दूसरी ओर, लैड हैलाइड पैरोव्स्काइट्स एक कुशल यौगिक अर्धचालक फोटोवोल्टिक में प्रयुक्त पारंपरिक सामग्रियों के विकल्प के रूप में उभरे हैं। सामग्री के इस वर्ग में उपयुक्त ऑप्टिकल बैंड अंतराल, लंबी वाहक प्रसार लंबाई, उच्च आवेश वाहक गतिशीलता और कम विनिर्माण लागत है। हालांकि, लैड की विषाक्तता और चरण अस्थिरता के बारे में चिंताएं बड़े पैमाने पर उनके उपयोग को प्रतिबंधित करती हैं। विषाक्तता और अस्थिरता से निपटने के प्रयास में, लैड-रहित हैलाइड डबल पैरोव्स्काइट्स जैसे $Cs_2M(I)M(III)X_6$ (M = धातु, X = हैलोजन) और चाल्कोजेनाइड पैरोव्स्काइट्स ABX_3 (A, B = धातु, X = चाल्कोजेन)) उभरे हैं। इस काम में, हमारा लक्ष्य बेहतर ऑप्टोइलेक्ट्रॉनिक गुणों के साथ लैड-रहित हैलाइड डबल पैरोव्स्काइट्स को डिज़ाइन करना है क्योंकि उन्होंने लैड हैलाइड पैरोव्स्काइट्स जैसी दक्षता नहीं दिखाई है। इसके अलावा, चाल्कोजेनाइड पैरोव्स्काइट्स के मामले में एक्साइटोनिक और ध्रुवीय प्रभाव सुलझाये हैं।

हम एक मजबूत कार्यप्रणाली दृष्टिकोण को नियोजित करते हैं जो ऑप्टिकल गुणों जैसे कि परावैद्युत फलन, अवशोषण स्पेक्ट्रा, एक्साइटन बाध्यकारी ऊर्जा और पैरोव्स्काइट्स में ध्रुवीय प्रभाव को संबोधित करने के लिए एक बहु-स्तरीय अनुरूपण में संयुक्त सिद्धांतों के विभिन्न स्तरों को एकीकृत करता है। इस शोध-प्रबन्ध कार्य में, वांछित उद्देश्यों को प्राप्त करने के लिए उपयोग की जाने वाली अत्याधुनिक पद्धतियां हैं: (i) ग्राउंड-स्टेट गुणों के लिए घनत्व कार्यात्मक सिद्धांत (डीएफटी), (ii) स्थिरता की भविष्यवाणी करने के लिए आदित परमाणु ऊष्मा गतिकी, (iii) एक्साइटिड-स्टेट गुणों के लिए बहुपिंडी क्षोभ सिद्धांत (जीडब्ल्यू, बीएसई और मॉडल-बीएसई), (iv) ऐक्साइटॉन बाध्यकारी ऊर्जा और ऐक्साइटॉन जीवनकाल निर्धारित करने के लिए वैनियर-मॉट दृष्टिकोण, और (v) घनत्व कार्यात्मक क्षोभ सिद्धांत (डीएफपीटी) परावैद्युत फलन में आयनिक योगदान को शामिल करने और इलेक्ट्रॉन-फोनॉन युग्मन के अध्ययन के लिए।

List of Publications

1. **Manish Kumar**, Pooja Basera, Shikha Saini, and Saswata Bhattacharya, “Role of defects in photocatalytic water splitting: Monodoped vs codoped $SrTiO_3$”, The Journal of Physical Chemistry C **124**, 10272 (2020).

2. **Manish Kumar**, Pooja Basera, Shikha Saini, and Saswata Bhattacharya, “Theoretical insights of codoping to modulate electronic structure of TiO_2 and $SrTiO_3$ for enhanced photocatalytic efficiency", Scientific Reports **10**, 15372 (2020).

3. **Manish Kumar**, Manjari Jain, Arunima Singh, and Saswata Bhattacharya, “Sublattice mixing in $Cs_2AgInCl_6$ for enhanced optical properties from first-principles”, Applied Physics Letters **118**, 021901 (2021).

4. **Manish Kumar**, Arunima Singh, Deepika Gill and Saswata Bhattacharya, “Optoelectronic properties of chalcogenide perovskites by many-body perturbation theory”, The Journal of Physical Chemistry Letters **12**, 5301 (2021).

5. Ashish Kumar, **Manish Kumar**, Navakoteswara Rao, Muthukonda Venkatakrishnan Shankar, Saswata Bhattacharya, and Venkata Krishnan, “Unraveling the structural and morphological stability of oxygen vacancy engineered leaf-templated $CaTiO_3$ towards photocatalytic H_2 evolution and N_2 fixation reactions”, Journal of Materials Chemistry A **9**, 17006 (2021).

6. Ekta Arora, Shikha Saini, Pooja Basera, **Manish Kumar**, Arunima Singh, and Saswata Bhattacharya, “Elucidating the role of temperature and pressure to the thermodynamic stability of charged defects in complex metal-hydrides: A case study of $NaAlH_4$”, The Journal of Physical Chemistry C **123**, 62 (2019).

7. Pooja Basera, Shikha Saini, Ekta Arora, Arunima Singh, **Manish Kumar**, and Saswata Bhattacharya, “Stability of non-metal dopants to tune the photo-absorption of TiO_2 at

realistic temperatures and oxygen partial pressures: A hybrid DFT study", Scientific Reports **9**, 11427 (2019).

8. Arunima Singh, Pooja Basera, Shikha Saini, **Manish Kumar**, and Saswata Bhattacharya, "Importance of many-body dispersion in the stability of vacancies and antisites in free-standing monolayer of MoS_2 from first-principles approaches", The Journal of Physical Chemistry C **124**, 1390 (2020).

9. Pooja Basera, **Manish Kumar**, Shikha Saini, and Saswata Bhattacharya, "Reducing lead toxicity in the methylammonium lead halide $MAPbI_3$: Why Sn substitution should be preferred to Pb vacancy for optimum solar cell efficiency", Physical Review B **101**, 054108 (2020).

10. Manjari Jain, Arunima Singh, Pooja Basera, **Manish Kumar**, and Saswata Bhattacharya, "Understanding the role of Sn-substitution and Pb-$\Box$ in enhancing the stability of $CH(NH_2)_2Pb_{1-X-Y}Sn_X\Box_YBr_3$: A hybrid density functional approach", Journal of Materials Chemistry C **8**, 10362 (2020).

11. Deepika Gill, **Manish Kumar**, Pooja Basera, and Saswata Bhattacharya, "Understanding the ionic diffusivity in (meta)stable (un)doped solid state electrolyte from first-principles: A case study of LISICON", The Journal of Physical Chemistry C **124**, 17485 (2020).

12. Gaurav Bahuguna, Indrajit Mondal, Mohit Verma, **Manish Kumar**, Saswata Bhattacharya, Ritu Gupta, and Giridhar U. Kulkarni, "Innovative approach to photo-chemiresistive sensing technology: Surface-fluorinated SnO_2 for VOC detection", ACS Applied Materials & Interfaces **12**, 37320 (2020).

13. Shikha Saini, Pooja Basera, **Manish Kumar**, Preeti Bhumla, and Saswata Bhattacharya, "Metastability triggered reactivity in clusters at realistic conditions: A case study of N-doped $(TiO_2)_n$ for photocatalysis", Journal of Physics Materials **4**, 015001 (2020).

14. Preeti Bhumla, **Manish Kumar**, and Saswata Bhattacharya, "Theoretical insights into C–H bond activation of methane by transition metal clusters: The role of anharmonic effects", Nanoscale Advances **3**, 575 (2021).

15. Deepika Gill, Preeti Bhumla, **Manish Kumar**, and Saswata Bhattacharya, "High-throughput

screening to modulate electronic and optical properties of alloyed $Cs_2AgBiCl_6$ for enhanced solar cell efficiency", Journal of Physics Materials **4**, 025005 (2021).

16. Kshetra Mohan Dehury, Pawan K. Kanaujia, Mohammad Adnan, **Manish Kumar**, Saswata Bhattacharya, and G. Vijaya Prakash, "Structure-dependent (non)linear optical excitons in primary cyclic ammonium ($C_nH_{2n-1}NH_2$; $n = 3 - 8$)-based inorganic-organic hybrid semiconductor series", The Journal of Physical Chemistry C **125**, 6821 (2021).

17. Sajjan Sheoran, **Manish Kumar**, Preeti Bhumla, and Saswata Bhattacharya, "Rashba spin splitting and anomalous spin textures in the bulk ferroelectric oxide perovskite KIO_3", Materials Advances **3**, 4170 (2022).

18. Manjari Jain, Preeti Bhumla, **Manish Kumar** and Saswata Bhattacharya, "Lead-free alloyed double perovskites: An emerging class of materials for optoelectronic applications", The Journal of Physical Chemistry C **126**, 6753 (2022).

Contents

List of Figures

List of Tables

CHAPTER 1

Introduction

1.1 Defects in solids

A defect generally refers to any region where the microscopic arrangement of ions differs from the perfect crystalline order. Defects can be classified into surface, line or point defects, depending on the disruption is bounded on the atomic scale in one, two, or three dimensions. A schematic diagram of various defects is shown in Figure 1.1. In this thesis work, we have studied various point defects such as vacancy, interstitial, and substitutional defects. Point defects play a pivotal role in field of semiconductors, and can alter their electronic and optical properties drastically. Furthermore, point defects, specifically, vacancies and interstitials are intrinsically present in a real crystal since their presence is a normal thermal equilibrium phenomenon. Many a time, it is very difficult for the experimentalists to probe the defects and their effect on various properties. Therefore, first-principles-based theoretical investigation comes in handy, which could complement experiments and serve as a predictive tool. This methodology

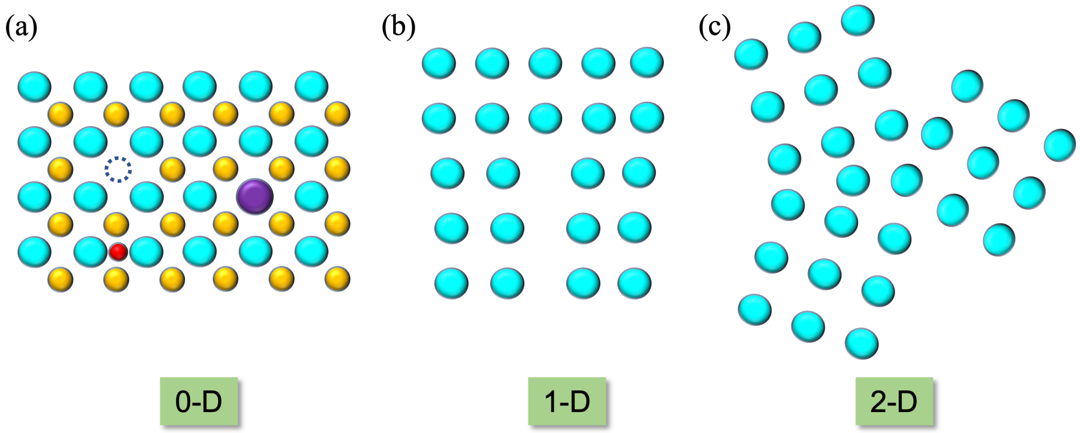

Figure 1.1: Schematic illustration of (a) point (e.g., vacancy, substitutional, and interstitial), (b) line (e.g., edge dislocation), and (c) surface (e.g., defect at grain boundaries) defects.

is now used by a large number of research groups around the world. Consequently, a number of textbooks and overview on this important active topic have been published [4, 5, 6, 7, 8, 9, 10]. In the next section, we have discussed a thermodynamic formalism for the formation of point defects and the basic rules for doping and alloying.

1.2 Thermodynamics of point defects

According to thermodynamics, point defects are inevitable in the thermal equilibrium crystal. We can illustrate this by considering a vacancy defect in a monoatomic Bravais lattice. A vacancy is a point defect in which an ion is missing from the regular lattice site. The number of vacancies, n in the thermal equilibrium crystal can be obtained by minimizing the appropriate thermodynamic potential. It will be Gibbs free energy G for the crystal to be at constant pressure p [11]

$$G = U - TS + pV \tag{1.1}$$

where U is the internal energy of the crystal. T represents the temperature, V is volume, and S is the entropy. To obtain the dependence of G on n, consider a crystal having $(N + n)$-ion sites with n number of vacancies. Then, the volume $V(n)$ is approximately $(N + n)v_0$, where v_0 is the volume per ion in the perfect crystal. The configurational entropy S^{config} arise from the fixed number of vacancies is given by

$$S^{\text{config}} = k_{\text{B}} \ln \frac{(N+n)!}{N!n!} \tag{1.2}$$

where k_{B} is the Boltzmann constant. Thus, the Gibbs free energy can be expressed as

$$G(n) = F_0(n) - TS^{\text{config}}(n) + p(N+n)v_0 \tag{1.3}$$

where $F_0(n) = U - TS$ is the Helmholtz free energy of the imperfect crystal containing n vacant sites. Using Stirling's formula (for large $N, \ln N! \approx N(\ln N - 1)$) and assuming $n << N$, one can obtain

$$\frac{\partial G}{\partial n} = \frac{\partial F_0}{\partial n} + pv_0 - k_B T \ln \frac{N}{n} \tag{1.4}$$

Also, for small n,

$$\frac{\partial F_0}{\partial n} \approx \left.\frac{\partial F_0}{\partial n}\right|_{n=0} = \mathcal{E} \tag{1.5}$$

where $\mathcal{E}$ is the defect formation energy and independent of n. Therefore, the number of vacancies that minimize G is given by

$$n = Ne^{-(\mathcal{E}+pv_0)/k_{\text{B}}T} \tag{1.6}$$

At atmospheric pressures, pv_0 is negligible in comparison to $\mathcal{E}$, and thus

$$n = Ne^{-\mathcal{E}/k_{\mathrm{B}}T} \tag{1.7}$$

Equation 1.7 implies that defects having a low formation energy will occur in high concentrations. Also, for $T > 0$, $n > 0$.

Point defects can be created thermally (i.e., by the thermodynamic equilibrium growth), chemically (due to the presence of impurity species), and by irradiation or mechanical damage. For appreciable solubility of impurities, a set of empirical requirements were put forward by Hume-Rothery [12]. One of the requirements is that the atomic diameters of the impurity species and the host atom should not differ by more than 14%. For the difference more than 14%, the lattice distortion is large and the solubility is restricted. The other requirements include that the electronegativity difference of the host and the guest atoms should be small. Moreover, the crystal structure of the host and the guest atoms should be similar.

1.3 Defect dependent properties

Even small concentrations of defect can influence key physical and chemical properties of the materials, most notably those controlling the transport of matter and the properties that stem from it. Moreover, they govern the thermal conductivity by scattering phonons, electronic conduction, and related properties by acting as acceptors or donors and the optical properties by introducing electronic states with optical transitions.

In a semiconductor, the role of impurity depends on the kind of localized energy level it introduces in the otherwise forbidden gap, as illustrated in Figure 1.2. It also depends on the concentration and the nature of other impurities present in the system. Mostly, shallow donors and acceptors (states appearing closely above the valence band maximum (VBM) or below the conduction band minimum (CBm) having an energetic distance within a few $k_{\mathrm{B}}T$) control the conductivity. At room temperature, the conductivity can be achieved from 10^{-9} to 10^{3} (Ω cm)$^{-1}$ [13]. Furthermore, the conductivity can be dominated by electrons (n-type) or holes (p-type) in a semiconductor.

The concentrations of shallow acceptors and donors can be made nonuniform, which can be exploited to generate various effects that can be utilized in devices. One of such devices is a p-n junction, which consists of adjacent p-type and n-type regions. A p-n junction can act as a laser or light-emitting diode (LED) on satisfying some additional conditions. Moreover, a

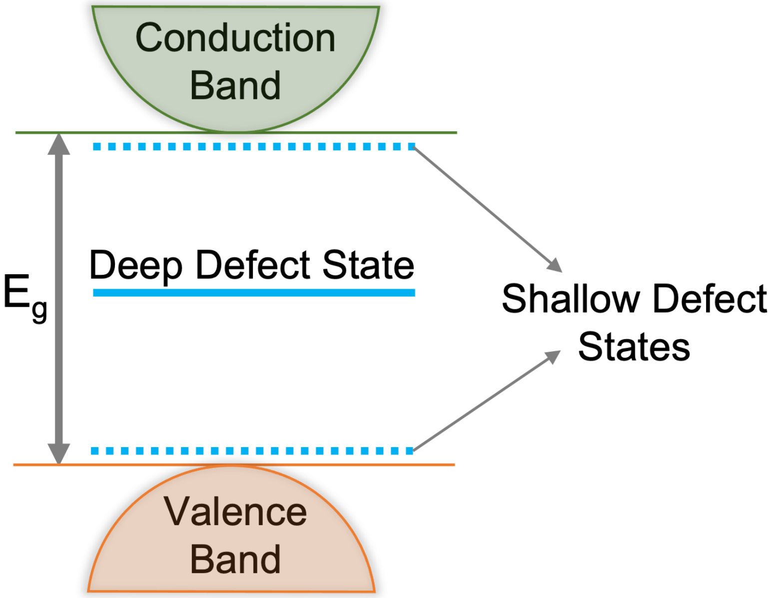

Figure 1.2: Schematic illustration of shallow and deep defect states. Here, E_g is the band gap of the pristine material.

consecutive p-n-p or n-p-n region is used to make transistor that act as an amplifier of signals. Similarly, other devices such as modulators, photodetectors, solar cells can be formed by p-type and n-type regions having different concentrations of acceptor and donor.

On the other hand, deep-level (states which are energetically away from the band edges, i.e., VBM and CBm) impurities stimulate the recombination of charge carriers. They control the lifetime of the charge carriers. For long carrier lifetimes in a device, deep-level impurities must be avoided. They are generally undesirable in optoelectronic devices since they limit the efficiency. In some cases, they can be used constructively. For instance, deep levels are needed in a photocell, which is used as a fast switch.

Point defects in semiconductor can exist in different charge states. Charged defects can change the structure of the defect configuration, rate of thermal diffusion, trapping rates of charge carriers, and luminescence quenching rates [14]. The formation energy of defects is also influenced by different charge states. Charged defects are formed mostly in the aliovalent doping, but they could be present with isovalent impurities as well.

Point defects are essential to engineer the properties of semiconductors that render them useful for electronic and optoelectronic devices. Therefore, unraveling the role of point defects on electronic and optical properties is of utmost importance. In this thesis work, we have studied the role of intrinsic as well as extrinsic defects in perovskites. We have used state-of-the-art first-principles calculations to investigate the same.

1.4 Defects in perovskites

Perovskites are a family of compounds having the chemical formula ABX_3, where A and B are cations and X is an anion [15, 16, 17]. In an ideal cubic structure, the B cation is octahedrally coordinated, and the $[BX_6]^{n-}$ octahedra form a corner-sharing network. Since the conduction and valence band edges of ABX_3 perovskites are formed by the B-X bonds, the major electronic and optical properties are controlled by $[BX_6]^{n-}$ octahedra. The A cation has a 12-fold cuboctahedral coordination and occupies the void formed by the $[BX_6]^{n-}$ octahedra [18]. It is mainly responsible for charge neutrality and structural stability, but can also affect the B-X octahedral network, which helps in fine tuning of electronic and optical properties [19]. The crystal structure of perovskite is shown at the center of Figure 1.3 alongside some of its applications. Depending on the anion X, perovskites can be categorized into oxide (O^{2-}), halide

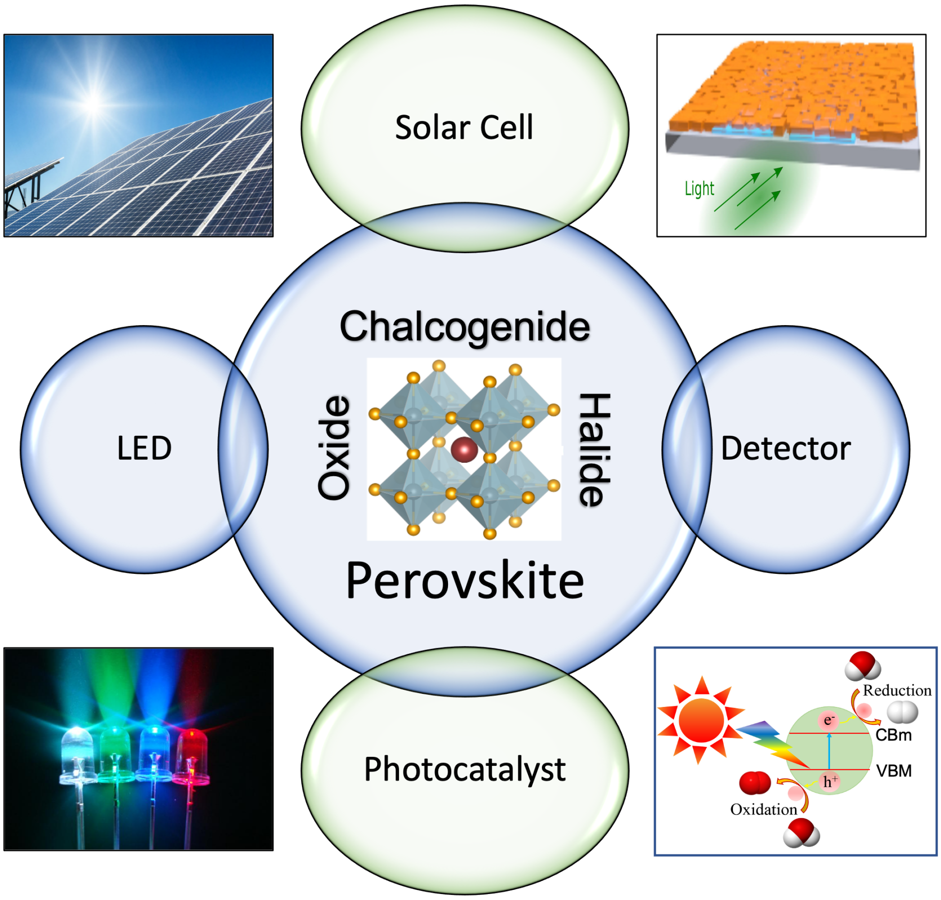

Figure 1.3: Schematic illustration of perovskites and their applications.

(Cl^-,Br^-, I^-) and chalcogenide (S^{2-}, Se^{2-}, Te^{2-}) perovskites. The first perovskite mineral $CaTiO_3$ was discovered in the Ural mountains of Russia by Gustav Rose in 1839 and named after a Russian mineralogist Lev Perovski, but did not become prominent until the 1940s when their appositeness for electronic applications was realized [20]. Historically, oxide-based compounds with chemical formula ABO_3, such as $CaTiO_3$, $BaTiO_3$, $PbTiO_3$, $SrTiO_3$, $BiFeO_3$, and others are the focus of perovskite research [15, 21]. Oxide perovskites are used in ferroelectric, piezoelectric, dielectric, pyroelectric and catalytic applications [15, 22]. They can also be used in photovoltaics, but their typical wide band gap (> 2.5 eV) restricts the efficiency of photovoltaic devices [23, 24]. They are more suitable for water splitting, but that too require the optimal band gap of ~ 2 eV [25]. The typical parameters that limit the photocatalytic performance are similar to photovoltaics, which include poor absorption, high electron-hole recombination rate and limited stability. The major concern in oxide perovskites is large band gap, which enables them to absorb only UV irradiation of the solar spectrum. Doping is one of the most prominent strategies to reduce the band gap of oxide perovskites. In this thesis work, we have investigated the role of extrinsic point defects (doping of nonmetals and metals) in $SrTiO_3$ to tune its physical properties, making it useful for photocatalytic water splitting. Furthermore, we have also examined the role of intrinsic point defect (O-vacancy) in $CaTiO_3$ for water splitting and nitrogen fixation.

Recently, lead halide perovskites (LHPs) have superseded oxide perovskites for solar absorbers [16, 18, 26]. Within just a few years, the power conversion efficiency of LHPs has increased from 3.8% (using methylammonium lead iodide, or $MAPbI_3$) in 2009 [27] to now over 25% [28, 29]. This outstanding performance is due to exceptional properties, including narrow band gaps (e.g., 1.55 eV for $MAPbI_3$) [30, 31], high absorption coefficients [32], high charge carrier mobilities [33], long charge carrier diffusion lengths [34], defect tolerance [35], high photoluminescence quantum efficiencies (PLQEs) [36], and low manufacturing costs [37]. Unfortunately, the toxicity of lead and limited environmental and thermal stability hinder the practical applications of LHPs on large scale [38]. Mixed halide and mixed cation perovskites have been explored to cope with the stability issues [39]. Moreover, to replace lead, group IV elements, tin [40] and germanium [41] have been employed. However, the device performance through this approach is poor. In addition, the easy oxidation of Sn and Ge from +2 to +4 state makes them less promising for application in stable perovskite solar cells [38]. It encourages researchers to develop new classes of materials, which can solve the problems of lead toxicity

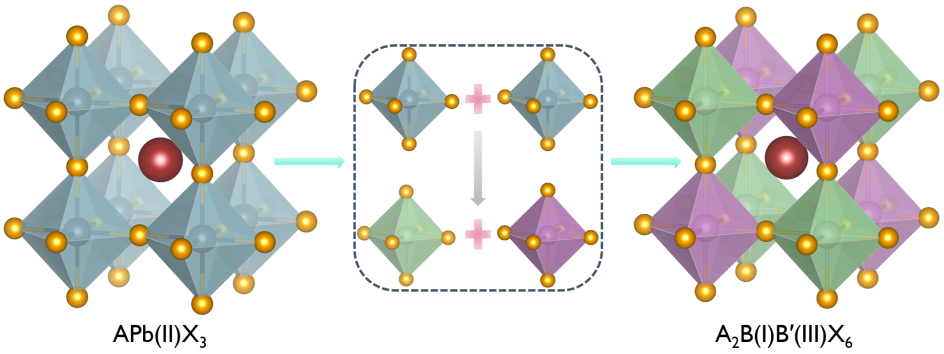

Figure 1.4: Schematic representation of formation of halide double perovskites $A_2B(I)B'(III)X_6$ to exclude Pb from LHPs $APbX_3$. The A^+, Pb(II), B(I), B′(III), X^- ions are denoted by dark red, light blue, light green, orchid, and golden color balls, respectively.

and stability while retaining the fascinating properties of LHPs. A possible alternative is the halide double perovskites in which two Pb^{2+} cations are replaced by a monovalent B(I) and a trivalent B′(III) cations, as shown in Figure 1.4. The $A_2B(I)B'(III)X_6$ crystal structure provides an avenue for easier substitution and incorporation of different metal cations with different oxidation states at the B-site, various organic and inorganic cations at the A-site, and various halide compositions at the X-site [42, 43, 44, 45, 46, 47]. They have found applications in various optoelectronic devices, such as LEDs, photodetectors, photocatalysts and solar cells [48]. However, despite being stable and environmentally benign, they do not show optimal performance in photovoltaic devices mainly due to an indirect or a wide direct band gap. Therefore, a pragmatic approach is required to tailor the properties of halide double perovskites via suitable alloying or doping for specific purposes. In this thesis work, we have investigated the electronic and optical properties of alloying in a prototypical halide double perovskite $Cs_2AgInCl_6$ to enhance its optical properties for optoelectronic devices.

Another alternative of LHPs for solar cell and other optoelectronic devices is chalcogenide perovskites. Only very few chalcogenide perovskites ABS_3 have been reported and explored so far. $AZrS_3$ (A = Ca, Ba) have smaller direct band gap ($\sim$ 1.9 eV) in comparison to halide double perovskites, which makes them potential candidates for photovoltaics and optoelectronic applications [49, 50]. Chalcogenide perovskites exhibit enhanced stability as compared to halide perovskites due to the larger Coulomb interaction and more covalent bonding character of the metal-chalcogenide bond in the former [51, 52]. Excited-state properties of chalcogenide perovskites such as exciton binding energy, and electron-phonon coupling effects have not been studied yet. Therefore, we have investigated the same using state-of-the-art many-body perturbation theory (MBPT) approaches [53], which provide scientific insights into the working of chalcogenide perovskites. This theoretical methodology can be applied to various semiconducting materials.

1.5 Problems and challenges

Understanding the defect physics of a semiconductor (e.g., a perovskite) is a key to attain an optimal performance in application. In an attempt to explore suitable dopants/codopants, the first step is to determine the thermodynamic stability at a realistic experimental condition (temperature, pressure, and Fermi level). Nevertheless, even the very first step is complex. Note that the free energy of formation of one isolated defect can be reduced significantly by several eVs, when the charge carriers (holes or electrons) are available in the material. Disentangling the relative stability of different types of charged defects is quite challenging. Following this, it is to investigate very accurately the electronic structure, optical properties, and the band-edge positions of the materials for specific applications. There are so many unknown parameters (viz. suitable exchange-correlation functional of density functional theory (DFT) [54, 55], thermodynamic stability, no trap states inside the forbidden region, optimum optical absorption, favorable positions of the VBM/CBm, etc.) that need to be addressed properly for finding a

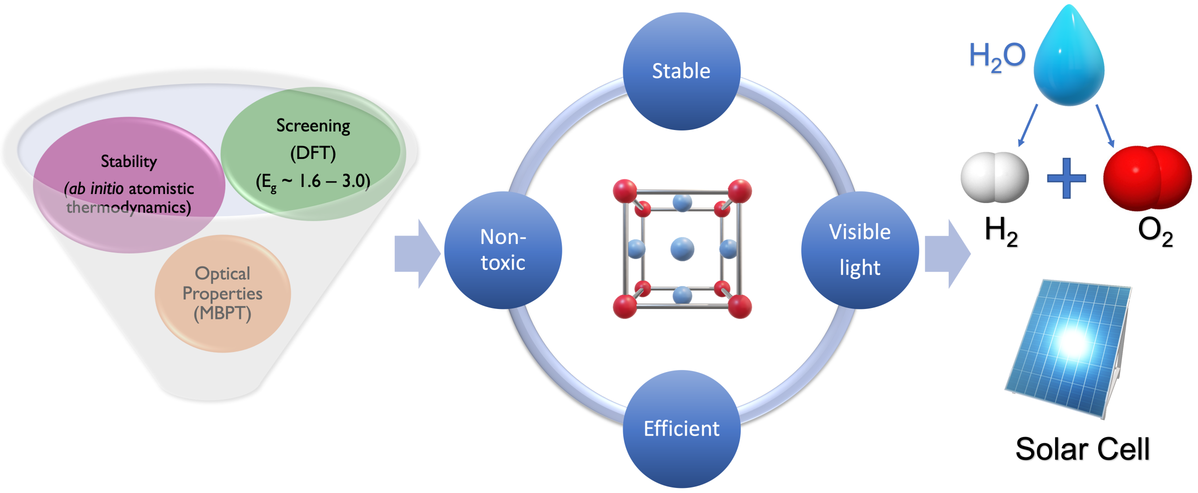

Figure 1.5: Schematic illustration of the proposed strategies to design and study thermodynamic stability, electronic and optical properties of semiconducting perovskites for various applications.

suitable material. A systematic study that have covered all these aspects with the help of a robust methodology has so far been lacking. A schematic diagram to design a material for various applications is shown in Figure 1.5.

Theoretically, the ground-state properties of a material are efficiently computed by DFT [56]. However, the accuracy of computational results is often constrained by the approximation of the exchange-correlation functionals. Another major issue, particularly for defect calculations, is the convergence of size of the supercell for an isolated defect. Even though they can be systematically improved until convergence is reached, limitations in computational resources put severe restrictions on the extent to which such convergence can be achieved.

For computing the formation energy of defect, the supercell approach is used. In this approach, a single defect is contained in large cell, which is periodically repeated. Since realistic defect concentrations are smaller than the defect concentration in a cell, the interaction of the defect with its periodic images is spurious and must be corrected [57]. Therefore, the supercell size should be large enough to localize the defect in the system. Furthermore, an efficient **k**-point sampling of the Brillouin zone should be chosen to converge the concerned physical quantity.

The local or semi-local exchange-correlation functionals (e.g., LDA [58] and PBE [59]) in DFT severely underestimate the band gap. Consequently, the formation energies and charge transition levels of defects in semiconductors computed using LDA or GGA are usually erroneous. Moreover, they fail to capture the charge localization emanating from narrow bands or local geometry distortions around defects. This is largely due to the electron's self-interaction error. This problem can be circumvented by using hybrid functional such as HSE06 [60, 61]. Defect energetics are improved by the hybrid functionals. However, they require an appropriate amount of exact exchange mixing in order to reproduce the experimental band gap [62].

To capture the excited-state properties, one needs to go beyond DFT. These are accurately determined by quasiparticle calculations based on Green's function methods within the MBPT (namely, the GW approximation [63, 64] and the Bethe-Salpeter equation (BSE) approach [65, 66]). In practice, these calculations depend on the DFT orbitals. Therefore, one needs to compare the theoretical results with the experimental ones to predict the reliability of the computational approach. Generally, the single-shot GW (G_0W_0) accurately predicts the band gaps [67]. However, GW and BSE calculations pose challenges due to a huge computational cost and memory requirements. In this thesis work, we have taken care of the aforementioned parameters to carry out our calculations and designed the perovskites for photocatalytic and optoelectronic applications.

1.6 A short overview of this thesis

- **Chapter 2:** This chapter presents the theoretical methodology adopted in this work. A brief overview of first-principles-based DFT is provided, which is used to determine the structural and electronic properties of the perovskites. A brief discussion of *ab initio* atomistic thermodynamics is also included, which is needed to figure out the thermodynamic stability. A discussion about the MBPT approaches, specifically, the GW approximation, and the BSE approach, which are useful to understand the optical properties including excitonic parameters, is also given. Furthermore, a brief introduction of the density functional perturbation theory (DFPT) is also included, which determines the lattice dynamics.

- **Chapter 3:** This chapter presents an exhaustive study of codoped (metal-nonmetal) $SrTiO_3$ for enhancing the photocatalytic efficiency under visible light. In order to search for suitable dopants/codopants, it's of paramount importance to provide theoretical guidance to experiment about the stability of different dopants as a function of charges at a realistic condition (temperature, pressure, and doping). Moreover, it is of utmost importance to investigate the electronic structure, optical properties as well as the band-edge positions of the materials for understanding the synergistic effects of codopants. Therefore, we have systematically studied the role of monodoping as well as codoping of a metal (namely, Mn, and Rh) and nonmetal (namely, N, and S) in $SrTiO_3$ in enhancing its photocatalytic efficiency for water splitting. With the framework of state-of-the-art hybrid DFT, and *ab initio* atomistic thermodynamics, we have studied the stability of various point defect configurations of monodoped and codoped $SrTiO_3$ by calculating the free energy of formation. Thereafter, we have analyzed the electronic structure of undoped, monodoped and codoped $SrTiO_3$. We have also studied the optical properties of pristine and doped $SrTiO_3$ using the MBPT approach which includes a first order Green's function technique (viz., G_0W_0@HSE06). Subsequently, we have obtained the band-edge positions of undoped and doped $SrTiO_3$ with respect to water redox potentials. Finally, we have determined the effective mass, which is helpful to estimate the effect on charge carrier mobility. We have found that the codoping of metal at the Sr site and nonmetal at the O site are stable mainly in positive charge states. All the dopants but Mn_{Sr} have reduced the band gap of $SrTiO_3$ and induced the visible light absorption. Our results infer that $Mn_{Ti}S_O$ and $Mn_{Sr}N_O$ codoped $SrTiO_3$ are the most promising candidates for producing hydrogen via photocatalytic water splitting because these reduce the band gap to ideal visible region ($\sim$ 2 eV), passivate the localized trap states, and form the shallow defect states with suitable band-edge positions.

- **Chapter 4:** In this chapter, we have systematically studied the role of O-vacancy in $CaTiO_3$ for H_2 evolution and N_2 fixation reactions using hybrid DFT. We have investigated the oxygen vacancy sites, which ameliorate the photocatalytic performance of $CaTiO_3$. To determine the nature of defect states, we have calculated electronic structure. Subsequently, we have done the band-edge alignment of (un)defective $CaTiO_3$ with respect to water redox potentials. Finally, we have calculated the Gibbs free energy of formation to know about the energy barrier for hydrogenation of N_2. Our results reveal that an O-vacancy in the TiO_2 plane can ameliorate the photocatalytic efficiency of $CaTiO_3$ for water splitting as well as N_2 fixation. The deep defect states are formed in the case of an O-vacancy in the CaO plane, which deteriorate the photocatalytic efficiency for water splitting. We have found that the defective $CaTiO_3$ (containing an O-vacancy) accelerates the hydrogenation of N_2.

- **Chapter 5:** This chapter presents a detailed study of the sublattice mixing by partial substitution of several metals M(I), M(II), M(III) and halogen X at Ag/In and Cl site, respectively, to bring about the visible light absorption in $Cs_2AgInCl_6$. The structural stability of the (un)alloyed $Cs_2AgInCl_6$ is determined by evaluating the Goldschmidt tolerance factor and octahedral factor. Subsequently, using the DFT and hybrid DFT, we have studied the thermodynamic stability of different configurations by calculating the decomposition energy. Further, we have analyzed the electronic structure of (un)doped $Cs_2AgInCl_6$ using hybrid DFT. The optical properties are investigated using the G_0W_0@HSE06. Our results show that partial mixing of Co(II), Ni(II), and Cu(II) in $Cs_2AgInCl_6$ is thermodynamically not stable. The sublattices with Cu(I) and Au(I) at the Ag site, Ir(III) at the In site, Zn(II) at the Ag and In site simultaneously, Mn(II) at the Ag and In site simultaneously, and Br and I substitutions at the Cl site have tuned the optical properties. These mixing can enhance the optical properties of $Cs_2AgInCl_6$ for various optoelectronic devices in the visible light spectrum.

- **Chapter 6:** This chapter reports a systematic study of electronic and optical properties of chalcogenide perovskites $AZrS_3$ (A = Ca, Sr, Ba) using DFT and MBPT approaches (viz., GW and BSE). The exciton binding energy and the oscillator strength are determined by solving BSE on top of G_0W_0@PBE. The carrier nonradiative lifetime is found to be longer for electrons in comparison to the holes. The exciton binding energies for $CaZrS_3$, $\alpha-SrZrS_3$, $\beta-SrZrS_3$, and $BaZrS_3$ are found to be 0.23, 0.54, 0.25, and 0.21 eV, respectively. The electron–phonon coupling parameters are determined using DFPT, which show that the charge-separated polaronic state is more stable than the bound exciton for the considered chalcogenide perovskites except $\alpha-SrZrS_3$. We have found that the ionic contribution to the effective dielectric screening is negligible and hence, does not affect the exciton binding energy. The calculated spectroscopic limited maximum efficiency (SLME) values at 1 µm absorber layer thickness are 21.33%, 25.45%, 21.19%, and 25.02% for $CaZrS_3$, $\alpha-SrZrS_3$, $\beta-SrZrS_3$, and $BaZrS_3$, respectively, suggesting their usage in photovoltaics.

- **Chapter 7:** This chapter concludes the work presented in this thesis and presents a brief description of future projects.

CHAPTER 2

Theoretical methodology

2.1 Computer simulation

A computer simulation is the process of running programs on an assembly of computers connected through network to depict the real-world process through an abstract model. It has become an integral part of scientific research and innovation as it can complement, confirm, or preclude the theory and experimentation. With the combination of mathematical modeling, computer simulations are used in various natural systems in the field of physics, chemistry, biology, climatology, as well as in human systems such as medical science, economics, social science, security, and engineering. Simulations can be applied to estimate the properties of the systems that are too complex to solve analytically. That's why “computer simulation" has entrenched itself as the third pillar of science apart from the theory and experiment. In the present scenario, advancement in computer architecture makes it possible to address the problem at a wide range of length and time scales. Multi-scale computer simulation includes length scale starting with the nucleus, electronic structure, atomistic and nanoscale, mesoscale, all the way to micro/macro-scale and time scale, from picoseconds, all the way to months and years. In physics, the properties of materials and their behavior in different environmental conditions can be determined from the multi-scale computer simulation of one level or the other. The methods used at various length and time scales to describe a system are shown in Figure 2.1. These levels are distinguished as: (i) atomistic methods, specifically, Electronic Structure calculations, Molecular Dynamics and Monte Carlo, (ii) mesoscale methods viz. Dislocation Dynamics and Phase Field, and (iii) continuum methods such as Finite Element and Finite Difference approaches. The results from one level are used in another level, while capturing the relevant physics. Multi-scale modeling is useful in computational materials engineering since it allows one to predict the material properties or the system behavior based on the information of atomic structure and properties of elementary processes. Computational techniques can be utilized to determine ground-state and excited-state properties such as geometries, ground-state energies, charge densities, band gaps, optical spectra, and vibrational spectra to name a few. Depending on the phenomena and properties one is interested in, the aforementioned classified models can be implemented.

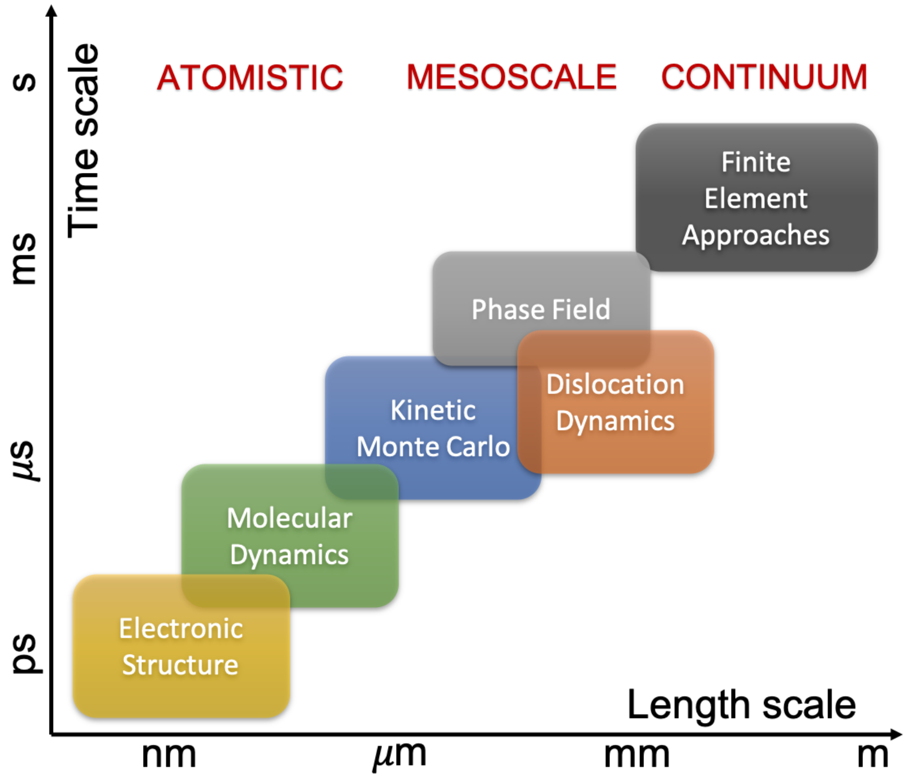

Figure 2.1: Multi-scale simulation in various length and time scales.

In this thesis work, the first-principles electronic structure calculations are employed to design the materials for photocatalysis and photovoltaics. The theoretical framework of our work is outlined as follows: First, a short description of the basic idea behind first-principles calculations is introduced, which explains how the properties of condensed matter system can be determined under quantum mechanical description by solving many-electron Schrödinger equation. Then, we discuss the origin behind the density functional theory (DFT), which is a practical route to solve many-electron quantum system. Further, we categorize the exchange-correlation functionals, which contain different approximations. For determining the excited-state properties of the systems, we introduce the Green's function approaches, specifically, GW approximation and Bethe-Salpeter equation (BSE).

2.2 First-principles calculation

The calculation that is based on the established science (i.e., follows the basic laws of physics) and does not assume any empirical law or parameter fitting is termed as "First-principles calculation". It is mainly governed by the principles of quantum mechanics and provides a detailed insight into the origin of electronic, optical, and magnetic properties of materials and molecules. Our surroundings consist of condensed matter having sufficiently low energy to form stable systems of atoms and molecules, specifically, solid, or liquid phases. The constituents of condensed matter are atoms, which are made of positively charged nucleus surrounded by negatively charged electron clouds. Therefore, the interactions between atoms, such as covalent, ionic, chemical, and molecular bonding can be traced to the interactions of their constituents, specifically, electrons and nuclei. These fundamental interactions are responsible for the physics behind the condensed matter system. The modeling of these basic interactions accurately is a daunting task. If we can model these interactions accurately, then the complex physical phenomena that arise because of these interactions should emerge naturally in our calculations. The rules that dictate the interaction of electrons and nuclei in condensed matter are relatively simple. The dynamics of these particles is governed by mathematical formalism of basic quantum mechanics, mainly by Schrödinger equation. The properties of condensed matter can be easily determined by solving Schrödinger equation. However, the size of the problem in terms of a numerical formulation, makes it difficult to solve the Schrödinger equation. The fundamental laws, which are essential for the mathematical treatment of major part of physics and chemistry, are fully known, but the equations that results from the applicability of these laws are very complicated to be solved. Therefore, the center of attention of the ongoing research in this field is the development of efficient and accurate computational techniques to deal with many-body problem.

2.3 Many-body physics: A theoretical framework

Many-body physics paves the way for understanding the collective behavior of many interacting quantum particles. The properties of a system can be determined by solving the fundamental equation of quantum mechanics, specifically, the Schrödinger equation. On solving the Schrödinger equation, one could get the many-body wave function that describes the quantum state of a system. Further, all the physical phenomena of a system can be obtained from wave function. However, solving the many-electron Schrödinger equation is practically impossible except for very simple cases, such as H-atom, He^+, harmonic oscillator etc. Due to finite speed and memory of computers, the numerical solution is possible only for a few number of electrons. Since determining the exact solution is computationally a daunting task, the normal strategy is to reduce it to a closely related problem, for which the exact solution is known. Then, the difference between these two, which is assumed to be small, is treated as a perturbation to the exactly solvable problem. Therefore, the approximate solution is determined in many-electron problem and subsequently, it is improved by small corrections to the previously obtained approximate value. To tackle the many-electron system, the first approximation is the Born-Oppenheimer approximation, in which the electrons and nuclei motion is decoupled. This is because as the nuclei are much heavier than the electrons, they can be assumed to be at rest with respect to electrons. Although this approximation makes the many-electron problem a bit easy, it is still challenging to deal with the electron-electron interaction. For an N-electron system, one needs to deal with $3N$-variables. Mainly, two types of approaches are common to solve N-electron system: (i) wave function-based approach, and (ii) DFT. The N-electron wave function in the former and the 3-dimensional electron density in the latter case are the quantities of concern in solving the N-electron problem. One of the traditional wave function methods is performed by Hartree in 1928, in which he treated the electrons as independent, and each electron interacts via only a central potential due to other electrons and nuclei. Therefore, the total wave function can be written as a product of N independent electrons wave functions. However, the wave function obtained from this method fails to satisfy the antisymmetric nature, which should be followed by the electrons being fermions. Later, in 1930, Fock replaced the Hartree product of wave functions with the Slater determinant that satisfies the antisymmetric condition. This approximation is the well-known Hartree–Fock approximation. The Hartree–Fock method considers the direct Coulomb and exact exchange interactions of electrons. However, the electronic correlation was still missing, leading to large deviation from experimental results. To overcome the drawbacks of Hartree–Fock method, post-Hartree-Fock methods are formulated, which include the electronic correlation in many-electron wave function. These include Møller-Plesset (MP) perturbation theory, configuration interaction (CI), coupled cluster (CC) methods, multi-configurational self-consistent field (MCSCF) and quantum Monte Carlo (QMC) methods. However, these accurate methods come with the price of very high computational cost, such that they are only applicable to a system of few atoms.

In search of the practical solution to many-electron problem, density functional based approaches have been devised that can take care of large number of interacting particles in the system as well as include the electronic correlation. DFT has been formulated as an exact theory to deal with many-electron system, in which the energy is a functional of electronic density. However, the exact relationship between energy and density is not known. Therefore, DFT is implemented with suitable approximations to the exchange and correlation effects. DFT has gained unparalleled success in determining the properties of various materials, which is ascribed to the good balance of accuracy and computational cost. Moreover, the DFT provides the good estimate for ground-state properties. For predicting the excited-state properties, *ab initio* many-body perturbation theory calculations such as GW approximation and Bethe-Salpeter equation (BSE) approach work better.

2.4 Time-independent many-body Schrödinger equation

The starting point of quantum mechanical approach to find the electronic structure of matter is the Schrödinger equation. One has to find the solution of time-independent non-relativistic Schrödinger equation

$$\hat{H}\Psi_k\left(\mathbf{r}_1, \mathbf{r}_2, \ldots, \mathbf{r}_N, \mathbf{R}_1, \mathbf{R}_2, \ldots, \mathbf{R}_M\right) = E_k\Psi_k\left(\mathbf{r}_1, \mathbf{r}_2, \ldots, \mathbf{r}_N, \mathbf{R}_1, \mathbf{R}_2, \ldots, \mathbf{R}_M\right) \tag{2.1}$$

Here, $\hat{H}$ is the Hamiltonian operator for a system of M nuclei and N electrons. The Hamiltonian operator $\hat{H}$ can be written as

$$\begin{aligned}\hat{H} = &-\sum_{i=1}^{N}\frac{\hbar^2}{2m_e}\nabla_i^2 - \sum_{I=1}^{M}\frac{\hbar^2}{2M_I}\nabla_I^2 - \sum_{i=1}^{N}\sum_{I=1}^{M}\frac{Z_I e^2}{|\mathbf{R}_I - \mathbf{r}_i|}\\ &+\frac{1}{2}\sum_{i=1}^{N}\sum_{j\neq i}^{N}\frac{e^2}{|\mathbf{r}_i - \mathbf{r}_j|} + \frac{1}{2}\sum_{I=1}^{M}\sum_{J\neq I}^{M}\frac{Z_I Z_J e^2}{|\mathbf{R}_I - \mathbf{R}_J|}\end{aligned} \tag{2.2}$$

where i and j run over N electrons while I and J run over M nuclei in the system. m_e is the mass of electron and M_I is the mass of nucleus I. Z_I is the nuclear charge of nucleus I. The first two terms of equation 2.2 represent the kinetic energies of an N electrons and M nuclei, respectively. The last three terms correspond to the attractive electrostatic interaction between the nuclei and electrons, the repulsive interaction between the electron-electron and nucleus-nucleus, respectively. The wave function $\Psi_k\left(\mathbf{r}_1, \mathbf{r}_2, \ldots, \mathbf{r}_N, \mathbf{R}_1, \mathbf{R}_2, \ldots, \mathbf{R}_M\right)$ corresponds to the state k of the system. E_k is the corresponding energy (eigenvalue). The wave function itself does not correspond to any physical quantity, but its square, i.e., $|\Psi|^2$ [1] represents the probability density. Simply put, $|\Psi|^2$ is the probability density to find a particle at a particular point in space, at a particular instant of time. For the wave function to be physically accepted, it should be continuous, doubly differentiable, and square integrable. An introduction to quantum mechanics can be found in Ref [68].

However, due to the large dimensionality (i.e., all constituting particles have three degrees of freedom) and constraints on wave function, the Schrödinger equation cannot be solved exactly for many-electron system. Hence, the approximations are used to solve the Schrödinger equation. The first and foremost approximation is the Born–Oppenheimer or adiabatic approximation, in which the dynamics of the electrons and nuclei is treated separately. Since the nuclei are much heavier than the electrons, the motion of electrons and nuclei can be separated. The electrons will adjust their positions instantly whenever nuclei move and the movement of electrons depends parametrically on the positions of nuclei. Therefore, under Born–Oppenheimer approximation, the wave functions of electrons and nuclei can be decoupled and expressed as follows

$$\Psi_{total} = \psi_{electronic} \times \psi_{nuclear}$$
$$\Psi\left(\mathbf{r}_1, \mathbf{r}_2, \ldots, \mathbf{r}_N, \mathbf{R}_1, \mathbf{R}_2, \ldots, \mathbf{R}_M\right) = \psi\left(\mathbf{r}_1, \mathbf{r}_2, \ldots, \mathbf{r}_N; \mathbf{R}_1, \mathbf{R}_2, \ldots, \mathbf{R}_M\right) \times \psi\left(\mathbf{R}_1, \mathbf{R}_2, \ldots, \mathbf{R}_M\right) \tag{2.3}$$

The components of energy due to nuclei (i.e., kinetic energy of nuclei and internuclear repulsion energy) can be added later after solving for the electrons. Therefore, the nuclear and electronic degrees of motion can be decoupled and the Hamiltonian for the theory of electronic structure can be written as

$$\hat{H} = \hat{T} + \hat{V}_{ext} + \hat{V}_{int} \tag{2.4}$$

In atomic units $\hbar = m_e = e = \frac{4\pi}{\epsilon_0} = 1$. The kinetic energy operator for the electrons $\hat{T}$ is

$$\hat{T} = -\sum_{i=1}^{N} \frac{1}{2} \nabla_i^2 \tag{2.5}$$

$\hat{V}_{ext}$ is the potential acting on the electrons due to the nuclei,

$$\hat{V}_{ext} = \sum_{i=1}^{N} \sum_{I=1}^{M} V_I\left(|\mathbf{r}_i - \mathbf{R}_I|\right) \tag{2.6}$$

and $\hat{V}_{int}$ is the electron-electron interaction,

$$\hat{V}_{int} = \frac{1}{2} \sum_{i=1}^{N} \sum_{j \neq i}^{N} \frac{1}{|\mathbf{r}_i - \mathbf{r}_j|} \tag{2.7}$$

---

[1] $|\Psi|^2 = \Psi^* \Psi$, where Ψ^* is the complex conjugate of Ψ.

After the implementation of Born–Oppenheimer approximation, it is still difficult to solve the Schrödinger equation with the electronic Hamiltonian. Therefore, further approximations are needed to solve the Schrödinger equation, which are discussed in the following sections.

2.4.1 The Hartree approximation

The assumption made by Hartree is that we may write the many-electron wave function as

$$\Psi\left(\mathbf{r}_1, \mathbf{r}_2, \ldots, \mathbf{r}_N\right) = \phi_1\left(\mathbf{r}_1\right)\phi_2\left(\mathbf{r}_2\right)\ldots\phi_N\left(\mathbf{r}_N\right) \tag{2.8}$$

where $\mathbf{r}_i$ contains the spatial coordinates and a spin coordinate for the i-th electron and $\phi_i\left(\mathbf{r}_j\right)$ is the single-electron spin-orbital. Equation 2.8 implies that the electrons are *independent*, and interact only with the averaged density of electrons. Now, the electronic Hamiltonian can be written as

$$\hat{H}_{el} = \sum_{i=1}^{N} \hat{h}_i + \hat{V}_{int} \tag{2.9}$$

where

$$\hat{h}_i = -\frac{1}{2}\nabla_i^2 + \hat{v}_i \tag{2.10}$$

and $\hat{h}_i$ only depends on coordinates $\mathbf{r}_i$ of i-th electron. $\hat{V}_{int}$ is approximated by the sum of the interaction of individual electron with averaged density of N-1 electrons as follows

$$\hat{V}_{int} \approx \sum_{i=1}^{N} \hat{g}_i\left(\mathbf{r}\right) \tag{2.11}$$

where

$$\hat{g}_k\left(\mathbf{r}\right) = \int \rho^{(k)}\left(\mathbf{r}'\right)\frac{1}{\left|\mathbf{r} - \mathbf{r}'\right|} d\mathbf{r}' \tag{2.12}$$

and

$$\rho^{(k)}\left(\mathbf{r}\right) = \sum_{\substack{i=1 \\ i\neq k}}^{N} \left|\phi_i\left(\mathbf{r}\right)\right|^2 \tag{2.13}$$

Therefore, many-electron Schrödinger equation becomes N independent single electron equations

$$\left(-\frac{1}{2}\nabla_i^2 + \hat{v}_i + \hat{g}_i\right)\phi_i\left(\mathbf{r}\right) = \epsilon_i\phi_i\left(\mathbf{r}\right) \tag{2.14}$$

The ϵ_i is the energy of the i-th electron. Practically, we make a guess of orbitals ϕ_i (e.g., from hydrogen atom wave function). From spin-orbitals, $\hat{g}_i$ can be calculated. Then, we solve the N independent single electron equations and get the N new spin-orbitals. Now, we use the new spin-orbitals as a starting point and iterate until convergence. The converged orbitals are known as *self-consistent field* spin-orbitals. We obtain the many-electron wave function Ψ using these spin-orbitals and then, find out the total energy E of the ground state. The total energy is not equal to the sum of individual orbital energies ϵ_i because the electron-electron interaction counted twice when we formulate the effective potential. Therefore, the corrected total energy is given by

$$E = \sum_{i=1}^{N} \epsilon_i - \frac{1}{2} \sum_{i=1}^{N} \sum_{j \neq i}^{N} J_{ij} \tag{2.15}$$

where J_{ij} is the Coulomb interaction between electron i and j. These are called Coulomb integrals and given by

$$J_{ij} = \int \int \frac{\rho_i(\mathbf{r}_1)\, \rho_j(\mathbf{r}_2)}{|\mathbf{r}_1 - \mathbf{r}_2|} d\mathbf{r}_1 d\mathbf{r}_2 = \int \int |\phi_i(\mathbf{r}_1)|^2 \frac{1}{|\mathbf{r}_1 - \mathbf{r}_2|} |\phi_j(\mathbf{r}_2)|^2 d\mathbf{r}_1 d\mathbf{r}_2 \tag{2.16}$$

$$J_{ij} = \int \int \phi_i^*(\mathbf{r}_1)\, \phi_i(\mathbf{r}_1) \frac{1}{|\mathbf{r}_1 - \mathbf{r}_2|} \phi_j^*(\mathbf{r}_2)\, \phi_j(\mathbf{r}_2)\, d\mathbf{r}_1 d\mathbf{r}_2 \tag{2.17}$$

Hartree approximation lays the foundation for subsequent developments in the methodologies to solve the many-electron system.

2.4.2 The Hartree–Fock approximation

A crucial drawback of Hartree approximation is that the antisymmetry property of the electronic wave function is not satisfied. The electronic wave function fails to satisfy the Pauli exclusion principle and hence, the description of electronic component is incomplete. The main purpose of Hartree–Fock approximation is to correct the failure of Hartree approximation. In this approximation, the variational wave function is in the form of a Slater determinant which satisfies the antisymmetric condition. Pauli exclusion principle is the direct consequence of the antisymmetric condition. According to this, any two fermions cannot occupy the same orbital at the same time.

Slater determinant for N orbitals is represented as

$$\Psi(\mathbf{r}_1, \mathbf{r}_2, \ldots, \mathbf{r}_N) = \frac{1}{\sqrt{N!}} \begin{vmatrix} \phi_1(\mathbf{r}_1) & \phi_2(\mathbf{r}_1) & \cdots & \phi_N(\mathbf{r}_1) \\ \phi_1(\mathbf{r}_2) & \phi_2(\mathbf{r}_2) & \cdots & \phi_N(\mathbf{r}_2) \\ \vdots & \vdots & \ddots & \vdots \\ \phi_1(\mathbf{r}_N) & \phi_2(\mathbf{r}_N) & \cdots & \phi_N(\mathbf{r}_N) \end{vmatrix} \tag{2.18}$$

where $\mathbf{r}_i$ contains the spatial coordinates and a spin coordinate for the i-th electron and $\phi_i\left(\mathbf{r}_j\right)$ is the i-th single-electron spin orbital. Now, the total energy is given by

$$E = \langle\Psi|H|\Psi\rangle = \sum_{i=1}^{N} H_i + \frac{1}{2}\sum_{i=1}^{N}\sum_{j=1}^{N}\left(J_{ij} - K_{ij}\right) \tag{2.19}$$

where

$$H_i = \int \phi_i^*\left(\mathbf{r}\right)\hat{h}_i\phi_i\left(\mathbf{r}\right)d\mathbf{r} \tag{2.20}$$

$\hat{h}_i$ is defined by equation 2.10, J_{ij} is Coulomb integral defined by equation 2.17, and K_{ij} is called as *exchange* integral, defined as

$$K_{ij} = \int\int \phi_i^*\left(\mathbf{r}_1\right)\phi_j\left(\mathbf{r}_1\right)\frac{1}{|\mathbf{r}_1 - \mathbf{r}_2|}\phi_i\left(\mathbf{r}_2\right)\phi_j^*\left(\mathbf{r}_2\right)d\mathbf{r}_1 d\mathbf{r}_2 \tag{2.21}$$

This exchange term is the consequence of the Pauli exclusion principle, and create repulsion for the electrons of same spin.

The Hartree–Fock approximation takes care of exact exchange, but electronic correlation is missing, which plays an important role in bond breaking and bond formation. Also, many wave functions are possible that satisfy antisymmetric nature, which cannot be described by the single Slater determinant form, and are unattainable within Hartree–Fock approximation. To account for the correlation effects, one needs to go to the correlated methods, which deal with the multi-determinant wave functions. However, these post-Hartree–Fock methods are computationally very expensive, and their computational demand increases further with increase in the size of the systems. On the other hand, density functional theory is a conceptually simple and computationally practicable strategy that incorporates the effects of both exchange and correlation.

2.5 Density functional theory (DFT)

In DFT, the basic quantity of concern is electron density, which is a scalar function of position. This approach is different from wave function approach to solve Schrödinger equation. The use of electron density rather than the wave function simplify the many-electron system problem since the dimensionality is reduced from $3N$ to 3. The electron density remains three-dimensional, i.e., it does not change the dimension on increasing the number of electrons. This facilitates the DFT to be used for a large number of atoms with reasonable computational cost. Therefore, DFT is widely used to tackle the many-electron systems, specifically, atoms, molecules and solids. It is mainly used to describe the ground-state properties of the systems, which are the functionals of electron density. The development of DFT is described in the subsequent sections.

2.5.1 Thomas-Fermi-Dirac approximation

Instead of the wave function approaches like Hartree and Hartree–Fock, a different approach was proposed by Thomas and Fermi in 1927. Thomas and Fermi proposed electronic density as the fundamental variable for calculating the energy of the many-electron system. In their original work, Thomas and Fermi proposed an expression for the kinetic energy of the many-electron system, which is approximated as a functional of density. They assumed the system as non-interacting uniformly distributed electron with density equal to the local density at any given point and used fermion statistical mechanics to derive the kinetic energy for uniform electron gas as particles in a box

$$T_{TF}\left[n\right] = C_1 \int n^{\frac{5}{3}}\left(\mathbf{r}\right) d\mathbf{r} \tag{2.22}$$

where $C_1 = \frac{3}{10}\left(3\pi^2\right)^{\frac{2}{3}} n(\mathbf{r})$ = 2.871 in atomic units and $n\left(\mathbf{r}\right)$ is the electronic density for a uniform electron gas. They neglected the exchange and correlation among electrons. Exchange can be introduced with local approximation by considering Slater's expression for the uniform electron gas (Dirac, 1930; Slater, 1951)

$$E_X\left[n\right] = C_2 \int n^{\frac{4}{3}}\left(\mathbf{r}\right) d\mathbf{r} \tag{2.23}$$

where $C_2 = -\frac{3}{4}\left(\frac{3}{\pi}\right)^{\frac{1}{3}}$ = 0.739 in atomic units. Therefore, the energy functional for electrons in presence of external potential $V_{ext}\left(\mathbf{r}\right)$

$$\begin{aligned} E_{TFD}\left[n\right] = C_1 \int n^{\frac{5}{3}}\left(\mathbf{r}\right) d^3r + \int V_{ext}\left(\mathbf{r}\right) n\left(\mathbf{r}\right) d^3r + C_2 \int n^{\frac{4}{3}}\left(\mathbf{r}\right) d^3r \\ + \frac{1}{2}\int \frac{n\left(\mathbf{r}\right) n\left(\mathbf{r}'\right)}{\left|\mathbf{r}-\mathbf{r}'\right|} d^3r d^3r' \end{aligned} \tag{2.24}$$

where the last term is the classical electrostatic Hartree energy. With including approximated exchange term, the theory is known as *Thomas-Fermi-Dirac* (TFD).

The ground-state density and energy can be found by minimizing the functional $E[n]$ for all possible $n\left(\mathbf{r}\right)$ subject to the constraint that the total integrated charge be equal to the number of electrons

$$\int n\left(\mathbf{r}\right) d^3r = N \tag{2.25}$$

Using the method of Lagrange multipliers, the solution can be found by an unconstrained minimization of the functional

$$\Omega_{TF}\left[n\right] = E_{TF}\left[n\right] - \mu\left\{\int n\left(\mathbf{r}\right) d^3r - N\right\} \tag{2.26}$$

where the Lagrange multiplier μ is the Fermi energy. Equation 2.26 leads to the expression

$$\frac{1}{2}\left(3\pi^2\right)^{\frac{2}{3}} n^{\frac{2}{3}}\left(\mathbf{r}\right) + V\left(\mathbf{r}\right) - \mu = 0 \tag{2.27}$$

where $V\left(\mathbf{r}\right) = V_{ext}\left(\mathbf{r}\right) + V_{Hartree}\left(\mathbf{r}\right) + V_x\left(\mathbf{r}\right)$ is the total potential.

This model is not good to describe the electronic structure of matter since it is based on crude approximations and essential physics (namely, correlation effects) is missing.

2.5.2 The Hohenberg-Kohn theorems

In 1964, Hohenberg and Kohn [54] proved two theorems in their famous paper which is the foundation of modern density functional theory.

Theorem I: *For any system of interacting electrons in an external potential $V_{ext}\left(\mathbf{r}\right)$, the potential $V_{ext}\left(\mathbf{r}\right)$ is determined uniquely, apart from a trivial additive constant, by the electronic ground-state density $n\left(\mathbf{r}\right)$.*

For the proof let us assume that there exists two different potentials $V_{ext}\left(\mathbf{r}\right)$ and $V'_{ext}\left(\mathbf{r}\right)$, which give rise to same ground-state density $n\left(\mathbf{r}\right)$. These two different potentials leads to two different Hamiltonians H and H'. On solving the Schrödinger equation, we will get different wave functions Ψ and Ψ' corresponding to Hamiltonians H and H'. Then, the ground-state energies corresponding to Ψ and Ψ' are calculated as: $E = \langle\Psi|H|\Psi\rangle$ and $E' = \langle\Psi'|H'|\Psi'\rangle$. Here, we have considered the non-degenerate case, but Hohenberg-Kohn theorem proof can be extended to degenerate case as well [69]. Further, using variational principle

$$E < \langle\Psi'|H|\Psi'\rangle = \langle\Psi'|H'|\Psi'\rangle + \langle\Psi'|H - H'|\Psi'\rangle = E' + \int n\left(\mathbf{r}\right)\left[V_{ext}\left(\mathbf{r}\right) - V'_{ext}\left(\mathbf{r}\right)\right] d\mathbf{r} \tag{2.28}$$

Similarly, if we solve for E', we can swap the indexes in Equation 2.28 such that

$$E' < \langle\Psi|H'|\Psi\rangle = \langle\Psi|H|\Psi\rangle + \langle\Psi|H' - H|\Psi\rangle = E + \int n\left(\mathbf{r}\right)\left[V'_{ext}\left(\mathbf{r}\right) - V_{ext}\left(\mathbf{r}\right)\right] d\mathbf{r} \tag{2.29}$$

On adding Equation 2.28 and 2.29, we obtain

$$E + E' < E + E' \tag{2.30}$$

which is a contradictory inequality. Therefore, our initial assumption was wrong and the ground-state density uniquely determines the potential.

Corollary I: Since $n\left(\mathbf{r}\right)$ uniquely determines $V_{ext}\left(\mathbf{r}\right)$, in turn, $V_{ext}\left(\mathbf{r}\right)$ fixes the Hamiltonian and hence, the many-body wave functions are determined. Therefore, all the properties of the system are determined provided only the ground-state density $n\left(\mathbf{r}\right)$.

Theorem II: *A universal energy functional $E[n]$ using density $n\left(\mathbf{r}\right)$ can be defined, valid for any number of particles and any external potential $V_{ext}\left(\mathbf{r}\right)$. For a given potential $V_{ext}\left(\mathbf{r}\right)$, the $E[n]$ equals the correct ground-state energy of the system which is the global minimum value for the correct ground-state density $n\left(\mathbf{r}\right)$.*

For the proof, we restrict the space of densities to be V-representable, which can be represented by a potential. It can also be proved without this restriction and a general proof can be found in Ref [70]. Since, all the properties of a system can be determined from the functional of the density, the energy functional can be written as

$$\begin{aligned} E_{HK}\left[n\right] &= T\left[n\right] + E_{int}\left[n\right] + \int V_{ext}\left(\mathbf{r}\right) n\left(\mathbf{r}\right) d\mathbf{r} \\ &= F_{HK}\left[n\right] + \int V_{ext}\left(\mathbf{r}\right) n\left(\mathbf{r}\right) d\mathbf{r} \end{aligned} \tag{2.31}$$

where

$$F_{HK}\left[n\right] = T\left[n\right] + E_{int}\left[n\right] \tag{2.32}$$

is the universal functional of $n\left(\mathbf{r}\right)$ which includes kinetic and interaction energy of electrons. Since $V_{ext}\left(\mathbf{r}\right)$ depends on nuclear coordinates, its contribution is system-specific. Now, consider the ground-state density of a system is $n_1\left(\mathbf{r}\right)$ corresponding to potential $V_{ext}^1\left(\mathbf{r}\right)$. Then, the energy is the expectation value of the Hamiltonian

$$E_1 = E_{HK}\left[n_1\right] = \langle\Psi_1|H|\Psi_1\rangle \tag{2.33}$$

where Ψ_1 is the wave function corresponding to the ground state. Let us consider a different density $n_2\left(\mathbf{r}\right)$ that corresponds to a different wave function Ψ_2. Then, using variational principle

$$E_1 = E_{HK}\left[n_1\right] = \langle\Psi_1|H|\Psi_1\rangle < \langle\Psi_2|H|\Psi_2\rangle = E_{HK}\left[n_2\right] = E_2 \tag{2.34}$$

Hence, the Hohenberg-Kohn functional obtained from the true ground-state density provides the lowest energy than for any other arbitrary density. It follows that if the functional of the density is known, then the ground-state energy and density can be determined by minimizing it with respect to the variations in the density. Note that only the ground state is accessible through this functional. The guidance regarding excited states is not provided.

Although these theorems prove the existence of a universal functional $F_{HK}[n]$, but there is no prescription on how to determine it. The Kohn-Sham equations provide a practical framework to solve the many-electron system.

2.5.3 The Kohn-Sham ansatz

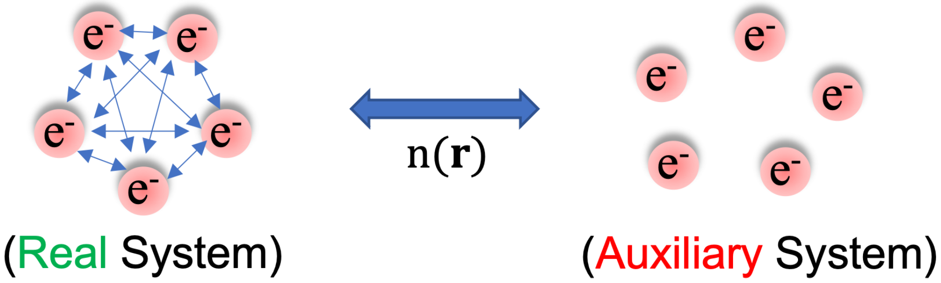

Figure 2.2: Schematic representation of mapping of interacting system to a non-interacting many-electron system through the same ground-state electron density.

In 1965, Kohn and Sham [55] suggested an approach to determine the unknown functional $F_{HK}[n]$. They introduced a non-interacting particle system and assumed that the ground-state density of the original interacting system and auxiliary non-interacting system is same. A schematic illustration of the same is shown in Figure 2.2. The auxiliary Hamiltonian is chosen to have the usual kinetic energy operator and an effective local potential $V^{\sigma}_{eff}(\mathbf{r})$ acting on an electron of spin σ at point $\mathbf{r}$

$$\hat{H}^{\sigma}_{aux} = -\frac{1}{2}\nabla^2 + V^{\sigma}_{eff}(\mathbf{r}) \tag{2.35}$$

$\psi^{\sigma}_i(\mathbf{r})$ are the eigenstates (Kohn-Sham orbitals) with the lowest eigenvalues ϵ^{σ}_i of the above Hamiltonian. The density of the auxiliary system is given by

$$n(\mathbf{r}) = \sum_{\sigma} n(\mathbf{r},\sigma) = \sum_{\sigma}\sum_{i=1}^{N^{\sigma}} |\psi^{\sigma}_i(\mathbf{r})|^2 \tag{2.36}$$

The kinetic energy T_s of independent-electron auxiliary system is expressed as a functional of the Kohn-Sham orbitals

$$T_s = -\frac{1}{2}\sum_{\sigma}\sum_{i=1}^{N^{\sigma}}\langle\psi^{\sigma}_i|\nabla^2|\psi^{\sigma}_i\rangle = \frac{1}{2}\sum_{\sigma}\sum_{i=1}^{N^{\sigma}}\int|\nabla\psi^{\sigma}_i(\mathbf{r})|^2 d\mathbf{r} \tag{2.37}$$

Classical coulomb interaction energy of the electron density $n(\mathbf{r})$ interacting with itself

$$E_{Hartree}[n] = \frac{1}{2}\int\frac{n(\mathbf{r})\,n(\mathbf{r}')}{|\mathbf{r}-\mathbf{r}'|}d\mathbf{r}d\mathbf{r}' \tag{2.38}$$

Therefore, the total energy in the Kohn-Sham formulation can be written as

$$E_{KS} = T_s\left[n\right] + \int V_{ext}\left(\mathbf{r}\right) n\left(\mathbf{r}\right) d\mathbf{r} + E_{Hartree}\left[n\right] + E_{xc}\left[n\right] \tag{2.39}$$

All the many-body interactions of exchange and correlation are wrapped into the exchange-correlation energy E_{xc}. E_{xc} can also be expressed as

$$E_{xc}\left[n\right] = F_{HK}\left[n\right] - \left(T_s\left[n\right] + E_{Hartree}\left[n\right]\right) \tag{2.40}$$

or

$$E_{xc}\left[n\right] = \langle\hat{T}\rangle - T_s\left[n\right] + \langle\hat{V}_{int}\rangle - E_{Hartree}\left[n\right] \tag{2.41}$$

Here, $\langle\hat{T}\rangle$ is the kinetic energy and $\langle\hat{V}_{int}\rangle$ is the internal interaction energy of the original many-body interacting system. $E_{xc}\left[n\right]$ is responsible for binding atoms into molecules and solids. Therefore, the Kohn-Sham equations can be written as

$$H_{KS}^{\sigma}\psi_i^{\sigma}\left(\mathbf{r}\right) = \epsilon_i^{\sigma}\psi_i^{\sigma}\left(\mathbf{r}\right) \tag{2.42}$$

where

$$H_{KS}^{\sigma}\left(\mathbf{r}\right) = -\frac{1}{2}\nabla^2 + V_{KS}^{\sigma}\left(\mathbf{r}\right) \tag{2.43}$$

and

$$\begin{aligned} V_{KS}^{\sigma}\left(\mathbf{r}\right) &= V_{ext}\left(\mathbf{r}\right) + \frac{\delta E_{Hartree}}{\delta n\left(\mathbf{r},\sigma\right)} + \frac{\delta E_{xc}}{\delta n\left(\mathbf{r},\sigma\right)} \\ &= V_{ext}\left(\mathbf{r}\right) + V_{Hartree}\left(\mathbf{r}\right) + V_{xc}^{\sigma}\left(\mathbf{r}\right) \end{aligned} \tag{2.44}$$

These equations can be solved self-consistently as shown in Figure 2.3. However, the exact dependence of $E_{xc}\left[n\right]$ on the density n is not known. Therefore, certain approximations are used to determine the exchange-correlation functional.

2.5.4 Exchange-correlation functionals

2.5.4.1 Local Density Approximation (LDA)

In 1965, Kohn–Sham approximated exchange-correlation functional $E_{xc}\left[n\right]$ as a local or nearly local functional of the density. $E_{xc}\left[n\right]$ provides a self-interaction correction. It also describes how one electron avoids another.

$$E_{xc}^{LDA}\left[n\right] = \int n\left(\mathbf{r}\right)\varepsilon_{xc}^{unif}\left(n\left(\mathbf{r}\right)\right) d\mathbf{r} \tag{2.45}$$

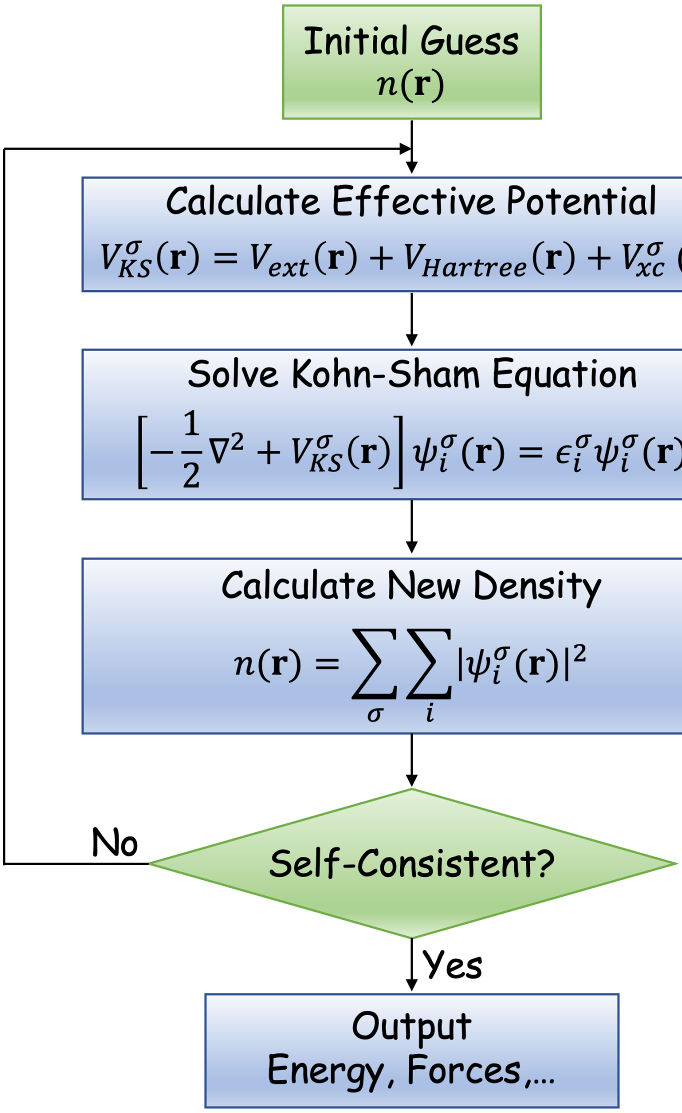

Figure 2.3: Flow chart to solve the Kohn-Sham equations self-consistently.

where $\varepsilon_{xc}^{unif}(n(\mathbf{r}))$ is the exchange-correlation energy per electron in a gas of electrons with uniform density $n(\mathbf{r})$. LDA is exact for *any* uniform density. LDA is accurate for any $n(\mathbf{r})$ that varies slowly over space:

$$\frac{|\nabla n|}{n} \ll k_F = \left(3\pi^2 n\right)^{\frac{1}{3}} \tag{2.46}$$

and

$$\frac{|\nabla n|}{n} \ll k_S = \frac{2}{\sqrt{\pi}}\left(3\pi^2 n\right)^{\frac{1}{6}} \tag{2.47}$$

where k_F is the Fermi wave vector and k_S is the Thomas-Fermi wave vector. From Wigner (1938) approximation, $\varepsilon_{xc}^{unif}(n)$ can be written as

$$\varepsilon_{xc}^{unif}(n) = \varepsilon_{x}^{unif}(n) + \varepsilon_{c}^{unif}(n) \tag{2.48}$$

Dirac (1930) formulated $\varepsilon_x^{unif}(n)$ as

$$\varepsilon_x^{unif}(n) = -\frac{3}{4\pi}\left(3\pi^2 n\right)^{\frac{1}{3}} = -\frac{3}{4\pi}k_F = -\frac{3}{4\pi}\frac{\left(\frac{9\pi}{4}\right)^{\frac{1}{3}}}{r_s} \tag{2.49}$$

where Seitz radius, $r_s = \left(\frac{3}{4\pi n}\right)^{\frac{1}{3}}$, is the radius of a sphere which on average contains one electron and

$$\varepsilon_c^{unif}(n) \approx -0.056\left(\frac{n^{\frac{1}{3}}}{0.079 + n^{\frac{1}{3}}}\right) \approx -\frac{0.44}{7.8 + r_s} \tag{2.50}$$

is formulated by Wigner (1938). In high density limit ($r_s \to 0$), $\varepsilon_c^{unif} \to -0.056$, and in low density limit ($r_s \to \infty$), $\varepsilon_c^{unif} \to -\frac{0.44}{r_s}$. Quantum Monte Carlo (QMC) calculations with exact high and low density limits give an accurate ε_c^{unif}.

In 1972, Barth and Hedin extend LDA to spin polarized case known as **local spin density approximation** (LSDA):

$$E_{xc}^{LSDA}[n_\uparrow, n_\downarrow] = \int n(\mathbf{r})\,\varepsilon_{xc}^{unif}(n_\uparrow(\mathbf{r}), n_\downarrow(\mathbf{r}))\,d\mathbf{r} \tag{2.51}$$

If a system is or can be spin polarized in its ground state, with same up and down spin dependent external potential, i.e., $v_\uparrow(\mathbf{r}) = v_\downarrow(\mathbf{r}) = v(\mathbf{r})$, LSDA energies are more accurate than LDA. LSDA is more useful for calculating energies of molecules and solids, usually, extended system where spin symmetry is broken.This suggests a strategy to construct functionals beyond LDA:

(1) Add additional ingredients to the argument list of ε_{xc}.

(2) Use these added ingredients to satisfy more exact constraints and more appropriate norms.

These two steps suggest the Jacob's ladder of density functional approximations for the exchange-correlation energy stretching from the Hartree world up to the heaven of chemical accuracy [1]. Figure 2.4 shows the Jacob's ladder. It shows the exchange-correlation functional approximations hierarchy. The complexity, accuracy, computational cost, and time increases as we step up the ladder.

Binding energies of atoms are overestimated by LSDA. Also, the bond lengths are underestimated. Therefore, we need more appropriate approximations.

2.5.4.2 Generalized Gradient Approximation (GGA)

The idea for the GGA is proposed by the Langreth and Mehl in 1983 [71].

$$E_{xc}^{GGA}[n] = \int n(\mathbf{r})\,\varepsilon_{xc}^{GGA}(n, |\nabla n|)\,d\mathbf{r} \tag{2.52}$$

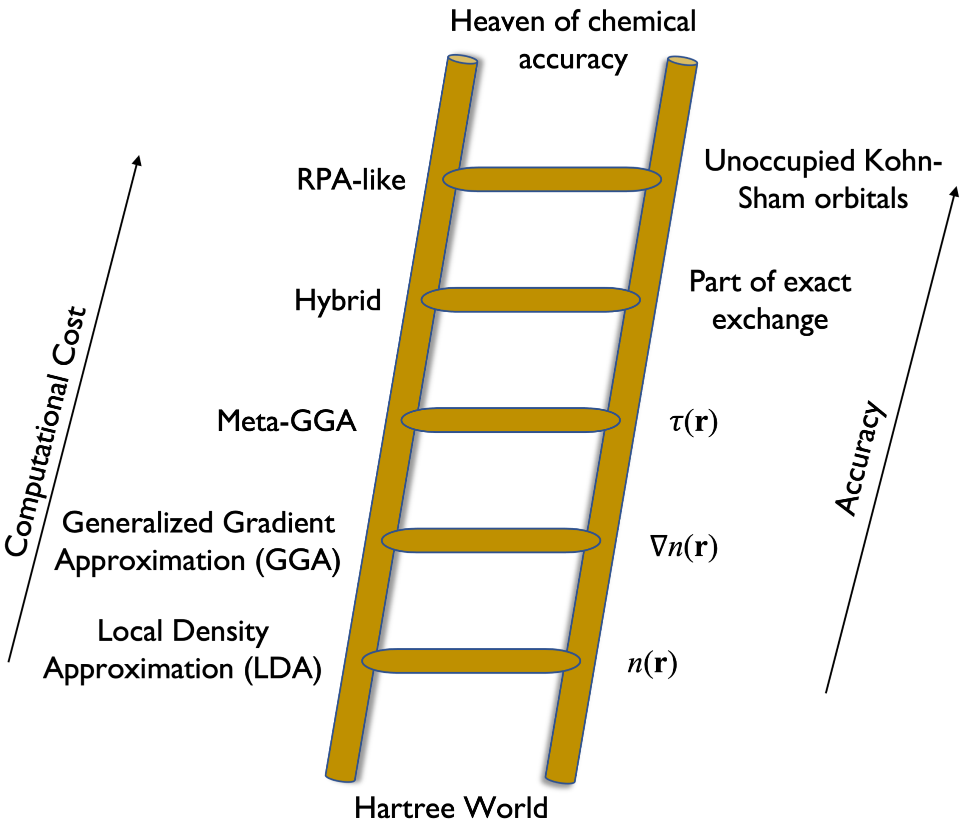

Figure 2.4: Jacob's ladder of density functional approximations [1]

Ma and Bruekner in 1968 [72] derived the gradient expansion (GE) as

$$E_{xc}^{GE} = \int n\left(\mathbf{r}\right) \varepsilon_{xc}^{unif}\left(n\left(\mathbf{r}\right)\right) d\mathbf{r} + \int B_{xc}\left(n\right) \frac{|\nabla n|^2}{n^{\frac{4}{3}}} d\mathbf{r} \tag{2.53}$$

where the coefficient $B_{xc}\left(n\right)$ is calculated approximately. $B_{xc}\left(n\right)$ has an exchange part which is independent of density n, and a correlation part which depends weakly on density n. It is exact for slowly varying electron gas, to order $|\nabla n|^2$. For real systems built up from atoms, the correlation part contains large error. So, GE is bad approximation for real systems. Therefore, the gradient expansion should be carried out more carefully retaining all the relevant contribution to desired order. Also, it should fulfill the exact constraints required by exchange and correlation hole. In order to satisfy these conditions, gradient expansions are modified, and named generalized gradient approximations (GGA's). In 1996, Perdew, Burke and Ernzerhof (PBE) presented a derivation of GGA, in which all parameters are fundamental constants [59]. It is widely used GGA. BLYP is another GGA functional used, where the parameters are fitted to experimental molecular data.

Binding energies of atoms are improved by GGA. Also, the bond lengths are improved. The GGA has certain limitations in the accuracy because non-local effect of exchange term is not taken into account completely, and self-interaction error is not fully recovered.

2.5.4.3 Meta-Generalized Gradient Approximation (meta-GGA)

Perdew *et. al.* (PZKB) in 1999 proposed

$$E_{xc}^{MGGA}[n] = \int n(\mathbf{r})\,\varepsilon_{xc}^{MGGA}(n, |\nabla n|, \tau)\, d\mathbf{r} \tag{2.54}$$

where τ is the kinetic energy density for the non-interacting system given by

$$\tau(\mathbf{r}) = \sum_{i}^{occup} \frac{1}{2}|\nabla\phi_i(\mathbf{r})|^2 \tag{2.55}$$

and

$$\int \tau(\mathbf{r})\, d\mathbf{r} = T_s[n] \tag{2.56}$$

τ can satisfy some exact constraints that no GGA can satisfies.

meta-GGA is semi-local functional. In spite of some improvement, meta-GGA still has certain issues. The self-interaction correction is incomplete in it. It can only be corrected by a non-local approximation.

2.5.4.4 Hybrid functionals

The idea of hybrid functionals is originated in 1993 by Becke. He mixed a fraction of exact exchange (Hartree-Fock (HF) exchange) with GGA exchange and correlation.

$$E_{xc}^{hyb} = \alpha E_x^{HF} + (1-\alpha)\, E_x^{GGA} + E_c^{GGA} \tag{2.57}$$

where coefficient α can be fitted empirically or estimated theoretically.

Accuracy of hybrid functionals is quite high. Non-local effects are taken into account in hybrid functionals. However, calculating the HF exchange computationally is a daunting task, especially for extended systems. Therefore, to circumvent this, Heyd, Scuseria and Ernzerhof proposed the screened hybrid functional (HSE) [60, 61]. In HSE, the long-range part of HF exchange is screened out by using a screened Coulomb potential. It lowers down the computational cost. The Coulomb potential is separated in short-range (SR) and long-range (LR) parts

$$\frac{1}{r} = \underbrace{\frac{1-\mathrm{erf}(\omega r)}{r}}_{\text{SR}} + \underbrace{\frac{\mathrm{erf}(\omega r)}{r}}_{\text{LR}} \tag{2.58}$$

where ω is the screening parameter that defines the range of separation, and the error function is given by

$$\mathrm{erf}(\omega r) = \frac{2}{\sqrt{\pi}} \int_0^{\omega r} e^{-x^2} dx \tag{2.59}$$

Then, the exchange-correlation energy is calculated as

$$E_{xc}^{HSE} = \alpha E_x^{HF,SR}(\omega) + (1-\alpha) E_x^{PBE,SR}(\omega) + E_x^{PBE,LR}(\omega) + E_c^{PBE} \tag{2.60}$$

HSE06 functional with $\alpha = 0.25$ and $\omega = 0.11$ bohr^{-1} as default values predicts the enthalpies of formation, ionization potentials, electron affinities, band gaps, and lattice constants with good accuracy. These parameters can also be varied to match the experimental values. This implies that we are lacking some understanding of how to construct them as they require at least one empirical parameter.

In the present thesis, we have mainly used PBE functional of GGA for relaxing the structure and HSE06 hybrid functional for energy calculations. Several codes are available to perform DFT calculations. We have performed the calculations as implemented in Vienna *ab initio* simulation package (VASP).

2.6 Basis set

The many-electron wave function is expanded in terms of the set of functions, which forms the basis set. The choice of basis functions is crucial for the efficiency of a given computational method and the first step in the implementation of a DFT method is to find a suitable basis set. Plane waves and Gaussian-type orbitals (GTOs) are two most commonly used basis functions. The former basis set is primarily used in the periodic crystals, whereas the latter one in the molecular systems. Plane waves basis sets are used in conjunction with pseudopotentials to treat the interaction of core electrons with nuclei. Plane waves pseodopotential method is free from basis set superposition error (BSSE), whereas BSSE is present in localized basis sets-based methods (GTOs calculations). Therefore, the corrections are needed to take care of BSSE. In this thesis work, we have performed the calculations on periodic solids and the plane waves pseudopotential method is used for the electronic structure calculations.

2.6.1 Plane waves basis set

A practical numerical scheme is required to solve the single-particle Kohn-Sham equations for the extended systems. The prevailing approach to handle this problem is to expand the single-particle eigenstates of the Kohn-Sham equations into a set of basis functions. This lead to the transformation of Schrödinger equation into algebraic equation of expansion coefficients, which could be solved numerically. Particularly, plane waves are the most suitable basis functions set for extended systems. Plane waves are orthonormal and do not depend on energy. Thus, the Schrödinger equation becomes a basic matrix eigenvalue problem for the expansion coefficients. Since plane waves are independent of atomic positions, the pulay forces are absent and the Hellmann-Feynman theorem can be applied directly to calculate atomic forces.

Typically, the plane wave basis set is comprised of plane waves up to a certain wave vector cutoff. The convergence of the basis set is simply specified by a single parameter, i.e., the length of the cut off wave vector. However, a large number of plane waves is required to represent the rapid oscillations that are exhibited by the valence wave functions in the core region near nuclei. Therefore, the plane waves are used in conjunction with the pseudopotentials to approximate the effect of core electrons.

Additionally, while implementing plane waves, various integrals and operations are easier to carry out with Fast Fourier Transforms (FFTs). It allows the usage of plane waves in larger systems.

Now, in this section we will introduce the basic terms that are used for describing infinitely extended periodic systems. After that, the usefulness of plane wave basis set for expansion of wave function is shown. In next sections, the pseudopotential approach is described.

Supercells

Despite the simplification of many-body electron problem to a set of single-particle equations, the calculation of the single-electron wave functions for an extended (or even infinite) system is still a daunting task. To make the solution feasible, the extended system can be represented by a box of atoms which is periodically repeated in all the three spatial directions. The box is described by three vectors $\mathbf{a_1}$, $\mathbf{a_2}$, and $\mathbf{a_3}$, which define a lattice in real space. The volume of the corresponding cell is given by

$$\Omega_c = |\,\mathbf{a_1} \cdot (\mathbf{a_2} \times \mathbf{a_3})| \tag{2.61}$$

The general lattice vectors are multiples of the primitive lattice vectors, such that any translation vector (**T**) can be written as

$$\mathbf{T} = N_1\mathbf{a_1} + N_2\mathbf{a_2} + N_3\mathbf{a_3} \tag{2.62}$$

where N_1, N_2, and N_3 are three integers. The box can be primitive unit cell or a large supercell containing a larger volume, mimicking the solid phase locally. The supercells are particularly useful to model the point defects, surfaces or isolated molecules. The supercell should be sufficiently large so that the periodic images of defects, surfaces or molecules do not interact. The convergence of a particular quantity should be checked with respect to the size of the supercell.

Fourier representations

The computational cost for solving the Kohn-Sham equations can be decreased by exploiting the translational symmetry of atomic arrangements. The effective potential experienced by the electron is a periodic function having periodicity of the lattice, which can be expressed as

$$V_{eff}(\mathbf{r} + \mathbf{T}) = V_{eff}(\mathbf{r}) \tag{2.63}$$

where the translation vector (**T**) is defined above in Equation 2.62. Since the effective potential V_{eff} is periodic, it can be expanded in Fourier series given by

$$V_{eff}(\mathbf{r}) = \sum_{\mathbf{G}} V_{eff}(\mathbf{G}) e^{i\mathbf{G}\cdot\mathbf{r}} \quad \text{and} \quad V_{eff}(\mathbf{G}) = \frac{1}{\Omega_c}\int_{\Omega_c} V_{eff}(\mathbf{r}) e^{-i\mathbf{G}\cdot\mathbf{r}} d\mathbf{r} \tag{2.64}$$

The sum runs over all the reciprocal lattice vectors **G**. These reciprocal lattice vectors **G** follow the condition $\mathbf{G} \cdot \mathbf{T} = 2\pi M$, where M is an integer and **T** is a translation vector of the unit cell. These vectors **G** form the reciprocal lattice, whose primitive vectors $\mathbf{b_1}$, $\mathbf{b_2}$, and $\mathbf{b_3}$ are defined as

$$\mathbf{a}_i \cdot \mathbf{b}_j = 2\pi\delta_{ij}\,; \quad i, j = 1, 2, \text{and}\, 3 \tag{2.65}$$

where the Kronecker delta δ_{ij} is 1 when $i = j$ and zero otherwise. The volume of the corresponding reciprocal unit cell is given by

$$|\,\mathbf{b_1} \cdot (\mathbf{b_2} \times \mathbf{b_3})| = \frac{(2\pi)^3}{\Omega_c} \tag{2.66}$$

Bloch's theorem

According to Bloch's theorem, the eigenstates of the single-particle Schrödinger equation in a periodic crystal in terms of plane waves can be expressed as

$$\psi\left(\mathbf{r}+\mathbf{T}\right)=e^{i\mathbf{k}\cdot\mathbf{T}}\psi\left(\mathbf{r}\right) \tag{2.67}$$

for every **T** in the Bravais lattice. Here, **k** is the wave vector. The values of **k** can be confined to the reciprocal unit cell. Conventionally, this unit cell is taken to be the first Brillouin zone (BZ). For a given **k**, different independent eigenstates exist, which can be labelled with a band index n.

Bloch theorem can also be stated in alternative form. All the eigenfunctions $\psi_{n\mathbf{k}}$ of single-particle Schrödinger equation with a periodic potential can be specified to have the form of a plane wave times a function $u_{n\mathbf{k}}$ with the periodicity of the Bravais lattice [11]:

$$\psi_{n\mathbf{k}}\left(\mathbf{r}\right)=e^{i\mathbf{k}\cdot\mathbf{r}}u_{n\mathbf{k}}\left(\mathbf{r}\right) \tag{2.68}$$

where

$$u_{n\mathbf{k}}\left(\mathbf{r}+\mathbf{T}\right)=u_{n\mathbf{k}}\left(\mathbf{r}\right) \tag{2.69}$$

for all **T** in the Bravais lattice. This allows to restrict the calculations of eigenfunctions to within one unit cell. The eigenfunctions in other unit cell can be determined using Equation 2.68. It is convenient to normalize the eigenfunctions with respect to single unit cell:

$$\int_{\Omega_c}\left|\psi_{n\mathbf{k}}\left(\mathbf{r}\right)\right|^2 d\mathbf{r}=1 \tag{2.70}$$

Since the functions $u_{n\mathbf{k}}\left(\mathbf{r}\right)$ are periodic, they can be expanded in a set of plane waves. Therefore, Equation 2.68 becomes

$$\psi_{n\mathbf{k}}\left(\mathbf{r}\right)=\sum_{\mathbf{G}}c_{n\mathbf{k}}\left(\mathbf{G}\right)e^{i(\mathbf{k}+\mathbf{G})\cdot\mathbf{r}} \tag{2.71}$$

where $c_{n\mathbf{k}}\left(\mathbf{G}\right)$ are the Fourier coefficients.

The Kohn-Sham equations in the notation of Bloch states can be written as

$$\left(-\frac{1}{2}\nabla^2+V_{eff}\left(\mathbf{r}\right)\right)\psi_{j\mathbf{k}}\left(\mathbf{r}\right)=\epsilon_{j\mathbf{k}}\psi_{j\mathbf{k}}\left(\mathbf{r}\right) \tag{2.72}$$

where

$$V_{eff}\left(\mathbf{r}\right)=V_{ext}\left(\mathbf{r}\right)+V_{Hartree}\left[n\left(\mathbf{r}\right)\right]+V_{xc}\left[n\left(\mathbf{r}\right)\right] \tag{2.73}$$

and

$$n\left(\mathbf{r}\right)=2\frac{\Omega_c}{\left(2\pi\right)^3}\sum_j\int_{\mathrm{BZ}}\left|\psi_{j\mathbf{k}}\left(\mathbf{r}\right)\right|^2\Theta\left(E_F-\epsilon_{j\mathbf{k}}\right)d\mathbf{k} \tag{2.74}$$

Here, to differentiate between electron density and band index, we have used n for electron density, and j for band index. The factor of two in Equation 2.74 is used to take the electron spin into account. Θ is the step function, which has the value one for positive and zero for negative arguments. E_F is the Fermi energy up to which the single-particle states have to be occupied.

Brillouin zone sampling

On applying Bloch's theorem, one only needs to know the finite number of eigenstates for wave vector **k** within the first Brillouin zone instead of calculating an infinite number of electronic states extended over the entire space of the solid. Ostensibly, the improvement is looking minor since very fine sampling of Brillouin zone is needed for the calculations. However, since the lattice-periodic part $u_{n\mathbf{k}}\left(\mathbf{r}\right)$ depends weakly on **k**, a small finite number of **k**-points is sufficient to sample the Brillouin zone [73]. Therefore, the integral over the Brillouin zone can be replaced by a discrete sum over the chosen **k**-point mesh of N_{kpt} **k**-points:

$$\frac{\Omega_c}{\left(2\pi\right)^3}\int_{\mathrm{BZ}}\ldots\Theta\left(E_F-\epsilon_{j\mathbf{k}}\right)d\mathbf{k}\quad\rightarrow\quad\frac{1}{N_{\mathrm{kpt}}}\sum_{\mathbf{k}}f_{j\mathbf{k}}\ldots \tag{2.75}$$

where $f_{j\mathbf{k}}$ are occupation numbers which are either one or zero. In literature, various methods have been proposed to construct the **k**-point meshes [74, 75, 76]. In this thesis work, Monkhorst-Pack scheme is used to sample the Brillouin zone. The error induced by replacing the integral to a discrete sum over a finite number of **k**-points can be reduced by using a dense **k**-point mesh. For a larger supercell, coarser **k**-point mesh is needed to get the converged results, since the Brillouin zone of the supercell is smaller (see Equation 2.66). Moreover, typically a coarser **k**-point mesh is required for insulators, whereas a denser **k**-point mesh is required for the metallic system in order to get a precise sampling of the Fermi surface.

Fourier representation of the Kohn-Sham equation

The Kohn-Sham equation assume a simple form when the wave function is expanded in plane waves. On substituting Equation 2.71 into Equation 2.72, and after doing some minor mathematics, we get the matrix eigenvalue equation [69]:

$$\sum_{\mathbf{G}}\left(\frac{1}{2}|\mathbf{k}+\mathbf{G}|^2\delta_{\mathbf{G}'\mathbf{G}}+V_{eff}\left(\mathbf{G}'-\mathbf{G}\right)\right)c_{\mathbf{G}}^{j\mathbf{k}}=\epsilon_{j\mathbf{k}}c_{\mathbf{G}'}^{j\mathbf{k}} \tag{2.76}$$

Practically, the Fourier expansion of wave function given by Equation 2.71 is truncated by considering only those plane waves that have a kinetic energy lower than a given cutoff value E_{cut}:

$$\frac{1}{2}|\mathbf{k}+\mathbf{G}|^2\leq E_{\text{cut}} \tag{2.77}$$

Therefore, the convergence of the concerned quantity should be done by increasing the value of E_{cut} systematically.

The Fourier representation of electron density is given by

$$n\left(\mathbf{G}\right)=\frac{2}{N_{\text{kpt}}}\sum_{j\mathbf{k}}f_{j\mathbf{k}}\sum_{\mathbf{G}'}\left(c_{\mathbf{G}'-\mathbf{G}}^{j\mathbf{k}}\right)^{*}c_{\mathbf{G}'}^{j\mathbf{k}} \tag{2.78}$$

Since the electron density $n\propto|\psi|^2$, it requires Fourier components that extend twice as far in each direction as those needed for the wave function ψ.

The calculation of all Fourier components using Equation 2.78 involves double sum that scales as N_G^2, where N_G is the number of $\mathbf{G}$ vectors needed to describe the electron density. This becomes very expensive for large systems. Moreover, if the Bloch states are known on a grid of N_R points in real space, the electron density can be determined as a square, in N_R operations. The use of fast Fourier transform (FFT) allows the transformation from one space to the other in $N\ln N$ operations, where $N=N_R=N_G$ [69]. Therefore, it is advantageous to work with plane waves since the evaluation of the expressions can be speeded up by the use of FFT.

2.6.2 Pseudopotentials

The solution of the Kohn-Sham equations is computationally challenging, since the wave functions need to be determined for N electrons. Additionally, a large number of plane waves is required to expand the tightly bound core orbitals and to follow the rapid oscillations of valence electrons wave functions in the core region [77]. The pseudopotential approach allows the electronic wave functions to be expanded by small number of plane waves basis set.

It is well known that the valence electrons are mainly responsible for the physical and chemical properties of a material in comparison to the core electrons. Therefore, the pseudopotential approximation exploits this fact by replacing the core electrons and the strong ionic potential

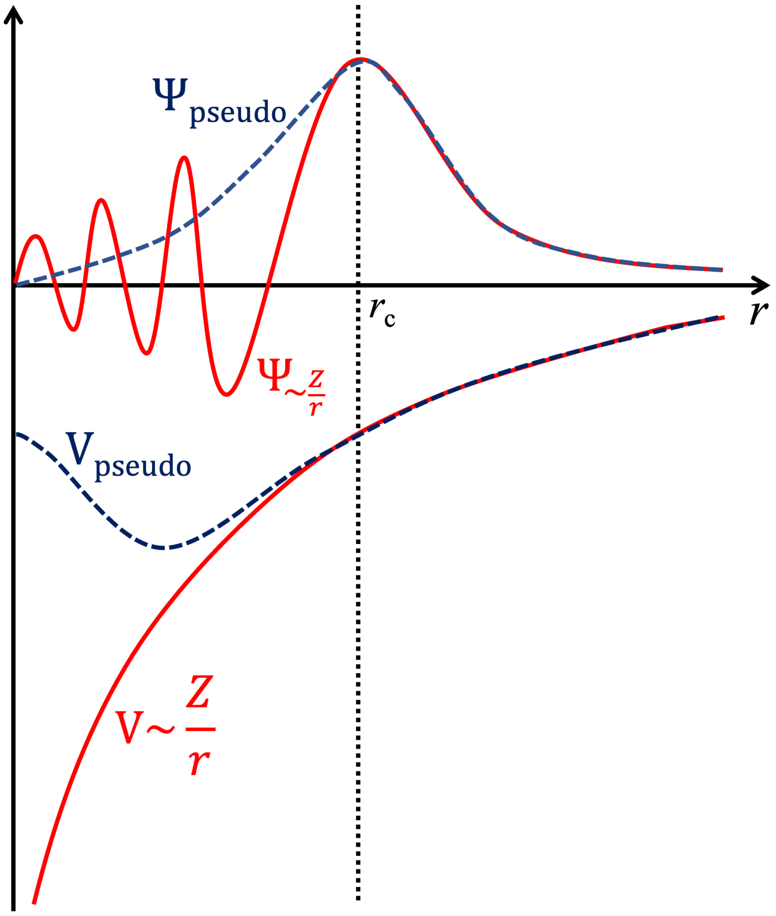

Figure 2.5: Schematic representation of pseudopotential technique. The all-electron wave function corresponding to Coulomb potential is shown by red color. The pseudo wave function corresponding to pseudopotential is shown by blue color.

by a weaker pseudopotential that acts on a set of pseudo wave functions instead of true valence wave functions. It has schematically illustrated in Figure 2.5. The Pauli exclusion principle requires the orthogonality between the core wave functions and the valence wave functions, which is maintained by this rapid oscillations of valence wave functions in the core electrons region. The pseudopotentials are constructed such that the wave functions of the valence electrons match with those of an all-electron calculation outside the core region defined by a cutoff radius r_c as shown in Figure 2.5 and inside the core region, they are nodeless and smooth. The pseudopotentials with larger r_c are softer, which converge with smaller number of plane waves basis set. But these soft pseudopotentials are less transferable, i.e., less accurate in reproducing valence properties in different chemical environments. Another advantage of using pseudopotentials is the inclusion of relativistic effects while the valence electrons are treated non-relativistically. In the following sections, we will discuss about the pseudopotentials used in DFT.

2.6.3 Norm-conserving pseudopotentials

In 1979, Hamann, Schlüter, and Chiang [69, 78] introduced energy-independent pseudopotentials that satisfy the following four criteria:

1. For a particular atomic configuration, all-electron (AE) and pseudo (PS) valence eigenvalues are equal.

$$\epsilon_{nl}^{\text{AE}} = \epsilon_{nl}^{\text{PS}} \tag{2.79}$$

   where n and l correspond to the principal quantum number and the angular momentum quantum number, respectively.

2. Beyond a chosen core radius r_c, AE and PS valence wave functions are equal.

$$\psi_{nl}^{\text{AE}}(r) = \psi_{nl}^{\text{PS}}(r) \quad \text{for} \quad r \geq r_c \tag{2.80}$$

3. The integrals of charge densities inside the core region due to the AE and PS wave functions are equal (norm conservation).

$$\int_0^{r_c} |\phi_{nl}^{\text{AE}}|^2 r^2 dr = \int_0^{r_c} |\phi_{nl}^{\text{PS}}|^2 r^2 dr \tag{2.81}$$

   where $\phi_{nl}(r)$ is the radial part of the wave function.

4. The logarithmic derivatives and the first energy derivative of the logarithmic derivatives of the AE and PS wave functions are equal at r_c.

$$\left[\left(r\phi_{nl}^{\text{AE}}(r)\right)^2 \frac{d}{d\epsilon}\frac{d}{dr}\ln\phi_{nl}^{\text{AE}}(r)\right]_{r_c} = \left[\left(r\phi_{nl}^{\text{PS}}(r)\right)^2 \frac{d}{d\epsilon}\frac{d}{dr}\ln\phi_{nl}^{\text{PS}}(r)\right]_{r_c} \tag{2.82}$$

Items 1 and 2 imply that the norm-conserving pseudopotential is equal to the AE atomic potential outside the core region of radius r_c, since the potential is uniquely determined by the wave function and the energy ϵ, that need not be an eigenenergy. The conservation of the integrated charge given by Equation 2.81 ensures the correctness of total charge inside the core region and matching of the normalized PS wave function with the AE wave function outside the core region defined by r_c. This also ensures that the potential is correct outside r_c. Point 4 ensures the transferability of the constructed pseudopotential in different environments. It has been shown that the point 4 is implied by the point 3 [69, 78].

To generate a norm-conserving pseudopotential, first the all-electron atomic calculations are carried out. Subsequently, the core states and valence states are identified. Thereafter, the pseudopotentials are generated for the valence states and pseudo orbitals are determined. The next step is the unscreening, in which the sum of Hartree and exchange-correlation potentials are subtracted from the total potential. The pseudopotential is generally written in terms of local (l-independent) part and the non-local part. Although the norm conservation condition needs to be satisfied, there are still many choices to construct this pseudopotential. Typically, there exist two competing factors:

- Accuracy and transferability results in choice of smaller cutoff radius r_c and hard potentials.
- Smoothness results in the choice of larger cutoff radius r_c and soft potentials.

2.6.4 Ultrasoft pseudopotentials

The efficacy of norm-conserving pseudopotentials to systems containing highly localized valence orbitals such as $2p$ and $3d$ is limited, which is attributed to the difficulty of representing the pseudo wave function in plane waves basis set. The norm-conserving constraint is relaxed in ultrasoft pseudopotentials and a smaller number of plane waves are required. The ultrasoft pseudopotential are fully nonlocal by construction and become local outside the core [79]. The nonlocal ultrasoft peudopotential depends self-consistently on the charge density, which improves its transferability. The smoothness of pseudo wave function can be optimized as the norm-conserving condition is lifted. The pseudo wave function is divided into two parts: (i) Ultrasoft valence wave function, which does not satisfy the norm conservation constraint and (ii) the core augmentation charge, which is the charge deficit in core region. The plane wave energy cutoff energy is substantially reduced due to the former feature. However, the latter feature introduces the additional terms in the Kohn-Sham formalism, which complicate the picture and more number of operations are needed to be performed per computational cycle. Despite this increment in the computational efforts, the gain in computational cost by lowering the plane wave energy cutoff dominates in many cases.

2.6.5 Projector augmented-wave (PAW) method

In 1994, Blöchl [80] devised the projector augmented-wave (PAW) method, which combined the ideas of both, the pseudopotential approach and the linearized augmented plane wave (LAPW) [81, 82] approach. The idea is to map the Kohn-Sham all-electron wave function $|\phi_s^0\rangle$ for state s onto the smooth pseudo wave function $|\tilde{\phi}_s^0\rangle$ and correction terms, through which the oscillatory behavior in the core region is restored. The mapping of $|\phi_s^0\rangle$ is done by a linear transformation $\hat{T}$:

$$|\phi_s^0\rangle = \hat{T}|\tilde{\phi}_s^0\rangle \tag{2.83}$$

Since $|\phi_s^0\rangle$ is oscillatory near the core region and smooth beyond a certain distance, the space can be divided into two regions according to LAPW method: (i) the augmentation region around the nuclei Ω_a, where a is an atom index and (ii) an interstitial region Ω_i [83]. The Ω_a is defined by a cutoff radius r_c^a, such that the overlap of augmentation spheres is avoided. Since, the pseudo wave function should coincide with the all-electron wave function outside Ω_a, the linear transformation $\hat{T}$ should modify $|\phi_s^0\rangle$ only in the augmentation region. Therefore, $\hat{T}$ can be rewritten as

$$\hat{T} = 1 + \sum_a \hat{T}^a \tag{2.84}$$

where atom-centered contribution $\hat{T}^a$ transforms $|\phi_s^0\rangle$ within Ω_a enclosing the atom. The transformation operator derived by defining the all-electron partial waves φ_j^a and pseudo partial waves $\tilde{\varphi}_j^a$ inside the augmentation region is given by

$$\hat{T} = 1 + \sum_a \sum_j \left(|\varphi_j^a\rangle - |\tilde{\varphi}_j^a\rangle\right) \langle\tilde{p}_j^a| \tag{2.85}$$

where $|\tilde{p}_j^a\rangle$ are smooth projector functions. Inside the augmentation sphere, the projector functions are orthonormal to the pseudo partial waves. Applying this into the all-electron wave function equation 2.83, one obtains the following expression

$$|\phi_s^0\rangle = |\tilde{\phi}_s^0\rangle + \sum_a \sum_j \left(|\varphi_j^a\rangle - |\tilde{\varphi}_j^a\rangle\right) \langle\tilde{p}_j^a|\tilde{\phi}_s^0\rangle \tag{2.86}$$

The following conditions hold inside the augmentation region, i.e., for $\mathbf{r} \in \Omega_a$

$$\begin{aligned} \phi_s^0(\mathbf{r}) &= \phi_s^a(\mathbf{r}) \\ \tilde{\phi}_s^0(\mathbf{r}) &= \tilde{\phi}_s^a(\mathbf{r}) \end{aligned} \tag{2.87}$$

and outside the augmentation region, i.e., for $\mathbf{r} \in \Omega_i$

$$\begin{aligned} \phi_s^0(\mathbf{r}) &= \tilde{\phi}_s^0(\mathbf{r}) \\ \phi_s^a(\mathbf{r}) &= \tilde{\phi}_s^a(\mathbf{r}) \end{aligned} \tag{2.88}$$

where $\phi_s^a(\mathbf{r})$ and $\tilde{\phi}_s^a(\mathbf{r})$ are expanded as follows

$$\begin{aligned} \phi_s^a(\mathbf{r}) &= \sum_j \varphi_j^a(\mathbf{r}) \langle \tilde{p}_j^a | \tilde{\phi}_s^0 \rangle \\ \tilde{\phi}_s^a(\mathbf{r}) &= \sum_j \tilde{\varphi}_j^a(\mathbf{r}) \langle \tilde{p}_j^a | \tilde{\phi}_s^0 \rangle \end{aligned} \tag{2.89}$$

The pseudo wave functions are expanded in plane waves basis set, with lower energy cutoff due to smoothness. The partial waves and the projectors are calculated as radial functions multiplied with spherical harmonics. The PAW method is computationally efficient in electronic structure calculations. In this thesis work, the DFT calculations have been carried out using PAW method as implemented in VASP.

2.7 Force theorem and geometry optimization

The equilibrium configuration in which the atoms are arranged in ground state is determined by the geometry optimization. An atom undergoing a net force moves in the direction of the force so that the total energy is minimized. The equilibrium configuration is attained when all such forces are equal to zero, or practically, when they are within some convergence criterion. These forces are calculated using force theorem, also known as Hellmann-Feynman theorem [84]. According to this theorem, the force acting on ion I can be determined by taking the derivative of the total energy E with respect to its position $\mathbf{R}_I$

$$\mathbf{F}_I = -\frac{\partial E}{\partial \mathbf{R}_I} \tag{2.90}$$

where

$$E = \frac{\langle \Psi | H | \Psi \rangle}{\langle \Psi | \Psi \rangle} \tag{2.91}$$

Assuming the wave function is normalized, and $\langle \Psi | \Psi \rangle = 1$, we have

$$\mathbf{F}_I = -\langle \Psi | \frac{\partial H}{\partial \mathbf{R}_I} | \Psi \rangle - \langle \frac{\partial \Psi}{\partial \mathbf{R}_I} | H | \Psi \rangle - \langle \Psi | H | \frac{\partial \Psi}{\partial \mathbf{R}_I} \rangle \tag{2.92}$$

When $|\Psi\rangle$ is an eigenstate of H, we get

$$\mathbf{F}_I = -\langle \Psi | \frac{\partial H}{\partial \mathbf{R}_I} | \Psi \rangle - E \frac{\partial}{\partial \mathbf{R}_I} \langle \Psi | \Psi \rangle \tag{2.93}$$

The last term vanishes and we obtain

$$\mathbf{F}_I = -\langle\Psi|\frac{\partial H}{\partial \mathbf{R}_I}|\Psi\rangle \tag{2.94}$$

Since only the external potential due to the nuclei $V_{ext}(\mathbf{r})$ and nuclei-nuclei interaction term E_{II} depend explicitly on nuclei position, the Equation 2.94 becomes

$$\mathbf{F}_I = -\int d\mathbf{r}\, n(\mathbf{r}) \frac{\partial V_{ext}(\mathbf{r})}{\partial \mathbf{R}_I} - \frac{\partial E_{II}}{\partial \mathbf{R}_I} \tag{2.95}$$

If the basis set is incomplete and depends on the nuclei positions, then it should be taken care of by adding the extra terms, which are known as the pulay correction terms.

In a periodic system, the shape and volume of the unit cell should also be optimized along with the atomic positions. This can be done by calculating the stress. If a strain $\epsilon_{\alpha\beta}$ defined as a scaling of space, i.e., $\mathbf{r}_\alpha \rightarrow (\delta_{\alpha\beta} + \epsilon_{\alpha\beta})\,\mathbf{r}_\beta$ is applied, then the stress $\sigma_{\alpha\beta}$ can be determined by taking the derivative of the energy with respect to strain per unit volume [85]

$$\sigma_{\alpha\beta} = -\frac{1}{\Omega}\frac{\partial E}{\partial \epsilon_{\alpha\beta}} \tag{2.96}$$

The ground-state Kohn-Sham orbitals are used for calculating it.

2.8 *Ab initio* atomistic thermodynamics

DFT provides the ground-state properties by electronic structure calculations at zero temperature and zero pressure, which lie in the microscopic regime. The potential energy surface (PES) $E(\{\mathbf{R}_I\})$ can be determined using the DFT, where $\{\mathbf{R}_I\}$ denotes the atomic configuration. In *ab initio* atomistic thermodynamics approach, the effect of finite temperature and pressure are included by using the DFT PES to calculate suitable thermodynamic potential functions such as the Gibbs free energy [86]. Therefore, by combining the thermodynamics with DFT calculations, one obtains the macroscopic system properties. This methodology is applicable in larger systems, which can be divided into smaller subsystems that are in thermal equilibrium with each other. The subsystems in contact are described by relating their corresponding thermodynamic potentials.

2.8.1 Thermodynamic potentials

The thermodynamic state of a system is represented by a thermodynamic potential. Internal energy U, Helmholtz free energy $F = U - TS$, enthalpy $H = U + pV$, and Gibbs free energy

$G = U + pV - TS = H - TS = F + pV$ are the four thermodynamic potentials. These are the function of natural variables, viz., temperature (T), entropy (S), pressure (p) and volume (V). At constant T and V, a system minimizes its Helmholtz free energy, whereas at constant (T, p), it minimizes its Gibbs free energy. Mostly, the chemical reactions are carried out at constant T and p, making the Gibbs free energy to be the most useful thermodynamic potential for determining the stable (equilibrium) geometry under the given environmental conditions.

2.8.2 Defect formation energy

The free energy of a system can be changed on creating a defect. Defects can be introduced intentionally or they may be present unintentionally, depending on the environmental conditions. We analyze the thermodynamic stability of a system containing a defect with respect to pristine by calculating the defect formation energy as follows [9, 87]

$$E_{\text{f}}(T, p) = E^{q}_{\text{def}} - E^{q=0}_{\text{host}} \pm \sum_{i} n_i \mu_i(T, p_i) + q\mu_{\text{e}} \tag{2.97}$$

where E^{q}_{def} and $E^{q=0}_{\text{host}}$ are the total energies of the system containing defect and the system without a defect, respectively. These are determined from the DFT calculations. q is the charge state. n_i is the number of atoms of a species i that have been added or removed from the system. $\mu_i(T, p_i)$ are the corresponding chemical potentials, which are the function of temperature T and partial pressure p_i. μ_e is the chemical potential of electron, referenced to the valence band maximum (VBM) of the host. Here, the vibrational free energy contribution is neglected since it is small (∼ meV) for the defects considered in this thesis work. A schematic illustration of defect formation energy as a function of chemical potential of electron at a particular (T, p) with different charge states q is shown in Figure 2.6.

2.8.3 Chemical potentials

The atomic chemical potentials appearing in Equation 2.97, involve the dependence of temperature and partial pressure. These reflect the reservoirs for atoms that are involved in creating the defect. We can vary the chemical potentials to explore different experimental scenarios. The chemical potentials can be regarded as variables, subjected to specific bounds. These bounds are set to avoid the formation of secondary phases.

The chemical potential of oxygen $\mu_{\text{O}}(T, p_{\text{O}_2})$ has to be taken into account for an oxygen vacancy in oxide perovskite. It is determined by the condition of thermodynamic equilibrium

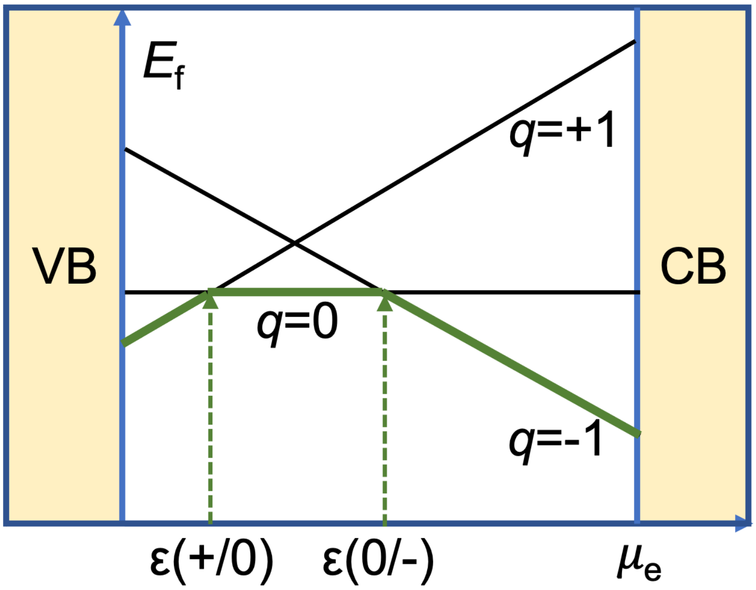

Figure 2.6: Schematic representation of defect formation energy as a function of chemical potential of electron at a particular (T, p), which can exist in three charge states $q = 0, +1$, and-1. $\varepsilon(+/0)$ and $\varepsilon(0/-)$ are the charge-state transition levels, denoting a deep donor level and a deep acceptor level, respectively. The thick green colored lines indicate the most favorable charge state for a given value of μ_e.

with the surrounding gas-phase reservoir, which can be approximately treated as an ideal gas composed of N indistinguishable O_2 molecules. $\mu_O(T, p_{O_2})$ is given by

$$\mu_O(T, p_{O_2}) = \frac{1}{2}\mu_{O_2}(T, p_{O_2}) = \frac{1}{2}\left(-k_B T \ln Q^{tot}_{O_2} + p_{O_2} V\right)/N \tag{2.98}$$

where k_B is the Boltzmann constant and V denotes the volume. The partition function of an ideal O_2 gas, $Q^{tot}_{O_2}$ can be evaluated as follows

$$Q^{tot}_{O_2} = \frac{1}{N!}\left(q_{O_2}\right)^N = \frac{1}{N!}\left(q^{trans}\, q^{rot}\, q^{vib}\, q^{electr}\, q^{nucl}\right)^N \tag{2.99}$$

Here, q_{O_2} is the partition function of one O_2 molecule, which can further be subdivided into different partition functions. The subdivision is based on the assumption that Born-Oppenheimer approximation holds, and thus, the nuclear and electronic degrees of freedom are decoupled from the vibrational and rotational degrees of freedom. Further, the vibrational and rotational motions can also be decoupled since they take place on different time scales. Using Equation 2.99 and 2.98, one obtains

$$\begin{aligned}\mu_O(T, p_{O_2}) = &-\frac{1}{2N}\left[k_B T \ln\left(\frac{1}{N!}(q^{trans})^N\right) - p_{O_2} V\right] \\ &+ \frac{1}{2}\mu^{rot} + \frac{1}{2}\mu^{vib} + \frac{1}{2}\mu^{electr} + \frac{1}{2}\mu^{nucl}\end{aligned} \tag{2.100}$$

Here, Statistical Mechanics can be applied to determine translational, rotational, vibrational, electronic and nuclear free energy terms [88]. The individual energy terms are given by

$$\begin{aligned}
-\frac{1}{2N}\left[k_\mathrm{B}T\ln\left(\frac{1}{N!}(q^\mathrm{trans})^N\right)-p_{\mathrm{O}_2}V\right] &= -\frac{1}{2}k_\mathrm{B}T\ln\left[\left(\frac{2\pi m}{h^2}\right)^{3/2}\frac{(k_\mathrm{B}T)^{5/2}}{p_{\mathrm{O}_2}}\right]\\
\mu^\mathrm{rot} &\approx -k_\mathrm{B}T\ln\left(\frac{8\pi^2 I k_\mathrm{B}T}{\sigma h^2}\right)\\
\mu^\mathrm{vib} = E^\mathrm{ZPE}+\Delta\mu^\mathrm{vib} &= \sum_{i=1}^{M}\left[\frac{\hbar\omega_i}{2}+k_\mathrm{B}T\ln\left(1-\exp\left(-\frac{\hbar\omega_i}{k_\mathrm{B}T}\right)\right)\right]\\
\mu^\mathrm{electr} &\approx E^\mathrm{total}_{\mathrm{O}_2}-k_\mathrm{B}T\ln\mathcal{M}
\end{aligned} \tag{2.101}$$

where m and I are the mass and moment of inertia of the molecule, respectively. σ is the symmetry number of the molecule, which represents the number of indistinguishable orientation that the molecule can have (for homonuclear diatomic molecules, $\sigma = 2$ and for hetronuclear diatomic molecules, $\sigma = 1$). Note that μ^rot in Equation 2.101 holds only for linear molecules. In the case of a complex molecule, the moments of inertia along all the three directions should be considered. In Equation 2.101, μ^vib is obtained within the harmonic approximation. E^ZPE is the zero point energy. M is the number of the vibrational modes of the molecule with corresponding frequencies ω_i. $E^\mathrm{total}_{\mathrm{O}_2}$ is the ground-state energy of the O_2 molecule calculated using DFT. $\mathcal{M}$ is the electronic spin degeneracy of the ground state. Since the nuclear state is rarely altered in chemical processes, q^nucl does not contribute to the thermodynamic changes. Therefore, we have omitted it here. Now, the chemical potential of oxygen can be written as

$$\mu_\mathrm{O}(T,p_{\mathrm{O}_2}) = \mu_\mathrm{O}^\mathrm{ref}+\Delta\mu_\mathrm{O}(T,p_{\mathrm{O}_2}) \tag{2.102}$$

where $\mu_\mathrm{O}^\mathrm{ref} = \frac{1}{2}E_{\mathrm{O}_2}+\frac{1}{2}E^\mathrm{ZPE}_{\mathrm{O}_2}$ acts as a reference chemical potential and $\Delta\mu_\mathrm{O}(T,p_{\mathrm{O}_2})$ contains all temperature and pressure dependent free energy contributions

$$\begin{aligned}
\Delta\mu_\mathrm{O}(T,p_{\mathrm{O}_2}) = \frac{1}{2}\Bigg[&-k_\mathrm{B}T\ln\left[\left(\frac{2\pi m}{h^2}\right)^{\frac{3}{2}}(k_\mathrm{B}T)^{\frac{5}{2}}\right]\\
&+k_\mathrm{B}T\ln p_{\mathrm{O}_2}-k_\mathrm{B}T\ln\left(\frac{8\pi^2 I k_\mathrm{B}T}{h^2}\right)\\
&+k_\mathrm{B}T\ln\left[1-\exp\left(-\frac{\hbar\omega_\mathrm{O}}{k_\mathrm{B}T}\right)\right]\\
&-k_\mathrm{B}T\ln\mathcal{M}+k_\mathrm{B}T\ln\sigma\Bigg]
\end{aligned} \tag{2.103}$$

A consistent choice should be made for chemical potential reference. Also, an appropriate ϵ_xc functional should be used for calculating the energies.

2.9 Many-body perturbation theory (MBPT): The Green's function approach

DFT is reliable to determine the ground-state properties of many-electron systems such as lattice parameters, phase transitions, charge density, bulk modulus, just to name a few. In practical implementation of DFT, the real interacting system is replaced by the non-interacting fictitious system, both having the same ground-state density. On solving the Kohn-Sham equation for that system, the single-particle eigenstates and eigenvalues are obtained. However, these eigenvalues cannot be interpreted as excitation energies since the Kohn-Sham eigenstates and eigenvalues are only the mathematical tools and do not contain a physical meaning. The energy of the highest occupied state is the only exception, which equals the exact ionization energy of the system [89, 90]. Consequently, the DFT often fails to predict the excited-state properties such as band gaps and optical absorption, etc. Therefore, one needs to go beyond the DFT to investigate the many-body physics. These excited-state properties can be determined accurately by the Green's function formulation of many-body perturbation theory (MBPT) [53]. It includes the one-particle Green's function approach, viz., GW approach to quasiparticles for charged excitations and two-particle Green's function approach, viz., the Bethe-Salpeter Equation (BSE) for neutral excitations.

Experimentally, band gaps are measured by the excited-state spectroscopies. Figure 2.7 shows a schematic representation of charged and neutral excitations. In direct photoemission, when light shines upon the sample, an electron is ejected from it. Consequently, one can determine the ionization potential (IP) by calculating the total energy difference of N and N-1 electrons system. On the other hand, inverse photoemission involves the injection of an electron to the system and emission of a photon. The total energy difference of N and N+1 electrons system provides the electron affinity (EA). The direct and inverse photoemission spectroscopies measure the excitation energy of a single charge particle (viz., electron or hole). Theoretically, these processes can be probed by the one-particle Green's function approach, viz., GW approximation. Furthermore, an electron is excited from the valence band to the conduction band on absorbing a photon in the case of optical absorption. Apparently, this process looks like the sum of a direct and an inverse photoemission. Instead, the excited electron and the hole are not free and they cannot be treated separately. These form a bound state, which is known as the exciton. This electron-hole interaction is well described theoretically by a two-particle Green's

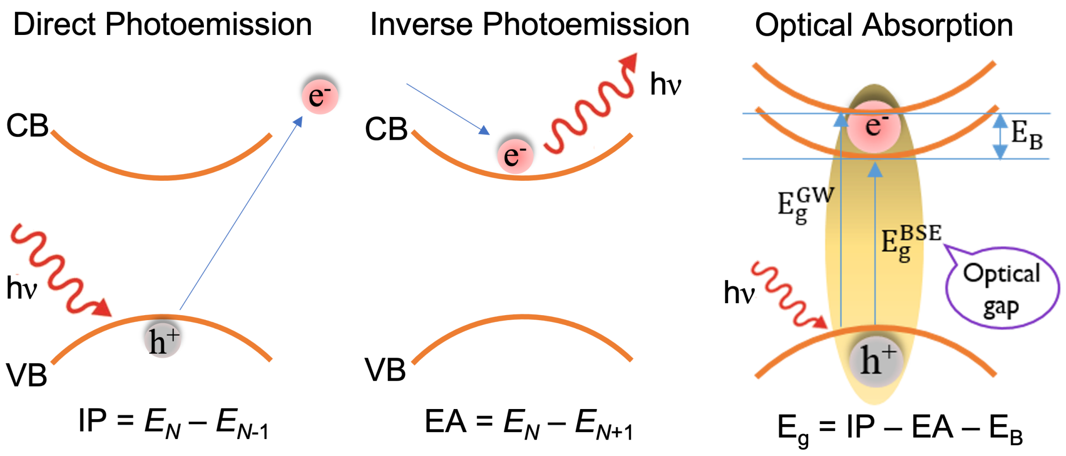

Figure 2.7: Schematic representation of excited-state spectroscopies, namely, direct photoemission, inverse photoemission, and optical absorption. Here, IP and EA represent the ionization potential and electron affinity, respectively. Also, E_N is the total energy of N-electron system. Moreover, $\mathrm{E_g^{GW}} = \mathrm{IP} - \mathrm{EA}$ is the quasiparticle (QP) band gap and $\mathrm{E_g^{BSE}} = \mathrm{IP} - \mathrm{EA} - \mathrm{E_B}$ is the optical band gap, where $\mathrm{E_B}$ is the exciton binding energy.

function approach, namely, the BSE.

2.9.1 Green's function

The processes that involve the injection or ejection of electrons can be described by a theoretical framework, which links the N-particle with the $(N\pm1)$-particle systems. This purpose is served by employing the MBPT. The time-ordered Green's function $G\left(\mathbf{r}t, \mathbf{r}'t'\right)$ is the central variable in MBPT. It contains the information of excitation energies as well as the excitation lifetime. The one-particle Green's function is defined as follows

$$\begin{aligned} G\left(\mathbf{r}t, \mathbf{r}'t'\right) = &- i\langle\Psi_0^N|\hat{\psi}(\mathbf{r}t)\hat{\psi}^{\dagger}(\mathbf{r}'t')|\Psi_0^N\rangle\Theta(t-t') \\ &+ i\langle\Psi_0^N|\hat{\psi}^{\dagger}(\mathbf{r}'t')\hat{\psi}(\mathbf{r}t)|\Psi_0^N\rangle\Theta(t'-t) \end{aligned} \tag{2.104}$$

where $\Theta(t-t')$ is the Heaviside step function given by

$$\Theta(t-t') = \begin{cases} 1 & \text{if } t > t' \\ 0 & \text{if } t < t' \end{cases}$$

In Equation 2.104, $|\Psi_0^N\rangle$ is the ground state of N-electron system. $\hat{\psi}^{\dagger}(\mathbf{r}t)$ and $\hat{\psi}(\mathbf{r}t)$ are the field operators that describe the creation and annihilation of an electron, respectively, at the position $\mathbf{r}$ and time t. In Heisenberg picture, $\hat{\psi}(\mathbf{r}t) = e^{i\hat{H}t}\hat{\psi}(\mathbf{r})e^{-i\hat{H}t}$. Physically, the Green's

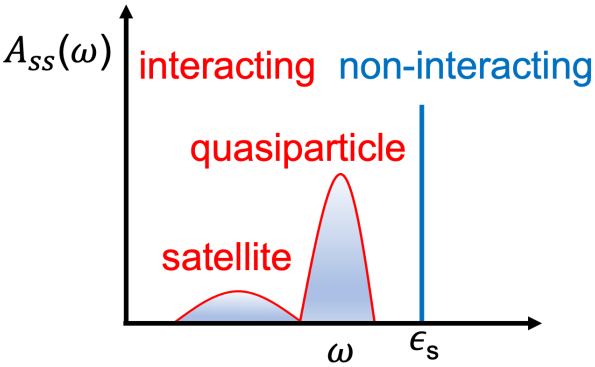

Figure 2.8: Schematic representation of spectral function in the case of non-interacting (electrons) single-particle excitation and interacting single-particle like (QP) excitation.

function for $t > t'$ creates an electron in the system at $\mathbf{r}'$ and t' and propagates it to $\mathbf{r}$, where it is annihilated at time t. For $t < t'$, it describes the propagation of a hole. Therefore, it is also known as a propagator.

The Lehmann or spectral representation of Green's function can be determined by taking the Fourier transform of G from the time to the energy axis and is given by

$$G(\mathbf{r},\mathbf{r}',\omega) = \lim_{\eta\to 0^+} \sum_s \psi_s(\mathbf{r})\psi_s^*(\mathbf{r}') \times \left[\frac{\Theta(\epsilon_s - E_F)}{\omega - (\epsilon_s - i\eta)} + \frac{\Theta(E_F - \epsilon_s)}{\omega - (\epsilon_s + i\eta)}\right] \tag{2.105}$$

where the excitation energies (ϵ_s) are expressed below

$$\epsilon_s = \begin{cases} E_N - E_{N-1} & \text{for } \epsilon_s < E_F \\ E_{N+1} - E_N & \text{for } \epsilon_s \geq E_F \end{cases}$$

and the transition amplitudes ($\psi_s(\mathbf{r})$) from the N to the $N \pm 1$-body states are defined as

$$\psi_s(\mathbf{r}) = \begin{cases} \langle \Psi_s^{N-1} | \hat{\psi}(\mathbf{r}) | \Psi_0^N \rangle & \text{for } \epsilon_s < E_F \\ \langle \Psi_0^{N} | \hat{\psi}(\mathbf{r}) | \Psi_s^{N+1} \rangle & \text{for } \epsilon_s \geq E_F \end{cases}$$

Here, E_F is the Fermi-level or chemical potential. The small imaginary part η is needed for the convergence of the Fourier transform. In Equation 2.105, ω denotes an energy (frequency). The poles of the Green's function hence provide the many-body excitation energies. The spectral function, i.e., the density of the excited states is related to the Green's function as follows

$$\begin{aligned} A(\mathbf{r},\mathbf{r}',\omega) &= \frac{1}{\pi}\,|\mathrm{Im}\, G(\mathbf{r},\mathbf{r}',\omega)| \\ &= \sum_s \psi_s(\mathbf{r})\psi_s^*(\mathbf{r}')\delta(\omega - \epsilon_s) \end{aligned} \tag{2.106}$$

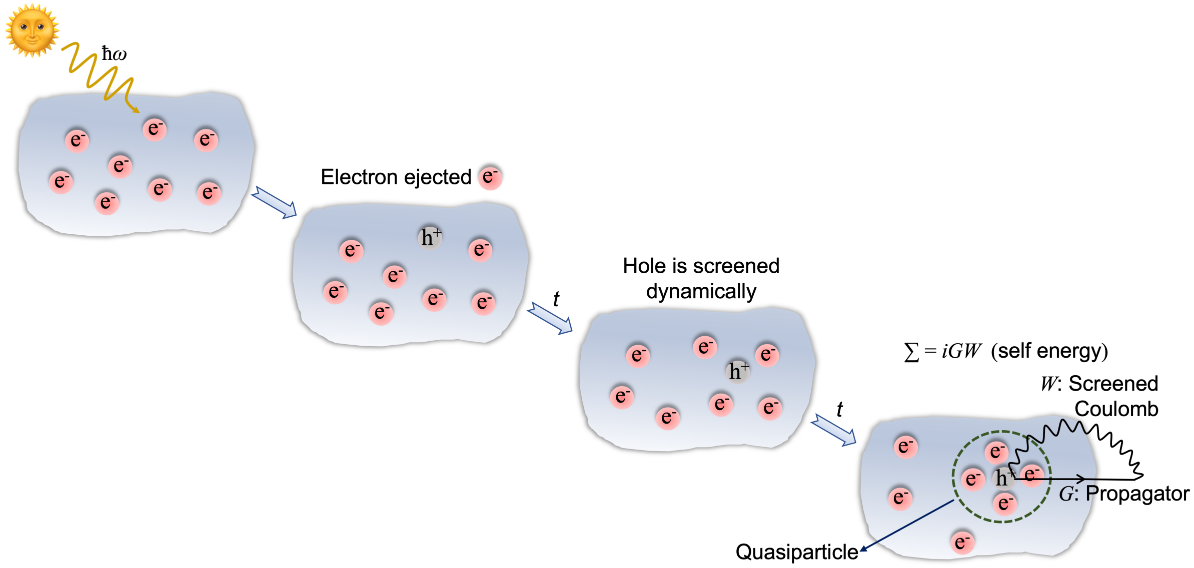

Figure 2.9: Illustration of a QP formation in the case of photoemission spectroscopy.

In the case of non-interacting electrons, the particle has infinite lifetime. Therefore, the spectral function contains a set of delta peaks corresponding to each transition (see the non-interacting particle peak in Figure 2.8). Contrarily, a finite width is observed experimentally at the peak position, which is attributed to a single-particle like excitation (QP) (see Figure 2.8). It is ascribed to the merging of several closely spaced delta peaks. Moreover, a broader peak with smaller intensity can also be seen, which is known as satellite peak. In essence, in addition to QP peak position, the spectral function contains information about: (i) the lifetime of the excitation due to electron-electron scattering, which is inversely proportional to the width of the QP peak, and (ii) the spectral weight associated with the QP. Therefore, the spectral function can also be expressed as

$$A \approx \frac{1}{\pi} \left| \frac{Z_s}{\omega - (\epsilon_s + i\Gamma)} \right| \tag{2.107}$$

where Z_s is the QP weight and Γ is the peak width. The QP concept in real-space is depicted in Figure 2.9. A charge particle “dressed" with the polarization cloud is considered as a QP. In photoemission spectroscopy, when we let the system evolve after the ejection (creation) of electron (hole), then the electrons surround the “bare" hole and screen its interaction with the rest of the system. This gives rise to the self-energy, i.e., the energy felt by the particle due to its own presence.

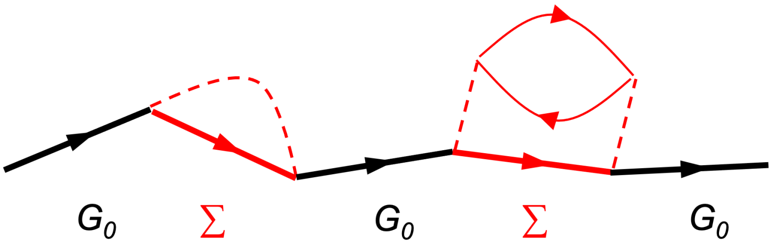

Figure 2.10: Schematic representation of the Dyson's equation, which relates the non-interacting (G_0) and interacting (G) Green's functions via the self-energy operator (Σ). Here, the black arrow describes the propagation of a non-interacting particle and the red color represents screening process of different orders.

2.9.2 Dyson's equation: The self-energy operator Σ

The computation of the exact one-particle Green's function is not possible, and therefore a suitable approximation is needed. The Green's function is related to Σ by the Dyson's equation, which is expressed below

$$G(\mathbf{r},\mathbf{r}',\omega) = G_0(\mathbf{r},\mathbf{r}',\omega) + \int\int G_0(\mathbf{r},\mathbf{r}'',\omega)\Sigma(\mathbf{r}'',\mathbf{r}''',\omega)G(\mathbf{r}''',\mathbf{r}',\omega)d\mathbf{r}''d\mathbf{r}''' \qquad (2.108)$$

where $G_0(\mathbf{r},\mathbf{r}',\omega)$ is the non-interacting Green's function determined using Equation 2.105 from a mean-field theory, which satisfies the following equation

$$\hat{h}_0\phi_i^0(\mathbf{r}) = \epsilon_i^0\phi_i^0(\mathbf{r}) \qquad (2.109)$$

where the single-particle Hamiltonian $\hat{h}_0 = -\frac{1}{2}\nabla^2 + V_{\text{ext}}(\mathbf{r}) + \int \frac{n(\mathbf{r}')}{|\mathbf{r}-\mathbf{r}'|}d\mathbf{r}'$. $\phi_i^0(\mathbf{r})$ and ϵ_i^0 are the corresponding eigenstates and eigenvalues, respectively. The non-local self-energy operator Σ depends on energy (frequency) and is non-Hermitian. All the many-body exchange and correlation effects are considered in the self-energy term. The Dyson equation can be reformulated to an effective single-particle equation, which describes the QP behavior

$$\hat{h}_0(\mathbf{r})\psi_s(\mathbf{r}) + \int \Sigma(\mathbf{r},\mathbf{r}',\epsilon_s)\psi_s(\mathbf{r}')d\mathbf{r}' = \epsilon_s\psi_s(\mathbf{r}) \qquad (2.110)$$

The wave functions $\psi_s(\mathbf{r})$ form a complete set, but are not orthonormal ascribed to the energy-dependence of the self-energy operator. The Dyson's equation can also be rewritten in algebraic form as follows

$$\begin{aligned} G &= G_0 + G_0\Sigma G_0 + G_0\Sigma G_0\Sigma G_0 + ... \\ G &= G_0 + G_0\Sigma G \end{aligned} \qquad (2.111)$$

It is illustrated in Figure 2.10. The different terms in Equation 2.111 describe the single, double, etc., scattering processes with Σ being the scattering potential. Therefore, the self-energy can also be defined as the sum of all scattering events. However, it is very difficult to determine the exact Σ attributed to multiple scattering processes. Therefore, an appropriate approximation is needed to evaluate it.

2.9.3 Hedin's equations and the *GW* approximation

In 1965 [63], Hedin derived a set of five self-consistent integro-differential equations, relating the self-energy to the Green's function and the screened Coulomb interaction (W), using the polarizability (P) and the vertex function (Γ):

$$\begin{aligned}
G(1,2) &= G_0(1,2) + \int d(3,4) G_0(1,3)\Sigma(3,4)G(4,2) \\
P(1,2) &= -i\int d(3,4) G(2,3)G(4,2^+)\Gamma(3,4;1) \\
W(1,2) &= v(1,2) + \int d(3,4) W(1,3)P(3,4)v(4,2) \\
\Sigma(1,2) &= i\int d(3,4) G(1,4)W(1^+,3)\Gamma(4,2;3) \\
\Gamma(1,2;3) &= \delta(1,2)\delta(1,3) + \int d(4,5,6,7)\frac{\delta\Sigma(1,2)}{\delta G(4,5)}G(4,6)G(7,5)\Gamma(6,7;3)
\end{aligned} \tag{2.112}$$

Here, the notation $1 = (\mathbf{r}_1, t_1)$ is adopted and v is the unscreened (bare) Coulomb interaction. 1^+ denotes $(\mathbf{r}_1, t_1{+}\eta)$, where η is a positive infinitesimal. The self-consistent iterative process is schematically shown in Figure 2.11. The vertex function contains the higher-order correction to the interaction between QPs. It is the most difficult term to compute as it contains a functional derivative and depends on three spacetime points. Therefore, to simply these equations, the vertex function is the usual target for an approximation.

In the GW approximation, the functional derivative of the self-energy with respect to the Green's function is neglected, leading to

$$\begin{aligned}
\Gamma(1,2;3) &= \delta(1,2)\delta(1,3) \\
P(1,2) &= -iG(1,2^+)G(2,1) \\
\Sigma(1,2) &= iG(1,2)W(1^+,2)
\end{aligned} \tag{2.113}$$

Hence, the self-energy is a product of the Green's function and the screened Coulomb interaction in the GW approximation. The GW method is analogous to Hartree-Fock theory, which uses the bare Coulomb interaction instead of the dynamically screened Coulomb interaction.

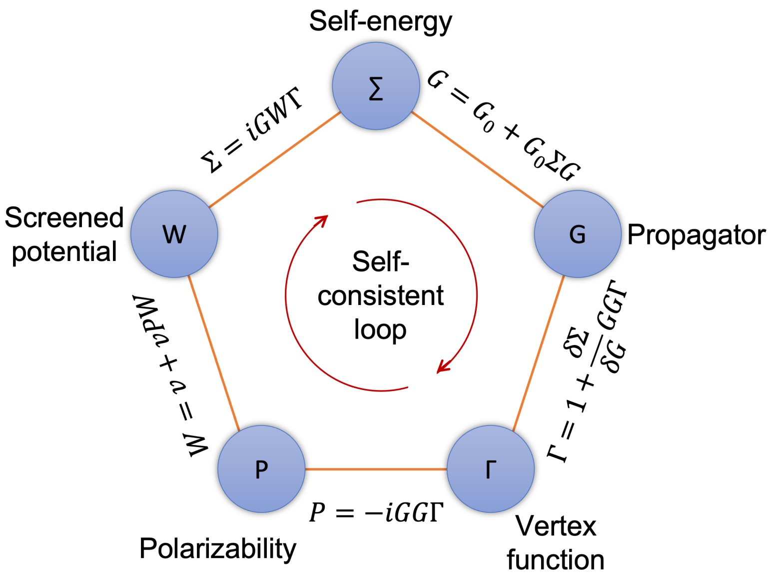

Figure 2.11: Schematic representation of the self-consistent Hedin's equations.

2.9.4 Practical implementation of the single-shot *GW* (G_0W_0)

In G_0W_0 approach, only one GW iteration is performed. The step by step procedure is given below

Step 1: Do a DFT calculation and get the Kohn-Sham eigenvalues (ϵ_s^{KS}) and eigenstates (ϕ_s^{KS}).

Step 2: Set up the Kohn-Sham Green's function

$$G_0(\mathbf{r},\mathbf{r}',\epsilon) = \lim_{\eta\to 0^+}\sum_s \frac{\phi_s^{\mathrm{KS}}(\mathbf{r})\phi_s^{\mathrm{KS}*}(\mathbf{r}')}{\epsilon - (\epsilon_s^{\mathrm{KS}} + i\eta\,\mathrm{sgn}(E_F - \epsilon_s^{\mathrm{KS}}))} \tag{2.114}$$

Step 3: Construct the polarizability

$$P(\mathbf{r},\mathbf{r}',\epsilon) = -\frac{i}{2\pi}\int d\epsilon' G_0(\mathbf{r},\mathbf{r}',\epsilon'-\epsilon)G_0(\mathbf{r}',\mathbf{r},\epsilon') \tag{2.115}$$

Step 4: Calculate the dielectric function

$$\varepsilon(\mathbf{r},\mathbf{r}',\epsilon) = \delta(\mathbf{r}-\mathbf{r}') - \int d\mathbf{r}'' v(\mathbf{r}-\mathbf{r}'')P(\mathbf{r}'',\mathbf{r}',\epsilon) \tag{2.116}$$

Step 5: Determine the screened Coulomb interaction

$$W_0(\mathbf{r},\mathbf{r}',\epsilon) = \int d\mathbf{r}''\varepsilon^{-1}(\mathbf{r},\mathbf{r}'',\epsilon)v(\mathbf{r}''-\mathbf{r}') \tag{2.117}$$

Step 6: Determine the self-energy

$$\Sigma(\mathbf{r},\mathbf{r}',\omega) = \frac{i}{2\pi}\int d\omega' e^{i\omega'\eta}G_0(\mathbf{r},\mathbf{r}',\omega+\omega')W_0(\mathbf{r},\mathbf{r}',\omega') \tag{2.118}$$

Step 7: Solve the QP Equation 2.110

The eigenvalues obtained by solving the QP equation are complex. The real part gives the QP energy (ϵ_s^{QP}), whereas the imaginary part contains the information about the lifetime (inversely proportional) of the QP. Since the QP equation is similar to the Kohn-Sham equation, the difference between the self-energy operator and the exchange-correlation potential can be treated as a perturbation to update the QP energies:

$$\epsilon_i^{QP} = \epsilon_i^{\text{KS}} + \langle\psi_i^{\text{KS}}|\Sigma(\epsilon_i^{\text{QP}}) - V_{xc}|\psi_i^{\text{KS}}\rangle \tag{2.119}$$

However, the energy dependence of Σ is not known. Therefore, the self-energy is linearized by expanding it in Taylor series around ϵ_s^{KS}, assuming the difference between ϵ_s^{KS} and ϵ_s^{QP} is small:

$$\Sigma(\epsilon_s^{\text{QP}}) \approx \Sigma(\epsilon_s^{\text{KS}}) + (\epsilon_s^{\text{QP}} - \epsilon_s^{\text{KS}})\frac{\partial\Sigma(\epsilon)}{\partial\epsilon}\bigg|_{\epsilon=\epsilon_s^{\text{KS}}} \tag{2.120}$$

Now, the QP energies can be determined from the following equation

$$\epsilon_i^{QP} = \epsilon_i^{\text{KS}} + Z_i\langle\psi_i^{\text{KS}}|\Sigma(\epsilon_i^{\text{KS}}) - V_{xc}|\psi_i^{\text{KS}}\rangle \tag{2.121}$$

where the renormalization factor Z_i is given by

$$Z_i = \left(1 - \langle\psi_i^{\text{KS}}|\frac{\partial\Sigma(\epsilon)}{\partial\epsilon}\bigg|_{\epsilon=\epsilon_s^{\text{KS}}}|\psi_i^{\text{KS}}\rangle\right)^{-1} \tag{2.122}$$

We have to choose the starting point (LDA/PBE/HSE06) carefully, as the QP energies depend on it. In most of the cases, G_0W_0 yields the band gap in good agreement with experimental measurements [91, 67]. In addition, a self-consistent GW (scGW) approach can be implemented in which both the QP energies and the corresponding orbitals are updated self-consistently [92]. Unfortunately, the scGW method overestimates the band gaps as compared to experimental values [93]. Imposing self-consistency in the absence of vertex correction deteriorates the agreement with experimental results. In our thesis work, we have mostly used the single-shot GW.

2.9.5 Bethe-Salpeter equation (BSE)

In neutral electron-hole excitations such as optical absorption, the total number of electrons remains unchanged. These excitations are described by solving the equation of motion for the two-particle Green's function, specifically, the Bethe-Salpeter equation (BSE). The BSE can be written as [94, 95]

$$L(1,2,1',2') = L_0(1,2,1',2') + \int d(3,4,5,6) L_0(1,4,1',3) K(3,5,4,6) L(6,2,5,2') \tag{2.123}$$

where $L(1,2,1',2')$ and $K(3,5,4,6)$ represent the electron-hole correlation function and the electron-hole interaction kernel, respectively. $L_0(1,2,1',2') = G(1,2')G(2,1')$ denotes the free electron-hole pairs without considering the interaction K. L is a function of four time variables, related to two creation (electron and hole) and two annihilation processes. Here, we consider simultaneous creation and simultaneous annihilation, resulting in two independent time variables. Moreover, only the time difference is relevent since time is homogeneous in the absence of external fields. The time-energy Fourier transform leads to $L(1,2,1',2',\omega)$, where $1, 2, 1'$, and $2'$ do not involve the time variable. For further discussion, this energy space is considered.

Now, L_0 can be written as

$$L_0(1,2,1',2',\omega) = i \sum_{v,c} \left[\frac{\psi_c(\mathbf{r}_1)\psi_v^*(\mathbf{r}_1')\psi_v(\mathbf{r}_2)\psi_c^*(\mathbf{r}_2')}{\omega - (E_c - E_v)} - \frac{\psi_v(\mathbf{r}_1)\psi_c^*(\mathbf{r}_1')\psi_c(\mathbf{r}_2)\psi_v^*(\mathbf{r}_2')}{\omega + (E_c - E_v)} \right] \tag{2.124}$$

where v and c run over the occupied hole states and unoccupied electron states, respectively. Note that the imaginary infinitesimals in the denominator should be included, which are not shown here for sake of easiness.

On including the electron-hole interaction, the correlation function L can be written in a form similar to Equation 2.124 as follows

$$L(1,2,1',2',\omega) = i \sum_{S} \left[\frac{\chi_S(\mathbf{r}_1,\mathbf{r}_1')\chi_S^*(\mathbf{r}_2',\mathbf{r}_2)}{\omega - \Omega_S} - \frac{\chi_S(\mathbf{r}_2,\mathbf{r}_2')\chi_S^*(\mathbf{r}_1',\mathbf{r}_1)}{\omega + \Omega_S} \right] \tag{2.125}$$

where S represents the correlated electron-hole states with the corresponding excitation energies Ω_S. In Equation 2.125, χ_S are the electron-hole amplitudes given by

$$\chi_S(\mathbf{r},\mathbf{r}') = -\langle N,0|\psi^\dagger(\mathbf{r}')\psi(\mathbf{r})|N,S\rangle \tag{2.126}$$

where $|N,0\rangle$ and $|N,S\rangle$ denote N-electron ground state and correlated electron-hole state, respectively. The electron-hole amplitudes can also be expressed using single-particle wave functions of the electron and hole states, given by

$$\chi_S(\mathbf{r},\mathbf{r}') = \sum_{v}^{\text{occ}} \sum_{c}^{\text{unocc}} A_{vc}^S \psi_c(\mathbf{r})\psi_v^*(\mathbf{r}') + B_{vc}^S \psi_v(\mathbf{r})\psi_c^*(\mathbf{r}') \tag{2.127}$$

where A^S_{vc} and B^S_{vc} are the coupling coefficients. Note that the combinations of two occupied or two unoccupied states do not appear. Using Equation 2.124, 2.125, and 2.127, the BSE (Equation 2.123) becomes a generalized eigenvalue problem

$$\begin{aligned}(E_c - E_v)A^S_{vc} + \sum_{v',c'} K^{AA}_{vc,v'c'}(\Omega_S)A^S_{v'c'} + \sum_{v',c'} K^{AB}_{vc,v'c'}(\Omega_S)B^S_{v'c'} &= \Omega_S A^S_{vc}, \\ \sum_{v',c'} K^{BA}_{vc,v'c'}(\Omega_S)A^S_{v'c'} + (E_c - E_v)B^S_{vc} + \sum_{v',c'} K^{BB}_{vc,v'c'}(\Omega_S)B^S_{v'c'} &= -\Omega_S B^S_{vc}\end{aligned} \tag{2.128}$$

where

$$K^{AA}_{vc,v'c'}(\Omega_S) = i\int d(3,4,5,6)\psi_v(\mathbf{r}_4)\psi^*_c(\mathbf{r}_3)K(3,5,4,6,\Omega_S)\psi^*_{v'}(\mathbf{r}_5)\psi_{c'}(\mathbf{r}_6) \tag{2.129}$$

$$K^{AB}_{vc,v'c'}(\Omega_S) = i\int d(3,4,5,6)\psi_v(\mathbf{r}_4)\psi^*_c(\mathbf{r}_3)K(3,5,4,6,\Omega_S)\psi^*_{v'}(\mathbf{r}_6)\psi_{c'}(\mathbf{r}_5) \tag{2.130}$$

and similarly, K^{BA} and K^{BB} can be defined.

The energy differences $(E_c - E_v)$ and the interaction matrix elements K^{AA} and K^{BB} form the diagonal block of the block-matrix structure of Equation 2.128. The off-diagonal blocks are formed by K^{AB} and K^{BA}. Generally, the off-diagonal blocks are small and can be neglected. Therefore, on setting $K^{AB} = K^{BA} = 0$, Equation 2.128 decouples into two equations for A^S_{vc} and B^S_{vc} separately. Both equations results in same excitations (with the only difference of negative sign in excitation energies for the solutions for B). Therefore, the eigenvalue equation that yields positive solutions is given by

$$(E_c - E_v)A^S_{vc} + \sum_{v',c'} K^{AA}_{vc,v'c'}(\Omega_S)A^S_{v'c'} = \Omega_S A^S_{vc} \tag{2.131}$$

The correlated electron-hole states can be expanded as

$$|N,S\rangle = \sum_v^{\text{hole}}\sum_c^{\text{elec}} A^S_{vc}\hat{a}^\dagger_v\hat{b}^\dagger_c|N,0\rangle =: \sum_v^{\text{hole}}\sum_c^{\text{elec}} A^S_{vc}|vc\rangle \tag{2.132}$$

where $\hat{a}^\dagger_v$ and $\hat{b}^\dagger_c$ are the creation operators for a hole and an electron, respectively, in the N-electron ground state $|N,0\rangle$. The expansion of Equation 2.132 is also called as the Tamm-Dancoff approximation.

The kernel K is determined from the functional derivative

$$K(3,4,5,6) = \frac{\delta\left[V_{\text{Coul}}(3)\delta(3,4) + \Sigma(3,4)\right]}{\delta G(6,5)} \tag{2.133}$$

we implement GW approximation to determine the self-energy operator Σ. Assuming that the derivative of W with respect to G can be neglected, K becomes

$$\begin{aligned} K(3,5,4,6) &= -i\delta(3,4)\delta(5^-,6)v(3,6) + i\delta(3,6)\delta(4,5)W(3^+,4) \\ &=: K^x(3,5,4,6) + K^d(3,5,4,6) \end{aligned} \tag{2.134}$$

The term K^x, resulting from the Coulomb potential is known as the exchange term, whereas K^d is known as the direct interaction term, ascribed to the screened-exchange self-energy. The direct interaction term K^d is attractive in nature and responsible for the formation of bound excitons. The exchange interaction term K^x determines details of the excitation spectrum, such as the spin-splitted excitations. Note that K^d and K^x contain the screened (W) and bare (v) Coulomb interactions, respectively.

The matrix elements of K are expressed as

$$\begin{aligned} \langle vc|K^{AA,d}(\Omega_S)|v'c'\rangle = \int d\mathbf{r}d\mathbf{r}'\psi_c^*(\mathbf{r})\psi_{c'}(\mathbf{r})\psi_v(\mathbf{r}')\psi_{v'}^*(\mathbf{r}') \times \frac{i}{2\pi}\int d\omega e^{-i\omega 0^+}W(\mathbf{r},\mathbf{r}',\omega) \\ \times \left[\frac{1}{\Omega_S - \omega - \left(E_{c'}^{\mathrm{QP}} - E_v^{\mathrm{QP}}\right) + i0^+} \right. \\ \left. + \frac{1}{\Omega_S + \omega - \left(E_c^{\mathrm{QP}} - E_v^{\mathrm{QP}}\right) + i0^+}\right] \end{aligned} \tag{2.135}$$

and

$$\langle vc|K^{AA,x}(\Omega_S)|v'c'\rangle = \int d\mathbf{r}d\mathbf{r}'\psi_c^*(\mathbf{r})\psi_v(\mathbf{r})v(\mathbf{r},\mathbf{r}')\psi_{c'}(\mathbf{r}')\psi_{v'}^*(\mathbf{r}') \tag{2.136}$$

K^d requires a frequency integration in addition to the real-space integration. This can be done by expanding the screened Coulomb interaction in the plasmon-pole model as follows

$$W(\mathbf{r},\mathbf{r}',\omega) = \sum_l W_l(\mathbf{r},\mathbf{r}')\frac{\omega_l}{2}\left(\frac{1}{\omega - \omega_l + i0^+} - \frac{1}{\omega + \omega_l - i0^+}\right) \tag{2.137}$$

where ω_l represents the plasmon frequency and $W_l(\mathbf{r},\mathbf{r}')$ denotes the spatial behavior of the plasmon mode l. On performing the frequency integration, Equation 2.135 becomes

$$\begin{aligned} \langle vc|K^{AA,d}(\Omega_S)|v'c'\rangle = \int d\mathbf{r}d\mathbf{r}'\psi_c^*(\mathbf{r})\psi_{c'}(\mathbf{r})\psi_v(\mathbf{r}')\psi_{v'}^*(\mathbf{r}')W_l(\mathbf{r},\mathbf{r}') \\ \times \frac{\omega_l}{2}\left[\frac{1}{\omega_l - (\Omega_S - (E_{c'}^{\mathrm{QP}} - E_v^{\mathrm{QP}}))} \right. \\ \left. + \frac{1}{\omega_l - (\Omega_S - (E_c^{\mathrm{QP}} - E_v^{\mathrm{QP}}))}\right] \end{aligned} \tag{2.138}$$

Mostly, the transition energies $(E_c^{\mathrm{QP}} - E_v^{\mathrm{QP}})$ are close to the excitation energies Ω_S in semiconductor crystals and thus, $\Omega_S - (E_c^{\mathrm{QP}} - E_v^{\mathrm{QP}})$ are much smaller than ω_l and can be neglected.

Therefore, Equation 2.138 reduces to

$$\langle vc|K^{AA,d}(\Omega_S)|v'c'\rangle = \int d\mathbf{r}d\mathbf{r}'\psi_c^*(\mathbf{r})\psi_{c'}(\mathbf{r})\psi_v(\mathbf{r}')\psi_{v'}^*(\mathbf{r}')W(\mathbf{r},\mathbf{r}',\omega=0) \tag{2.139}$$

Equation 2.139 ignores the dynamical properties of W altogether. In the case of atoms and molecules, the differences $\Omega_S - (E_c^{\mathrm{QP}} - E_v^{\mathrm{QP}})$ may be larger. In that case, Equation 2.139 no longer holds, and Equation 2.138 is used to evaluate the electron-hole interaction kernel K. Since K^d depends on excitation energies Ω_S (Equation 2.138), it poses a challenge to calculate the electron-hole interaction and solve the BSE self-consistently. It can be done iteratively. First, we determine the static screened Coulomb interaction W, and K^d is evaluated using Equation 2.139. Thereafter, BSE is solved to get excitations $|S\rangle$ and the first estimate of excitation energies $\Omega_S^{(0)}$. After that, K^d is determined from Equation 2.135 using the $\Omega_S^{(0)}$. Further, the difference of updated K^d and the previous step $K^{d,0}$ is treated as a perturbation in first order, and update the Ω_S. In this way, these steps are repeated to converge the Ω_S.

2.9.6 Optical Spectrum

The macroscopic transverse dielectric function $\epsilon(\omega)$ of a system describes the interaction of an external light field with the excitations in the system. The imaginary part $(\epsilon_2(\omega))$ of dielectric function is given by

$$\epsilon_2(\omega) = \frac{16\pi e^2}{\omega^2}\sum_S \left|\vec{\lambda}\cdot\langle 0|\vec{v}|S\rangle\right|^2 \delta(\omega - \Omega_S) \tag{2.140}$$

where $\vec{\lambda} = \frac{\vec{A}}{|\vec{A}|}$ is the polarization vector of the light and $\vec{v} = i/\hbar[H,\vec{r}]$ is the single-particle velocity operator. In the absence of electron-hole interaction, the excitations are given by vertical transitions between independent hole and electron states, and Equation 2.140 reduces to the expression

$$\epsilon_2^{(0)}(\omega) = \frac{16\pi e^2}{\omega^2}\sum_{v,c} \left|\vec{\lambda}\cdot\langle v|\vec{v}|c\rangle\right|^2 \delta(\omega - (E_c - E_v)) \tag{2.141}$$

where v and c denote the valence and conduction states, respectively. Since the excitations $|S\rangle$ are the correlated electron-hole states, the optical transition matrix elements can be written as

$$\langle 0|\vec{v}|S\rangle = \sum_v^{\text{hole}}\sum_c^{\text{elec}} A_{vc}^s\langle v|\vec{v}|c\rangle \tag{2.142}$$

The transition matrix elements $\langle v|\vec{v}|c\rangle$ should be carefully determined, which account for the nonlocal pseudopotential and the QP renormalization effects [95].

2.10 Density functional perturbation theory (DFPT)

In a crystal, the dynamical behavior of its lattice affects various physical properties such as infrared, Raman, and neutron-diffraction spectra; specific heats, thermal expansion, and heat conduction; the electron-phonon interaction related phenomena, specifically, the resistivity of metals, superconductivity, and the temperature dependence of optical spectra [96]. Density functional perturbation theory (DFPT) is a method that deals with the phonons of the materials within the linear response framework of DFT.

2.10.1 Lattice dynamics from electronic structure theory

Under the Born–Oppenheimer approximation, the lattice dynamics is described by the eigenvalues $\mathcal{E}$ and eigenstates Φ of the following Schrödinger equation

$$\left(-\sum_I \frac{\hbar^2}{2M_I}\frac{\partial^2}{\partial \mathbf{R}_I^2} + E(\mathbf{R})\right)\Phi(\mathbf{R}) = \mathcal{E}\Phi(\mathbf{R}) \tag{2.143}$$

where M_I is the mass of the Ith nucleus, $\mathbf{R}_I$ its coordinate, and $\mathbf{R} \equiv \{\mathbf{R}_I\}$ the set of all the nuclear coordinates. Here, $E(\mathbf{R})$ is the ground-state energy of a system of interacting electrons moving in the field of fixed nuclei, which is also known as the Born–Oppenheimer energy surface. The equilibrium geometry of the system is attained when the forces acting on individual nuclei become zero

$$\mathbf{F}_I \equiv -\frac{\partial E(\mathbf{R})}{\partial \mathbf{R}_I} = 0 \tag{2.144}$$

and the eigenvalues of the Hessian of the Born–Oppenheimer energy determines the vibrational frequencies ω

$$\det\left|\frac{1}{\sqrt{M_I M_J}}\frac{\partial^2 E(\mathbf{R})}{\partial \mathbf{R}_I \partial \mathbf{R}_J} - \omega^2\right| = 0 \tag{2.145}$$

The force can be determined using the Hellmann-Feynman theorem as follows

$$\mathbf{F}_I = -\frac{\partial E(\mathbf{R})}{\partial \mathbf{R}_I} = -\left\langle \Psi(\mathbf{R}) \left| \frac{\partial H_{BO}(\mathbf{R})}{\partial \mathbf{R}_I} \right| \Psi(\mathbf{R}) \right\rangle \tag{2.146}$$

where $\Psi(\mathbf{r};\mathbf{R})$ is the electronic ground-state wave function of the Born–Oppenheimer Hamiltonian, which depends parametrically upon $\mathbf{R}$

$$\begin{aligned} H_{BO}(\mathbf{R}) = &-\sum_i \frac{\hbar^2}{2m_e}\frac{\partial^2}{\partial \mathbf{r}_i^2} - \sum_{i,I}\frac{Z_I e^2}{|\mathbf{R}_I - \mathbf{r}_i|} \\ &+ \frac{e^2}{2}\sum_{i\neq j}\frac{1}{|\mathbf{r}_i - \mathbf{r}_j|} + \frac{e^2}{2}\sum_{I\neq J}\frac{Z_I Z_J}{|\mathbf{R}_I - \mathbf{R}_J|} \end{aligned} \tag{2.147}$$

Here, Z_I is the charge of the Ith nucleus. Therefore, $\mathbf{F}_I$ can be written as

$$\mathbf{F}_I = -\int d\mathbf{r}\, n(\mathbf{r}) \frac{\partial V_{ext}(\mathbf{r})}{\partial \mathbf{R}_I} - \frac{\partial E_{II}(\mathbf{R})}{\partial \mathbf{R}_I} \tag{2.148}$$

where

$$V_{ext}(\mathbf{r}) = -\sum_{i,I} \frac{Z_I e^2}{|\mathbf{R}_I - \mathbf{r}_i|} \quad \text{and} \quad E_{II}(\mathbf{R}) = \frac{e^2}{2} \sum_{I \neq J} \frac{Z_I Z_J}{|\mathbf{R}_I - \mathbf{R}_J|} \tag{2.149}$$

$n(\mathbf{r})$ is the electron charge density of the ground state. The Hessian in Equation 2.145 is determined by differentiating $\mathbf{F}_I$ with respect to nuclear coordinates

$$\frac{\partial^2 E(\mathbf{R})}{\partial \mathbf{R}_I \partial \mathbf{R}_J} \equiv -\frac{\partial \mathbf{F}_I}{\partial \mathbf{R}_J} = \int d\mathbf{r}\, \frac{\partial n(\mathbf{r})}{\partial \mathbf{R}_J} \frac{\partial V_{ext}(\mathbf{r})}{\partial \mathbf{R}_I} + \int d\mathbf{r}\, n(\mathbf{r}) \frac{\partial^2 V_{ext}(\mathbf{r})}{\partial \mathbf{R}_I \partial \mathbf{R}_J} + \frac{\partial^2 E_{II}(\mathbf{R})}{\partial \mathbf{R}_I \partial \mathbf{R}_J} \tag{2.150}$$

It defines the matrix of the interatomic force constants. The Hessian depends upon $n(\mathbf{r})$ and its first-order variation. Therefore, it is sufficient to consider only the linear response of the electron system.

2.10.2 Linear response

In DFPT, the Kohn-Sham equation is linearized along with the charge density, Kohn-Sham eigenstates and the self-consistent field (SCF) potential. The variation of Kohn-Sham orbitals is determined by the first-order perturbation theory [68]

$$(H_{SCF} - \epsilon_n)|\Delta\psi_n\rangle = -(\Delta V_{SCF} - \Delta\epsilon_n)|\psi_n\rangle \tag{2.151}$$

where the unperturbed SCF Hamiltonian is given by

$$H_{SCF} = -\frac{\hbar^2}{2m} \frac{\partial^2}{\partial \mathbf{r}^2} + V_{SCF}(\mathbf{r}) \tag{2.152}$$

The SCF potential, V_{SCF} has the following form

$$V_{SCF}(\mathbf{r}) = V_{ext}(\mathbf{r}) + \int d\mathbf{r}' \frac{n(\mathbf{r}')}{|\mathbf{r} - \mathbf{r}'|} + v_{\text{xc}}(\mathbf{r}) \tag{2.153}$$

where $v_{\text{xc}}(\mathbf{r}) \equiv \frac{\delta E}{\delta n(\mathbf{r})}$ is the exchange-correlation potential. In Equation 2.151, ΔV_{SCF} is the first-order correction to the SCF potential, given by the following expression

$$\Delta V_{SCF}(\mathbf{r}) = \Delta V_{ext}(\mathbf{r}) + \int d\mathbf{r}' \frac{\Delta n(\mathbf{r}')}{|\mathbf{r} - \mathbf{r}'|} + \left.\frac{dv_{\text{xc}}}{dn}\right|_{n=n(\mathbf{r})} \Delta n(\mathbf{r}) \tag{2.154}$$

and $\Delta\epsilon_n = \langle\psi_n|\Delta V_{SCF}|\psi_n\rangle$ is the first-order correction to Kohn-Sham eigenstates ϵ_n. For the nonmagnetic systems, the linearized charge density, $\Delta n(\mathbf{r})$ is given by

$$\Delta n(\mathbf{r}) = 4 \sum_{n=1}^{N/2} \psi_n^*(\mathbf{r}) \Delta\psi_n(\mathbf{r}) \tag{2.155}$$

where $\Delta(\equiv \Delta^{\lambda})$ is the finite-difference operator, defined as

$$\Delta^{\lambda} F = \sum_i \frac{\partial F_{\lambda}}{\partial \lambda_i} \Delta \lambda_i \tag{2.156}$$

Here, λ is a set of parameters, which is $\mathbf{R}_I$ for the lattice dynamics. The first-order correction to the eigenfunctions in Equation 2.151 can be expressed as

$$\Delta \psi_n(\mathbf{r}) = \sum_{m \neq n} \psi_m(\mathbf{r}) \frac{\langle \psi_m | \Delta V_{SCF} | \psi_n \rangle}{\epsilon_n - \epsilon_m} \tag{2.157}$$

where the summation runs over all the occupied and unoccupied states, except the states for which the denominator vanishes. Using Equation 2.157 and 2.155, $\Delta n(\mathbf{r})$ can be written as

$$\Delta n(\mathbf{r}) = 4 \sum_{n=1}^{N/2} \sum_{m \neq n} \psi_n^*(\mathbf{r}) \psi_m(\mathbf{r}) \frac{\langle \psi_m | \Delta V_{SCF} | \psi_n \rangle}{\epsilon_n - \epsilon_m} \tag{2.158}$$

It can be seen from Equation 2.158 that the contributions due to products of occupied states cancel. Therefore, the label n can be identified as attaching to valence band states v, and the index m attaches itself only to conduction band states c.

To evaluate $\Delta \psi_n(\mathbf{r})$, the projection operator P_c is introduced in Equation 2.151, resulting in the Sternhiemer equation

$$(H_{SCF} + \alpha P_v - \epsilon_v) | \Delta \psi_n \rangle = -P_c \Delta V_{SCF} | \psi_v \rangle \tag{2.159}$$

where $P_c = \sum\limits_c |\psi_c\rangle\langle\psi_c| = 1 - \sum\limits_v |\psi_v\rangle\langle\psi_v|$. A multiple of the projector operator P_v is added to make Equation 2.151 nonsingular. To solve Equation 2.159, only the knowledge of occupied states is required instead of the full eigenvalue spectrum. Consequently, the computational cost is of the same order as that required to solve the Kohn-Sham equations.

CHAPTER 3

Role of defects in photocatalytic water splitting: Monodoped vs codoped $SrTiO_3$

3.1 Introduction

Semiconductor-based photocatalysts have attracted considerable interest because of their potential in harnessing the solar energy for solving the current energy demand of the world and environmental degradation [97, 98, 99, 100, 101]. The criteria satisfied by a photocatalyst involve suitable band-edge positions that straddle the reduction and oxidation potential of a desired chemical compound, high separation rate, slow recombination rate, high mobility of photoexcited charge carriers, and longer lifetime [102]. Among various perovskite photocatalysts, $SrTiO_3$ has emerged as one of the most promising energy materials for photocatalytic water splitting and pollutant degradation in the past few years because of its exceptional electronic structure, optical properties, photochemical stability, and low cost [103, 104, 105, 106, 107, 108]. However, one of the major concerns is its large band gap (3.25 eV) due to which it only responses to ultraviolet (UV) irradiation, which consists only 4% of the solar spectrum [109]. Therefore, it delimits the application of $SrTiO_3$ at a commercial level. Thus, several works have been endeavored to reduce the band gap of $SrTiO_3$ in order to induce visible light absorption via doping with metals [110, 111], nonmetals [112, 113] or a combination of several elements [114, 115, 116, 117, 118].

Earlier, different metal cations, particularly transition metal (TM) dopants, were used to expand the spectral response [110, 111, 119, 120, 121]. However, merely the band gap reduction cannot ensure the enhancement in photocatalytic efficiency as it also depends on the location of the conduction band minimum (CBm) and valence band maximum (VBM). For TM doped $SrTiO_3$, TM d-states hybridize with those states of the $SrTiO_3$ that contribute to the conduction band, and thus, the reduction in band gap occurs by shifting of CBm in a downward direction. However, due to this, the reducing power is deteriorated. Also, in general, doping by 3d elements leads to localized states in the gap, which are detrimental to the photocatalysis [111, 122]. Therefore, the transition metal alone is not suitable for improvement in photocatalytic activity. On the other hand, nonmetal doped $SrTiO_3$ is found to narrow the band gap by elevating the VBM. However, in this case also, localized states appeared deep inside the forbidden region, which can trap the photoexcited charge carriers and accelerate the electron–hole recombination. This in turn degrades the photocatalytic efficiency [111, 122]. The codoping with a metal is one of the pre-eminent solutions to passivate such discrete states of nonmetal dopants in the forbidden region and form the continuum band [122, 123, 124, 125]. This has motivated us for codoping. Earlier studies have suggested that codoping of metal in nonmetal-doped $SrTiO_3$ stabilizes the system, i.e., the solubility of nonmetal gets increased [122, 123]. By means of codoping, band edges can be engineered to comply with the needs; i.e., the spectral response expands to the visible region while retaining the reduction and oxidation power [126, 127].

In view of this, we have done a careful prescreening of various codopants (only those elements were chosen, which have been used as a monodopant in the literature) by calculating the band gap using PBE [59] exchange-correlation (ϵ_{xc}) functional of density functional theory (DFT) [54, 55] (see Table 3.1). Note that even if PBE is not so good to estimate the band gap, it is good enough to give us some meaningful trend. We find, in this class of oxide perovskites, the typical error in PBE band gap with respect to HSE06 [60, 61] is $\sim$ 1.0-1.5 eV [for example, the pristine has the PBE (HSE06) band gap of 1.75 (3.28) eV]. Therefore, keeping this in mind, we have identified few promising systems (marked as red) and we have chosen N and Mn codoped system as a test case. The decrement in band gap is suitable for the Mn and N codoped system, whereas in rest of the cases (not marked as red), the band gap decrement is either larger or smaller than what is needed for the maximum efficiency in photocatalytic water splitting ($\sim$ 2 eV [128, 129]). Moreover, one of the important factors for choosing Mn is that it has d-d transition, and its d-orbitals' energy facilitates the suitable potentials for water redox reactions. Note that the individual monodopants (i.e., N and Mn) have already been experimentally synthesized [130, 131, 132, 133, 134]. However, for the codoping of Mn and N in bulk $SrTiO_3$, any experimental or theoretical reports are obscure.

In this chapter, we have, therefore, studied codoped (N–Mn) $SrTiO_3$ for enhancing the photocatalytic efficiency under visible light. After examining this test case, we have also studied

Table 3.1: Band gap of different codopants in $SrTiO_3$ using PBE ϵ_{xc} functional

Codoped System	Band gap (eV)
$Cr_{Ti}B_O$	0.57
$Cr_{Ti}C_O$	metallic
$Cr_{Ti}F_O$	1.13
$Cr_{Ti}N_O$	0.34
$Cr_{Ti}S_O$	0.35
$Fe_{Ti}B_O$	0.17
$Fe_{Ti}C_O$	metallic
$Fe_{Ti}F_O$	0.30
$Fe_{Ti}N_O$	metallic
$Fe_{Ti}S_O$	metallic
$Mn_{Ti}B_O$	0.38
$Mn_{Ti}C_O$	0.13
$Mn_{Ti}F_O$	1.39
$Mn_{Ti}N_O$	0.70
$Mn_{Ti}S_O$	0.89
$Rh_{Ti}B_O$	0.07
$Rh_{Ti}C_O$	0.34
$Rh_{Ti}F_O$	1.03
$Rh_{Ti}N_O$	1.19
$Rh_{Ti}S_O$	0.85
$La_{Sr}B_O$	1.41
$La_{Sr}C_O$	0.27
$La_{Sr}F_O$	2.19
$La_{Sr}N_O$	1.42
$La_{Sr}S_O$	1.43
$Pr_{Sr}B_O$	1.33
$Pr_{Sr}C_O$	1.65
$Pr_{Sr}F_O$	2.06
$Pr_{Sr}N_O$	1.25
$Pr_{Sr}S_O$	1.47

other codoped cases, viz., S–Mn, S–Rh, and N–Rh. First, the thermodynamic stability of doped $SrTiO_3$ has been evaluated using hybrid DFT and *ab initio* atomistic thermodynamics at realistic conditions (temperature (T) and partial pressure of oxygen (p_{O_2})) [87]. On doping $SrTiO_3$ with a nonmetal dopant (e.g., N), the possible defects that could occur are N_O (N substituted at the O position), N_i (N as an interstitial making a bond with O), and $(N_2)_O$ split-interstitial (one N is at the interstitial position, and another one is substituted by the nearby O, making a bond with each other) [130, 131, 132]. In the case of metal dopant (e.g., Mn), Mn could be substituted either at the Ti (Mn_{Ti}) or Sr (Mn_{Sr}) site, or it could also be present as an interstitial (Mn_i) in $SrTiO_3$ [133, 134]. These defects are not stable in neutral form because of the uncompensated charge. Therefore, we have calculated the stability of charged defects in addition to neutral defects with charge states q (-2, -1, 0, $+1$, $+2$). Note that in order to compensate the charge, one can adapt either of the approaches: (i) explicit presence of oxygen vacancies for the neutral dopants [135, 136] or (ii) addition of external charge to the dopant [87, 137, 138]. Both the approaches yield the same conclusion as they are doing effectively the same charge compensation at the defect site. Moreover, the formation energy plots provide the information of the most prominent charge defect at different environmental conditions, which removes the ambiguity of the preferred defect site in doped $SrTiO_3$. Next, to get the insights on synergistic effect of codoping, electronic density of states for pristine, monodoped, and codoped $SrTiO_3$ have been compared. In addition, the optical response using single-shot GW [63, 139] method is also analyzed. Furthermore, from the perspective of its usage in photocatalytic water splitting, we have examined the band-edge alignment of (un)doped $SrTiO_3$ w.r.t. water redox potential levels. Finally, the effective mass of charge carriers has been determined, which reflects the charge carrier mobility of the system.

3.2 Computational methods

The DFT calculations were performed using the Vienna *ab initio* simulation package (VASP) [140, 141]. The projector-augmented wave (PAW) potentials [142] were used to describe the ion-electron interactions in all the elemental constituents. The total energy calculations were performed using the hybrid ϵ_{xc} functional HSE06 [61]. To introduce defects in $SrTiO_3$, we have used a 40-atom supercell, which is constructed by a $2 \times 2 \times 2$ repetition of cubic $SrTiO_3$ unit cell (5 atoms). To ensure the convergence of supercell size, test calculations were performed with 90-atom supercell ($3\times3\times2$ repetition of unit cell of SrTiO$_3$) for the case of N$_\text{O}$, so that the defect is fully localized. The results obtained from 40- and 90-atom supercells were consistent with each other. Therefore, we performed all the calculations with 40-atom supercell.

We benchmarked the ϵ_{xc} functionals, viz., local-density approximation (LDA [58]), semi-local PBE and a more pronounced non-local hybrid HSE06, to ensure that our results are not an artifact of chosen treatment for the ϵ_{xc}. The LDA and PBE ϵ_{xc} functionals underestimate the band gap, giving a value of 1.37 and 1.75 eV, respectively. Whereas, the hybrid ϵ_{xc} functional HSE06 reproduces the band gap of 3.28 eV by taking the 28% of Hartree-Fock exact exchange into account, which is in nice match with the experimental value of 3.25 eV [143]. We have also calculated the defect formation energy for single O-vacancy $E_\text{f}(\square)^q$ in our system with charge states $q = 0, +1, +2, -1,$ and -2 using LDA, PBE, and HSE06 ϵ_{xc} functionals since we need to find out the stability of the defected systems. The $E_\text{f}(\square)^q$ was calculated as follows [87, 137, 138]

$$\begin{aligned} E_\text{f}(\square)^q = E_\text{tot}(\square)^q - E_\text{tot}(\text{SrTiO}_3) + \mu_\text{O} \\ + q(\mu_\text{e} + \text{VBM} + \Delta V) \end{aligned} \tag{3.1}$$

where $E_\text{tot}(\square)^q$ is the total energy of supercell containing single O-vacancy with charge state q, and $E_\text{tot}(\text{SrTiO}_3)$ is the total energy of the same supercell without any defect. μ_O is the chemical potential of the oxygen atom, which is equal to the energy required to remove an oxygen atom from the pristine supercell and put it into the oxygen reservoir; $\mu_\text{O} = \frac{1}{2}E_\text{tot}(\text{O}_2)$, and $E_\text{tot}(\text{O}_2)$ is the total energy of an isolated O$_2$ molecule. μ_e is the chemical potential of electron, that is referenced from VBM of the pristine supercell. ΔV is the core level alignment between the pristine and defected supercells. We found from Figure 3.1 that $q = +2$ and $q = -2$ are the stable charge states near VBM and CBm, respectively, using both LDA and PBE ϵ_{xc} functionals. However, this is not the case with hybrid ϵ_{xc} functional HSE06. Using HSE06, we observed that only $q = +2$ charge state is stable througout the band gap. It implies that, results which are obtained from LDA, and PBE are different from that of the HSE06. Since the deficiency of a single O-vacancy results in two free electrons in the system, it should be stable after releasing these electrons (i.e., in charge state $q = +2$). Moreover, as HSE06 ϵ_{xc} functional is more accurate being non-local, containing a fraction of exact exchange, HSE06 ϵ_{xc} functional is more reliable for our system. Therefore, we did our further calculations with HSE06 ϵ_{xc} functional.

A k-mesh of $4\times4\times4$ was used, which was generated using Monkhorst-Pack [75] scheme.

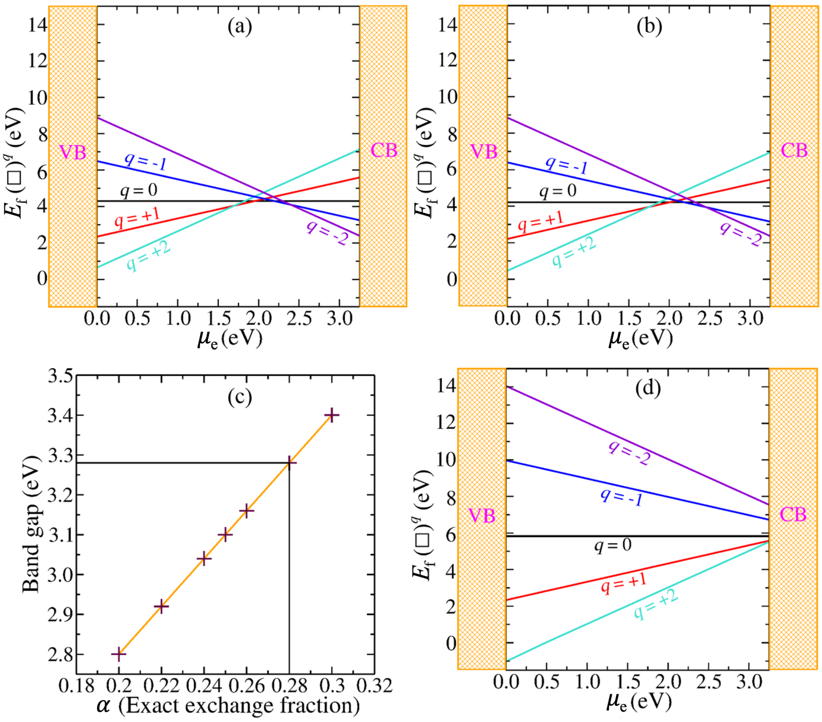

Figure 3.1: The formation energy of a single O-vacancy defect as a function of chemical potential of electron under O-rich condition using (a) LDA, (b) PBE, and (d) HSE06 ϵ_{xc} functionals. (c) The variation in band gap of pristine supercell as a function of exact exchange fraction (α) contained in HSE06 ϵ_{xc} functional.

The self-consistency loop was converged with a threshold of 0.01 meV energy. The cutoff energy of 600 eV was used for the plane wave basis set convergence. Note that we performed the spin-polarized calculations because the doped systems contain unpaired electrons. The quasiparticle energy calculations were carried out using single-shot G_0W_0 approximation starting from the orbitals obtained using HSE06 ϵ_{xc} functional. The polarizability calculations were performed on a grid of 50 frequency points. To make computation feasible, the number of bands was set to 480, which is around four times the number of occupied bands.

3.3 Results and discussion

3.3.1 Stabilitiy of defects in $SrTiO_3$: *Ab initio* atomistic thermodynamics

To analyze the thermodynamic stability of the defected configuration w.r.t. pristine $SrTiO_3$, we have calculated the formation energy by means of *ab initio* atomistic thermodynamics [87, 137, 144, 145, 146]. For an X-related defect with charge state q, the formation energy ($E_f(X^q)$) is calculated as follows [87, 137, 138]

$$\begin{aligned} E_{\text{f}}(X^q) &= E_{\text{tot}}(X^q) - E_{\text{tot}}(\text{pristine}^0) - \sum_i n_i \mu_i \\ &+ q(\mu_{\text{e}} + \text{VBM} + \Delta V) \end{aligned} \tag{3.2}$$

where, $E_{\text{tot}}(X^q)$ and $E_{\text{tot}}(\text{pristine}^0)$ are the total DFT energies with defect (at charge state q) and pristine neutral, respectively. n_i is the number of atoms i added (positive) or removed (negative) from the system (i = N, S, O, Mn, Rh, Sr, or Ti), and μ_i is the corresponding chemical potential. μ_i is referenced from the total DFT energy $(E_{\text{tot}}(i))$ of species i, i.e., $\mu_i = \Delta\mu_i + E_{\text{tot}}(i)$. The chemical potentials, $\Delta\mu_i$, have been chosen carefully to reflect the appropriate environmental growth conditions. μ_{e} is the chemical potential of electron varied from the VBM to CBm of the pristine system, and ΔV accounts for the core level alignment of the defected system w.r.t. the pristine neutral system.

The effect of temperature and pressure is explicitly taken into chemical potential term. For oxygen, the chemical potential $\Delta\mu_{\text{O}}$ as a function of temperature (T) and the partial pressure of oxygen (p_{O_2}) is calculated using the relation [144]

$$\begin{aligned} \Delta\mu_{\text{O}}(T, p_{\text{O}_2}) = \frac{1}{2} \Bigg[&-k_{\text{B}}T \ln \left[\left(\frac{2\pi m}{h^2} \right)^{\frac{3}{2}} (k_{\text{B}}T)^{\frac{5}{2}} \right] \\ &+ k_{\text{B}}T \ln p_{\text{O}_2} - k_{\text{B}}T \ln \left(\frac{8\pi^2 I_A k_{\text{B}} T}{h^2} \right) \\ &+ k_{\text{B}}T \ln \left[1 - \exp\left(\frac{-h\nu_{\text{OO}}}{k_{\text{B}}T} \right) \right] \\ &- k_{\text{B}}T \ln \mathcal{M} + k_{\text{B}}T \ln \sigma \Bigg] \end{aligned} \tag{3.3}$$

where m is the mass, I_A is the moment of inertia of O_2 molecule, ν_{OO} is the O–O stretching frequency, $\mathcal{M}$ is the spin multiplicity and σ is the symmetry number.

Under equilibrium growth conditions, the chemical potentials are related to the enthalpy of formation of $SrTiO_3$ $(\Delta H_{\text{f}}(SrTiO_3))$ by

$$\Delta\mu_{\text{Sr}} + \Delta\mu_{\text{Ti}} + 3\Delta\mu_{\text{O}} = \Delta H_{\text{f}}(\text{SrTiO}_3) \tag{3.4}$$

To ensure the suppression of secondary phases, constraints are imposed on the different chem-

Table 3.2: The chemical potentials at different environmental conditions

Growth Conditions	$\Delta\mu_{\mathrm{O}}$	$\Delta\mu_{\mathrm{N}}$	$\Delta\mu_{\mathrm{Ti}}$	$\Delta\mu_{\mathrm{Sr}}$	$\Delta\mu_{\mathrm{Mn}}$	$\Delta\mu_{\mathrm{Rh}}$	$\Delta\mu_{\mathrm{S}}$
O-poor (Ti-rich)	-4.55	-1.48	0.00	-3.98	0.00	0.00	-2.10
O-intermediate	-1.58	-1.48	-5.95	-6.96	-2.44	0.00	0.00
O-rich (Ti-poor)	0.00	-1.48	-9.11	-8.54	-5.61	-2.21	0.00

ical potentials as given below

$$\Delta\mu_{\mathrm{Ti}} + 2\Delta\mu_{\mathrm{O}} \leq \Delta\mathrm{H_f}(\mathrm{TiO_2}) \tag{3.5a}$$

$$\Delta\mu_{\mathrm{Mn}} + 2\Delta\mu_{\mathrm{O}} \leq \Delta\mathrm{H_f}(\mathrm{MnO_2}) \tag{3.5b}$$

$$\Delta\mu_{\mathrm{Ti}} + 2\Delta\mu_{\mathrm{S}} \leq \Delta\mathrm{H_f}(\mathrm{TiS_2}) \tag{3.5c}$$

$$2\Delta\mu_{\mathrm{Rh}} + 3\Delta\mu_{\mathrm{O}} \leq \Delta\mathrm{H_f}(\mathrm{Rh_2O_3}) \tag{3.5d}$$

$$\Delta\mu_X \leq 0;\ (X = \text{Ti, Sr, Mn, Rh, O, S, N}) \tag{3.5e}$$

We can see that the chemical potentials could be determined by imposing bounds on the formation of the precursors (TiO_2, MnO_2, TiS_2, and Rh_2O_3) or the secondary phases and are inter-related. We have calculated the formation energy in three regimes, viz. O-rich ($\Delta\mu_{\mathrm{O}} = 0$ eV), O-intermediate ($\Delta\mu_{\mathrm{O}} = -1.58$ eV) and O-poor ($\Delta\mu_{\mathrm{O}} = -4.55$ eV) conditions. The $\Delta\mu_X$ for different growth conditions are given in Table 3.2. O-rich and O-poor conditions are the extreme growth conditions, which show the abundance and scarcity of O-content. For O-rich and O-poor conditions, $\Delta\mu_{\mathrm{O}}$ is determined by the bound of Equation 3.5e, and bound on the formation of TiO_2 (Equation 3.5a), respectively. O-intermediate condition ($\Delta\mu_{\mathrm{O}} = -1.58$ eV) reflects the experimentally relevant condition (T = 1373 K, $p_{\mathrm{O_2}} = 1$ atm [147]) at which generally the growth of the system takes place. For O-intermediate condition, $\Delta\mu_{\mathrm{O}}$ is calculated using Equation 3.3. We have fixed the $\Delta\mu_{\mathrm{N}} = -1.48$ eV, which is obtained at experimental growth condition. Under O-rich and O-intermediate conditions, $\Delta\mu_{\mathrm{Ti}}$ and $\Delta\mu_{\mathrm{Mn}}$ are limited by the formation of TiO_2 and MnO_2, respectively. Under O-poor (Ti-rich) condition, $\Delta\mu_{\mathrm{Ti}}$ and $\Delta\mu_{\mathrm{Mn}}$ are limited by the formation of metallic phase of Ti and Mn, respectively. The $\Delta\mu_{\mathrm{Rh}}$ is determined using the bound of Equation 3.5d and 3.5e. Moreover, $\Delta\mu_{\mathrm{S}}$ is calculated by the bound of Equation 3.5c and 3.5e. By knowing the stability of different dopants under certain conditions, one could deliberately dope the $SrTiO_3$ in accordance with the need.

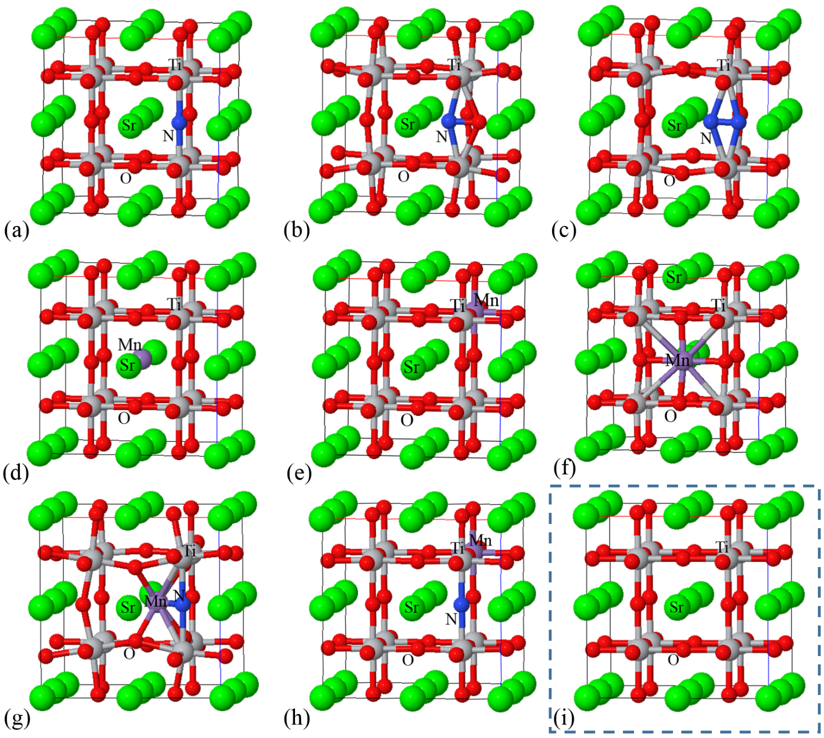

Figure 3.2: Ball and stick model of the optimized structures of (a) N_O, (b) N_i, (c) $(N_2)_O$, (d) Mn_{Sr}, (e) Mn_{Ti}, (f) Mn_i (g) $Mn_{Sr}N_O$, (h) $Mn_{Ti}N_O$, and (i) pristine SrTiO$_3$.

3.3.1.1 N-related defects

The optimized structures of all the (N,Mn) doped and pristine SrTiO$_3$ supercells are shown in Figure 3.2. SrTiO$_3$ has a cubic structure with space group $Pm\bar{3}m$ at room temperature (see Figure 3.2i). On doping N in pristine, N-related defects, viz. N_O, N_i, and $(N_2)_O$, could form. N_O shows negligible distortion, whereas N_i and $(N_2)_O$ show more distortion in the lattice (see Figure 3.2a, 3.2b, and 3.2c). We can sum up about the stability of all the three configurations of N-related defects at different environmental conditions by observing the 3D phase diagram as shown in Figure 3.3a. Here, on the x-axis, $\Delta\mu_O$ is varied from O-poor to O-rich conditions in accordance with T and p_{O_2}. On the y-axis, we have scanned the entire forbidden region by means of μ_e, which is referenced from the VBM of pristine SrTiO$_3$. On the z-axis, we have shown the most stable phases having a minimum formation energy at a given environmental condition using the colored surfaces. The charge states $+1$ and -1 are energetically stable in the case of N_O near the VBM and CBm, respectively. N_i is energetically stable in charge states $+1$, 0, and -1. The positive charge states are more favorable for smaller value of μ_e, i.e., near the VBM (p-type), whereas negative charge states are stable near the CBm (n-type) for a larger value of μ_e. Since O-poor and O-rich conditions also correspond to lesser and more content of O, respectively; therefore N_O is more difficult/easier to form in O-rich/O-poor conditions. N_O is stable with the charge state -1 near CBm, as it has one electron less than the O atom. The thermodynamic transition level $(+/-)$ lies in between the VBM and CBm, indicating that N_O acts as both a deep donor/acceptor depending on the nature of doping (i.e., p-type or n-type). From Figure 3.3a, we can easily see that N_O is the predominant defect in N-doped $SrTiO_3$ for a wide range of environmental conditions including the experimental

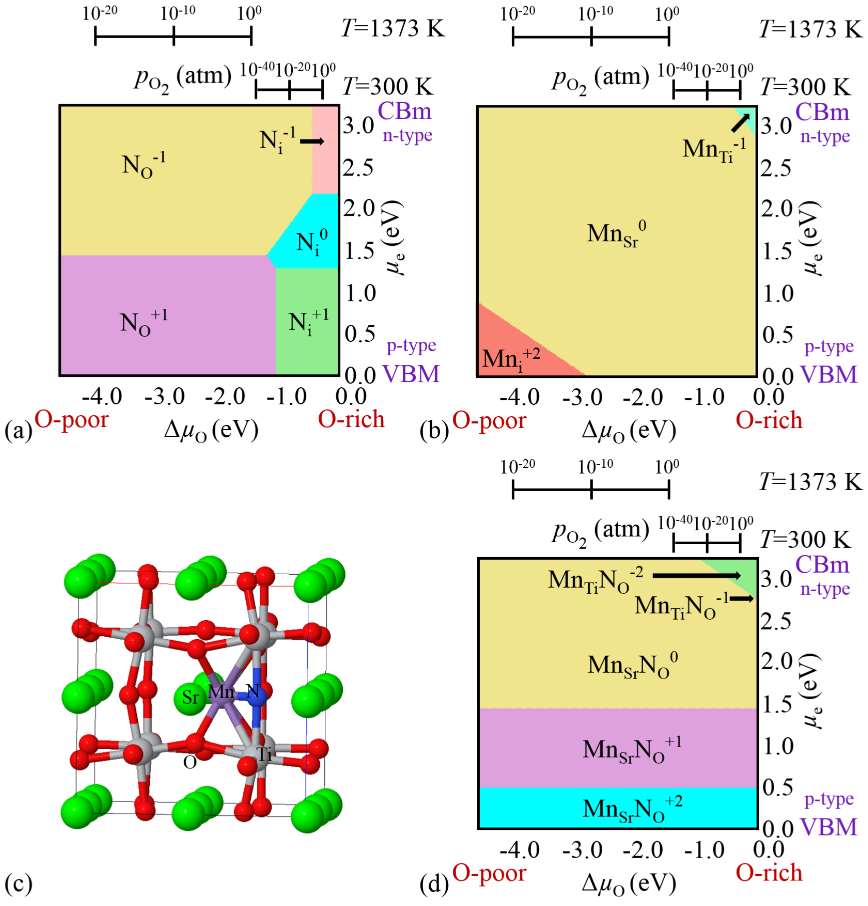

Figure 3.3: 2D projection of the 3D phase diagram that manifests the stable phases of (a) N-related, (b) Mn-related and (d) (N–Mn)-related charged defects having minimum formation energy as a function of μ_e and $\Delta\mu_O$. Here, on the x-axis, $\Delta\mu_O$ is varied according to T and p_{O_2}, and on the y-axis, μ_e is varied from the VBM to CBm of the pristine $SrTiO_3$. Colored regions show the most stable phases having a minimum formation energy at a given environmental condition. Top axes are showing the pressure (p_{O_2}) range at two temperatures: T=300 K and 1373 K. (c) Ball and stick model of the optimized structure of $Mn_{Sr}N_O$ defect configuration.

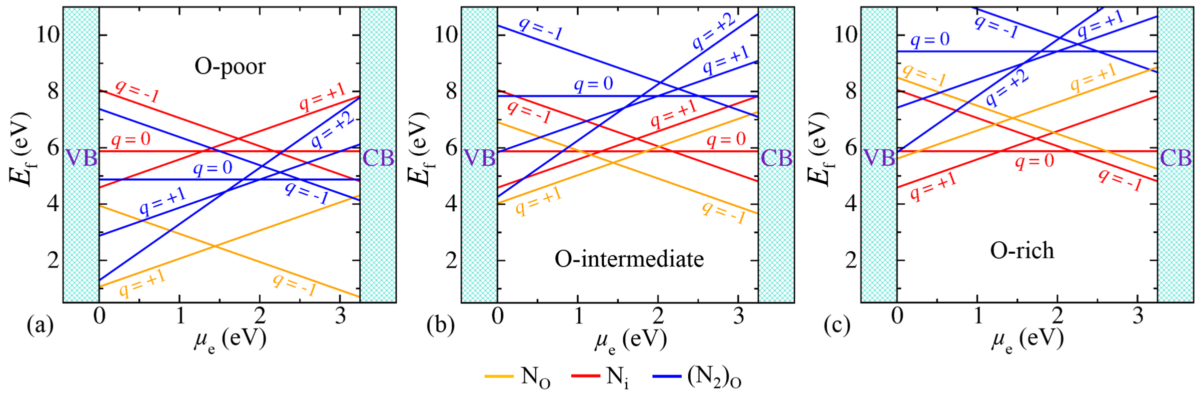

Figure 3.4: Formation energy of N-related defects in $SrTiO_3$ as a function of chemical potential of electron at (a) O-poor, (b) O-intermediate, and (c) O-rich conditions. Only those charge states of a particular defect are shown, which have lowest formation energies.

growth condition ($T = 1373$ K, $p_{O_2} = 1$ atm [147]), whereas N_i is only favorable in O-rich condition. These results are in accordance with the 2D phase diagrams (see Figure 3.4). The formation energy of all the N-related defect configurations is large in O-rich and O-intermediate conditions, which implies that N is less soluble in $SrTiO_3$ (see Figure 3.4b and 3.4c).

3.3.1.2 Mn-related defects

On doping Mn in $SrTiO_3$, the structures that could form are Mn_{Sr}, Mn_{Ti}, and Mn_i (see Figure 3.2d, 3.2e, and 3.2f). In the case of Mn_{Sr}, only neutral defect is stable, which signifies that Mn exists in the Mn^{2+} oxidation state when substituted at the Sr (Sr^{2+} oxidation state) site in $SrTiO_3$ (see Figure 3.3b). Mn_{Ti} is stable in the -1 charge state, indicating that in addition to Mn^{4+} oxidation state, Mn^{3+} oxidation state could also exist, though unlikely, when Mn is substituted at the Ti (Ti^{4+} oxidation state) site. Mn_i with a $+2$ charge state is stable in p-type $SrTiO_3$ under O-poor condition, while Mn_{Ti} with a -1 charge state is stable in n-type $SrTiO_3$ under O-rich condition, as shown in the 3D phase diagram (see Figure 3.3b). Neutral Mn_{Sr} is the prominent defect under all the three environmental conditions. The formation energy for Mn-doped $SrTiO_3$ in all oxygen environmental conditions is small, particularly in O-intermediate condition (see Figure 3.5), which implies that it is easier to dope Mn in $SrTiO_3$.

3.3.1.3 Codoped $SrTiO_3$

From the above analysis, we conclude that in the case of monodoped $SrTiO_3$, substitutional doping is the most stable for a wider region of the environmental conditions, including the

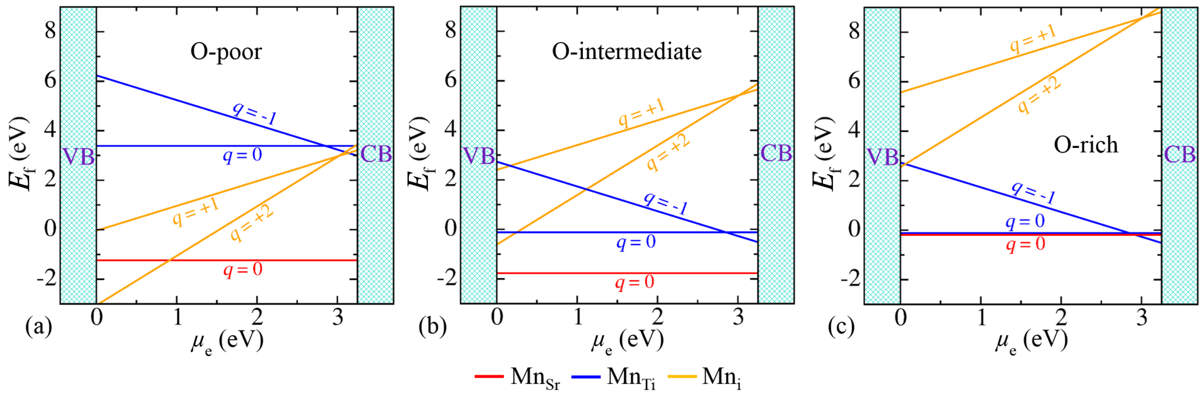

Figure 3.5: Formation energy of Mn-related defects in $SrTiO_3$ as a function of chemical potential of electron at (a) O-poor, (b) O-intermediate, and (c) O-rich conditions.

experimental growth conditions. Therefore, we have considered only the substitutional position for codoping of Mn (Mn at Sr or Ti site) and N (N at O sites) in $SrTiO_3$ (see Figure 3.2g and 3.2h). The formation energy of $Mn_{Sr}N_O$ ($E_f(Mn_{Sr}N_O^q)$) is calculated as follows

$$\begin{aligned} E_f(\mathrm{Mn_{Sr}N_O^q}) = E_{\mathrm{tot}}(\mathrm{Mn_{Sr}N_O^q}) - E_{\mathrm{tot}}(\mathrm{SrTiO_3^0}) + \mu_{\mathrm{O}} - \mu_{\mathrm{N}} \\ + \mu_{\mathrm{Sr}} - \mu_{\mathrm{Mn}} + q(\mu_e + \mathrm{VBM} + \Delta V) \end{aligned} \tag{3.6}$$

where $E_{\mathrm{tot}}(\mathrm{Mn_{Sr}N_O^q})$ and $E_{\mathrm{tot}}(\mathrm{SrTiO_3^0})$ are the DFT energies of the codoped system (Mn at Sr and N at O) with charge q and the pristine neutral $SrTiO_3$, respectively. μ_O and μ_N are the chemical potentials of the oxygen and nitrogen atom, referenced from the total DFT energy with the addition of zero-point energy of O_2 and N_2 molecules, respectively, i.e., $\mu_O = \Delta\mu_O + \frac{1}{2}\left(E_{\mathrm{tot}}(O_2) + \frac{h\nu_{OO}}{2}\right)$ and $\mu_N = \Delta\mu_N + \frac{1}{2}\left(E_{\mathrm{tot}}(N_2) + \frac{h\nu_{NN}}{2}\right)$. In the latter terms, ν_{OO} and ν_{NN} are the O–O and N–N stretching frequencies, respectively. The chemical potentials $\Delta\mu_X$ are chosen carefully (as discussed above). Figure 3.3d shows the 3D phase diagram for the stability of (N–Mn) codoped systems. $Mn_{Sr}N_O$ is the predominant defect in all the environmental growth conditions and is stable in +2, +1, and neutral charge states. This will act as a donor in p-type $SrTiO_3$. Whereas, $Mn_{Ti}N_O$ is stable only for a smaller region in extreme O-rich/Ti-poor condition with charge states -1 and -2 near CBm (n-type); i.e., it will act as an acceptor (see Figure 3.3d). The results are in accordance with the 2D phase diagrams (see Figure 3.6). To further confirm that the formation of the defect pair (N–Mn) in $SrTiO_3$ is stable, the binding energy (E_b) of the defect pair (N–Mn) in $SrTiO_3$ has also been checked [124, 148]. Note that we have taken the difference between total DFT energies (of codoped and pristine $SrTiO_3$) and total DFT energies (of respective monodoped $SrTiO_3$), which is opposite to the convention that

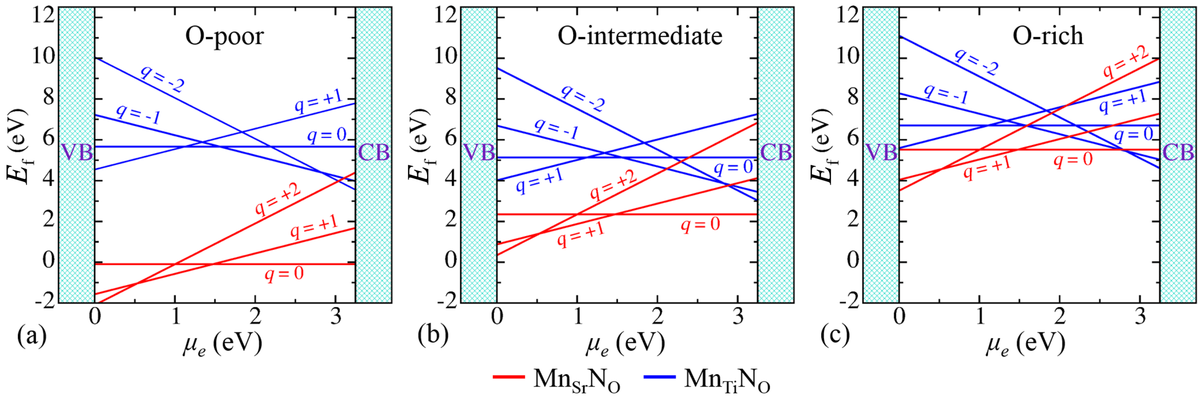

Figure 3.6: Formation energy of (N–Mn)-related defects as a function of chemical potential of electron at (a) O-poor, (b) O-intermediate and (c) O-rich conditions.

has been considered in Refs [124, 148]. Therefore, the pair that has negative binding energy is stable. A more negative value of E_b indicates that the defect pair is more stable when both the dopants are present in the sample. E_b values for Mn$_{Sr}$N$_O$ and Mn$_{Ti}$N$_O$ pairs are -1.46 and -0.33 eV, respectively. These values indicate that defect pairs are more stable than the isolated impurities in SrTiO$_3$ supercell. Also, Mn$_{Sr}$N$_O$ is a more stable configuration than Mn$_{Ti}$N$_O$ since Mn$_{Sr}$N$_O$ has higher (more negative) binding energy than Mn$_{Ti}$N$_O$. In the (N–Mn) codoped system, Mn acts as a donor, whereas N acts as an acceptor. The charge transfer takes place from donor to acceptor, and strong Coulomb interaction arises between a positively charged donor and negatively charged acceptor. Hence, the defect pair is stable. The extra stability in Mn$_{Sr}$N$_O$ is due to the shift of Mn away from the Sr center toward N as shown in Figure 3.3c and making strong bonds with its neighbor atoms.

After studying the test case of N–Mn, we have studied the thermodynamic stability of other codoped cases, specifically, S–Mn, S–Rh, and N–Rh. Under all the three conditions (namely, O-rich, O-intermediate, and O-poor), formation energy of Mn$_{Ti}$S$_O$ depends only on the charge states q. Therefore, it remains same for all the three conditions (see Figure 3.7). Whereas, formation energy of Mn$_{Sr}$S$_O$ depends linearly on $\Delta\mu_O$ in addition to charge states q. Therefore, E_f(Mn$_{Sr}$S$_O^q$) shifts by a constant amount for a particular growth condition. It is most negative in O-poor condition (see Figure 3.7c). This implies that formation of Mn$_{Sr}$S$_O$ in SrTiO$_3$ is easier in O-poor condition. Moreover, from Figure 3.7a-c, we can see that Mn$_{Ti}$S$_O$ is stable only in O-rich condition near the CBm (n-type) with charge state -1, whereas the positive charge states are stable for Mn$_{Sr}$S$_O$ codoped SrTiO$_3$. In the case of Mn$_{Sr}$S$_O$, $+2$ charge state is stable near the VBM and thereafter, in between $+1$ charge state is the most stable. This indicates that the

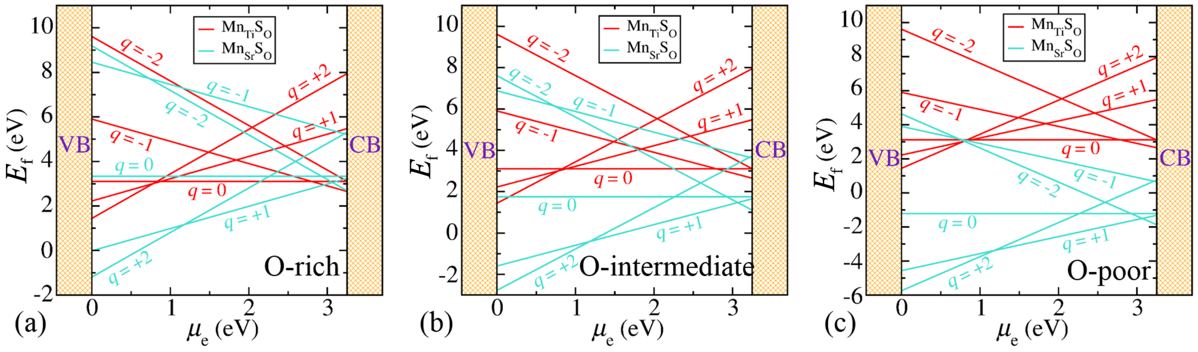

Figure 3.7: Formation energy of (S–Mn)-related defect in $SrTiO_3$ at (a) O-rich, (b) O-intermediate, and (c) O-poor conditions.

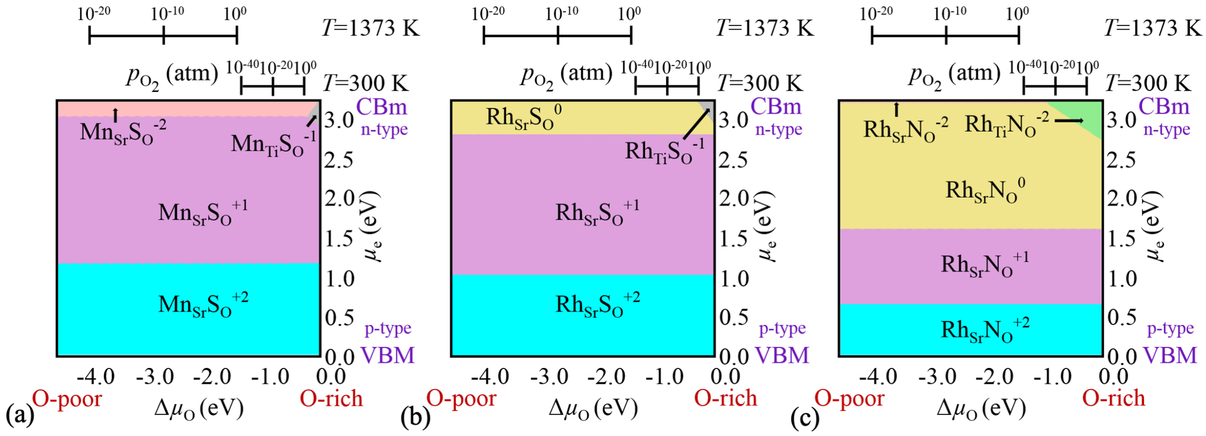

Figure 3.8: 3D phase diagram that shows the most stable phases of (a) S–Mn, (b) S–Rh, and (c) N–Rh codoped $SrTiO_3$ having minimum formation energy as a function of $\Delta\mu_O$ and μ_e.

defect will act as a donor. Near the CBm, -2 charge state of $Mn_{Sr}S_O$ is the most stable. This whole result of 2D formation energy plots at different growth conditions can be summarized by a 3D phase diagram that show only the most stable phases having minimum formation energy (see Figure 3.8a). From Figure 3.8a, we can easily see that $Mn_{Sr}S_O$ is stable in $+2$, $+1$ and -2 charge states in all the conditions, which is also confirmed from Figure 3.7. Whereas, $Mn_{Ti}S_O$ is only stable in -1 charge state at O-rich condition near the CBm, which can also be seen from Figure 3.7a. As these transition metals have partially filled d-orbitals, these could accept electrons from the host as well as donate electrons to the host. The Sr site is more favorable than the Ti site for substitution in $SrTiO_3$ (see Figure 3.8a-c and 3.3d). The Ti site could be substituted in O-rich (Ti-poor) condition near the CBm (in n-type host). Mostly, $Rh_{Sr}S_O$, $Rh_{Sr}N_O$, $Mn_{Sr}S_O$, and $Mn_{Sr}N_O$ codopants act as donor as they are stable in $+2$ and $+1$ charge states for a wide range of μ_e or in neutral charge state. However, when metal is substituted at the Ti position, the defect configuration will act as an acceptor. Furthermore, $Rh_{Ti}N_O$, and $Mn_{Ti}N_O$ codoped $SrTiO_3$ will get stabilized after accepting an extra electron in comparison to $Rh_{Ti}S_O$, and $Mn_{Ti}S_O$ since N has one electron less than O, and thus, N could accept an extra electron in comparison to S (S and O have the same valence electron configuration).

3.3.2 Electronic structure analysis

To get more insights about the effect of dopants in $SrTiO_3$, we have calculated atom-projected partial density of states (pDOS). The pDOS plots for pristine and monodoped (N/Mn) $SrTiO_3$ are shown in Figure 3.9a-d. In pristine $SrTiO_3$, the O 2p orbitals contribute to the VBM, and Ti 3d orbitals contribute to the CBm with a wide band gap of 3.28 eV. The pDOS of pristine $SrTiO_3$ is symmetric w.r.t. spin alignments (i.e. spin up or down), whereas in the case of N_O, the pDOS is asymmetrical due to a devoid of an electron in comparison to pristine $SrTiO_3$ (see Figure 3.9a and 3.9b). In the latter case, some occupied states are appeared above the pristine VBM and some unoccupied discrete states can also be seen deep inside the forbidden region (since the N 2p orbitals have higher energy than the O 2p orbitals) (see Figure 3.9b). This leads to a reduction in the band gap. However, these midgap states increase the recombination rate and decrease the charge mobility which lead to degradation in the photocatalytic activity.

We have considered two sites for the substitution of Mn, viz., Sr and Ti sites. In the case of monodoping of Mn at Sr site, the band gap (3.25 eV) is not getting reduced and thus cannot induce visible light absorption (see Figure 3.9c). The occupied and unoccupied states of Mn orbitals appeared deep inside the valence and conduction band, respectively, indicating that Mn_{Sr} is very stable. However, in the case of Ti site substitution, we get interesting features in the pDOS (see Figure 3.9d). The localized states bring down the CBm. Hence, the band gap is reduced to 2.57 eV, resulting in the visible light absorption. However, due to a shift of the CBm in downward direction, its reduction power is degraded. Therefore, it cannot be a potential candidate for H_2 production from water splitting.

In the case of codoping (N–Mn), the substitution of Mn at both sites, Sr and Ti in addition to N_O, helps to passivate the localized mid gap states (introduced by N substitution) and form continuum states as shown in Figure 3.9e and 3.9f. The passivation of states is concomitant with the hybridization of O and N orbitals, and Mn and O orbitals in the $Mn_{Sr}N_O$ defect configuration as shown in Figure 3.9e (near the VBM). However, in the case of $Mn_{Ti}N_O$, Mn states arise only near the CBm as shown in Figure 3.9f. The recombination of photogenerated charge carriers

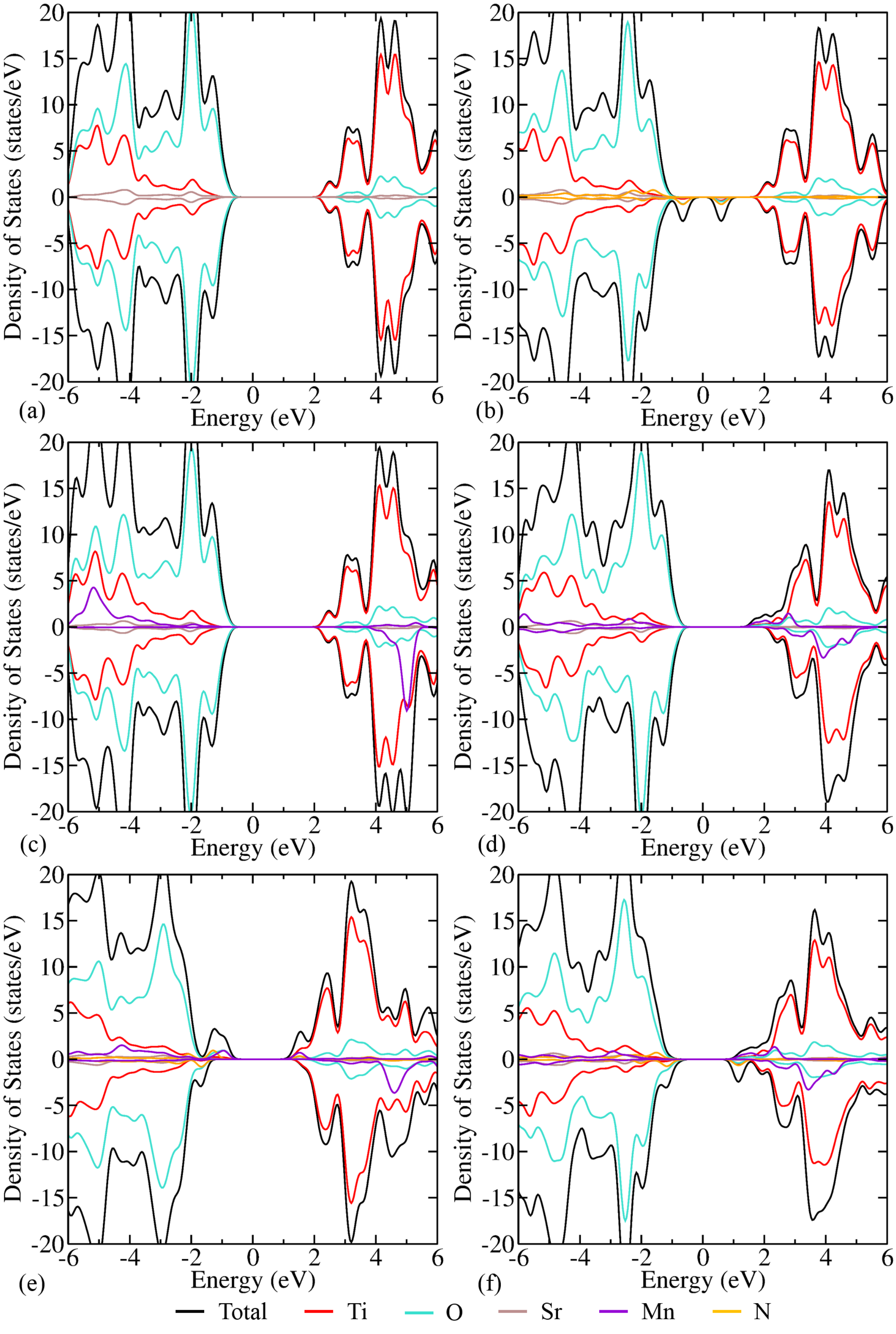

Figure 3.9: Electronic density of states for the supercell of (a) pristine $SrTiO_3$, (b) N_O, (c) Mn_{Sr}, (d) Mn_{Ti}, (e) $Mn_{Sr}N_O$, and (f) $Mn_{Ti}N_O$ defect configurations.

is suppressed, and the diffusion and mobility are increased owing to the passivation of discrete localized states. The band gaps of $Mn_{Sr}N_O$ and $Mn_{Ti}N_O$ are 2.34 and 1.94 eV, respectively, which are the desirable ones for visible light absorption. In the case of $Mn_{Ti}N_O$, CBm is shifted downward by a large amount and hence adversely affects the reduction power for hydrogen generation. However, in the case of $Mn_{Sr}N_O$, this downward shift is very small. Consequently, the codoping of Mn at the Sr site and N at the O site is favorable for overall photocatalytic water splitting. Also, from Figure 3.3c, we can see a relatively large distortion in case of $Mn_{Sr}N_O$ codoping, which builds up the internal field, that is helpful for photogenerated charge carrier separation and thus enhances the photocatalytic efficiency. Therefore, $Mn_{Sr}N_O$ codoping in $SrTiO_3$ is a promising candidate to enhance the photocatalytic efficiency and generate hydrogen from water splitting.

In the case of S_O, the band gap is reduced having the value of 2.59 eV and hence responses to the visible light irradiation (see Figure 3.10a). For Rh_{Ti}, the unoccupied states of Rh orbitals appear at the VBM, and the difference between the highest occupied and lowest unoccupied state is 0.23 eV (see Figure 3.10b). Thus, it is not a promising candidate for enhanced photocatalytic activity. A lowering of the CBm in the case of Rh_{Sr} is occured due to the presence of Rh localized states contribution at the CBm and therefore, it doesn't have enough reduction power to produce hydrogen via water splitting (see Figure 3.10c). In $Rh_{Ti}S_O$ and $Rh_{Sr}S_O$ codoped $SrTiO_3$, the deep trap states arise in the forbidden region, which increase the non-radiative recombination of photogenerated charge carriers and thus degrade the photocatalytic activity (see Figure 3.10d and 3.10e). Since there is a occurrence of trap states in $Rh_{Ti}N_O$ and $Mn_{Sr}S_O$ codoped $SrTiO_3$, it will result in poor photocatalytic activity (see Figure 3.10f and 3.10g). The Rh and N orbitals elevate the VBm of $Rh_{Sr}N_O$ codoped $SrTiO_3$, which results in a band gap of 2.69 eV (see Figure 3.10h). The band gap is reduced to 1.95 eV in the case of $Mn_{Ti}S_O$. The VBM elevation is concomitant with a occurrence of S orbitals at the VBM and Mn orbitals at the CBm (see Figure 3.10i). The shifts in the CBm and VBM are such that the band edges straddle the redox potential levels of water and the defect states are shallow, which serve the purpose of efficient photocatalyst.

3.3.3 Optical properties

The optical spectra have been determined by calculating the frequency dependent complex dielectric function $\varepsilon(\omega)$ = Re (ε) + Im (ε) using HSE06 ϵ_{xc} functional. The real [Re (ε)] and

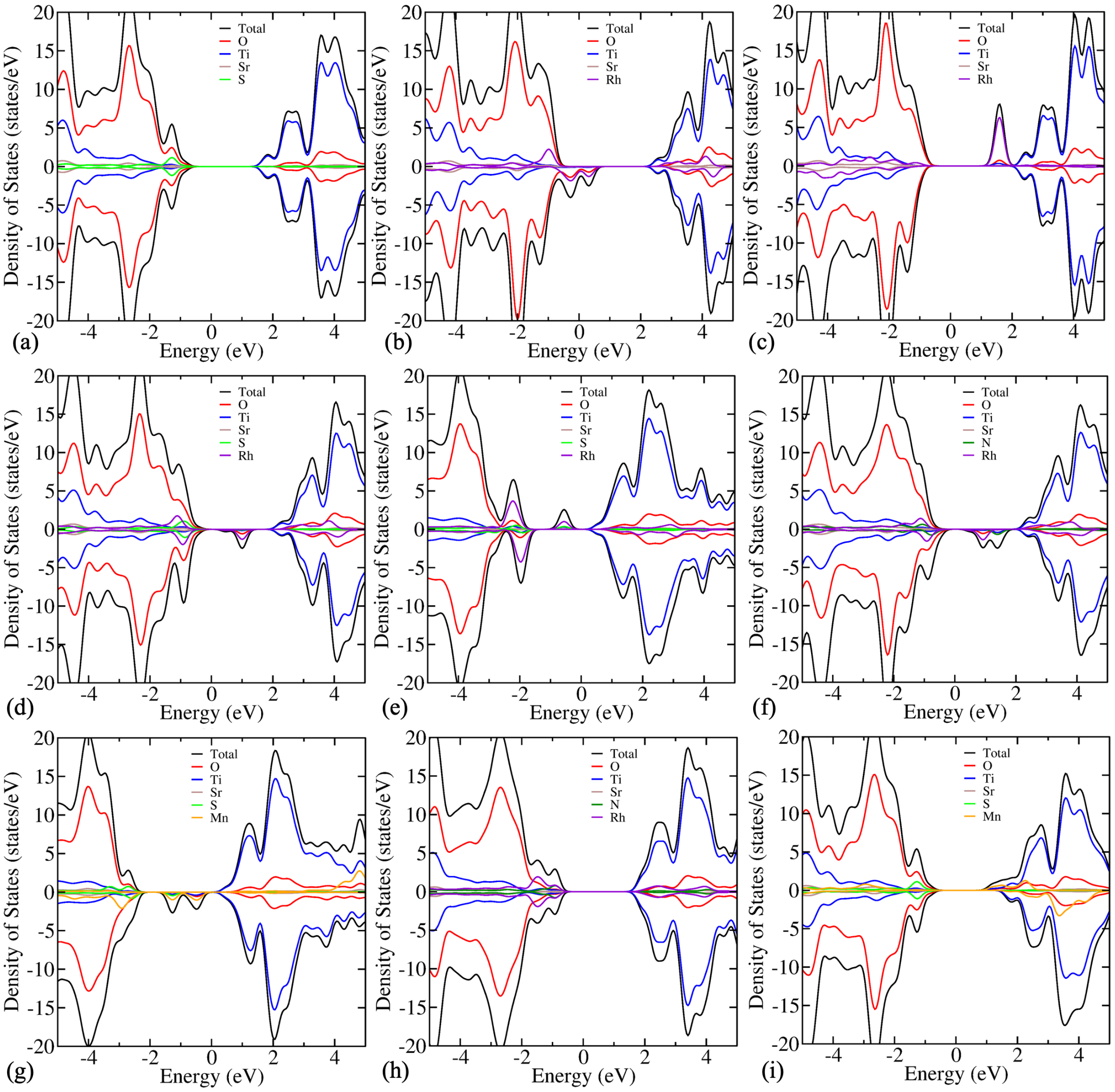

Figure 3.10: Atom-projected partial density of states of (a) S_O, (b) Rh_{Ti}, (c) Rh_{Sr}, (d) $Rh_{Ti}S_O$, (e) $Rh_{Sr}S_O$, (f) $Rh_{Ti}N_O$, (g) $Mn_{Sr}S_O$, (h) $Rh_{Sr}N_O$, and (i) $Mn_{Ti}S_O$ codoped $SrTiO_3$.

imaginary [Im (ε)] parts are associated with the electronic polarizability and optical absorption of the material, respectively. The sum of all possible transitions from the occupied to the unoccupied states gives the direct interband transition, which is reflected in the imaginary part of the dielectric function. For codoped $SrTiO_3$, the spatially average imaginary and real parts of the dielectric function are shown in Figure 3.11(a) and 3.11(b), respectively (the corresponding results for monodoped $SrTiO_3$ are shown in Figure 3.11(c) and 3.11(d)). The static real part of the dielectric function for pristine $SrTiO_3$ is estimated as 4.7 (experimental value is 5.27 [149]) and its value is increased with codopants [see Figure 3.11(b)]. The first absorption peak is observed at 4.08 eV for pristine $SrTiO_3$ as shown in Figure 3.11(a) (experimental value is

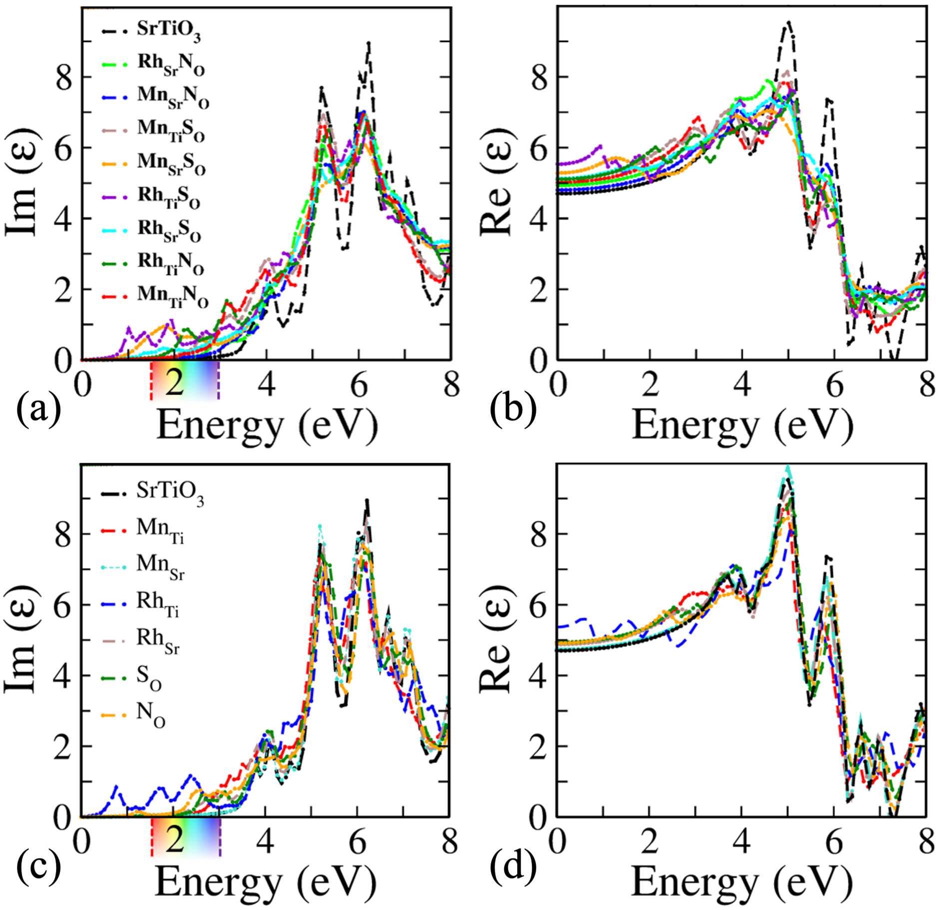

Figure 3.11: Spatially average (a) imaginary [Im (ε)] and (b) real [Re (ε)] part of the dielectric function for codoped $SrTiO_3$ obtained using HSE06 ϵ_{xc} functional. Spatially average (c) imaginary [Im (ε)] and (d) real [Re (ε)] part of the dielectric function for monodoped $SrTiO_3$.

4.7 eV [149]). The peaks are shifted to visible region for the monodoped and codoped cases (except for Mn_{Sr}, which does not reduce the band gap). Note that the optical properties in the high energy range are controlled by the electronic transitions between O 2p states and Ti 3d states. Therefore, the spectra of all the configurations are nearly identical in high energy range. However, the optical properties in low energy range (less than 3 eV) are different; these are affected by the transitions involving the impurity states. The observed visible light absorption could be ascribed to the presence of the dopant states (as shown in pDOS near Fermi-level), which reduce the electron transition gap for optical absorption. This leads to a new absorption edge in the visible light region.

We have also calculated the dielectric function of (N,Mn) doped cases using G_0W_0@HSE06 for comparison, as shown in Figure 3.12. The static ($\omega = 0$) real part of $\varepsilon(\omega)$ for pristine $SrTiO_3$ is found to be 3.46, which is underestimated in comparison to the value obtained using HSE06

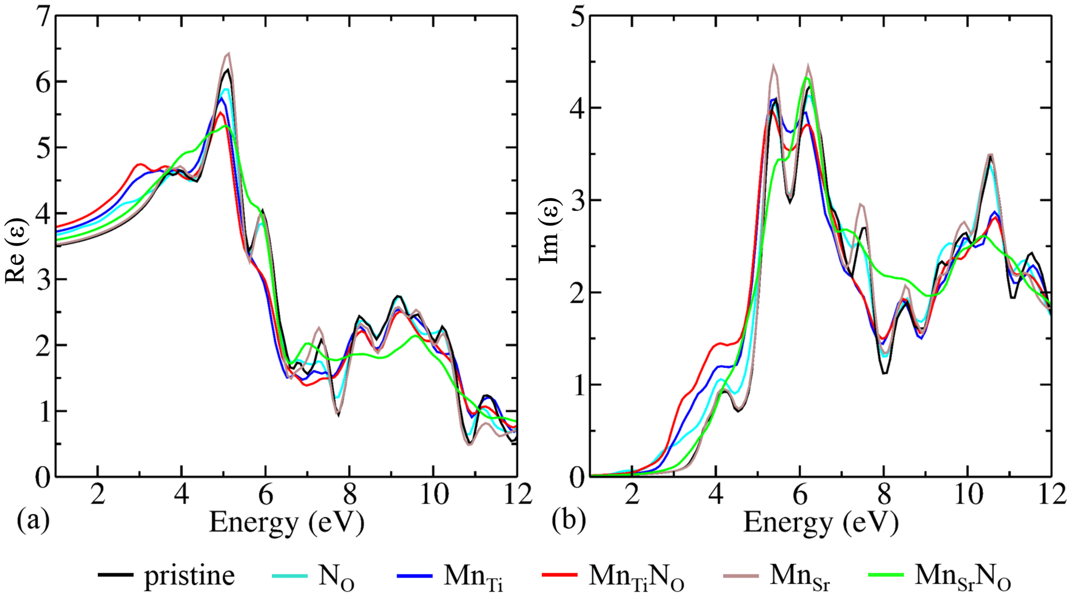

Figure 3.12: Spatially average (a) real (ε_1) and (b) imaginary (ε_2) part of the dielectric function obtained by G_0W_0@HSE06 for the pristine, (N/Mn) monodoped and (N–Mn) codoped $SrTiO_3$.

ϵ_{xc} functional. On doping, its value is increased (see Figure 3.12a). We have found the first optical peak at 4.2 eV for pristine $SrTiO_3$ (see Figure 3.12b), which is larger in comparison to the HSE06 value). Therefore, the optical properties obtained from HSE06 ϵ_{xc} functional are in good agreement with the experimental values.

3.3.4 Band-edge alignment

Note that only a reduction in band gap can not ensure the hydrogen generation via photocatalytic water splitting. The band edges (VBM and CBm) should have appropriate position. For water splitting, the CBm must lie above the water reduction potential level (H^+/H_2), and the VBM must be positioned below the water oxidation potential level (O_2/H_2O). The methodology we have adopted to align the band edges could be found in Ref. [126, 150]. First, we have aligned the band edges of pristine $SrTiO_3$ w.r.t. water redox potential levels. The CBm lies 0.8 eV above the water reduction potential (H^+/H_2) and the VBM lies 1.25 eV below water oxidation potential [151]. Thereafter, we align the band edges of doped $SrTiO_3$ by observing the shift in energy of the VBM and CBm w.r.t. undoped $SrTiO_3$. From Figure 3.13, we have found that in the case of N_O, the VBM is shifted upwards, and the CBm is not disturbed. However, some deep localized states are present in the forbidden region, which degrade the photocatalytic efficiency. These deep states increase the non-radiative recombination and decrease the mobility of

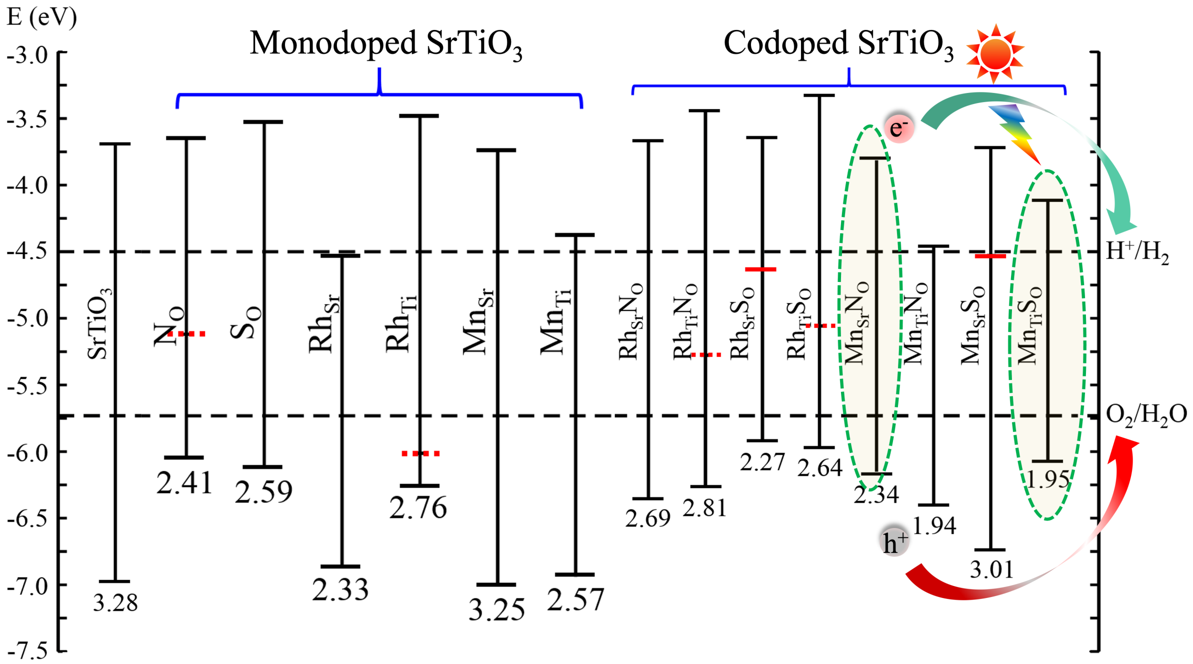

Figure 3.13: Band-edge alignment of pristine, monodoped, and codoped $SrTiO_3$ w.r.t. water redox potential levels (H^+/H_2, O_2/H_2O). The solid and dashed red lines in forbidden region represent the highest occupied and lowest unoccupied defect states, respectively. The highlighted ellipses indicate the most potent candidates for photocatalytic water splitting.

photogenerated charge carriers. Hence, N_O is not the promising one for water splitting. Likewise, for Rh dopant (in monodoping as well as in codoping), there is occurrence of trap states. These states degrade the photocatalytic efficiency. Therefore, monodoping and codopoing of Rh with a nonmetal could reduce the band gap, but cannot result in an efficient photocatalyst. The monodoped S_O could enhance the photocatalytic efficiency and split water as their band edges straddle the redox potential of water (see Figure 3.13). However, the band gap (2.59) is slightly higher than the desirable band gap (∼ 2 eV [128, 129]), and thus, its efficiency will be smaller. Similarly, in the case of Mn_{Ti}, the band gap is 2.57 eV, and due to shift of its CBm toward the Fermi level, its reduction power will be degraded. On the other hand, for Mn_{Sr}, the band gap is not reduced and thus, it cannot induce the visible light response.

The Rh doping does not aid in enhancing the photocatalytic activity ascribed to the formation of recombination centers except for $Rh_{Sr}N_O$. In $Rh_{Sr}N_O$, defect configuration enhances the photocatalytic efficiency, however its band gap (2.69 eV) is little bit larger in comparison to the maximum efficient photocatalyst (∼ 2 eV). In $Mn_{Sr}S_O$, since the occupied deep states lie below the CBm, this configuration is not a desirable photocatalyst. The reduction in band gap for $\mathrm{Mn_{Ti}N_O}$ is concomitant with the lowering of CBm, which deteriorates its reduction power. The $\mathrm{Mn_{Sr}N_O}$, and $\mathrm{Mn_{Ti}S_O}$ codoped $\mathrm{SrTiO_3}$ configurations are the potential candidates for overall photocatalytic water splitting (i.e., for hydrogen evolution reaction (HER) as well as oxygen evolution reaction (OER)) attributable to their desirable band gap ($\sim$ 2 eV) with congenial band-edge positions (see Figure 3.13).

3.3.5 Band structure and effective mass of pristine, $\mathrm{Mn_{Sr}N_O}$, and $\mathrm{Mn_{Ti}S_O}$ codoped $\mathrm{SrTiO_3}$

We have also determined the effective mass of charge carriers for the pristine, $\mathrm{Mn_{Sr}N_O}$, and $\mathrm{Mn_{Ti}S_O}$ codoped $\mathrm{SrTiO_3}$ using the HSE06 ϵ_{xc} functional (see Table 3.3) to see the effect on mobility. The effective mass (m^*) is obtained from the curvature of band edges by calculating the inverse of the second derivative of band energy w.r.t. k (wave vector) at the band edges as follows

$$\frac{1}{m^*} = \frac{1}{\hbar^2}\frac{d^2E}{dk^2}, \tag{3.7}$$

where $\hbar$ is the reduced Planck constant. The effective masses for the pristine system (except for heavy-hole) are validated by previous studies [150, 152, 153].

Note that we have used a supercell so that the periodic images of the defects do not interact and the defects get localized in the system. However, as the size of the supercell increases, the bands in the first (primitive) Brillouin zone of primitive/conventional cell get folded, and the supercell Brillouin zone shrinks. Consequently, the energy levels in the band structure become very dense, and thus, for a large supercell, we do not get much information from a band structure. Therefore, unfolding of the band structure is used in general to get a real picture of the band structure (for details, see Ref. [154, 155]). Despite the use of a supercell

Table 3.3: Effective masses (in terms of free-electron mass m_{e}) at the band edge for pristine, $\mathrm{Mn_{Sr}N_O}$, and $\mathrm{Mn_{Ti}S_O}$ codoped $\mathrm{SrTiO_3}$. The masses $m_{\mathrm{he}}, m_{\mathrm{le}}, m_{\mathrm{hh}},$ and m_{lh} correspond to heavy-electron, light-electron, heavy-hole, and light-hole bands, respectively.

Configuration	m_{he}	m_{le}	m_{hh}	m_{lh}
pristine	5.18	0.38	−10.36	−0.74
$\mathrm{Mn_{Sr}N_O}$	3.04	–	–	−1.53
$\mathrm{Mn_{Ti}S_O}$	–	0.25	–	−0.66

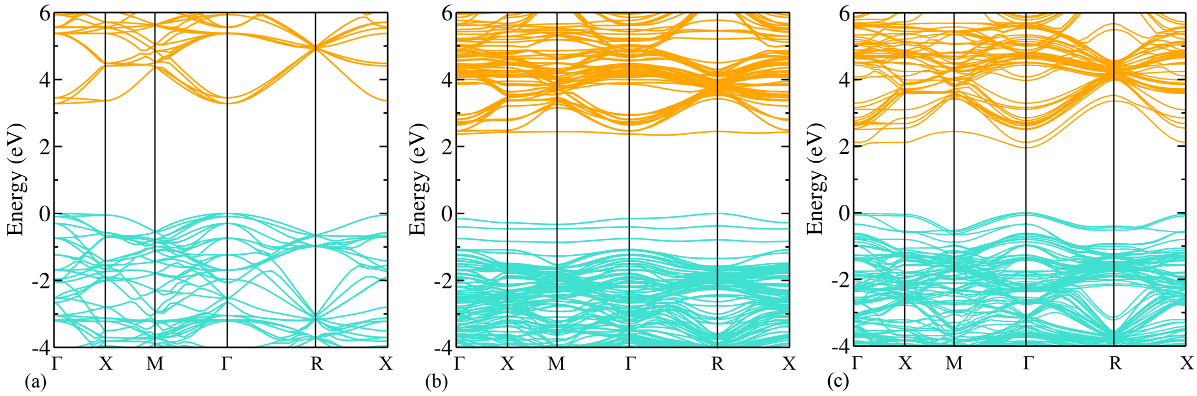

Figure 3.14: Band structure calculated using the HSE06 ϵ_{xc} functional of (a) pristine $SrTiO_3$, (b) $Mn_{Sr}N_O$, and (c) $Mn_{Ti}S_O$ codoped $SrTiO_3$.

(which is not too big in our case), we can see from Figure 3.14 that the density of the bands near the VBM and CBm is not very high. Also, there is no overlap of bands at the VBM and CBm in codoped $SrTiO_3$. Therefore, band folding does not create much of a problem for these cases, and in principle, we can get the correct result for the effective masses.

From Figure 3.14a, we can see that the pristine has 3-fold degeneracy at the CBm (at the Γ k-point). This degeneracy is lifted as one moves away from the Γ k-point in the direction of X, M, or, R k-point. The effective mass of electron/hole due to a heavy-, light-electron/hole and spin split-off band is obtained along the Γ-X high symmetry path for pristine $SrTiO_3$. The effective mass of the electron/hole corresponding to spin split-off band is found to be same as that for the light-electron/hole band. After the validation for the pristine system, we have calculated the effective mass for codoped systems. In contrast to pristine $SrTiO_3$, codoped systems have non-degenerate bands (highest occupied and lowest unoccupied) [see Figure 3.14]. Note that here, we have shown the total bands containing both the spin up and spin down contribution. The CBm for $Mn_{Sr}N_O$ lies at the [0.2 0.2 0.2] k-point and the VBM lies at the R k-point (see Figure 3.14b). The effective mass of the electron is $3.04m_\mathrm{e}$ and $5.09m_\mathrm{e}$ along the CBm-X and CBm-Γ directions, respectively. Moreover, the effective mass of the hole is $-1.53m_\mathrm{e}$ and $-2.58m_\mathrm{e}$ along the R-X and R-Γ directions, respectively. These different values along different directions indicate the anisotropic nature of the effective mass. For $Mn_{Ti}S_O$ codoped $SrTiO_3$, the effective mass of both the charge carriers (calculated along the Γ-X direction) is decreased. It is also clear from the large curvature of the bands around the CBm and VBM in comparison to pristine $SrTiO_3$ [see Figure 3.14c]. For larger effective mass, the mobility will be smaller and the recombination rate will also be greater. Therefore, from Table 3.2, we can see that in the case of $\text{Mn}_{\text{Ti}}\text{S}_{\text{O}}$ codoped SrTiO_3, the mobility of charge carriers will be large, and for $\text{Mn}_{\text{Sr}}\text{N}_{\text{O}}$ codoped SrTiO_3, the effective mass values are comparable with pristine SrTiO_3, and thus the mobility will not be affected much. This is because the mobility depends on both the effective mass and scattering (relaxation) time. The carrier mobility (μ) is defined as follows

$$\mu = \frac{q\tau}{m^*} \tag{3.8}$$

where q is the elementary charge, and τ is the relaxation time (average scattering time). On doping, the scattering rate is expected to get decreased as the degeneracy will be lifted. As a consequence of this, despite a small increment in effective mass, the mobility will not be affected considerably, especially here due to low doping concentration [156]. These effective mass studies should assist future experimental as well as theoretical investigations to tailor the transport properties of the systems.

3.4 Conclusions

In summary, we have systematically studied the thermodynamic stability of different types of dopants and codopants in SrTiO_3 using hybrid DFT and *ab initio* atomistic thermodynamics. Our results indicate that the most stable codopants (codoping of metal at the Sr site and non-metal at the O site) mostly act as donors. We have found that the codoping expands the spectral response and induces visible light absorption. However, the recombination centers are occurred in Rh-related defect configurations attributable to Rh localized orbitals in the forbidden region, and moreover, there is a large shift in the CBm or VBM. This will lead to degradation in photocatalytic efficiency. The mobility of the charge carriers is maximum in the $\text{Mn}_{\text{Ti}}\text{S}_{\text{O}}$, and in $\text{Mn}_{\text{Sr}}\text{N}_{\text{O}}$, it is not affected much. Our results reveal that $\text{Mn}_{\text{Ti}}\text{S}_{\text{O}}$ and $\text{Mn}_{\text{Sr}}\text{N}_{\text{O}}$ codoped SrTiO_3 are the most favorable candidates for enhancing photocatalytic overall water splitting owing to the passivation of the trap states and congenial band-edge positions with desirable visible light absorption.

CHAPTER 4

Unraveling the role of oxygen vacancy in $CaTiO_3$ for photocatalytic applications

4.1 Introduction

The utilization of natural sunlight is one of the most promising strategies for controlling our carbon-based energy consumption and emissions [157]. Hydrogen (H_2) has been recognized as a green energy source as it is an emission-free fuel with a high energy capacity of 143 MJ kg^{-1} [158]. Currently, H_2 is the feedstock of several industrial reactions and is mainly prepared by the steam reforming process, which liberates a huge amount of CO_2 in the atmosphere contributing significantly to the greenhouse effect [159]. N_2 gas is abundant in the Earth's atmosphere [160] and ammonia (NH_3) is an important nitrogenous compound, which is recognized as a potential hydrogen carrier due to its high hydrogen content and is the backbone of the fertilizer industry. NH_3 is generally produced by the well-known Haber–Bosch process in which H_2 and N_2 react under high temperature and pressure conditions (400–500 °C and 15–30 MPa), which consumes about 1–2% of the global annual energy [161]. To curb the increasing dependence on non-renewable energy sources, it is a global demand to come up with sustainable green energy solutions. In this regard, semiconductor photocatalysis has emerged as a fascinating and feasible approach, by which H_2 and NH_3 can be generated from abundant water and N_2 gas in the presence of natural sunlight and suitable photocatalytic materials. However, both of these processes are not realized on a large scale yet due to the low efficiency of photocatalytic materials reported so far [162].

Researchers have devoted substantial efforts after the dawn of the photocatalysis era [163] in 1972 and employed several strategies like band gap engineering, suppression of photogenerated charge recombination, defect engineering, etc. to address the main bottlenecks (low light absorption and charge recombination) of photocatalytic processes [164, 165, 166, 167, 168]. Among these, defect engineering is an attractive strategy wherein the catalytically active sites can be planted on the surface of materials, which can boost the rate of the reactions and improve the light absorption and photogenerated charge transfer properties [169, 170]. For example, oxygen vacancies have been engineered on TiO_2 [171, 172], ZnO [173], BiOX (X = Cl, Br) [174, 175], $SrTiO_3$ [176], $CaTiO_3$ [177], etc., and found to be beneficial for different photocatalytic reactions by improving the light absorption and separation of photogenerated charge carriers. It has been reported that the oxygen vacancies can undergo self-healing and helps in the adsorption and dissociation of water molecules during photocatalysis [171, 177]. Oxygen vacancies can also activate the N_2 molecules (bond dissociation energy = 945.33 kJ mol^{-1}) by chemically adsorbing them on the engineered catalyst surface and facilitate NH_3 formation by their photocatalytic reduction [178, 179]. Therefore, engineering a semiconductor catalyst with controlled oxygen vacancy concentration is of great importance and interest in photocatalysis applications.

In this context, alkaline-earth titanates ($ATiO_3$) are good candidates for exploring the effects of oxygen vacancies on photocatalytic H_2 evolution and N_2 fixation reactions owing to their highly negative conduction band potential, wide band gap and excellent thermal and chemical stability [180, 181]. It has been reported that an optimal amount of oxygen vacancies can enhance the photocatalytic H_2 evolution performance of $CaTiO_3$ and $SrTiO_3$ materials [176, 177, 108, 182]. For example, Cai *et al.* have utilized H_2 annealing treatment to engineer oxygen vacancies on $CaTiO_3$ nanosheets, which showed enhanced photocatalytic H_2 evolution in comparison to the pristine $CaTiO_3$ nanosheets [177]. In another study, Tan *et al.* have reported the synthesis of oxygen vacancy engineered $SrTiO_3$ by using $NaBH_4$ as a reducing agent in an Ar atmosphere and utilized the obtained catalysts for photocatalytic H_2 evolution [108]. In our work, we have revealed the actual oxygen vacancy sites (either in the CaO plane or in the TiO_2 plane of $CaTiO_3$), which contribute toward the enhanced photocatalytic performance for H_2 evolution. In addition, the photocatalytic N_2 fixation ability of pristine and defective $CaTiO_3$ has been examined for the first time in this work to the best of our knowledge.

In this chapter, we have performed a systematic density functional theory (DFT) [54, 55] study using hybrid exchange-correlation (ϵ_{xc}) functional HSE06 [61] to understand the role of oxygen vacancy in $CaTiO_3$ for H_2 evolution and N_2 fixation reactions. First, we have determined the atom-projected partial density of states (pDOS) to know the nature of defect states in a single O-vacant defective $CaTiO_3$. Thereafter, we have aligned the band edges to know whether the CBm and VBM straddle the reduction and oxidation potentials of water for photocatalytic water splitting. Finally, we have determined the Gibbs free energy of formation for hydrogenation of N_2 to comment upon the preferred site for the oxygen vacancy. We anticipate that this work could provide critical insights and directions to experimetalists for the synthesis of upcoming efficient catalytic materials for different applications.

4.2 Computational methods

The spin polarized DFT calculations were performed by Vienna *ab initio* simulation package (VASP) [140, 141]. The electron-ion interactions were considered by using projector-augmented wave (PAW) pseudopotentials [142] for each species (viz., Ca, Ti, O, N and H). All the structures were optimized (only atomic positions, not the lattice parameters) using PBE [59] ϵ_{xc} functional. The geometries were optimized until the Hellmann-Feynman forces acting on atoms are smaller than 0.001 eV/Å. The self-consistency loop was converged with an energy threshold of 0.01 meV. The single-point energy calculations were carried out using HSE06 ϵ_{xc} functional with exact Fock exchange parameter of 18% (Note that the default 25% exact Fock exchange parameter overestimated the band gap. It yields a band gap of 3.95 eV). Note that it is already well known that in oxides the HSE06 ϵ_{xc} functional is absolutely indispensable, whereas usual local/semi-local functionals yield wrong results. The $2 \times 2 \times 1$ supercell (80-atom) was used to carry out the calculations, so that the defects get fully localized into the system. A k-mesh of $4 \times 4 \times 6$ generated using Monkhorst-Pack [75] scheme was used for Brillouin zone sampling while optimization. A k-mesh of $2 \times 2 \times 3$ was used for single-point energy calculations. An energy cutoff of 500 eV was used for plane-wave basis set expansion.

Further, for N_2 fixation, the $CaTiO_3$ (001) surfaces with CaO- and TiO_2-termination were modeled as (2×2) supercell with a periodic 4-layer wherein the lower two layers were fixed and the upper two layers were relaxed. A vacuum thickness of 15 Å was used in order to eliminate the interaction between the periodic slabs. A k-mesh of $2 \times 2 \times 1$ was used for single-point energy calculations of the surfaces. The Gibbs free energy of formation (ΔG) for H adsorption is calculated as follows

$$\Delta G = E_{\text{surf+H}} - E_{\text{surf}} - \frac{1}{2}E_{\text{H}_2} + \Delta E_{\text{ZPE}} - T\Delta S \tag{4.1}$$

where $E_{\text{surf+H}}$, and E_{surf} are the total energies of surface with and without H adsorbates, respectively. E_{H_2} is the total energy of H_2 molecule. ΔE_{ZPE} is the difference in zero point energy between the adsorbed and the gas phase, T is the temperature and ΔS is the change in entropy. The vibrational energies of the species determine the ΔE_{ZPE} and ΔS (see Ref. [183]). For creating a single O-vacancy at CaO- and TiO_2-terminated surfaces, we have scanned different positions and found out the minimum energy configuration. Subsequently, the N_2 has been adsorbed at the defected site. Further, the hydrogenation is taken into account for N_2 fixation.

4.3 Results and discussion

4.3.1 Electronic structure of (un)defective $CaTiO_3$

The DFT calculations have been performed to understand the role of defect states in the photocatalytic H_2 evolution performance of $CaTiO_3$. The pDOS of pristine and defective (with single O-vacancy) $CaTiO_3$ have been plotted to get insights into the O-vacancy defect. In the pristine $CaTiO_3$, the O 2p orbitals contribute to the VBM and Ti 3d orbitals contribute to the CBm as shown in Figure 4.1a and have a wide band gap of 3.51 eV. The states are symmetric with respect to the spin alignments (i.e., spin up or down) due to the absence of any unpaired electron. The Fermi level (fixed at 0 eV) is near the VBM, which implies that the pristine $CaTiO_3$ is of p-type nature intrinsically. The O1 site is in the CaO plane and the O2 site is in the TiO_2 plane of $CaTiO_3$. The pDOS of single O-vacancy at the O1 site is shown in Figure 4.1b. The localized states are formed near the CBm and the Fermi level gets shifted to the CBm. It becomes n-type upon creation of the O-vacancy. These states become asymmetric due to the unpaired electrons in the system. These states act as donor states and the system will become stable after releasing two electrons. Therefore, due to the O-vacancy, these extra electrons in the system help in the reduction of water to produce hydrogen. However, these localized states will also act as recombination centers, which is detrimental to the photocatalytic efficiency. In contrast, the vacancy at the O2 site leads to delocalized states at the CBm, which is shown in Figure 4.1c. Herein, for single O-vacancy, two inequivalent sites are considered (marked as O_1 and O_2) as shown in Figure 4.1d. Hence, the O-vacancy in the TiO_2 plane of $CaTiO_3$ ameliorates the efficiency of hydrogen production.

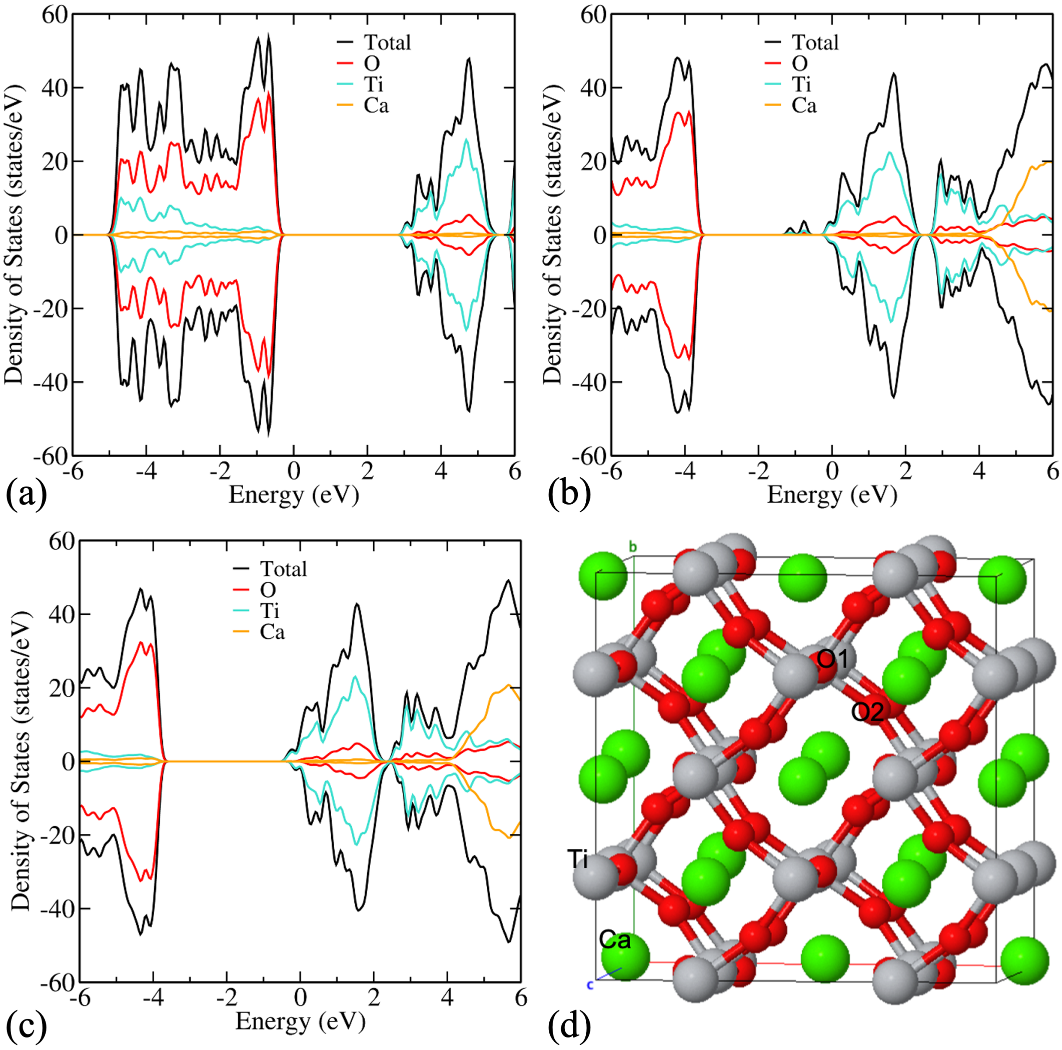

Figure 4.1: Atom-projected partial density of states (pDOS) of (a) pristine, (b) defective $CaTiO_3$ (O-vacancy at the O1 site, i.e., in the CaO plane), (c) defective $CaTiO_3$ (O-vacancy at the O2 site, i.e., in the TiO_2 plane), (d) crystal structure of orthorhombic (space group $Pbnm$) $CaTiO_3$.

4.3.2 H_2 evolution in (un)defective $CaTiO_3$ from photocatalytic water splitting

To verify whether the $CaTiO_3$ with oxygen vacancies can reduce water to produce hydrogen, the band-edge alignment of the pristine and the defective $CaTiO_3$ has been performed (see Figure 4.2a). To reduce water, the CBm must lie above the water reduction potential. In addition, for overall water splitting, the VBM must also be positioned below the water oxidation potential to oxidize the water and produce oxygen. To align the band edges of defective $CaTiO_3$, first, the

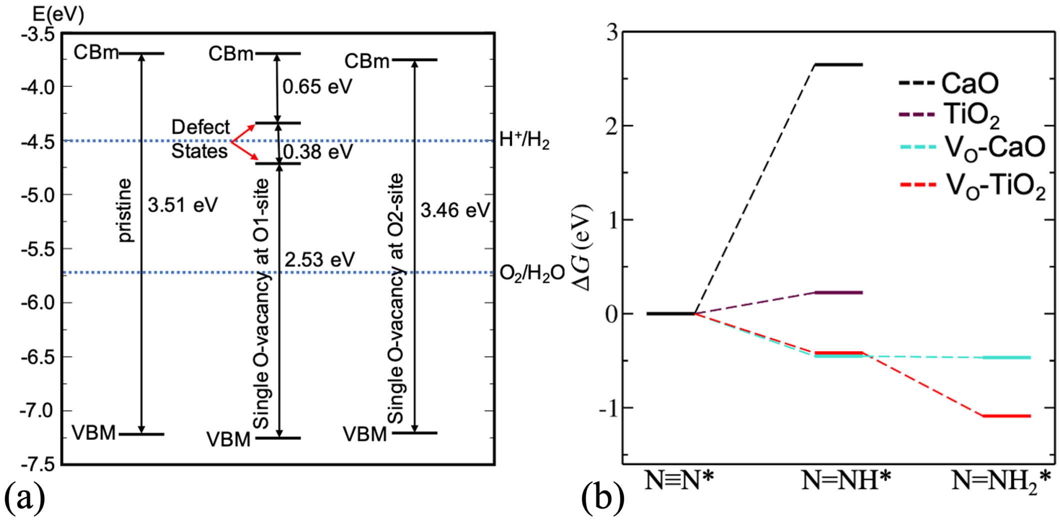

Figure 4.2: (a) Band-edge alignment of pristine and defective $CaTiO_3$ (bulk) and (b) the Gibbs free energy of formation (ΔG) for N_2 fixation over the (001) surface of pristine and defective $CaTiO_3$ (here, V_O represents single O-vacancy at the surface). Here, the second step of hydrogenation to form $N_2H_2^*$ is not considered over the pristine surface, as the first step of hydrogenation to form N_2H^* is endothermic.

band edges of pristine $CaTiO_3$ are aligned with respect to water redox potentials. The CBm of $CaTiO_3$ lies 0.8 eV above the water reduction potential (H^+/H_2) [184]. The VBM is positioned 1.48 eV below the water oxidation potential (O_2/H_2O), as the band gap of pristine $CaTiO_3$ is 3.51 eV. Furthermore, the band edges of defective $CaTiO_3$ (having a single O-vacancy at the O1 and O2 sites) are aligned by observing the shifts of the VBM and CBm with respect to pristine $CaTiO_3$. The shifts in the VBM and CBm are small in both the cases. However, the localized deep donor defect states appear in the case of an O-vacancy at the O1 site (i.e., in the CaO plane). Therefore, the aforementioned configuration is not suitable for enhancing the efficiency of water splitting, as these states increase the non-radiative recombination rate. Moreover, these defect states hinder the water reduction to H_2. In the case of a vacancy at the O2 site, the defect states are shallower, and a continuum of bands is formed at the CBm. Therefore, this configuration will be more suitable for H_2 evolution.

4.3.3 N_2 fixation in (un)defective $CaTiO_3$

To investigate the N_2 fixation with pristine and defective $CaTiO_3$ using DFT, the Gibbs free energy of formation (ΔG) has been determined. The sequential hydrogenation of the adsorbed

N_2 molecules on the catalyst surface is the key process involved in photocatalytic N_2 fixation and the first hydrogenation step to form N_2H^* is the primary step in the whole N_2 fixation process [185]. The $CaTiO_3$ (001) surfaces with CaO- and TiO_2-termination have been modeled to determine the ΔG values (see computational methods). The ΔG values for the first hydrogenation step to form N_2H^* are found to be 2.65 and 0.22 eV on CaO- and TiO_2-terminated surfaces of pristine $CaTiO_3$, respectively (see Figure 4.2b), which are endothermic in nature. On the other hand, a more facile hydrogenation of N_2 is observed on the $CaTiO_3$ surface with O-vacancies as per the obtained ΔG values. The ΔG values for the first step of N_2 fixation over single O-vacant CaO- and TiO_2-terminated surfaces are found to be -0.45 and -0.42 eV, respectively, as shown in Figure 4.2b. For further hydrogenation to form $N_2H_2^*$ at O-vacant CaO- and TiO_2-terminated surfaces, the ΔG values are -0.47 and -1.09 eV, respectively (see Figure 4.2b). It is important to note that the second step of hydrogenation to form $N_2H_2^*$ is not considered over the pristine surface, as the first step of hydrogenation to form N_2H^* is endothermic. Overall, the obtained ΔG values suggest that the defective TiO_2-terminated surface is the most favorable for N_2 fixation. Moreover, the N_2 bond length is increased by 0.1 Å on adsorption at the O-vacant defective site in comparison to the pristine surface, which leads to the weakening of the N_2 bond and activation of N_2 molecule for further photocatalytic reaction. Hence, the O-vacancy defects in $CaTiO_3$ increase the efficiency of photocatalytic N_2 fixation.

4.4 Conclusions

In summary, we have done a systematic study of pristine and defective $CaTiO_3$ for H_2 evolution and N_2 fixation reactions using hybrid DFT. We have found that a single oxygen vacancy in the CaO plane creates the localized states near the CBm, whereas the delocalized states are appeared at the CBm in the case of a single oxygen vacancy in the TiO_2 plane of $CaTiO_3$. Furthermore, an oxygen vacancy in the CaO plane results in deterioration of the reduction power for H_2 evolution. On the other hand, in the case of an oxygen vacancy in the TiO_2 plane, the photocatalytic efficiency for water splitting is ameliorated owing to the shallow defect states and the availability of electrons in the CBm. Moreover, the defective $CaTiO_3$ having a single oxygen vacancy in the TiO_2 plane is the most promising candidate for the N_2 fixation reaction attributed to the smaller energy barriers for hydrogenation steps. Based on the obtained results, it can be inferred that oxygen vacancy engineering in the ABO_3 perovskites could lead to the design and development of efficient photocatalytic materials for both H_2 evolution and N_2 fixation reactions.

CHAPTER 5

Sublattice mixing in $Cs_2AgInCl_6$ for enhanced optical properties from first-principles

5.1 Introduction

Lead halide perovskites $APbX_3$ ($A = CH_3NH_3{}^+$, $HC(NH_2)_2{}^+$, Cs^+, and $X = Cl^-$, Br^-, I^-) have created a huge sensation in the field of optoelectronics, particularly in photovoltaics owing to their suitable optical band gap, long carrier diffusion length, high carrier mobility and low manufacturing cost [27, 186, 187, 188, 189, 190, 191, 192, 193, 194, 195, 196, 197, 198, 199]. Moreover, the band gap is tunable with high defect tolerance [190, 191]. These materials find applications in various optoelectronic devices, namely, solar cells [186, 192, 193], light emitting diodes [194, 195], lasers [196, 197] and photodetectors [198, 199]. In spite of their great potential in vast number of applications, there are two major challenges: (i) instability against exposure to humidity, heat or light and (ii) toxicity of Pb. To tackle these issues, many works have been endeavored to find the alternative stable and environmentally sustainable metal halide perovskites with fascinating optoelectronic properties akin to lead halide perovskites [200, 201, 202, 203, 204, 205, 206, 207, 208].

One of the approaches for removing Pb-toxicity is to replace Pb^{2+} with some other divalent metal. However, this replacement results in either indirect or large band gap materials with degraded optoelectronic properties [204, 205, 206]. Substitutions of group 14 divalent cations, viz., Sn^{2+} and Ge^{2+}, have also been synthesized by researchers, but these are not stable at ambient conditions due to the easy oxidation to tetravalent Sn^{4+} and Ge^{4+}, respectively [207, 208]. Another promising approach is to substitute a monovalent M(I) and a trivalent M(III) metal alternatively in place of two divalent Pb, which forms the double perovskite $A_2M(I)M(III)X_6$. Many high-throughput calculations have been performed on double perovskites for a variety of potential applications [209, 210, 211]. Recently, lead-free metal halide double perovskites have been synthesized, which are stable and environmentally benign, viz., Cs_2AgBiX_6 (X = Cl^-, Br^-, I^-) and $Cs_2AgInCl_6$ [42, 47, 212, 213, 43, 214, 215]. Cs_2AgBiX_6 perovskites possess indirect band gap, which results in weaker absorption and high non-radiative recombination loss [42, 47, 212]. In contrast, $Cs_2AgInCl_6$ has direct band gap and long carrier lifetimes. However, its wide band gap (3.3 eV) does not show an optical response in the visible region [43, 214]. Alloying with suitable elements could be the best solution to reduce its band gap and expand the spectral response in the visible light region. In recent studies, $Cs_2AgInCl_6$ has been doped to tune its optical properties [215, 216, 217, 218, 219].

In this chapter, we have done the sublattice mixing by partial substitution of several metals M(I), M(II), M(III) and halogen X at Ag/In and Cl site, respectively, to reduce the band gap of $Cs_2AgInCl_6$, thereby, enhancing its optical properties. The charge neutrality condition has been maintained by forming substitutional defects. We have performed hierarchical calculations using first-principles-based approaches, viz., density functional theory (DFT) with semi-local exchange-correlation (ϵ_{xc}) functional (PBE [59]), hybrid DFT with HSE06 [60, 61] and single-shot GW [63, 139] (G_0W_0) under the many-body perturbation theory (MBPT). First, the structural stability analysis has been done by examining the Goldschmidt tolerance factor and octahedral factor. Since structural stability is not the sufficient condition to confirm the formation of perovskites, the decomposition energy [220] has been calculated, which reflects the thermodynamic stability of the materials. We have taken the difference between total energy of the configurations and their components (binary/ternary, in which they can decompose), which is opposite in convention to what has been considered in Ref. [220] Therefore, the configurations that have negative decomposition energy are stable. Furthermore, to get better insights, we have investigated the reduction in band gap via atom-projected partial density of states (pDOS). Finally, by calculating the frequency dependent complex dielectric function, we have determined the optical properties of the materials that can be applied in the field of optoelectronics.

5.2 Computational methods

The DFT calculations were performed using the Vienna *ab initio* simulation package (VASP) [140]. The ion-electron interactions in all the elemental constituents were described using projector-augmented wave (PAW) potentials [142]. All the structures were optimized using generalized gradient approximation (PBE ϵ_{xc} functional) until the forces were smaller than 0.001 eV/Å. Here, the PBE ϵ_{xc} functional is used because the HSE06 ϵ_{xc} functional is extremely slow for relaxing the structure. In the case of double perovskite $Cs_2AgInCl_6$, the lattice constant is overestimated by 1.56% using PBE ϵ_{xc} functional (and by 1.22% using HSE06 ϵ_{xc} functional) in comparison to experimental value obtained by Volonakis *et al.* [43] Whereas, the PBEsol ϵ_{xc} functional underestimates the lattice constant by 1%. The electronic self-consistency loop convergence was set to 0.01 meV, and the kinetic energy cutoff used was 500 eV for plane wave basis set convergence. A k-mesh of $4 \times 4 \times 4$ was used for Brillouin zone integration, which was generated using Monkhorst-Pack [75] scheme. Advanced hybrid ϵ_{xc} functional HSE06 was used for the better estimation of band gap as well as thermodynamic stability. Furthermore, we checked the role of van der Waals (vdW) forces and configurational entropy, while analyzing the stability of compounds. The latter has lesser effect on the stability. The consideration of vibrational energy contributes to second decimal place of the decomposition energy. It may change the number by very small amount, but neither changes the stability nor the hierarchy of stability of the compounds. On the other hand, the van der Waals forces (two-body Tkatchenko-Scheffler [221]) contribute to first decimal place of the decomposition energy. Most of the compounds' stability has not been affected. However, in very few cases, it has minutely changed the stability of the compounds, that have decomposition energy value close to zero. In the case of determination of the optical properties, single-shot GW (G_0W_0) calculations were performed on top of the orbitals obtained from HSE06 ϵ_{xc} functional [G_0W_0@HSE06]. The polarizability calculations were performed on a grid of 50 frequency points. The number of bands was set to $\sim$ 4 times the number of occupied bands (for band gap convergence see Table 5.1). With increasing number of unoccupied bands, the band gap gets converged. Moreover, the negligible

Table 5.1: Band gap evolution with respect to the number of bands using G_0W_0@PBE of $Cs_2AgInCl_6$

Number of bands	Band gap (eV)
240	3.71
480	2.95
640	2.77
800	2.65

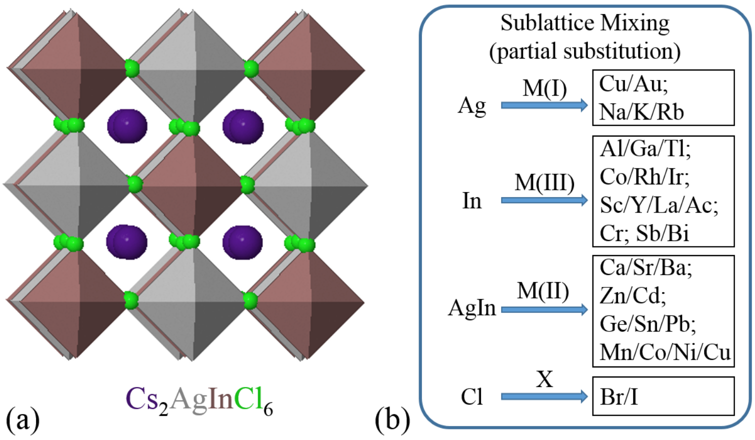

Figure 5.1: (a) Structure of $Cs_2AgInCl_6$, and (b) Partial substitution with metals M(I), M(II), M(III) and with halogen X at Ag/In and Cl sites, respectively.

effect of spin-orbit coupling (SOC) has been discussed.

5.3 Results and discussion

5.3.1 Stability of defected systems

5.3.1.1 Structural stability

The double perovskite $Cs_2AgInCl_6$ has a cubic structure with space group $Fm\bar{3}m$. The corresponding sublattice is composed of alternate octahedra of $InCl_6$ and $AgCl_6$, as shown in Figure 5.1a. On partial substitution of different elements as shown in Figure 5.1b (metals and/or halogens), the distortion is negligible. We have not observed any octahedral tilting, as the structures remain cubic on mixing the ions. The difference of Goldschmidt tolerance factor in comparison to pristine is only 0.03, which do not likely induce the tilting. The only thing that has minutely changed is the bond length B-X/B′-X ($\sim$0.1 Å). This is confirmed by plotting the radial distribution function of the octahedral units of pristine and alloyed system. We have shown here for a test case, viz., $Cs_2Cu_{0.25}Ag_{0.75}InCl_6$, in which the octahedral unit just stretches inwards on substituting 25% Cu at Ag site (see Figure 5.2). Similar is the case with other dopants as well, where the change in the bond length of octahedra is $\sim \pm 0.1$ Å. Hence, the distortion is negligible.

Also, it should be noted that these structures are considerable at room temperatures. This can be understood by the fact that, the synthesis of halide perovskites is often performed near

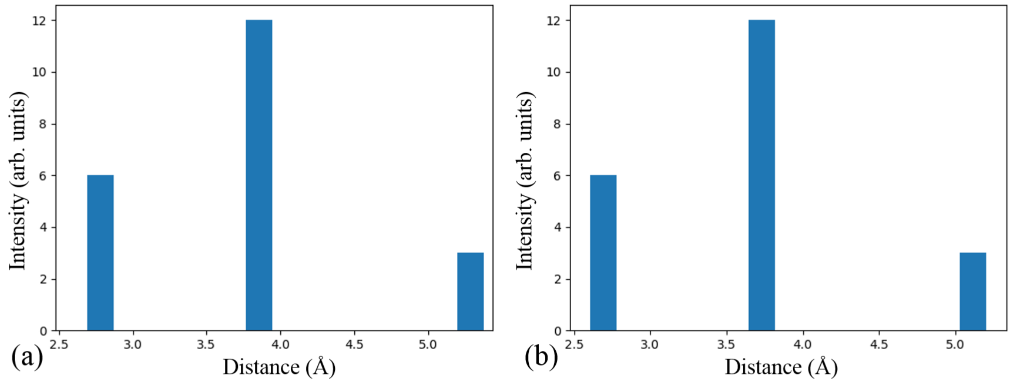

Figure 5.2: Radial distribution function of (a) $AgCl_6$ octahedral unit of $Cs_2AgInCl_6$, and (b) $CuCl_6$ octahedral unit of $Cs_2Cu_{0.25}Ag_{0.75}InCl_6$.

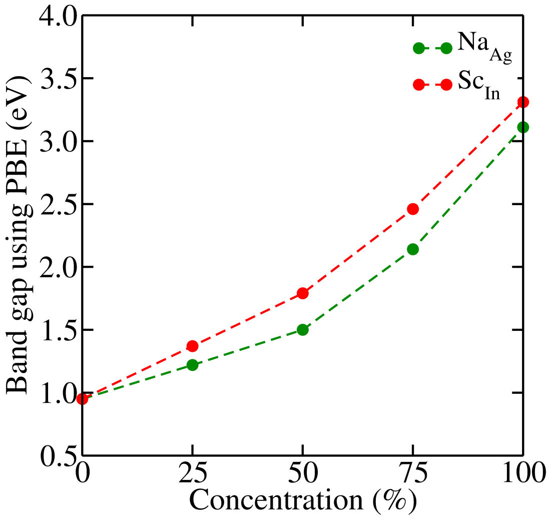

Figure 5.3: Change in band gap on increasing the concentration of impurity atoms.

room temperature, where the 0 K enthalpy of solid-state compounds is a good approximation to predict the thermodynamic stability. Hence, thermodynamic stability along with negligible octahedral distortion indicates the stable cubic structure at room temperature as well.

Here, we have started with 32 primary set of combinations of metals M(I), M(II), M(III) and halogen X at Ag/In and Cl sites, respectively, where concentration of each set is varied to build a database of nearly 140 combinations. However, note that here, we have presented the results of 25% substitution for metals and 4% substitution for halogen atoms. This is because we have seen and thoroughly checked that, with the increase in concentration of the external element, if the band gap is increased (or decreased), the same trend is followed with further increase in concentration. Two such test cases are shown in Figure 5.3. We have also reported this, to be the case in our previous experimental finding [222]. Moreover, some combinations beyond 25% substitution are not considered in the following cases: (i) toxic elements [viz., Tl(III), Cd(II), and Pb(II)], (ii) elements that lead to instability on 25% substitution [viz., Co(II), Cu(II), and Ni(II)], and (iii) elements that result in larger indirect band gap (with respect to pristine $Cs_2AgInCl_6$) on 25% substitution [viz., Ac(III), Ba(II), Ge(II), and Sn(II)]. The structural stability of all the configurations has been determined by calculating two geometrical parameters, viz., the Goldschmidt tolerance factor (t) and the octahedral factor (μ). For single perovskite ABX_3, $t = (r_\mathrm{A} + r_\mathrm{X})/\sqrt{2}(r_\mathrm{B} + r_\mathrm{X})$ and $\mu = r_\mathrm{B}/r_\mathrm{X}$, where r_A, r_B, and r_X are the ionic radii of cation A, B, and anion X, respectively. In the case of double perovskites, r_B is the average of the ionic radii at B sites. For stable perovskites, the ranges of t and μ are $0.8 \leq t \leq 1.0$ and $\mu > 0.41$ [223]. The Shannon ionic radii [224] have been considered to evaluate t and μ. For the configurations we have considered, t lies between 0.85 and 0.91, and μ has the value between 0.50 and 0.59 (see Table 5.2). Therefore, these probable structures are stable.

5.3.1.2 Thermodynamic stability

In order to determine the thermodynamic stability, we have computed the decomposition energy (ΔH_D) using PBE and HSE06 ϵ_xc functionals. We have substituted the external elements in $Cs_8Ag_4In_4Cl_{24}$ supercell framework to model a solid solution.[1] In order to model the defected system, we have used an iterative procedure as shown in Refs. [225, 226]. The ΔH_D for the decomposition of $Cs_8Ag_4In_4Cl_{24}$ into binary compounds is calculated as follows:

$$\begin{aligned} \Delta H_\mathrm{D}(\mathrm{Cs_8Ag_4In_4Cl_{24}}) = \mathrm{E}(\mathrm{Cs_8Ag_4In_4Cl_{24}}) - 8\mathrm{E}(\mathrm{CsCl}) \\ - 4\mathrm{E}(\mathrm{AgCl}) - 4\mathrm{E}(\mathrm{InCl_3}) \end{aligned} \tag{5.1}$$

where $\mathrm{E}(\mathrm{Cs_8Ag_4In_4Cl_{24}})$, $\mathrm{E}(\mathrm{CsCl})$, $\mathrm{E}(\mathrm{AgCl})$, and $\mathrm{E}(\mathrm{InCl_3})$ are the DFT energies of the respective compounds. The configurations having negative value of the ΔH_D are stable. The entropy of mixing is not considered here as it will not change the overall trend, i.e., the relative stability will remain same [227, 9, 228]. Figure 5.4a and 5.4b show the decomposition energy for the decomposition of $Cs_2AgInCl_6$ and other mixed sublattices into binary compounds using PBE and HSE06 ϵ_xc functionals, respectively (decomposition reactions are shown below). Only those elements, which lead to decrement in band gap using PBE ϵ_xc functional, are further

---

[1] As most of the sites in double perovskite are equivalent under same symmetry point, the energy difference in case of different sites (i.e., non-equivalent cells with same stoichiometry) is very small. Thus, even if we take thermodynamic average considering alloying, the results do not change.

Table 5.2: Tolerance factor, octahedral factor, band gap, and decomposition energy (for decomposition into binary compounds) using PBE and HSE06 ϵ_{xc} functionals of different configurations

Configuration	Tolerance factor (t)	Octahedral factor (μ)	Band gap (PBE) (eV)	ΔH_D (binary decomposition) (PBE) (eV/atom)	Band gap HSE06 (eV)	ΔH_D (binary decomposition) (HSE06) (eV/atom)
$Cs_2AgInCl_6$	0.88	0.54	0.95	-0.233	2.31	-0.248
$Cs_2Cu_{0.25}Ag_{0.75}InCl_6$	0.90	0.51	0.04	-0.224	1.51	-0.237
$Cs_2Au_{0.25}Ag_{0.75}InCl_6$	0.87	0.55	0.32	-0.212	1.54	-0.228
$Cs_2Na_{0.25}Ag_{0.75}InCl_6$	0.89	0.53	1.22	-0.232	-	-
$Cs_2K_{0.25}Ag_{0.75}InCl_6$	0.87	0.55	1.37	-0.216	-	-
$Cs_2Rb_{0.25}Ag_{0.75}InCl_6$	0.87	0.56	1.43	-0.200	-	-
$Cs_2AgAl_{0.25}In_{0.75}Cl_6$	0.89	0.52	1.03	-0.196	-	-
$Cs_2AgGa_{0.25}In_{0.75}Cl_6$	0.89	0.53	0.87	-0.192	2.23	-0.202
$Cs_2AgTl_{0.25}In_{0.75}Cl_6$	0.88	0.54	0.37	-0.218	-	-
$Cs_2AgCo_{0.25}In_{0.75}Cl_6$	0.89	0.52	0.73	-0.217	2.09	-0.230
$Cs_2AgRh_{0.25}In_{0.75}Cl_6$	0.89	0.53	0.91	-0.195	2.53	-0.204
$Cs_2AgIr_{0.25}In_{0.75}Cl_6$	0.89	0.53	0.43	-0.191	2.08	-0.202
$Cs_2AgSc_{0.25}In_{0.75}Cl_6$	0.89	0.53	1.37	-0.200	-	-
$Cs_2AgY_{0.25}In_{0.75}Cl_6$	0.88	0.54	1.54	-0.194	-	-
$Cs_2AgLa_{0.25}In_{0.75}Cl_6$	0.87	0.55	1.89	-0.178	-	-
$Cs_2AgAc_{0.25}In_{0.75}Cl_6$	0.87	0.56	1.78	-0.161	-	-
$Cs_2AgCr_{0.25}In_{0.75}Cl_6$	0.89	0.53	1.06	-0.197	-	-
$Cs_2AgSb_{0.25}In_{0.75}Cl_6$	0.89	0.54	1.72	-0.197	-	-
$Cs_2AgBi_{0.25}In_{0.75}Cl_6$	0.87	0.55	1.96	-0.200	-	-
$Cs_2Ca_{0.50}Ag_{0.75}In_{0.75}Cl_6$	0.88	0.54	1.89	-0.177	-	-
$Cs_2Sr_{0.50}Ag_{0.75}In_{0.75}Cl_6$	0.87	0.57	2.11	-0.148	-	-
$Cs_2Ba_{0.50}Ag_{0.75}In_{0.75}Cl_6$	0.85	0.59	2.29	-0.096	-	-
$Cs_2Zn_{0.50}Ag_{0.75}In_{0.75}Cl_6$	0.90	0.51	0.61	-0.176	1.87	-0.186
$Cs_2Cd_{0.50}Ag_{0.75}In_{0.75}Cl_6$	0.89	0.54	0.64	-0.180	-	-
$Cs_2Ge_{0.50}Ag_{0.75}In_{0.75}Cl_6$	0.90	0.50	1.43	-0.196	-	-
$Cs_2Sn_{0.50}Ag_{0.75}In_{0.75}Cl_6$	0.87	0.57	1.18	-0.176	-	-
$Cs_2Pb_{0.50}Ag_{0.75}In_{0.75}Cl_6$	0.87	0.57	1.72	-0.160	-	-
$Cs_2Mn_{0.50}Ag_{0.75}In_{0.75}Cl_6$	0.90	0.52	0.31	-0.187	1.77	-0.194
$Cs_2Co_{0.50}Ag_{0.75}In_{0.75}Cl_6$	0.90	0.51	metallic	-0.166	0.95	-0.140
$Cs_2Ni_{0.50}Ag_{0.75}In_{0.75}Cl_6$	0.91	0.50	metallic	-0.160	1.98	-0.168
$Cs_2Cu_{0.50}Ag_{0.75}In_{0.75}Cl_6$	0.90	0.50	metallic	-0.172	1.89	-0.140
$Cs_2AgInBr_{0.04}Cl_{5.96}$	0.88	0.54	0.80	-0.226	2.10	-0.242
$Cs_2AgInI_{0.04}Cl_{5.96}$	0.88	0.54	0.64	-0.206	1.85	-0.224

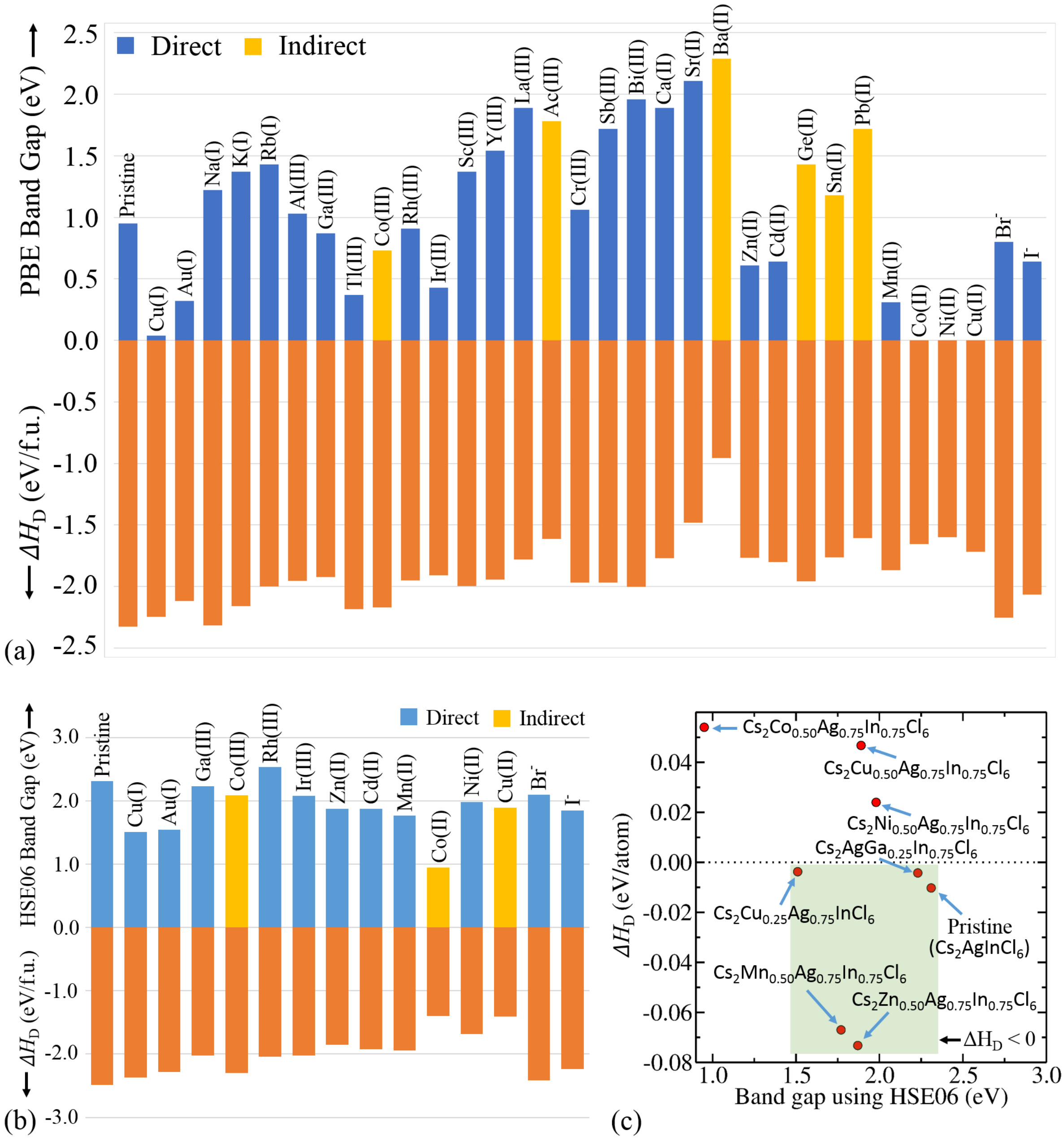

Figure 5.4: Decomposition energy (ΔH_{D}) for the decomposition of pristine and other configurations into binary compounds, and band gap using the ϵ_{xc} functionals (a) PBE and (b) HSE06. (c) Decomposition energy (ΔH_{D}) for decomposition into ternary compounds using HSE06 ϵ_{xc} functional.

considered with HSE06 ϵ_{xc} functional.

Reactions for the decomposition of pristine and alloyed $Cs_2AgInCl_6$ into binary/ternary compounds:

(1) $Cs_2AgInCl_6$

$Cs_8Ag_4In_4Cl_{24} \longrightarrow 8\,CsCl + 4\,AgCl + 4\,InCl_3$

$Cs_8Ag_4In_4Cl_{24} \longrightarrow 2\,CsAgCl_2 + 2\,Cs_3In_2Cl_9 + 2\,AgCl$

(2) $Cs_2Cu_{0.25}Ag_{0.75}InCl_6$

$Cs_8Cu_1Ag_3In_4Cl_{24} \longrightarrow 8\,CsCl + 3\,AgCl + CuCl + 4\,InCl_3$

$Cs_8Cu_1Ag_3In_4Cl_{24} \longrightarrow \frac{1}{2}\,CsCu_2Cl_3 + 2\,Cs_3In_2Cl_9 + 3\,AgCl + \frac{3}{2}\,CsCl$

(3) $Cs_2Au_{0.25}Ag_{0.75}InCl_6$

$Cs_8Au_1Ag_3In_4Cl_{24} \longrightarrow 8\,CsCl + 3\,AgCl + AuCl + 4\,InCl_3$

(4) $Cs_2Na_{0.25}Ag_{0.75}InCl_6$

$Cs_8Na_1Ag_3In_4Cl_{24} \longrightarrow 8\,CsCl + 3\,AgCl + NaCl + 4\,InCl_3$

(5) $Cs_2K_{0.25}Ag_{0.75}InCl_6$

$Cs_8K_1Ag_3In_4Cl_{24} \longrightarrow 8\,CsCl + 3\,AgCl + KCl + 4\,InCl_3$

(6) $Cs_2Rb_{0.25}Ag_{0.75}InCl_6$

$Cs_8Rb_1Ag_3In_4Cl_{24} \longrightarrow 8\,CsCl + 3\,AgCl + RbCl + 4\,InCl_3$

(7) $Cs_2AgAl_{0.25}In_{0.75}Cl_6$

$Cs_8Ag_4Al_1In_3Cl_{24} \longrightarrow 8\,CsCl + 4\,AgCl + 3\,InCl_3 + AlCl_3$

(8) $Cs_2AgGa_{0.25}In_{0.75}Cl_6$

$Cs_8Ag_4Ga_1In_3Cl_{24} \longrightarrow 8\,CsCl + 4\,AgCl + 3\,InCl_3 + GaCl_3$

$Cs_8Ag_4Ga_1In_3Cl_{24} \longrightarrow CsGaCl_4 + \frac{3}{2}\,Cs_3In_2Cl_9 + 4\,AgCl + \frac{5}{2}\,CsCl$

(9) $Cs_2AgTl_{0.25}In_{0.75}Cl_6$

$Cs_8Ag_4Tl_1In_3Cl_{24} \longrightarrow 8\,CsCl + 4\,AgCl + 3\,InCl_3 + TlCl_3$

(10) $Cs_2AgCo_{0.25}In_{0.75}Cl_6$

$Cs_8Ag_4Co_1In_3Cl_{24} \longrightarrow 8\,CsCl + 4\,AgCl + 3\,InCl_3 + CoCl_3$

(11) $Cs_2AgRh_{0.25}In_{0.75}Cl_6$

$Cs_8Ag_4Rh_1In_3Cl_{24} \longrightarrow 8\,CsCl + 4\,AgCl + 3\,InCl_3 + RhCl_3$

(12) $Cs_2AgIr_{0.25}In_{0.75}Cl_6$

$Cs_8Ag_4Ir_1In_3Cl_{24} \longrightarrow 8\,CsCl + 4\,AgCl + 3\,InCl_3 + IrCl_3$

(13) $Cs_2AgSc_{0.25}In_{0.75}Cl_6$

$Cs_8Ag_4Sc_1In_3Cl_{24} \longrightarrow 8\,CsCl + 4\,AgCl + 3\,InCl_3 + ScCl_3$

(14) $Cs_2AgY_{0.25}In_{0.75}Cl_6$

$Cs_8Ag_4Y_1In_3Cl_{24} \longrightarrow 8\,CsCl + 4\,AgCl + 3\,InCl_3 + YCl_3$

(15) $Cs_2AgLa_{0.25}In_{0.75}Cl_6$

$Cs_8Ag_4La_1In_3Cl_{24} \longrightarrow 8\,CsCl + 4\,AgCl + 3\,InCl_3 + LaCl_3$

(16) $Cs_2AgAc_{0.25}In_{0.75}Cl_6$

$Cs_8Ag_4Ac_1In_3Cl_{24} \longrightarrow 8\,CsCl + 4\,AgCl + 3\,InCl_3 + AcCl_3$

(17) $Cs_2AgCr_{0.25}In_{0.75}Cl_6$

$Cs_8Ag_4Cr_1In_3Cl_{24} \longrightarrow 8\,CsCl + 4\,AgCl + 3\,InCl_3 + CrCl_3$

(18) $Cs_2AgSb_{0.25}In_{0.75}Cl_6$

$Cs_8Ag_4Sb_1In_3Cl_{24} \longrightarrow 8\,CsCl + 4\,AgCl + 3\,InCl_3 + SbCl_3$

(19) $Cs_2AgBi_{0.25}In_{0.75}Cl_6$

$Cs_8Ag_4Bi_1In_3Cl_{24} \longrightarrow 8\,CsCl + 4\,AgCl + 3\,InCl_3 + BiCl_3$

(20) $Cs_2Ca_{0.50}Ag_{0.75}In_{0.75}Cl_6$

$Cs_8Ca_2Ag_3In_3Cl_{24} \longrightarrow 8\,CsCl + 3\,AgCl + 3\,InCl_3 + 2\,CaCl_2$

(21) $Cs_2Sr_{0.50}Ag_{0.75}In_{0.75}Cl_6$

$Cs_8Sr_2Ag_3In_3Cl_{24} \longrightarrow 8\,CsCl + 3\,AgCl + 3\,InCl_3 + 2\,SrCl_2$

(22) $Cs_2Ba_{0.50}Ag_{0.75}In_{0.75}Cl_6$

$Cs_8Ba_2Ag_3In_3Cl_{24} \longrightarrow 8\,CsCl + 3\,AgCl + 3\,InCl_3 + 2\,BaCl_2$

(23) $Cs_2Zn_{0.50}Ag_{0.75}In_{0.75}Cl_6$

$Cs_8Zn_2Ag_3In_3Cl_{24} \longrightarrow 8\,CsCl + 3\,AgCl + 3\,InCl_3 + 2\,ZnCl_2$

$Cs_8Zn_2Ag_3In_3Cl_{24} \longrightarrow 2\,Cs_2ZnCl_4 + \frac{1}{2}\,Cs_3In_2Cl_9 + 3\,AgCl + \frac{5}{2}\,CsCl + 2\,InCl_3$

(24) $Cs_2Cd_{0.50}Ag_{0.75}In_{0.75}Cl_6$

$Cs_8Cd_2Ag_3In_3Cl_{24} \longrightarrow 8\,CsCl + 3\,AgCl + 3\,InCl_3 + 2\,CdCl_2$

(25) $Cs_2Ge_{0.50}Ag_{0.75}In_{0.75}Cl_6$

$Cs_8Ge_2Ag_3In_3Cl_{24} \longrightarrow 8\,CsCl + 3\,AgCl + 3\,InCl_3 + 2\,GeCl_2$

(26) $Cs_2Sn_{0.50}Ag_{0.75}In_{0.75}Cl_6$

$Cs_8Sn_2Ag_3In_3Cl_{24} \longrightarrow 8\,CsCl + 3\,AgCl + 3\,InCl_3 + 2\,SnCl_2$

(27) $Cs_2Pb_{0.50}Ag_{0.75}In_{0.75}Cl_6$

$Cs_8Pb_2Ag_3In_3Cl_{24} \longrightarrow 8\,CsCl + 3\,AgCl + 3\,InCl_3 + 2\,PbCl_2$

(28) $Cs_2Mn_{0.50}Ag_{0.75}In_{0.75}Cl_6$

$Cs_8Mn_2Ag_3In_3Cl_{24} \longrightarrow 8\,CsCl + 3\,AgCl + 3\,InCl_3 + 2\,MnCl_2$

$Cs_8Mn_2Ag_3In_3Cl_{24} \longrightarrow 2\,CsMnCl_3 + \frac{3}{2}\,Cs_3In_2Cl_9 + 3\,AgCl + \frac{3}{2}\,CsCl$

(29) $Cs_2Co_{0.50}Ag_{0.75}In_{0.75}Cl_6$

$Cs_8Co_2Ag_3In_3Cl_{24} \longrightarrow 8\,CsCl + 3\,AgCl + 3\,InCl_3 + 2\,CoCl_2$

$Cs_8Co_2Ag_3In_3Cl_{24} \longrightarrow 2\,CsCoCl_3 + \frac{3}{2}\,Cs_3In_2Cl_9 + 3\,AgCl + \frac{3}{2}\,CsCl$

(30) $Cs_2Ni_{0.50}Ag_{0.75}In_{0.75}Cl_6$

$Cs_8Ni_2Ag_3In_3Cl_{24} \longrightarrow 8\,CsCl + 3\,AgCl + 3\,InCl_3 + 2\,NiCl_2$

$Cs_8Ni_2Ag_3In_3Cl_{24} \longrightarrow 2\,CsNiCl_3 + \frac{3}{2}\,Cs_3In_2Cl_9 + 3\,AgCl + \frac{3}{2}\,CsCl$

(31) $Cs_2Cu_{0.50}Ag_{0.75}In_{0.75}Cl_6$

$Cs_8Cu_2Ag_3In_3Cl_{24} \longrightarrow 8\,CsCl + 3\,AgCl + 3\,InCl_3 + 2\,CuCl_2$

$Cs_8Cu_2Ag_3In_3Cl_{24} \longrightarrow 2\,CsCuCl_3 + \frac{3}{2}\,Cs_3In_2Cl_9 + 3\,AgCl + \frac{3}{2}\,CsCl$

(32) $Cs_2AgInBr_{0.04}Cl_{5.96}$

$Cs_8Ag_4In_4Br_1Cl_{23} \longrightarrow 8\,CsCl + 3\,AgCl + AgBr + 4\,InCl_3$

(33) $Cs_2AgInI_{0.04}Cl_{5.96}$

$Cs_8Ag_4In_4I_1Cl_{23} \longrightarrow 8\,CsCl + 3\,AgCl + AgI + 4\,InCl_3$

The quaternary compounds can be decomposed into ternary compounds. Therefore, we have also considered those pathways for the materials [see decomposition reactions that are more probable (as per the smaller value of decomposition energy)], which have the favorable band gap. The decomposition energy for the decomposition of $Cs_2AgInCl_6$ and other mixed sublattices into ternary compounds is shown in Figure 5.4c. For the decomposition of $Cs_8Ag_4In_4Cl_{24}$ into ternary compounds, the ΔH_D is determined as follows:

$$\begin{aligned}\Delta H_D(Cs_8Ag_4In_4Cl_{24}) = {} & E(Cs_8Ag_4In_4Cl_{24}) - 2E(CsAgCl_2) \\ & - 2E(Cs_3In_2Cl_9) - 2E(AgCl)\end{aligned} \tag{5.2}$$

The ΔH_D has the value of -2.48 eV/f.u. and -0.10 eV/f.u. for the decomposition of $Cs_8Ag_4In_4Cl_{24}$ into binary and ternary compounds, respectively. These negative values confirm that the perovskite $Cs_8Ag_4In_4Cl_{24}$ is stable. We have found that all the selected elements for sublattice mixing are stable with respect to the decomposition into binary compounds (see Table 5.2). However, for ternary decomposition pathway, Co(II), Ni(II), and Cu(II) are not stable (see Figure 5.4c, where shaded region indicates the stable compounds, i.e., $\Delta H_D < 0$). This may be attributed to the smaller size of these cations that are unable to accommodate two octahedra with Cl_6, and the lowest octahedral factor of Ni(II) and Cu(II) (see Table 5.2). Also, Cu(I) and Ga(III) are less stable than pristine (see Figure 5.4c). Moreover, we have noticed that Cu(I) is not stable at all (as positive value of ΔH_D = 0.32 eV/f.u. (see Table 5.3)) when it has fully

Table 5.3: Decomposition energy (for the decomposition into ternary compounds) of $Cs_2Cu_xAg_{1-x}InCl_6$

Compounds	ΔH_{D} (eV/f.u.)	
	PBE	HSE06
$Cs_2AgInCl_6$	-0.098	-0.103
$Cs_2Cu_{0.25}Ag_{0.75}InCl_6$	-0.070	-0.039
$Cs_2Cu_{0.50}Ag_{0.50}InCl_6$	0.058	0.122
$Cs_2Cu_{0.75}Ag_{0.25}InCl_6$	0.190	0.354
$Cs_2CuInCl_6$	0.322	0.472

replaced the Ag, i.e., for 100% substitution, which is in agreement with previous studies [220]. It is only stable for 25% substitution. Therefore, it is concluded that, if the difference between sizes of the substitutional cation/anion and pristine's cation/anion is large, then that configuration would become unstable on increment in concentration.

5.3.2 Electronic structure analysis

A screening of various atoms for sublattice mixing has been done by calculating the band gap first using generalized gradient approximation (PBE) and, subsequently, with inclusion of SOC. The respective band gaps as obtained for pristine $Cs_2AgInCl_6$ are 0.95 eV and 0.93 eV, implying insignificant SOC effect on its electronic properties. Also, as per existing literature, SOC has negligible effect in Ag/In- [229, 210] and Au- [230, 231] based double perovskite. We have checked the SOC effects for Au-based system. On substituting 25% Au, only the band gap is changed by 0.1 eV. The nature of the band gap still remains direct at Γ-point. There is no splitting at band edges, i.e., at conduction band minimum (CBm) or valence band maximum (VBM) (see Figure 5.5). The bands remain degenerate at the VBM and CBm. Only the VBM level is lifted by 0.1 eV. Hence, SOC has negligible effect in the case of Au-based system. This corroborates with the fact that it does not contain any heavy element like Pb or Bi, where some significant effect of SOC is expected in the electronic properties of such materials. Therefore, we have ignored the effect of SOC in our further calculations. However, the band gap is highly underestimated by PBE ϵ_{xc} functional due to the well-known self-interaction error. Therefore, we have further performed the calculations using hybrid ϵ_{xc} functional HSE06 for those mixed

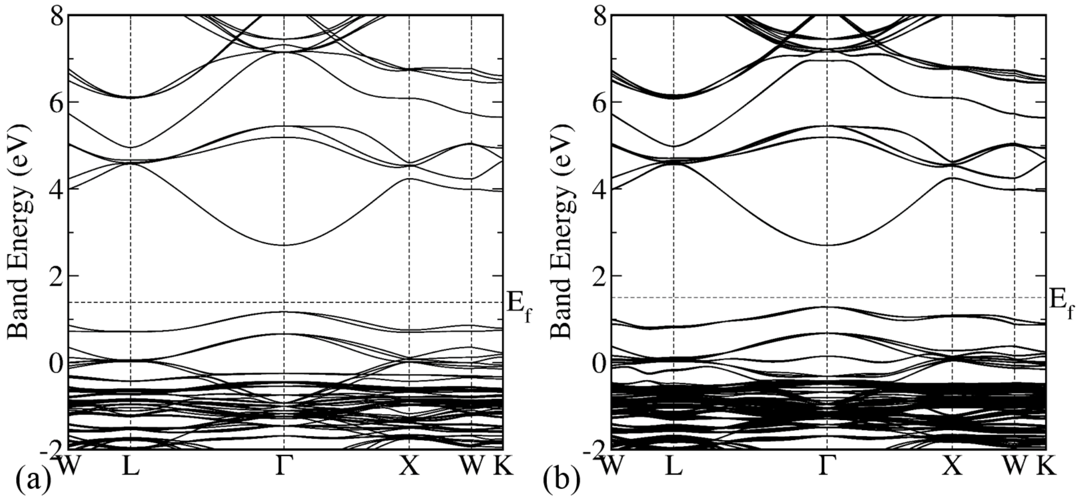

Figure 5.5: Bandstructure of $Cs_2Au_{0.25}Ag_{0.75}InCl_6$ (a) without SOC, and (b) with SOC using HSE06 ϵ_{xc} functional.

sublattices, where in comparison to pristine, the band gap was reduced (see Figure 5.4a, 5.4b, and Table 5.2). The calculated value of band gap for $Cs_2AgInCl_6$ is 2.31 eV using default exact Fock exchange of 25%, which is in good agreement with previously reported theoretical value, but still underestimated in comparison to the experimental value (3.3 eV) [43]. We have also validated that the band gap becomes 3.19 eV on increasing the exact Fock exchange parameter to 40%. Despite the proximity of this value to that of experiments, it can be drastically changed for the systems having defects (substitution of different elements), and determining it accurately is not possible without the experimental inputs. In view of this, we have used the default 25% exact Fock exchange parameter for our study, assuming this will give atleast the correct trends. In the case of Cu(I) and Au(I) substitutional alloying at Ag site, the band gap is reduced by $\sim$ 0.8 eV, having a value of 1.51 and 1.54 eV, respectively. On the other hand, in the case of substitution of M(III) at In site, it does not have much effect on reduction in band gap. Only Co(III) and Ir(III) substitutional alloying are able to reduce the band gap from 2.31 to 2.08 eV, whereas the rest are either increasing it or have no effect on the band gap. In the case of M(II) substitutional alloying, one at Ag and other one at In site, only Zn(II) and Mn(II) are able to reduce the band gap effectively, having a band gap value of 1.87 and 1.77 eV, respectively. In the case of halogen substitution, viz., Br and I, it helps to reduce the band gap to 2.10 and 1.85 eV, respectively (see Table 5.2). In the aforementioned cases, while reducing the band gap, the direct gap nature remains intact, except for Co(III) substitution. We have also calculated the band gap using G_0W_0@HSE06, which is overestimated and nearer to the experimental value. In the case of pristine $Cs_2AgInCl_6$, the band gap is 3.77 eV. The comparison of band gap computed using PBE, HSE06, and G_0W_0@HSE06 can be seen from Table 5.4.

Table 5.4: Band gap (in eV) using PBE, HSE06, and G_0W_0@HSE06 for different configurations

Configuration	PBE	HSE06	G_0W_0@HSE06
$Cs_2AgInCl_6$	0.95	2.31	3.77
$Cs_2Cu_{0.25}Ag_{0.75}InCl_6$	0.04	1.51	2.69
$Cs_2Au_{0.25}Ag_{0.75}InCl_6$	0.32	1.54	2.79
$Cs_2AgGa_{0.25}In_{0.75}Cl_6$	0.87	2.23	3.68
$Cs_2AgCo_{0.25}In_{0.75}Cl_6$	0.73	2.09	3.15
$Cs_2AgIr_{0.25}In_{0.75}Cl_6$	0.43	2.08	3.32
$Cs_2Zn_{0.50}Ag_{0.75}In_{0.75}Cl_6$	0.61	1.87	3.32
$Cs_2Mn_{0.50}Ag_{0.75}In_{0.75}Cl_6$	0.31	1.77	3.34
$Cs_2AgInBr_{0.04}Cl_{5.96}$	0.80	2.10	3.53
$Cs_2AgInI_{0.04}Cl_{5.96}$	0.64	1.85	3.21

The reduction in band gap can be explained by observing the atom-projected pDOS (see Figure 5.6). In the pristine $Cs_2AgInCl_6$, the Cl p-orbitals and Ag d-orbitals contribute to the VBM, whereas the In and Ag s-orbitals contribute to the CBm (see Figure 5.6a). In the case of substitutional alloying of Cu(I) and Au(I), their d-orbitals are at higher energy level than the d-orbitals of Ag, thereby, reducing the band gap by elevating the VBM (see Figure 5.6c and 5.6d). However, in the case of the M(III) substitution at In site, generally, the states lie inside the valence band (VB) or the conduction band (CB), and thus, do not reduce the band gap effectively. From Figure 5.6b, we can see that the Ga(III) is reducing the band gap by a negligible amount (as the states contributed by the Ga are lying inside VB and CB). Whereas, the Co(III) and Ir(III) substitution at In site show a finite decrease in the band gap. This is due to the Co d-orbitals and Ir d-orbitals contribution at CBm and VBM, respectively (see Figure 5.7a and 5.7b). In the case of M(II), there is a little contribution from d- and s-orbitals of M(II) at VBM and CBm, respectively, and therefore, reducing the band gap by introducing the shallow states (see Figure 5.6e and 5.6(f)). Moreover, the Mn states are asymmetric (with respect to spin states), which indicates that Zn(II) will be more stable than Mn(II). This can also be seen from the more negative value of ΔH_D for Zn(II) in comparison to Mn(II). The

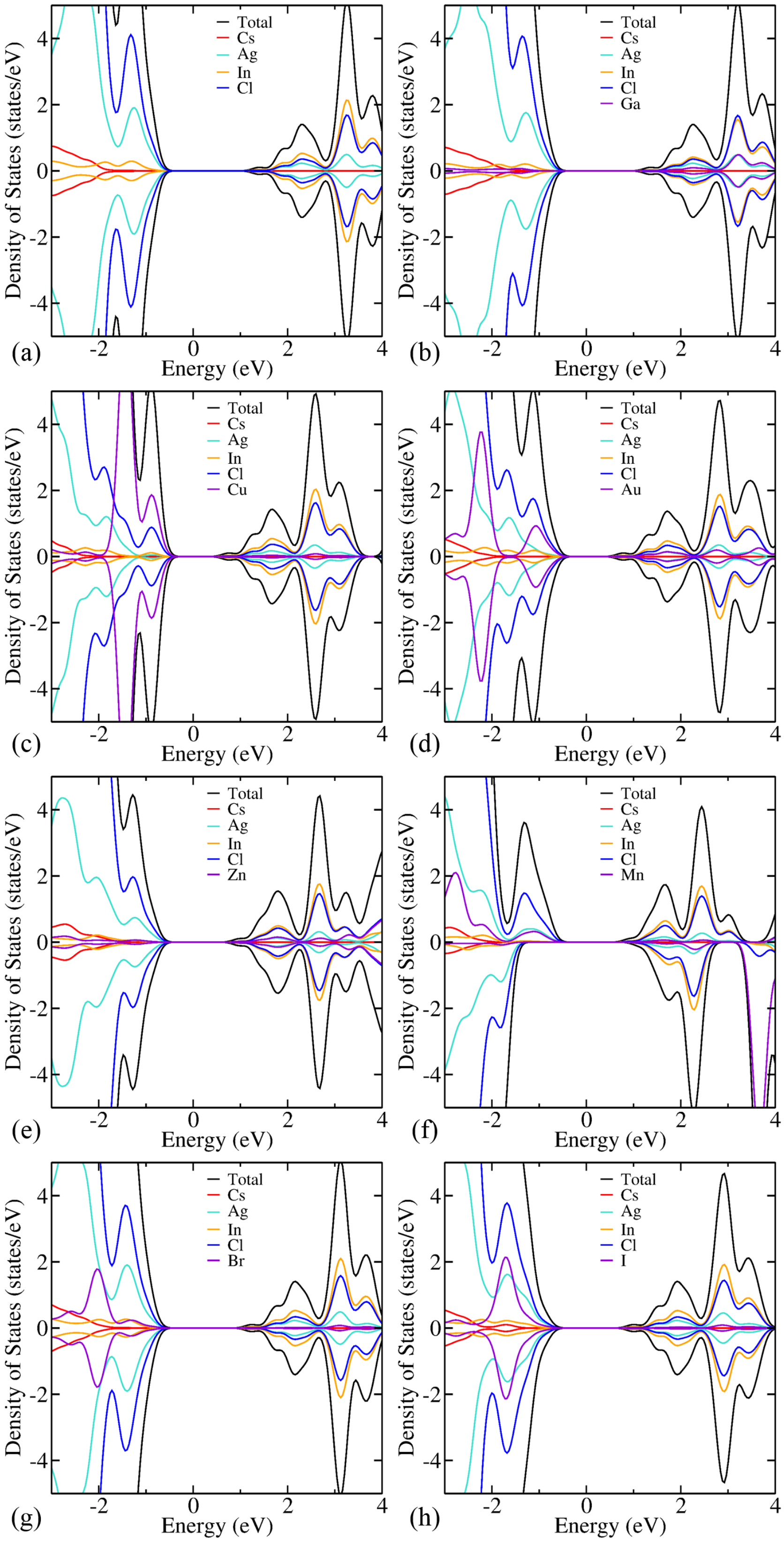

Figure 5.6: Atom-projected pDOS using HSE06 ϵ_{xc} functional of (a) pristine $Cs_2AgInCl_6$, (b) $Cs_2AgGa_{0.25}In_{0.75}Cl_6$, (c) $Cs_2Cu_{0.25}Ag_{0.75}InCl_6$, (d) $Cs_2Au_{0.25}Ag_{0.75}InCl_6$, (e) $Cs_2Zn_{0.50}Ag_{0.75}In_{0.75}Cl_6$, (f) $Cs_2Mn_{0.50}Ag_{0.75}In_{0.75}Cl_6$, (g) $Cs_2AgInBr_{0.04}Cl_{5.96}$, and (h) $Cs_2AgInI_{0.04}Cl_{5.96}$.

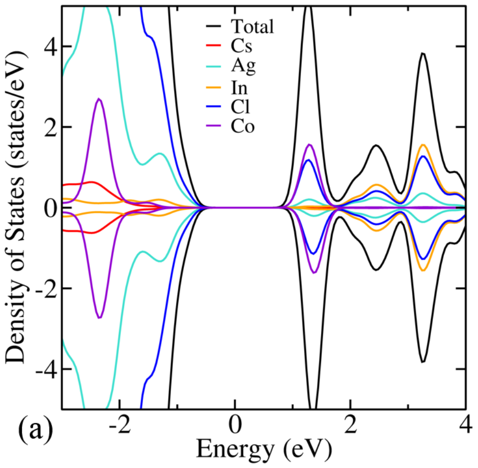

Figure 5.7: Atom-projected pDOS using HSE06 ϵ_{xc} functional of (a) $Cs_2AgCo_{0.25}In_{0.75}Cl_6$ and (b) $Cs_2AgIr_{0.25}In_{0.75}Cl_6$.

band gap reduction on substituting Br/I at Cl site is occurred by elevating the VBM, which is due to Br/I p-orbitals contribution at VBM (see Figure 5.6g and 5.6h). The reduction in band gap on mixing the halides is in line with the previous studies [47, 43]. In all these cases, the defect levels are shallow, which is a desirable property for optoelectronic devices. Shallow defect states ensure that the recombination of photogenerated charge carriers is not prominent and thus, the decrement in charge carrier mobility and diffusion will be insignificant.

5.3.3 Optical properties

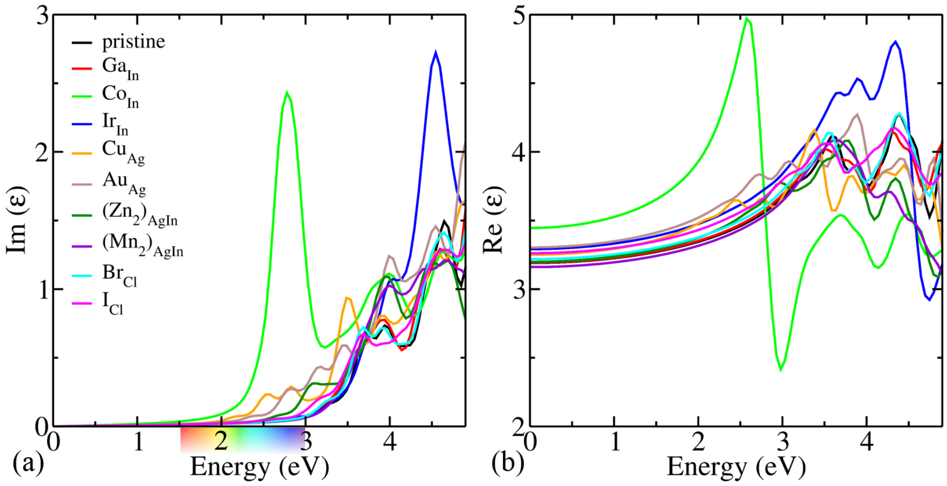

Figure 5.8: Spatially average (a) imaginary [Im (ε)] and (b) real [Re (ε)] part of the dielectric function obtained by HSE06 for the pristine, and alloyed $Cs_2AgInCl_6$.

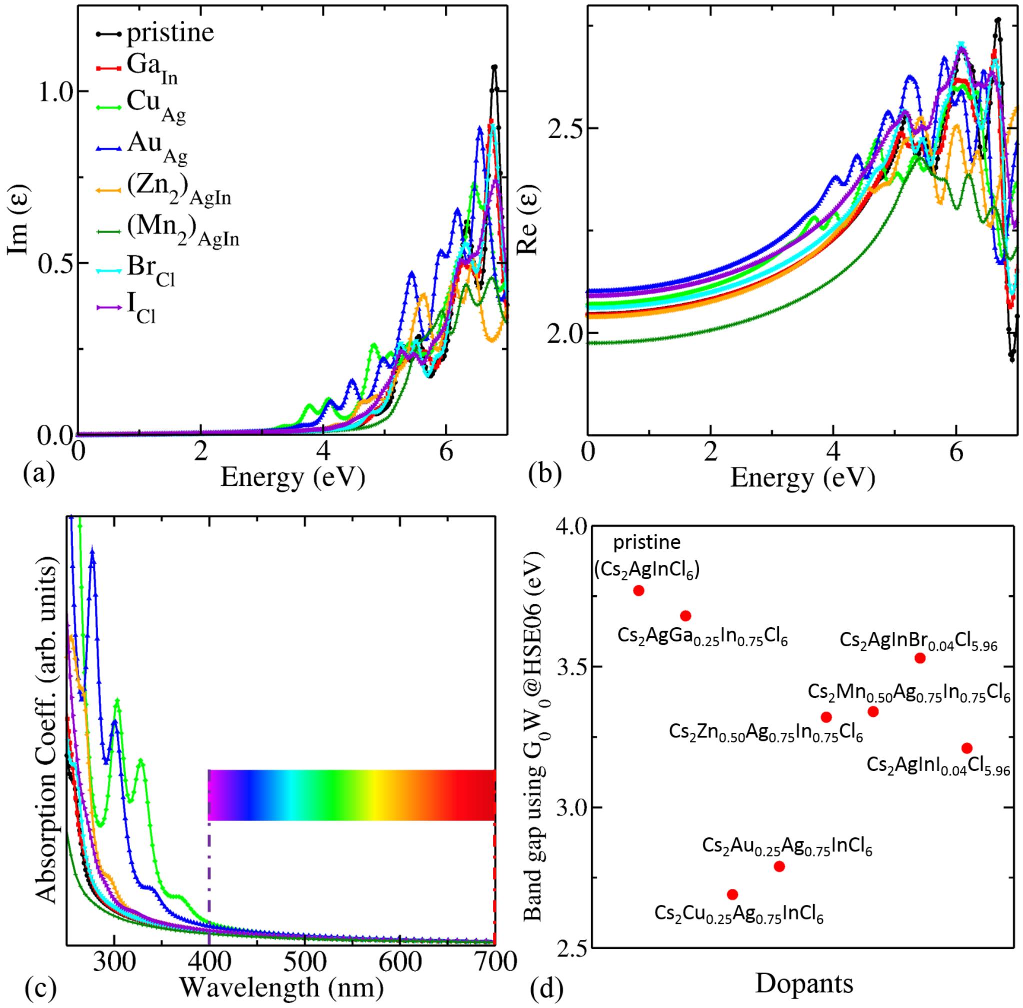

Figure 5.9: Spatially average (a) imaginary [Im (ε)] and (b) real [Re (ε)] part of the dielectric function, (c) absorption coefficient and (d) band gap obtained by G_0W_0@HSE06 for the pristine $Cs_2AgInCl_6$ and other mixed sublattices.

To obtain the optical properties, which are crucial for the perovskite to be used in optoelectronic devices, we have calculated the frequency dependent complex dielectric function $\varepsilon(\omega) = \mathrm{Re}\,(\varepsilon(\omega)) + \mathrm{Im}\,(\varepsilon(\omega))$ using G_0W_0@HSE06 [the results obtained by HSE06 ϵ_{xc} functional are shown in Figure 5.8 for comparison]. Figure 5.9a and 5.9b show the imaginary [Im (ε)] and real [Re (ε)] part of the dielectric function, respectively. The real static part (at $\omega = 0$) of the dielectric function is a direct measure of refractive index. Higher the refractive index, better will be the probability to absorb light. On alloying, the refractive index is increased in most of the cases (range: $1.98 - 2.15$), and thus, the optical properties are enhanced. The static Re (ε) is 2.05 for pristine $Cs_2AgInCl_6$, and the value has increased on alloying (see Figure 5.9b, Figure 5.10b and Table 5.5). The imaginary part reflects the transitions from occupied to unoc-

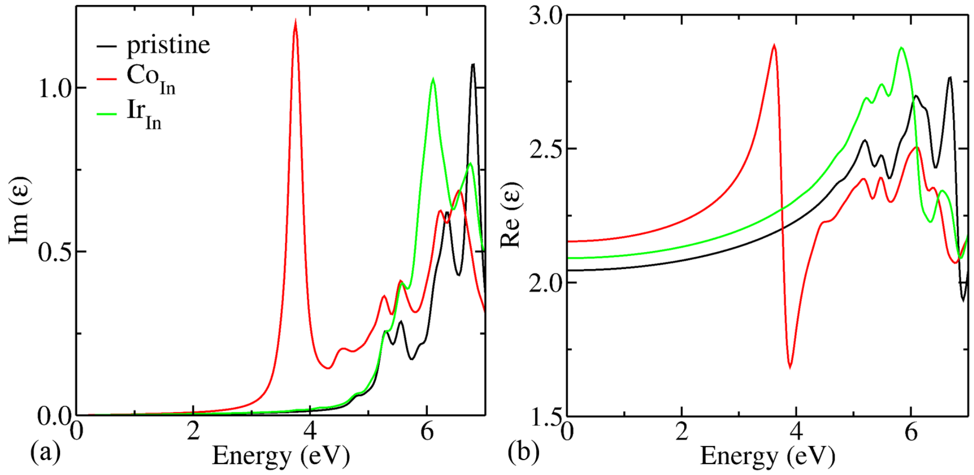

Figure 5.10: Spatially average (a) imaginary [Im (ε)] and (b) real [Re (ε)] part of the dielectric function obtained by G_0W_0@HSE06 for the pristine, $Cs_2AgCo_{0.25}In_{0.75}Cl_6$, and $Cs_2AgIr_{0.25}In_{0.75}Cl_6$.

cupied bands. The absorption edge is red shifted and hence, the visible light response has been achieved upon alloying (see Figure 5.9a). The absorption spectra have also been obtained that corroborates with the red shift observed (see Figure 5.9c). The absorption coefficient $\alpha(\omega)$ is related to the dielectric function as follows:

$$\alpha(\omega) = \sqrt{2}\,\frac{\omega}{c}\left(\sqrt{\mathrm{Re}(\varepsilon(\omega))^2 + \mathrm{Im}(\varepsilon(\omega))^2} - \mathrm{Re}(\varepsilon(\omega))\right)^{\frac{1}{2}} \tag{5.3}$$

This visible response is attributed to the reduction in band gap as shown in Figure 5.9d. The optical parameters viz. refractive index (η), extinction coefficient (κ), reflectivity (R), absorption coefficient (α), optical conductivity (σ), and energy loss spectrum (L), are related to dielectric function (ε) as follows:

$$\eta = \frac{1}{\sqrt{2}}\left[\sqrt{\mathrm{Re}(\varepsilon)^2 + \mathrm{Im}(\varepsilon)^2} + \mathrm{Re}(\varepsilon)\right]^{\frac{1}{2}} \tag{5.4}$$

$$\kappa = \frac{1}{\sqrt{2}}\left[\sqrt{\mathrm{Re}(\varepsilon)^2 + \mathrm{Im}(\varepsilon)^2} - \mathrm{Re}(\varepsilon)\right]^{\frac{1}{2}} \tag{5.5}$$

$$R = \frac{[\eta - 1]^2 + \kappa^2}{[\eta + 1]^2 + \kappa^2} \tag{5.6}$$

$$\alpha = \frac{2\omega\kappa}{c} \tag{5.7}$$

Table 5.5: The high frequency ‘ion-clamped’ dielectric constant (ε_∞) using G_0W_0@HSE06

Configurations	ε_∞
pristine	2.05
$Cs_2AgGa_{0.25}In_{0.75}Cl_6$	2.04
$Cs_2AgCo_{0.25}In_{0.75}Cl_6$	2.15
$Cs_2AgIr_{0.25}In_{0.75}Cl_6$	2.09
$Cs_2Cu_{0.25}Ag_{0.75}InCl_6$	2.07
$Cs_2Au_{0.25}Ag_{0.75}InCl_6$	2.10
$Cs_2Zn_{0.50}Ag_{0.75}In_{0.75}Cl_6$	2.04
$Cs_2Mn_{0.50}Ag_{0.75}In_{0.75}Cl_6$	1.98
$Cs_2AgInBr_{0.04}Cl_{5.96}$	2.06
$Cs_2AgInI_{0.04}Cl_{5.96}$	2.09

$$\sigma = \frac{\alpha \eta c}{4\pi} \tag{5.8}$$

$$L = \frac{\text{Im}(\varepsilon)}{\text{Re}(\varepsilon)^2 + \text{Im}(\varepsilon)^2} \tag{5.9}$$

From Figure 5.11a, we observe that the static value of refractive index increases on alloying, which is in direct relation with the real part of dielectric tensor. The increment in high frequency dielectric constant (real part of dielectric tensor) indicates more effective screening of electron-hole interactions without phonon contribution in comparison to pristine. This increment is due to reduction in band gap on alloying in comparison to pristine $Cs_2AgInCl_6$. The value of refractive index increases and has a maximum peak at first transition energy (for transition of an electron from VB to CB). The maxima are shifted to lower values of energies, indicating the transition will occur at lower energies. There is an abnormal behavior in the case of Co(III) substitutional alloying, which is due to the indirect nature of the band gap. In this case, there will be large phonon scattering. Figure 5.11b shows the extinction coefficient variation with photon energy. It is a measure of absorption in materials. The smaller values of extinction coefficient indicate weaker absorption in the mixed sublattices at lower energies. Further, the values of reflectivity in these materials are smaller, that suggest their usage in transparent coat-

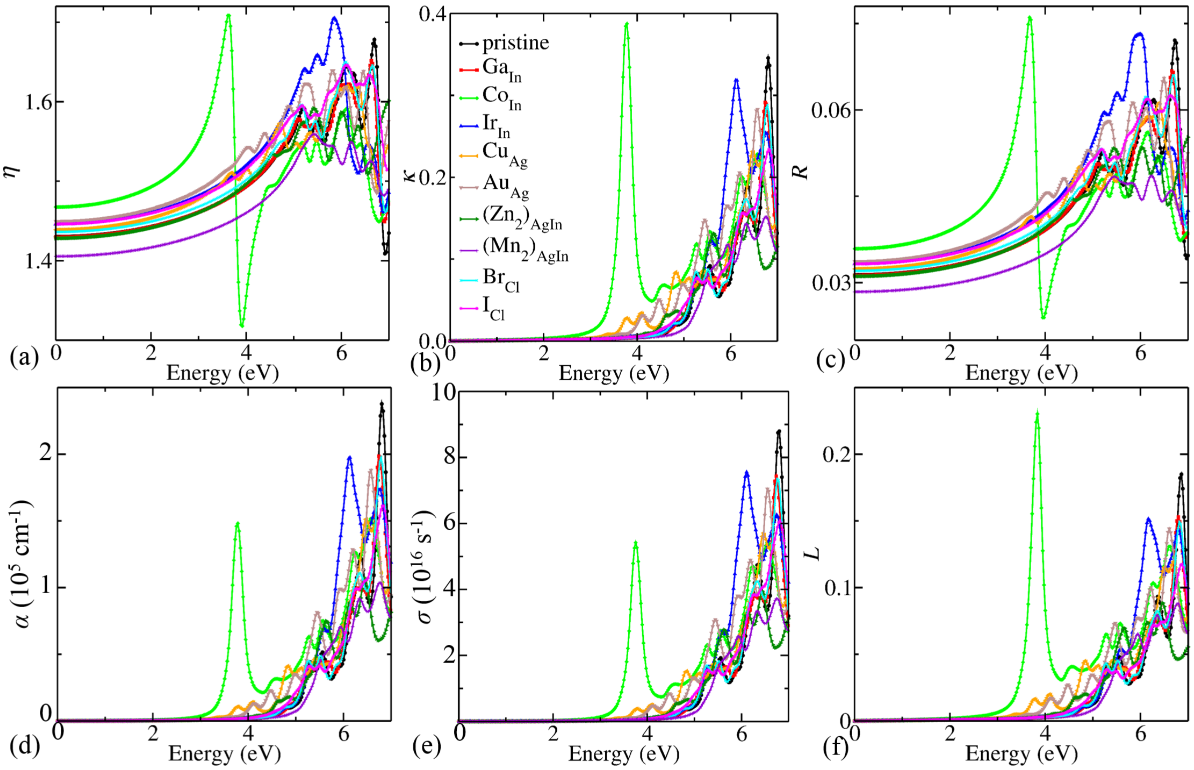

Figure 5.11: Optical properties of (un)mixed $Cs_2AgInCl_6$: (a) refractive index (η), (b) extinction coefficient (κ), (c) reflectivity (R), (d) absorption coefficient (α), (e) optical conductivity (σ), and (f) energy loss spectrum (L) using G_0W_0@HSE06.

ings (see Figure 5.11c). The peaks of the absorption coefficient and optical conductivity lie at the same values as that of the imaginary part of dielectric tensor (see Figure 5.11d and 5.11e). The absorption coefficient lies at lower energies in comparison to pristine, which implies that alloyed systems can absorb visible light of the solar spectrum. It is of the order $\sim 10^4$ cm^{-1} in lower energy region for the mixed sublattices. The optical conductivity behaves similar to the absorption coefficient. Figure 5.11f shows the loss spectrum function, which indicates the behavior of fast moving electrons, i.e., lose energy while passing through the material. The sharp peak in loss spectrum indicates the abrupt decrement in reflectivity spectrum for these materials.

5.4 Conclusions

In conclusion, we have investigated the role of metals M(I), M(II), M(III) and halogen X in $Cs_2AgInCl_6$ with mixed sublattices for inducing the visible light response by tuning its electronic properties, using state-of-the-art DFT and beyond DFT methods. We have found that the Goldschmidt tolerance factor and octahedral factor lie in the suitable range to form stable perovskite structure. The decomposition energy of all the mixed sublattices is negative with respect to the binary decomposition, indicating the alloyed systems will not decompose into their binary precursors and thus, are thermodynamically stable. However, Co(II), Ni(II), and Cu(II) are thermodynamically unstable and could decompose into ternary compounds. We have observed that SOC effect is negligible in the double perovskite $Cs_2AgInCl_6$ as it does not contain any heavy element like Lead (Pb) and Bismuth (Bi). Many partially substituted configurations help to tune the band gap, thereby increasing the absorption. We have inferred that the sublattices with Cu(I) and Au(I) at the Ag site, Ir(III) at the In site, Zn(II) at the Ag and In site simultaneously, Mn(II) at the Ag and In site simultaneously, and Br and I substitutions at the Cl site have tuned the band gap in the visible region. Hence, these can be considered as the most promising candidates for various optoelectronic devices, viz., tandem solar cells, LEDs, photodetectors, and photocatalysts.

CHAPTER 6

Optoelectronic properties of chalcogenide perovskites by many-body perturbation theory

6.1 Introduction

Inorganic-organic (IO) hybrid halide perovskites have emerged as an efficient compound semiconductor alternative to conventional materials used in photovoltaics [27, 186, 15, 28, 232]. The power conversion efficiency (PCE) of a solar cell based on IO hybrid perovskites has increased from 3.8% to 25.5% in the past decade [27, 28]. Nevertheless, the concerns regarding the long term stability and toxicity of lead restrict the commercialization of these perovskites [233, 225]. In pursuit of alternative materials having similar kind of optoelectronic properties, chalcogenide perovskites have been investigated in past few years. Sun *et al.* [234] first theoretically reported the optoelectronic properties of chalcogenide perovskites, which can be utilized in solar cells. Subsequently, other theoretical studies have also characterized different chalcogenide perovskites for a high solar cell efficiency and photoelectrochemical water splitting [235, 236, 237, 238, 239]. Many chalcogenide perovskites such as $AZrS_3$ (A = Ca, Sr, Ba), have been synthesized experimentally as well [235, 2, 3, 50, 49, 240, 241, 242], which are stable and consist of earth-abundant non-toxic elements. These chalcogenide perovskites have a high optical absorption, optimal photoluminescence, and good charge carrier mobility, which suggest the possibility of their usage in various optoelectronic devices [232, 49, 243, 244].

Zr-based chalcogenide perovskites contain the d-orbital character, wherein the 4d states are less localized than 3d states, resulting in a large absorption coefficient and a small effective mass of the charge carriers in these compounds [234]. Therefore, many experimental and theoretical studies have been performed on Zr-based chalcogenide perovskites ($AZrS_3$, where A is alkaline earth metal).

Note that the charge separation in a solar cell gets hugely influenced by the formation of excitons. Therefore, the operation mechanism of a solar cell highly depends on it, as these excitons thermally dissociate into free electrons and holes, giving rise to the required free-charge transport. However, currently, because of the huge computational cost, any detailed study with adequate accuracy of the excitonic properties is not very well-known. Therefore, it is of profound interest to employ advanced theoretical methodologies for an accurate understanding of the excitonic properties that will sufficiently correlate with the experimental studies to disentangle the scientific insights of excitons. Despite several theoretical studies on the chalcogenide perovskites, investigations of the optical properties using the excited-state methods remain unexplored. In view of this, presumably for the first time, we have reported the excitonic properties of the chalcogenide perovskites.

In this chapter, we did a systematic study of electronic and optical properties of chalcogenide perovskites $AZrS_3$ (A = Ca, Sr, Ba) using ground- and excited-state methods. First, we have employed density functional theory (DFT) [54, 55] with a semi-local exchange-correlation (ϵ_{xc}) functional PBE [59] to optimize the crystal structures. To study the electronic structure, we calculated atom-projected electronic partial density of states (pDOS) using hybrid ϵ_{xc} functional HSE06 [61]. Subsequently, we determined the optical properties using an excited-state method, specifically, many-body perturbation theory (MBPT). The Bethe-Salpeter equation (BSE) [65, 66] was solved to get the electronic contribution to a dielectric function on top of a single-shot G_0W_0@PBE [63, 139]. Further, to investigate the ionic contribution to dielectric function, density functional perturbation theory (DFPT) was used. Finally, using the quasiparticle (QP) band gap and optical properties, the maximum theoretical photoconversion efficiency has been determined by a calculation of the spectroscopic limited maximum efficiency (SLME) [245] metric.

6.2 Computational methods

The DFT [54, 55] calculations were performed as implemented in the Vienna *ab initio* simulation package (VASP) [140, 141]. The ion-electron interactions in all the elemental constituents were described using projector-augmented wave (PAW) pseudopotentials [141, 142]. The PAW pseudopotentials with the valence states $3s^23p^64s^2$, $4s^24p^65s^2$, $5s^25p^66s^2$, $4s^24p^65s^24d^2$, and $3s^23p^4$ were considered for Ca, Sr, Ba, Zr, and S, respectively. All the structures were opti-

Table 6.1: Band gap (in eV) of $CaZrS_3$, $\alpha-SrZrS_3$, $\beta-SrZrS_3$, and $BaZrS_3$ using the PBE ϵ_{xc} functional

Configurations	Without SOC	With SOC
$CaZrS_3$	1.24	1.22
$\alpha-SrZrS_3$	0.60	0.59
$\beta-SrZrS_3$	1.22	1.19
$BaZrS_3$	1.06	1.01

mized using a generalized gradient approximation, namely, the PBE [59] ϵ_{xc} functional, until the forces were smaller than 0.001 eV/Å. The electronic self-consistency loop convergence was set to 0.001 meV, and the kinetic energy cutoff was set to 500 eV for the plane wave basis set expansion. A k-mesh of $7 \times 7 \times 5$ was used for Brillouin zone integration, which was generated using the Monkhorst–Pack [75] scheme. The effective mass was calculated by SUMO [246] using a parabolic fitting of the band edges. The advanced hybrid ϵ_{xc} functional HSE06 [61] was used for a better estimation of the band gap. Note that spin–orbit coupling (SOC) has not been taken into account because it negligibly affects the electronic structure of considered chalcogenide perovskites. The band gap is changed by a small amount (on the second decimal place), which can be seen from Table 6.1. Also, the band gap remains direct at the same high-symmetry k-point Γ on including the SOC. In order to determine optical properties, Bethe-Salpeter equation (BSE) [65, 66] was solved on top of single-shot GW [63, 139] (G_0W_0) calculations. The initial step for the G_0W_0 calculation was performed by the PBE ϵ_{xc} functional. The polarizability calculations were carried out on a grid of 50 frequency points.

Table 6.2: Band gap (in eV) of $CaZrS_3$, $\alpha-SrZrS_3$, $\beta-SrZrS_3$, and $BaZrS_3$ using G_0W_0@PBE with different number of bands

Total number of bands	$CaZrS_3$	$\alpha-SrZrS_3$	$\beta-SrZrS_3$	$BaZrS_3$
320	2.39	1.63	2.42	2.20
480	2.32	1.60	2.35	2.12
640	2.29	1.60	2.32	2.10
720	2.29	1.60	2.32	2.10
800	2.30	1.61	2.32	2.09

The number of unoccupied bands was set to 8 times the number of occupied orbitals (for the convergence of empty states, see Table 6.2). The number of occupied bands is 80, whereas the number of unoccupied bands is set to be 640. A Γ-centered $3 \times 3 \times 2$ k-mesh was used, for BSE calculations. To construct the electron–hole kernel for BSE calculations, 24 occupied and 24 unoccupied states were used. The convergence for the same was determined by calculating the imaginary part of the electronic dielectric function, which is shown in Figure 6.1. To check the convergence with respect to the Brillouin zone sampling, model-BSE (mBSE) [247] was done. In mBSE, the dielectric function is replaced by a model local function given below:

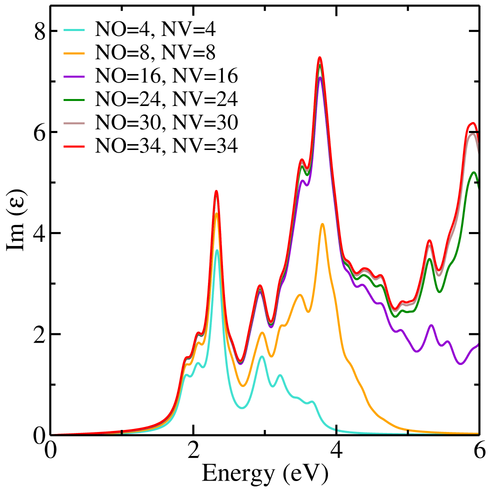

Figure 6.1: Imaginary part of the electronic dielectric function with light polarization perpendicular to c-axis (ε_{xx}) for $BaZrS_3$ with different number of valence (NO) and conduction bands (NV) used in electron-hole interaction kernel.

$$\varepsilon^{-1}_{\mathbf{G},\mathbf{G}}(\mathbf{q}) = 1 - (1 - \varepsilon^{-1}_{\infty})\exp\left(-\frac{|\mathbf{q}+\mathbf{G}|^2}{4\lambda^2}\right) \tag{6.1}$$

where ε_{∞} is the static ion-clamped dielectric function in high frequency limit calculated using G_0W_0@PBE. λ is the screening length parameter, determined by fitting the ε^{-1} at small wave vectors ($\mathbf{q}$) with respect to $|\mathbf{q}+\mathbf{G}|$ and $\mathbf{G}$ is the reciprocal lattice vector. We found that there is a negligible shift of the lower energy peak on increasing the k-mesh (see Figure 6.2). Further, we saw that the chalcogenide perovskites are optically active along all the three directions, signifying a minute anisotropy of dielectric function in chalcogenide perovskites (see Figure 6.3). The ionic contribution to the dielectric function was calculated using DFPT with a $7\times7\times5$ k-mesh generated using a Monkhorst–Pack scheme.

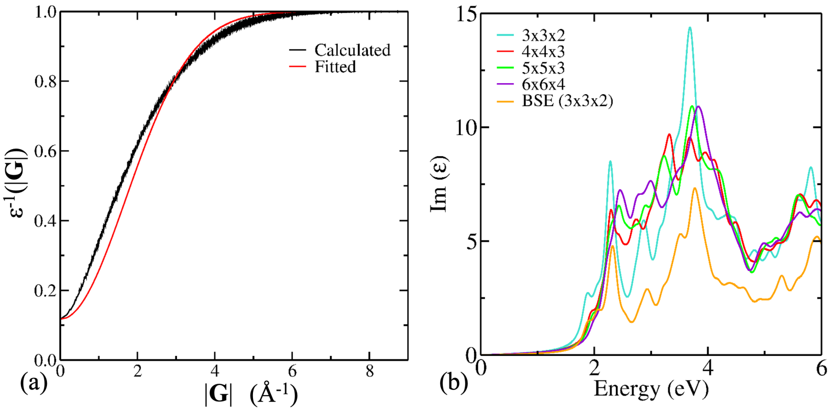

Figure 6.2: (a) Model fitting for model-BSE (mBSE). (b) Spatially average imaginary [Im (ε)] part of the dielectric function for BaZrS$_3$ with different k-mesh using mBSE. Imaginary part using GW-BSE is shown for reference by orange color. Calculated values of inverse of the static ion-clamped dielectric function $\varepsilon_{\infty}^{-1}$ = 0.117 and the screening length parameter λ = 1.20 are used in mBSE.

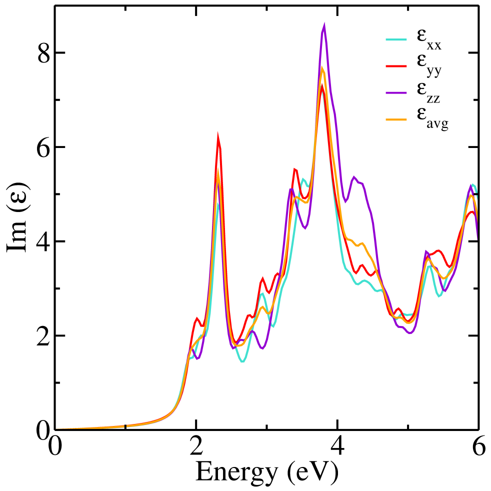

Figure 6.3: Imaginary part of electronic dielectric function for BaZrS$_3$ with light polarization along all three lattice vectors. For other chalcogenide perovskites as well, the minute anisotropy in dielectric function is existed.

6.3 Results and discussion

6.3.1 Electronic structure

Here, we considered the distorted orthorhombic phase of chalcogenide perovskites AZrS$_3$ (A = Ca, Sr, Ba) having the space group $Pnma$ [2] (see Figure 6.4a). In addition, we considered the needle-like phase of $SrZrS_3$ (see Figure 6.4b), since the same has been found in two crystallized phases ($\alpha-$phase, which is needle-like and β-phase, which is a distorted-perovskite phase) [3]. The lattice parameters of the optimized structures calculated using PBE ϵ_{xc} functional are given in Table 6.3. These are in close agreement with previous experimental results [2, 3].

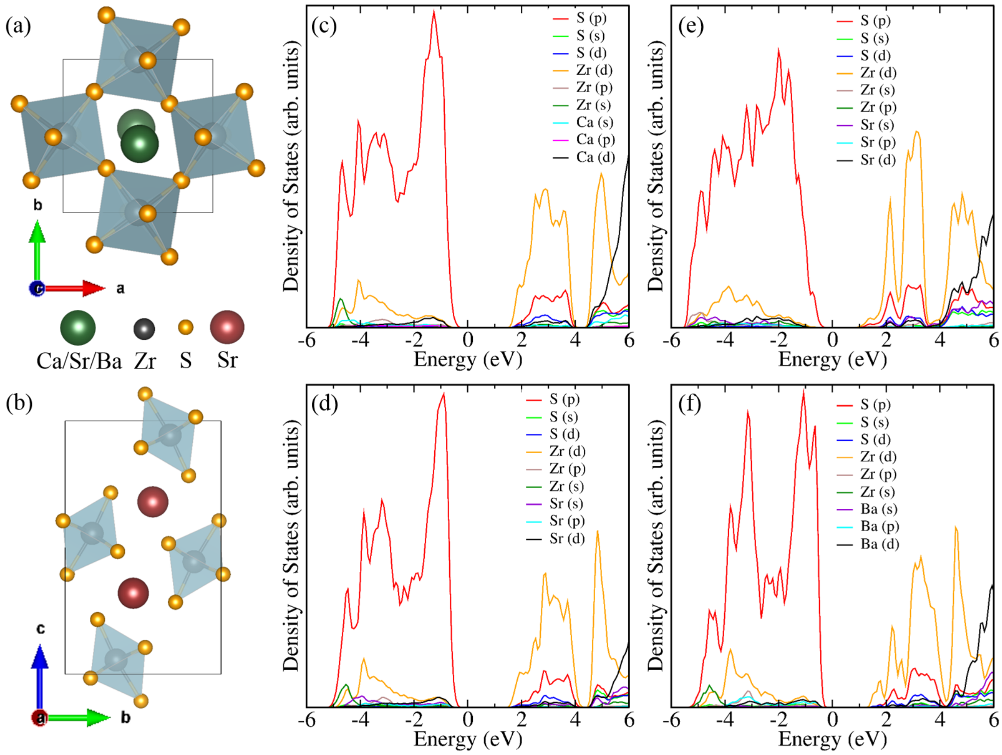

Figure 6.4: Schematic crystal structure of orthorhombic (a) $AZrS_3$ (A = Ca, Sr, Ba) in distorted phase and (b) $\alpha-SrZrS_3$ in needle-like phase. Electronic pDOS of (c) $CaZrS_3$, (d) $\beta-SrZrS_3$, (e) $\alpha-SrZrS_3$, and (f) $BaZrS_3$ using HSE06 ϵ_{xc} functional.

We calculated the electronic pDOS of the aforementioned configurations using the HSE06 ϵ_{xc} functional as shown in Figure 6.4c-f. The valence band maximum (VBM) is mostly contributed by S 3p orbitals, whereas the conduction band minimum (CBm) is mainly from Zr 4d orbitals. The rest of the orbitals have a small contribution at VBM and CBm. The peaks in pDOS are narrow and sharper at the VBM (see Figure 6.4c-f) in comparison to CBm, which indicates that the electronic nonradiative lifetime will be longer than that of the holes nonradiative lifetime. This is because narrow peaks in the pDOS signify a large number of carrier relaxation path, and hence, shorter carrier lifetimes [248, 249]. Further, with the change in the A-cation species, there is a shift in the CBm, which has altered the band gap. Moreover, in case of a distorted-perovskite phase, as we go down the group from Ca to Ba, the bands become more

Table 6.3: Calculated lattice parameters of $AZrS_3$ (A = Ca, Sr, Ba) perovskites. The experimental values are provided in brackets. For distorted perovskites, specifically, $CaZrS_3$, $\beta-SrZrS_3$, and $BaZrS_3$, the experimental values are from Ref [2]. For $\alpha-SrZrS_3$, the experimental values are from Ref [3]

Configurations	a (Å)	b (Å)	c (Å)
$CaZrS_3$	6.56 (6.54)	7.06 (7.03)	9.63 (9.59)
$\alpha-SrZrS_3$	3.84 (3.83)	8.63 (8.53)	13.99 (13.92)
$\beta-SrZrS_3$	6.78 (6.74)	7.16 (7.11)	9.82 (9.77)
$BaZrS_3$	7.03 (7.03)	7.16 (7.06)	10.01 (9.98)

dispersive at the CBm (see Figure 6.5). Hence, the effective mass of the electron decreases (see Table 6.4). Contrastingly, the effective mass of hole is not affected much. We find $\alpha-SrZrS_3$ to have the smallest electron and hole effective masses. Therefore, these perovskites are expected to have a better charge carrier transport as indicated by the smaller values of effective masses.

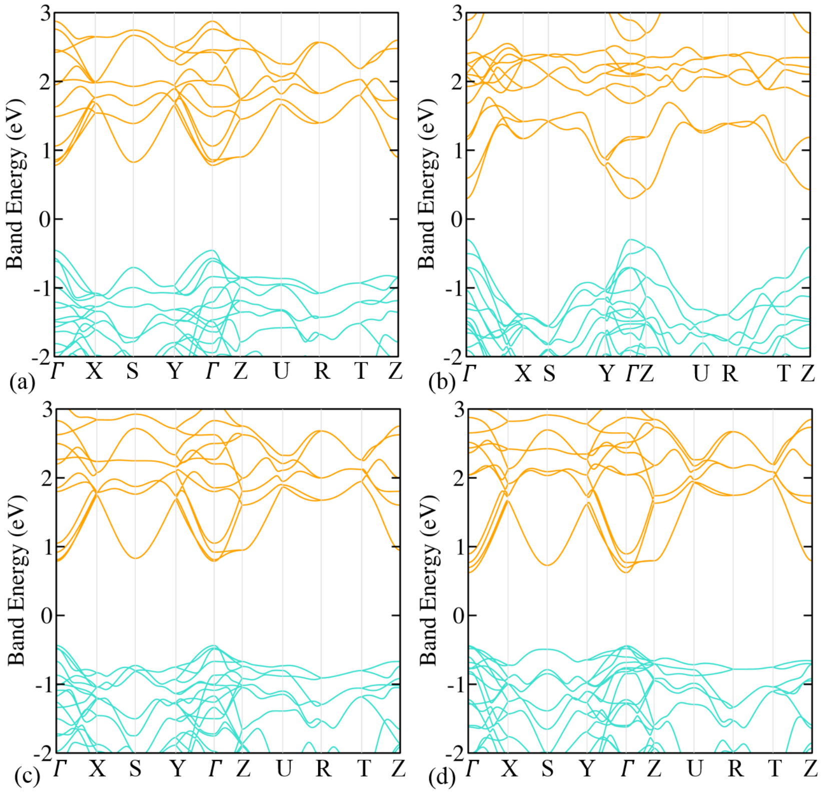

Figure 6.5: Electronic band structure of (a) $CaZrS_3$, (b) $\alpha-SrZrS_3$, (c) $\beta-SrZrS_3$, and (d) $BaZrS_3$ using PBE ϵ_{xc} functional.

Table 6.4: Effective mass of electron, hole, and reduced mass (in terms of free-electron mass m_e) of chalcogenide perovskites along a $\Gamma-Z$ high-symmetry path

Configurations	m_e^*	m_h^*	μ
$CaZrS_3$	0.503	0.588	0.271
$\alpha-SrZrS_3$	0.323	0.545	0.203
$\beta-SrZrS_3$	0.440	0.580	0.250
$BaZrS_3$	0.411	0.587	0.242

6.3.2 Optical properties

All the considered chalcogenide perovskites exhibit a direct band gap at Γ high-symmetry point, which is the desired property for an effective absorption. The band gaps are underestimated by a semi-local ϵ_{xc} functional PBE (see Table 6.5), which is due to the well-known self-interaction error. The hybrid ϵ_{xc} functional HSE06 corrects the band gaps that are well in agreement with the experimental values (see Table 6.5). Therefore, the electronic structure can be well-described by the HSE06 functional. However, the latter is less accurate in predicting the optical features of the systems [250]. Therefore, the MBPT-based GW-BSE method has been used to compute the optical response, which explicitly considers the electron-hole interaction [251]. Since the single-shot GW (G_0W_0) calculation depends on its starting point, we validated it by calculating the optical response of $BaZrS_3$, that is, the imaginary part of the complex dielectric function (see Figure 6.6). The first peak represents the optical transition corresponding to the band gap. The peak position, which is underestimated by PBE (1.06 eV), is improved by G_0W_0 on top of both the PBE and HSE06, which are at 2.10 and 2.32 eV, respectively (see Figure 6.6). However, still there is quite some overestimation with respect to the experimental

Table 6.5: Band gap (in eV) of chalcogenide perovskites

Configurations	PBE	HSE06	G_0W_0@PBE	Experimental
$CaZrS_3$	1.24	2.04	2.29	1.90 [50]
$\alpha-SrZrS_3$	0.60	1.40	1.60	1.52 [49]
$\beta-SrZrS_3$	1.22	2.05	2.32	2.05 [49]
$BaZrS_3$	1.06	1.87	2.10	1.83 [49]

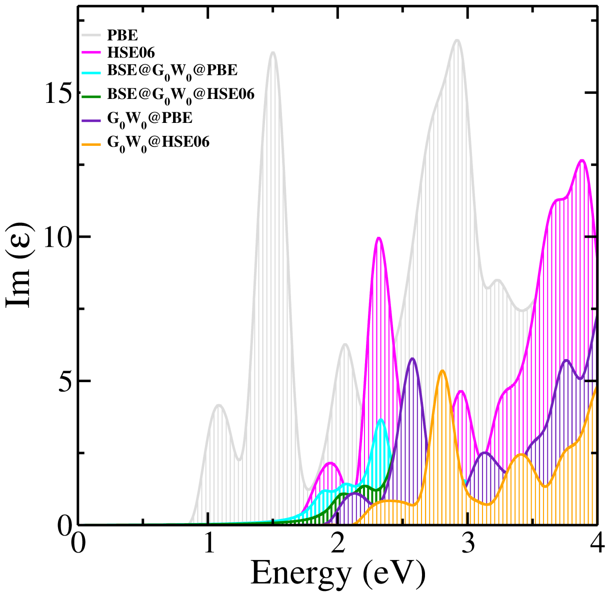

Figure 6.6: Imaginary [Im (ε)] part of the dielectric function for $BaZrS_3$ with light polarization perpendicular to c-axis (ε_{xx}), obtained using different level of theories. specifically, PBE, HSE06, G_0W_0@PBE, G_0W_0@HSE06, BSE@G_0W_0@PBE, and BSE@G_0W_0@HSE06. First peak corresponds to the band gap of $BaZrS_3$.

band gap [49]. It may appear that this disagreement between experiment and theory is ascribed because G_0W_0 is not converged yet; that is, single-shot GW is not sufficient and needs to be iterated further to reproduce the experimental value. In view of this, next we performed a self-consistent GW (scGW) by taking $CaZrS_3$ as our prototypical model system. In the considered scGW calculations, the energies are updated in both G and W [252]. We observed an increment in the band gap by 0.4 eV in comparison to the G_0W_0 to the third iteration. As observed from the optical spectra (see Figure 6.7), the onset in case of scGW is shifted by 0.4 eV in comparison to G_0W_0. Since the value of the band gap as obtained by the G_0W_0 is closer to the experimental value and the computational cost of scGW is very high ($\sim$ 3 times the G_0W_0), we did not consider scGW for further calculations. We rather conclude that the QP gap computed using G_0W_0 is overestimated in comparison to the experimental band gap, since it does not take into account the exciton binding energy. Therefore, this gap is attempted to correct by solving the BSE. For $BaZrS_3$, the peak positions obtained using BSE@G_0W_0@PBE and BSE@G_0W_0@HSE06 are at 1.88 and 2.02 eV, respectively (see Figure 6.6). The former is in close agreement with the experimental band gap, whereas the latter is overestimated. Hence, the PBE is more accurate than the HSE06 as a starting point for calculating the optical properties using the MBPT approach. The QP gaps of $AZrS_3$ (A = Ca, Sr, Ba) calculated using

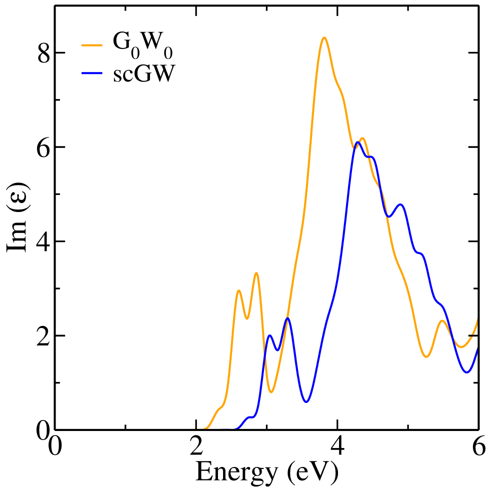

Figure 6.7: Optical spectra of $CaZrS_3$ calculated using single-shot GW (G_0W_0) and self-consistent GW (scGW) on top of PBE orbitals.

G_0W_0@PBE are provided in Table 6.5.

Figure 6.8 shows the imaginary part of the dielectric function [Im (ε)] and oscillator strength calculated using BSE@G_0W_0@PBE. In the same figure, Im (ε) calculated using G_0W_0@PBE is also shown. The exciton binding energy (E_B) can be computed from this figure, as the E_B is the difference between QP band gap (G_0W_0@PBE peak position) and optical band gap (BSE@G_0W_0@PBE peak position). Hence, from Figure 6.8, the E_B of the first bright exciton for $CaZrS_3$, $\alpha-$SrZrS$_3$, $\beta-$SrZrS$_3$ and $BaZrS_3$ are 0.23, 0.54, 0.25, and 0.21 eV, respectively. As per the BSE eigenvalue analysis, we found that a dark exciton (optically inactive) also exists in case of $BaZrS_3$ below the bright exciton. Moreover, several dark excitons exist in the case of $\alpha-$SrZrS$_3$. The E_B for the lowest energetic dark exciton is 1.53 and 0.22 eV for $\alpha-$SrZrS$_3$ and $BaZrS_3$, respectively. Furthermore, the oscillator strength for all the considered perovskites is mainly distributed within the spectral window of 2–4 eV and matches well with the excitonic peak positions (see Figure 6.8). It signifies the high radiative recombination between electron and hole in the considered energy range. Moreover, using the exciton binding energy, dielectric function, and reduced mass, several excitonic parameters can be determined [253] such as exciton temperature (T_{exc}) and radius (r_{exc}) given in Table 6.6. The exciton temperature is determined as follows

$$T_{exc} = \frac{E_B}{k_B} \tag{6.2}$$

where E_B is the exciton binding energy and k_B is the Boltzmann constant. The exciton radius

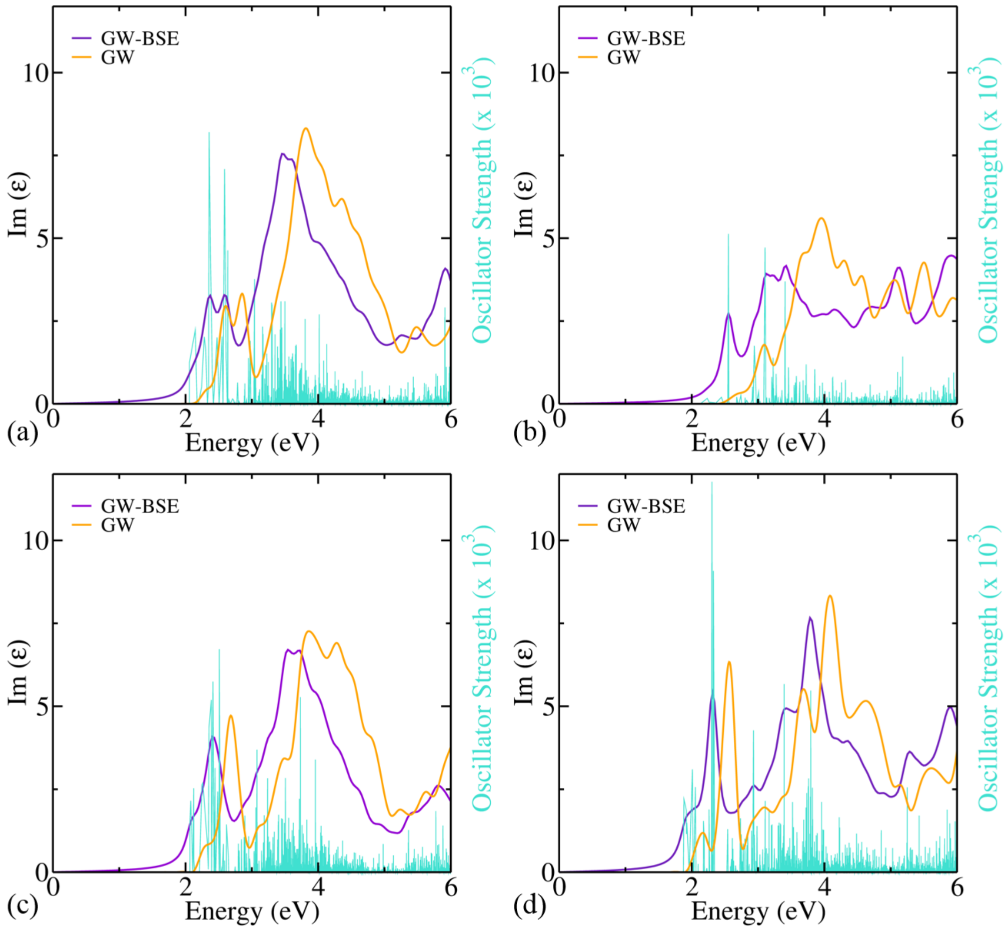

Figure 6.8: Spatially averaged imaginary [Im (ε)] part of the dielectric function for (a) $CaZrS_3$, (b) $\alpha-SrZrS_3$, (c) $\beta-SrZrS_3$, and (d) $BaZrS_3$ obtained using G_0W_0@PBE and BSE@G_0W_0@PBE. Peaks with turquoise color represent the oscillator strength.

is calculated as follows:

$$r_{exc} = \frac{m_0}{\mu} \varepsilon_{eff}\, n^2 r_{Ry} \tag{6.3}$$

where m_0 is the free electron mass, μ is the reduced mass, ε_{eff} is the static effective dielectric constant (here, the electronic dielectric constant has been taken since the ionic contribution to dielectric screening is negligible), n is the exciton energy level (n = 1 provides the smallest exciton radius) and r_{Ry} (0.0529 nm) is the Bohr radius. The exciton lifetime (τ) is inversely proportional to the probability of a wave function for electron–hole pair at zero seperation ($|\phi_n(0)|^2$). The value of $|\phi_n(0)|^2$ is determined as follows

$$|\phi_n(0)|^2 = \frac{1}{\pi (r_{exc})^3 n^3} \tag{6.4}$$

Therefore, the τ values for the considered perovskites are in the order α-$SrZrS_3$ > $BaZrS_3$ > $CaZrS_3$ > β-$SrZrS_3$.

Table 6.6: Excitonic parameters for chalcogenide perovskites

Excitonic parameters	$CaZrS_3$	α-$SrZrS_3$	β-$SrZrS_3$	$BaZrS_3$
E_B (eV)	0.23	0.54	0.25	0.21
T_{exc} (K)	2669	6267	2901	2437
r_{exc} (nm)	0.79	0.93	0.73	0.92
$\lvert\phi_n(0)\rvert^2(10^{27}m^{-3})$	0.65	0.40	0.82	0.41

The high E_B in comparison to halide perovskite [254] can be understood from the ionic contribution to dielectric screening. It has been recently shown that if the E_B calculated using a vertical transition is much greater than the energy of the longitudinal optical phonon mode (ω_{LO}), then the ionic contribution to the dielectric screening is negligible and hence, does not alter the E_B [255]. In the case of chalcogenide perovskites, $E_B \gg \hbar\omega_{LO}$, which can be seen from the ionic contribution to the dielectric function (see Figure 6.9). Therefore, the lowering of E_B by the ionic screening can be excluded. Further, by employing the Wannier-Mott approach as well, we calculated the E_B. According to this model, the E_B is related to reduced mass of the charge carriers (μ) and effective dielectric constant (ε_{eff}) as follows

$$E_B = \frac{\mu}{\varepsilon_{eff}^2} R_\infty \tag{6.5}$$

where, R_∞ is the Rydberg constant. Here, the ε_{eff} lies between the static value of dielectric constants as contributed by electrons and ions. The static electronic and ionic dielectric constants provide the upper and lower bounds to the exciton binding energy. For $CaZrS_3$, $\alpha-SrZrS_3$, $\beta-SrZrS_3$ and $BaZrS_3$, the static electronic dielectric constants are 4.06, 3.55, 3.44 and 4.19, respectively, which are calculated using the BSE. The respective static ionic dielectric constants are 57.07, 20.86, 74.51, and 99.74 calculated using DFPT (see Figure 6.9). For

Table 6.7: Upper and lower bounds on exciton binding energy E_B for chalcogenide perovskites

Configurations	Upper bound (eV)	Lower bound (meV)
$CaZrS_3$	0.22	1.13
$\alpha-SrZrS_3$	0.22	6.35
$\beta-SrZrS_3$	0.29	0.61
$BaZrS_3$	0.19	0.33

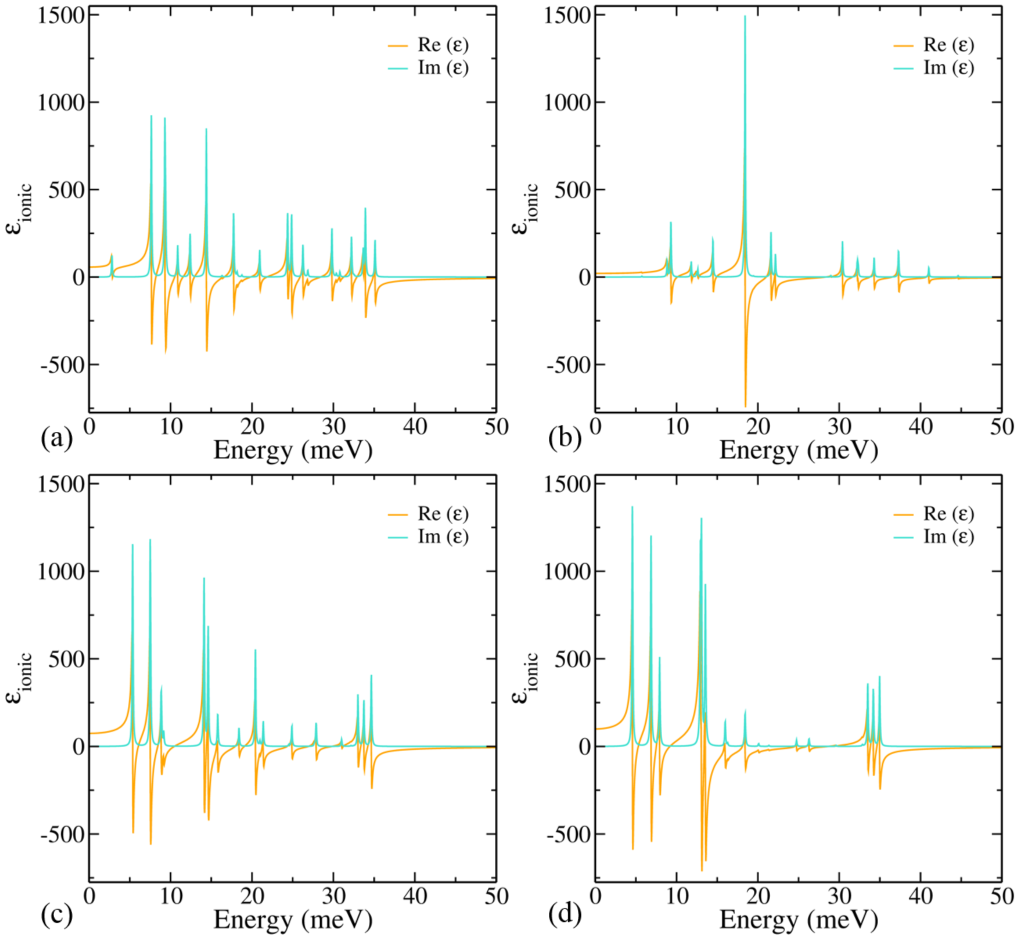

Figure 6.9: Ionic contribution to the dielectric function for (a) $CaZrS_3$, (b) $\alpha-SrZrS_3$, (c) $\beta-SrZrS_3$, and (d) $BaZrS_3$ obtained using DFPT.

$BaZrS_3$, the calculated value of the static ionic dielectric constant is in close agreement with that of previous experimental results [256]. From the reduced mass (provided in Table 6.4), and the static dielectric constants, we determined the upper and lower bounds of E_B using Equation 6.5, which are listed in Table 6.7 (also shown in Figure 6.10). The upper bounds are in good agreement with the E_B calculated by taking the difference of GW and BSE peak positions, except for $\alpha-SrZrS_3$. Thus, the electronic contribution is more prominent than the ionic contribution in dielectric screening for chalcogenide perovskites.

6.3.3 Polaronic effects

Further, we determined the electron–phonon coupling using the Fröhlich model [257, 258]. In this model, the electron moving through the lattice interacts with the polar optical phonons via

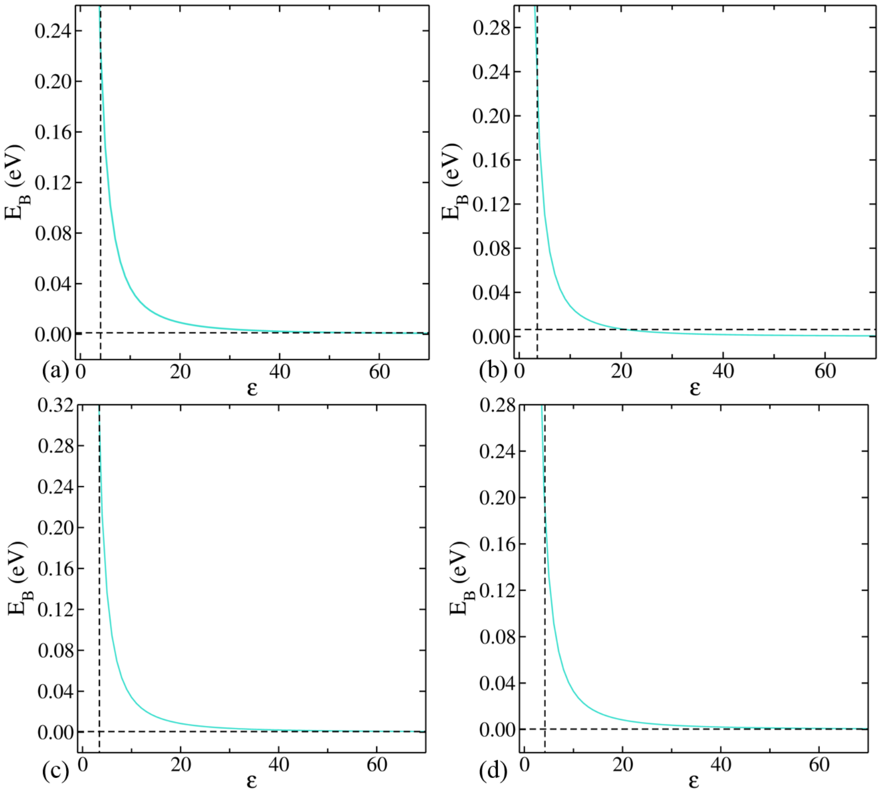

Figure 6.10: Exciton binding energy (E_B) of (a) $CaZrS_3$, (b) $\alpha-SrZrS_3$, (c) $\beta-SrZrS_3$, and (d) $BaZrS_3$, as a function of dielectric constant. The intersection of the curve with vertical dashed line defines the upper bound obtained using the static electronic dielectric constant (at high frequency) and horizontal dashed line defines the lower bound obtained by the static ionic dielectric constant (at low frequency).

Fröhlich parameter α, given by

$$\alpha = \left(\frac{1}{\varepsilon_\infty} - \frac{1}{\varepsilon_{\text{static}}}\right)\sqrt{\frac{R_\infty}{ch\omega_{\text{LO}}}}\sqrt{\frac{m^*}{m_e}} \tag{6.6}$$

where ε_∞ and $\varepsilon_{\text{static}}$ are the static electronic and ionic dielectric constants, respectively. h is Planck's constant and c is the speed of light. The characteristic frequency ω_{LO} is determined from the multiple phonon branches using athermal 'B' scheme of Hellwarth *et al.* [259] The calculated values of α are provided in Table 6.8. From these, the reduction in the QP gap attributed to polaron formation can be determined using the following relation for lowering of QP energy of the electron and hole [255, 260]:

$$E_p = (-\alpha - 0.0123\alpha^2)\hbar\omega_{\text{LO}} \tag{6.7}$$

where, E_p is the polaron energy. For $CaZrS_3$, $\alpha-SrZrS_3$, $\beta-SrZrS_3$, and $BaZrS_3$, the QP gap is lowered by 0.24, 0.25, 0.27, and 0.21 eV, respectively. On comparing these values with E_B,

Table 6.8: Electron-phonon coupling parameters for chalcogenide perovskites

Configurations	ω_{LO} (cm^{-1})	α_{e}	α_{h}
$CaZrS_3$	142.03	4.51	8.29
$\alpha-SrZrS_3$	152.74	3.56	8.49
$\beta-SrZrS_3$	117.86	5.61	11.1
$BaZrS_3$	107.51	4.68	9.53

Table 6.9: Polaron mobilities (μ) of $CaZrS_3$, $\alpha-SrZrS_3$, $\beta-SrZrS_3$, and $BaZrS_3$ at $T = 300$ K

Configurations	μ_{e} (cm^2/Vs)	μ_{h} (cm^2/Vs)
$CaZrS_3$	8.16	5.96
$\alpha-SrZrS_3$	18.77	6.81
$\beta-SrZrS_3$	6.84	3.76
$BaZrS_3$	11.35	5.58

we infer that, except for $\alpha-SrZrS_3$ and $BaZrS_3$, the charge-separated polaronic state is more stable than the bound exciton. For $BaZrS_3$, both states are comparable, whereas excitonic state is more stable in $\alpha-SrZrS_3$. Furthermore, at temperature T, the Hellwarth polaron mobility can be determined from the static dielectric constants, effective mass, and optical phonon frequency [258]. The computed polaron mobilities are given in Table 6.9.

6.3.4 Theoretical efficiency

We observed that the $AZrS_3$ (A = Ca, Sr, Ba) perovskites exhibit a large absorption coefficient and direct band gap in the visible region. These two make them interesting materials for photovoltaic applications. Therefore, we calculated the spectroscopic limited maximum efficiency (SLME) [245, 261], which has been proved to be a good metric to determine the maximum efficiency that an absorber material can reach in a single-junction solar cell. SLME is an improved version of Shockley and Queisser (SQ) efficiency [262], as it takes into account the nature of the band gap, the shape of the absorption spectra and the material-dependent nonradiative recombination losses, in addition to the band gap. The standard solar spectrum, material's band gap and the absorption coefficient are given as inputs for the SLME calculation. Figure 6.11 shows the calculated SLME of $AZrS_3$ (A = Ca, Sr, Ba). Except for $\alpha-SrZrS_3$, the SLME

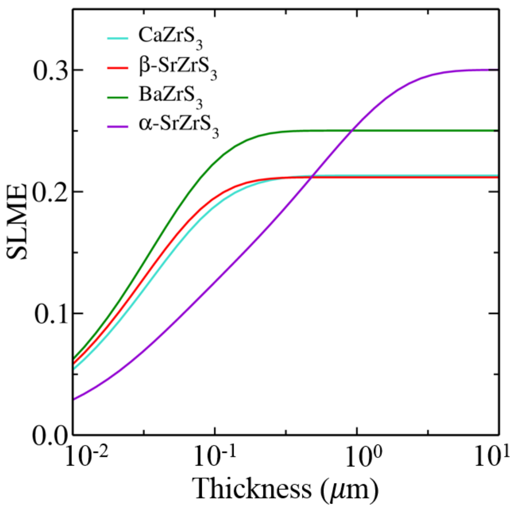

Figure 6.11: Spectroscopic limited maximum efficiency of AZrS$_3$ (A = Ca, Sr, and Ba).

becomes constant for a layer thickness greater than 1 μm. $\alpha-$SrZrS$_3$ requires a thicker absorption layer ($\sim$10 μm) for the maximum efficiency. This is because the absorption onset in the case of $\alpha-$SrZrS$_3$ is at a larger value than the band gap. SLME values at 1 μm absorber layer thickness are 21.33%, 25.45%, 21.19%, and 25.02% for CaZrS$_3$, $\alpha-$SrZrS$_3$, $\beta-$SrZrS$_3$ and BaZrS$_3$, respectively (see Figure 6.11). The theoretically predicted SLME of BaZrS$_3$ (25.02%) is in good agreement with previously reported theoretical efficiency ($\sim$25% at 1 μm thickness) [235]. These values of SLME are encouraging for their photovoltaic applications.

6.4 Conclusions

In conclusion, we have determined the electronic and optical properties of chalcogenide perovskites AZrS$_3$ (A = Ca, Sr, Ba) by state-of-the-art ground- and excited-state methods. The effective mass of the electron has been observed as decreasing down the group from Ca to Sr for distorted-perovskite phase, thereby enhancing the charge carrier transport. Further, the carrier nonradiative lifetime is found to be shorter for holes in comparison to the electrons. The optical band gap is well-reproduced by solving the Bethe-Salpeter equation (BSE). The exciton binding energies for CaZrS$_3$, $\alpha-$SrZrS$_3$, $\beta-$SrZrS$_3$, and BaZrS$_3$ are computed as 0.23, 0.54, 0.25, and 0.21 eV, respectively. In addition, by calculating the electron–phonon coupling parameters, we have observed that the charge-separated polaronic state is more stable than the bound exciton for CaZrS$_3$ and $\beta-$SrZrS$_3$. We also report a negligible ionic contribution to the effective dielectric screening that determines the exciton binding energy. Finally, the calculated spectroscopic limited maximum efficiency (SLME) suggests their usage in photovoltaics.

CHAPTER 7

Epilogue and outlook

Perovskites (ABX_3 compound, where A and B are cations and X is an anion) are a versatile family of materials exhibiting a vast range of properties, including the photovoltaic effect, photocatalytic effect, ferroelectricity, piezoelectricity, and superconductivity. These functionalities are mainly controlled by the BX_6 octahedra. Therefore, by substituting different cations at the B-site or anions at the X-site, electronic and optical properties of these materials can be tuned. Moreover, the A-site substitution can fine-tune the aforementioned properties. This tunable option opens up the ability to control the stability, band gap, exciton binding energy, mobility, and defect tolerance, which is crucial for the efficient photovoltaic devices and photocatalysts.

Oxide perovskites such as $SrTiO_3$ and $CaTiO_3$ are fascinating materials for photocatalysis because of their high thermal stability, excellent resistance to photocorrosion, appropriate band-edge positions for reduction and oxidation of a desired compound, non-toxicity, and low cost. However, their typical wide band gap (>3 eV) impede the photocatalytic performance. The intrinsic and extrinsic point defects can make them visible light responsive materials. These defects not only reduce the band gap but also ameliorate the photocatalytic efficiency by suppressing the recombination of photogenerated charges. In this thesis work, we have explored the role of point defects in $SrTiO_3$ and $CaTiO_3$ to enhance their optical absorption and photocatalytic performance using state-of-the-art first-principles density functional approach. The band gap of $SrTiO_3$ is tailored by incorporating the foreign impurities in its crystal lattice. Firstly, the stability of different doped $SrTiO_3$ is determined as a function of temperature, pressure and Fermi energy using hybrid density functional theory (DFT) in combination with *ab initio* atomistic thermodynamics. This is done by calculating and comparing the defect formation energy of different configurations. The substitution of nonmetal at the O-site and metal at the Sr-site is found to be the most stable for most of the environmental growth conditions. Subsequently, the electronic structure is investigated to probe the defect states. In the case of monodoping, generally, either deep defect states are appeared or the band edge is altered by a large amount, whereas shallow levels are found in the case of codoping. Furthermore, the optical properties are determined using hybrid DFT and GW approach. The light absorption is enhanced in most of the cases via band tailing or shift in the absorption peak. The usage of various defect configurations in photocatalytic water splitting is further determined by band-edge alignment and mobility calculations. By comparing various factors, it is found that $Mn_{Sr}N_O$ (codoping of Mn at the Sr-site and N at the O-site in $SrTiO_3$) and $Mn_{Ti}S_O$ are the most potential candidates for photocatalytic water splitting among various defect configurations.

Oxygen vacancies in oxide perovskites can enhance the photocatalytic performance for H_2 evolution and N_2 fixation reactions. We have evaluated the same in $CaTiO_3$ using hybrid DFT. In the case of O-vacancy in the CaO plane, mid gap defect states are found that can degrade the photocatalytic efficiency by increasing the non-radiative recombination rate, whereas in the case of O-vacancy in the TiO_2 plane, delocalized states are formed near the conduction band minimum. Furthermore, for hydrogenation of N_2, the Gibbs free energy of formation is calculated. Our results suggest that the O-vacancy present in the TiO_2 plane is favorable for both H_2 evolution as well as for N_2 fixation reaction as compared to pristine $CaTiO_3$ and O-vacancy in the CaO plane. These defect studies will act as a guide in the smart design of three-dimensional photocatalysts.

Lead-free halide double perovskites and chalcogenide perovskites have emerged as alternative materials to lead halide perovskites for photovoltaic applications. In replacing Pb with non-toxic elements, the band gap is altered in general, which is not suitable for photovoltaic applications. For instance, halide double perovskite $Cs_2AgInCl_6$ is non-toxic and stable, but its direct band gap (3.3 eV) is large. We have tuned the band gap of $Cs_2AgInCl_6$ by sublattice mixing for enhancing its light absorption. Since the quaternary compounds can decompose into binary or ternary compounds, firstly, the structural and thermodynamic stability of various alloyed double perovskites is determined. Subsequently, their electronic structure and optical properties are determined using hybrid DFT and GW approach, respectively. The enhanced optical absorption is shown by various sublattice mixing.

Chalcogenide perovskites exhibit suitable band gap, high absorption coefficient, and high charge carrier mobility, which make them applicable in optoelectronic devices. However, an in-depth study of their excited-state properties such as exciton binding energy, and polaronic effect was absent. Here, we have studied these properties in chalcogenide perovskites $AZrS_3$ (A

= Ca, Sr, Ba) using many-body perturbation theory approaches (viz., GW approximation and Bethe-Salpeter equation (BSE)). To capture the ionic contribution to dielectric function, density functional perturbation theory is used. Our results show that the exciton binding energy of $AZrS_3$ chalcogenide perovskites is $\sim$ 220 meV. Also, we find strong electron-phonon coupling in these perovskites such that the charged-separated polaronic state is more stable than the bound exciton. These properties along with environmentally benign nature and good stability suggest their use in various optoelectronic devices.

Overall, perovskites offer a rich plethora of future opportunities for materials development that will enable photocatalytic and photovoltaic devices that are more efficient with improved stability, but particular attention is needed to pay on the defects present in the materials developed. The role of various parameters and theoretical foundation discussed in this thesis work can guide these future endeavor to discover and develop perovskites and perovskite-inspired materials for photocatalytic and photovoltaic applications.

Bibliography

[1] John P. Perdew and Karla Schmidt. Jacob's ladder of density functional approximations for the exchange-correlation energy. *AIP Conference Proceedings*, 577:1–20, 2001.

[2] R. Lelieveld and D. J. W. IJdo. Sulphides with the $GdFeO_3$ structure. *Acta Crystallographica Section B*, 36:2223–2226, 1980.

[3] Chi-Shen Lee, Katja M. Kleinke, and Holger Kleinke. Synthesis, structure, and electronic and physical properties of the two $SrZrS_3$ modifications. *Solid State Sciences*, 7:1049 – 1054, 2005.

[4] Stefan K Estreicher. Hydrogen-related defects in crystalline semiconductors: a theorist's perspective. *Materials Science and Engineering: R: Reports*, 14:319–412, 1995.

[5] Chris G Van de Walle and Jörg Neugebauer. First-principles calculations for defects and impurities: Applications to III-nitrides. *Journal of Applied Physics*, 95:3851–3879, 2004.

[6] David A Drabold and Stefan K Estreicher. Defect theory: An armchair history. In *Theory of Defects in Semiconductors*, pages 11–28. Springer, 2007.

[7] Audrius Alkauskas and Alfredo Pasquarello. Band-edge problem in the theoretical determination of defect energy levels: The O vacancy in ZnO as a benchmark case. *Physical Review B*, 84:125206, 2011.

[8] Robert A Evarestov. *Quantum chemistry of solids: LCAO treatment of crystals and nanostructures*, volume 153. Springer Science & Business Media, 2013.

[9] Christoph Freysoldt, Blazej Grabowski, Tilmann Hickel, Jörg Neugebauer, Georg Kresse, Anderson Janotti, and Chris G. Van de Walle. First-principles calculations for point defects in solids. *Rev. Mod. Phys.*, 86:253–305, 2014.

[10] Jürgen Spitaler and Stefan K. Estreicher. Perspectives on the theory of defects. *Frontiers in Materials*, 5, 2018.

[11] Neil W. Ashcroft and N David Mermin. Solid state physics, 1976.

[12] William Hume-Rothery, W. Mabbott, Gilbert, K. M. Channel Evans, and Henry Cort Harold Carpenter. The freezing points, melting points, and solid solubility limits of the alloys of sliver and copper with the elements of the b sub-groups. *Philosophical Transactions of the Royal Society of London. Series A, Containing Papers of a Mathematical or Physical Character*, 233:1–97, 1934.

[13] Sokrates T. Pantelides. The electronic structure of impurities and other point defects in semiconductors. *Rev. Mod. Phys.*, 50:797–858, 1978.

[14] Edmund G. Seebauer and Meredith C. Kratzer. Charged point defects in semiconductors. *Materials Science and Engineering: R: Reports*, 55:57–149, 2006.

[15] Ajay Kumar Jena, Ashish Kulkarni, and Tsutomu Miyasaka. Halide perovskite photovoltaics: Background, status, and future prospects. *Chemical Reviews*, 119:3036–3103, 2019.

[16] Henry J Snaith. Present status and future prospects of perovskite photovoltaics. *Nature Materials*, 17:372–376, 2018.

[17] Wan-Jian Yin, Baicheng Weng, Jie Ge, Qingde Sun, Zhenzhu Li, and Yanfa Yan. Oxide perovskites, double perovskites and derivatives for electrocatalysis, photocatalysis, and photovoltaics. *Energy Environ. Sci.*, 12:442–462, 2019.

[18] Sebastian F Hoefler, Gregor Trimmel, and Thomas Rath. Progress on lead-free metal halide perovskites for photovoltaic applications: a review. *Monatshefte für Chemie-Chemical Monthly*, 148:795–826, 2017.

[19] Mona Mittal, Atanu Jana, Sagar Sarkar, Priya Mahadevan, and Sameer Sapra. Size of the organic cation tunes the band gap of colloidal organolead bromide perovskite nanocrystals. *The Journal of Physical Chemistry Letters*, 7:3270–3277, 2016.

[20] Anton R Chakhmouradian and Patrick M Woodward. Celebrating 175 years of perovskite research: a tribute to roger h. mitchell. *Physics and Chemistry of Minerals*, 41:387–391, 2014.

[21] Robert LZ Hoye, Juanita Hidalgo, Robert A Jagt, Juan-Pablo Correa-Baena, Thomas Fix, and Judith L MacManus-Driscoll. The role of dimensionality on the optoelectronic properties of oxide and halide perovskites, and their halide derivatives. *Advanced Energy Materials*, page 2100499, 2021.

[22] M. A. Peña and J. L. G. Fierro. Chemical structures and performance of perovskite oxides. *Chemical Reviews*, 101:1981–2018, 2001.

[23] Fengang Zheng, Yu Xin, Wen Huang, Jinxing Zhang, Xiaofeng Wang, Mingrong Shen, Wen Dong, Liang Fang, Yongbin Bai, Xiaoqing Shen, and Jianhua Hao. Above 1% efficiency of a ferroelectric solar cell based on the $Pb(Zr,Ti)O_3$ film. *J. Mater. Chem. A*, 2:1363–1368, 2014.

[24] Riad Nechache, C Harnagea, S Li, L Cardenas, W Huang, Joyprokash Chakrabartty, and Federico Rosei. Bandgap tuning of multiferroic oxide solar cells. *Nature Photonics*, 9:61–67, 2015.

[25] A.B. Murphy, P.R.F. Barnes, L.K. Randeniya, I.C. Plumb, I.E. Grey, M.D. Horne, and J.A. Glasscock. Efficiency of solar water splitting using semiconductor electrodes. *International Journal of Hydrogen Energy*, 31:1999–2017, 2006.

[26] Nam-Gyu Park. Perovskite solar cells: an emerging photovoltaic technology. *Materials Today*, 18:65–72, 2015.

[27] Akihiro Kojima, Kenjiro Teshima, Yasuo Shirai, and Tsutomu Miyasaka. Organometal halide perovskites as visible-light sensitizers for photovoltaic cells. *Journal of the American Chemical Society*, 131:6050–6051, 2009.

[28] National renewable energy laboratory (nrel) best research-cell efficiency chart. https://www.nrel.gov/pv/cell-efficiency.html. accessed: January 26, 2021.

[29] Thomas R. Hopper, Ahhyun Jeong, Andrei A. Gorodetsky, Franziska Krieg, Maryna I. Bodnarchuk, Xiaokun Huang, Robert Lovrincic, Maksym V. Kovalenko, and Artem A.

Bakulin. Kinetic modelling of intraband carrier relaxation in bulk and nanocrystalline lead-halide perovskites. *Phys. Chem. Chem. Phys.*, 22:17605–17611, 2020.

[30] Pablo Docampo, James M Ball, Mariam Darwich, Giles E Eperon, and Henry J Snaith. Efficient organometal trihalide perovskite planar-heterojunction solar cells on flexible polymer substrates. *Nature Communications*, 4:1–6, 2013.

[31] Giles E. Eperon, Tomas Leijtens, Kevin A. Bush, Rohit Prasanna, Thomas Green, Jacob Tse-Wei Wang, David P. McMeekin, George Volonakis, Rebecca L. Milot, Richard May, Axel Palmstrom, Daniel J. Slotcavage, Rebecca A. Belisle, Jay B. Patel, Elizabeth S. Parrott, Rebecca J. Sutton, Wen Ma, Farhad Moghadam, Bert Conings, Aslihan Babayigit, Hans-Gerd Boyen, Stacey Bent, Feliciano Giustino, Laura M. Herz, Michael B. Johnston, Michael D. McGehee, and Henry J. Snaith. Perovskite-perovskite tandem photovoltaics with optimized band gaps. *Science*, 354:861–865, 2016.

[32] Pablo P. Boix, Shweta Agarwala, Teck Ming Koh, Nripan Mathews, and Subodh G. Mhaisalkar. Perovskite solar cells: Beyond methylammonium lead iodide. *The Journal of Physical Chemistry Letters*, 6:898–907, 2015.

[33] Rebecca L. Milot, Giles E. Eperon, Henry J. Snaith, Michael B. Johnston, and Laura M. Herz. Temperature-dependent charge-carrier dynamics in $CH_3NH_3PbI_3$ perovskite thin films. *Advanced Functional Materials*, 25:6218–6227, 2015.

[34] Samuel D. Stranks, Giles E. Eperon, Giulia Grancini, Christopher Menelaou, Marcelo J. P. Alcocer, Tomas Leijtens, Laura M. Herz, Annamaria Petrozza, and Henry J. Snaith. Electron-hole diffusion lengths exceeding 1 micrometer in an organometal trihalide perovskite absorber. *Science*, 342:341–344, 2013.

[35] Riley E. Brandt, Jeremy R. Poindexter, Prashun Gorai, Rachel C. Kurchin, Robert L. Z. Hoye, Lea Nienhaus, Mark W. B. Wilson, J. Alexander Polizzotti, Raimundas Sereika, Raimundas Žaltauskas, Lana C. Lee, Judith L. MacManus-Driscoll, Moungi Bawendi, Vladan Stevanović, and Tonio Buonassisi. Searching for “defect-tolerant” photovoltaic materials: Combined theoretical and experimental screening. *Chemistry of Materials*, 29:4667–4674, 2017.

[36] Ian L Braly, Dane W DeQuilettes, Luis M Pazos-Outón, Sven Burke, Mark E Ziffer, David S Ginger, and Hugh W Hillhouse. Hybrid perovskite films approaching the ra-

diative limit with over 90% photoluminescence quantum efficiency. *Nature Photonics*, 12:355–361, 2018.

[37] Zongqi Li, Yingzhi Zhao, Xi Wang, Yuchao Sun, Zhiguo Zhao, Yujing Li, Huanping Zhou, and Qi Chen. Cost analysis of perovskite tandem photovoltaics. *Joule*, 2:1559–1572, 2018.

[38] Femi Igbari, Zhao-Kui Wang, and Liang-Sheng Liao. Progress of lead-free halide double perovskites. *Advanced Energy Materials*, 9:1803150, 2019.

[39] Waqaas Rehman, David P. McMeekin, Jay B. Patel, Rebecca L. Milot, Michael B. Johnston, Henry J. Snaith, and Laura M. Herz. Photovoltaic mixed-cation lead mixed-halide perovskites: links between crystallinity, photo-stability and electronic properties. *Energy Environ. Sci.*, 10:361–369, 2017.

[40] Nakita K. Noel, Samuel D. Stranks, Antonio Abate, Christian Wehrenfennig, Simone Guarnera, Amir-Abbas Haghighirad, Aditya Sadhanala, Giles E. Eperon, Sandeep K. Pathak, Michael B. Johnston, Annamaria Petrozza, Laura M. Herz, and Henry J. Snaith. Lead-free organic–inorganic tin halide perovskites for photovoltaic applications. *Energy Environ. Sci.*, 7:3061–3068, 2014.

[41] Indira Kopacic, Bastian Friesenbichler, Sebastian F. Hoefler, Birgit Kunert, Harald Plank, Thomas Rath, and Gregor Trimmel. Enhanced performance of germanium halide perovskite solar cells through compositional engineering. *ACS Applied Energy Materials*, 1:343–347, 2018.

[42] Adam H. Slavney, Te Hu, Aaron M. Lindenberg, and Hemamala I. Karunadasa. A bismuth-halide double perovskite with long carrier recombination lifetime for photovoltaic applications. *Journal of the American Chemical Society*, 138:2138–2141, 2016.

[43] George Volonakis, Amir Abbas Haghighirad, Rebecca L. Milot, Weng H. Sio, Marina R. Filip, Bernard Wenger, Michael B. Johnston, Laura M. Herz, Henry J. Snaith, and Feliciano Giustino. $Cs_2InAgCl_6$: A new lead-free halide double perovskite with direct band gap. *The Journal of Physical Chemistry Letters*, 8:772–778, 2017.

[44] Pengfei Cheng, Tao Wu, Yajuan Li, Lei Jiang, Weiqiao Deng, and Keli Han. Combining theory and experiment in the design of a lead-free ($(CH_3NH_3)_2AgBiI_6$) double perovskite. *New J. Chem.*, 41:9598–9601, 2017.

[45] George Volonakis and Feliciano Giustino. Surface properties of lead-free halide double perovskites: Possible visible-light photo-catalysts for water splitting. *Applied Physics Letters*, 112:243901, 2018.

[46] Jiajun Luo, Xiaoming Wang, Shunran Li, Jing Liu, Yueming Guo, Guangda Niu, Li Yao, Yuhao Fu, Liang Gao, Qingshun Dong, et al. Efficient and stable emission of warm-white light from lead-free halide double perovskites. *Nature*, 563:541–545, 2018.

[47] Eric T. McClure, Molly R. Ball, Wolfgang Windl, and Patrick M. Woodward. Cs_2AgBiX_6 (X = Br, Cl): New visible light absorbing, lead-free halide perovskite semiconductors. *Chemistry of Materials*, 28:1348–1354, 2016.

[48] Liang Chu, Waqar Ahmad, Wei Liu, Jian Yang, Rui Zhang, Yan Sun, Jianping Yang, and Xing'ao Li. Lead-free halide double perovskite materials: a new superstar toward green and stable optoelectronic applications. *Nano-Micro Letters*, 11:1–18, 2019.

[49] Shanyuan Niu, Huaixun Huyan, Yang Liu, Matthew Yeung, Kevin Ye, Louis Blankemeier, Thomas Orvis, Debarghya Sarkar, David J. Singh, Rehan Kapadia, and Jayakanth Ravichandran. Bandgap control via structural and chemical tuning of transition metal perovskite chalcogenides. *Advanced Materials*, 29:1604733, 2017.

[50] Samanthe Perera, Haolei Hui, Chuan Zhao, Hongtao Xue, Fan Sun, Chenhua Deng, Nelson Gross, Chris Milleville, Xiaohong Xu, David F. Watson, Bernard Weinstein, Yi-Yang Sun, Shengbai Zhang, and Hao Zeng. Chalcogenide perovskites – an emerging class of ionic semiconductors. *Nano Energy*, 22:129 – 135, 2016.

[51] Feng Hong, Bayrammurad Saparov, Weiwei Meng, Zewen Xiao, David B. Mitzi, and Yanfa Yan. Viability of lead-free perovskites with mixed chalcogen and halogen anions for photovoltaic applications. *The Journal of Physical Chemistry C*, 120:6435–6441, 2016.

---

[52] Qingde Sun, Hangyan Chen, and Wan-Jian Yin. Do chalcogenide double perovskites work as solar cell absorbers: A first-principles study. *Chemistry of Materials*, 31:244–250, 2019.

[53] Giovanni Onida, Lucia Reining, and Angel Rubio. Electronic excitations: density-functional versus many-body green's-function approaches. *Rev. Mod. Phys.*, 74:601–659, 2002.

[54] P. Hohenberg and W. Kohn. Inhomogeneous electron gas. *Phys. Rev.*, 136:B864–B871, 1964.

[55] W. Kohn and L. J. Sham. Self-consistent equations including exchange and correlation effects. *Phys. Rev.*, 140:A1133–A1138, 1965.

[56] Nicola Marzari, Andrea Ferretti, and Chris Wolverton. Electronic-structure methods for materials design. *Nature Materials*, 20:736–749, 2021.

[57] Jörg Neugebauer and Tilmann Hickel. Density functional theory in materials science. *WIREs Computational Molecular Science*, 3:438–448, 2013.

[58] John P. Perdew and Yue Wang. Accurate and simple analytic representation of the electron-gas correlation energy. *Phys. Rev. B*, 45:13244–13249, 1992.

[59] John P. Perdew, Kieron Burke, and Matthias Ernzerhof. Generalized gradient approximation made simple. *Phys. Rev. Lett.*, 77:3865–3868, 1996.

[60] Jochen Heyd, Gustavo E. Scuseria, and Matthias Ernzerhof. Hybrid functionals based on a screened coulomb potential. *The Journal of Chemical Physics*, 118:8207–8215, 2003.

[61] Aliaksandr V. Krukau, Oleg A. Vydrov, Artur F. Izmaylov, and Gustavo E. Scuseria. Influence of the exchange screening parameter on the performance of screened hybrid functionals. *The Journal of Chemical Physics*, 125:224106, 2006.

[62] Audrius Alkauskas, Peter Broqvist, and Alfredo Pasquarello. Defect levels through hybrid density functionals: Insights and applications. *physica status solidi (b)*, 248:775–789, 2011.

[63] Lars Hedin. New method for calculating the one-particle green's function with application to the electron-gas problem. *Phys. Rev.*, 139:A796–A823, 1965.

[64] Mark S. Hybertsen and Steven G. Louie. Electron correlation in semiconductors and insulators: Band gaps and quasiparticle energies. *Phys. Rev. B*, 34:5390–5413, 1986.

[65] Stefan Albrecht, Lucia Reining, Rodolfo Del Sole, and Giovanni Onida. Ab initio calculation of excitonic effects in the optical spectra of semiconductors. *Phys. Rev. Lett.*, 80:4510–4513, 1998.

[66] Michael Rohlfing and Steven G. Louie. Electron-hole excitations in semiconductors and insulators. *Phys. Rev. Lett.*, 81:2312–2315, 1998.

[67] M. Shishkin and G. Kresse. Self-consistent GW calculations for semiconductors and insulators. *Phys. Rev. B*, 75:235102, 2007.

[68] David J. Griffiths and Darrell F. Schroeter. *Introduction to Quantum Mechanics*. Cambridge University Press, 2018.

[69] Richard M. Martin. *Electronic structure: Basic theory and practical methods*. Cambridge university press, 2004.

[70] Robert G. Parr and Weitao Yang. *Density-functional theory of atoms and molecules*. Oxford University Press, 1994.

[71] David C. Langreth and M. J. Mehl. Beyond the local-density approximation in calculations of ground-state electronic properties. *Phys. Rev. B*, 28:1809–1834, 1983.

[72] SHANG-kENG MA and KEITH A. BRUECKNER. Correlation energy of an electron gas with a slowly varying high density. *Phys. Rev.*, 165:18–31, 1968.

[73] Peter Kratzer and Jörg Neugebauer. The basics of electronic structure theory for periodic systems. *Frontiers in Chemistry*, 7:106, 2019.

[74] D. J. Chadi and Marvin L. Cohen. Special points in the brillouin zone. *Phys. Rev. B*, 8:5747–5753, 1973.

[75] Hendrik J. Monkhorst and James D. Pack. Special points for brillouin-zone integrations. *Phys. Rev. B*, 13:5188–5192, 1976.

[76] Juana Moreno and José M. Soler. Optimal meshes for integrals in real- and reciprocal-space unit cells. *Phys. Rev. B*, 45:13891–13898, 1992.

[77] M. C. Payne, M. P. Teter, D. C. Allan, T. A. Arias, and J. D. Joannopoulos. Iterative minimization techniques for ab initio total-energy calculations: molecular dynamics and conjugate gradients. *Rev. Mod. Phys.*, 64:1045–1097, 1992.

[78] D. R. Hamann, M. Schlüter, and C. Chiang. Norm-conserving pseudopotentials. *Phys. Rev. Lett.*, 43:1494–1497, 1979.

[79] David Vanderbilt. Soft self-consistent pseudopotentials in a generalized eigenvalue formalism. *Phys. Rev. B*, 41:7892–7895, 1990.

[80] Peter E Blöchl. Projector augmented-wave method. *Physical review B*, 50:17953, 1994.

[81] O. Krogh Andersen. Linear methods in band theory. *Phys. Rev. B*, 12:3060–3083, 1975.

[82] J. C. Slater. Wave functions in a periodic potential. *Phys. Rev.*, 51:846–851, 1937.

[83] Dorothea Golze, Marc Dvorak, and Patrick Rinke. The GW compendium: A practical guide to theoretical photoemission spectroscopy. *Frontiers in Chemistry*, 7:377, 2019.

[84] Richard Phillips Feynman. Forces in molecules. *Physical review*, 56:340, 1939.

[85] O. H. Nielsen and Richard M. Martin. First-principles calculation of stress. *Phys. Rev. Lett.*, 50:697–700, 1983.

[86] Jutta Rogal and Karsten Reuter. Ab initio atomistic thermodynamics for surfaces: A primer. Technical report, Max-planck-gesellschaft zur foerderung der wissenschaften ev berlin (germany . . . , 2006.

[87] Saswata Bhattacharya, Daniel Berger, Karsten Reuter, Luca M. Ghiringhelli, and Sergey V. Levchenko. Theoretical evidence for unexpected O-rich phases at corners of MgO surfaces. *Phys. Rev. Materials*, 1:071601, 2017.

[88] Donald A. McQuarrie. *Statistical Mechanics*. Harper & Row: New York, 1976.

[89] L. J. Sham and W. Kohn. One-particle properties of an inhomogeneous interacting electron gas. *Phys. Rev.*, 145:561–567, 1966.

[90] John P. Perdew, Robert G. Parr, Mel Levy, and Jose L. Balduz. Density-functional theory for fractional particle number: Derivative discontinuities of the energy. *Phys. Rev. Lett.*, 49:1691–1694, 1982.

[91] M. Shishkin and G. Kresse. Implementation and performance of the frequency-dependent GW method within the paw framework. *Phys. Rev. B*, 74:035101, 2006.

[92] Sergey V. Faleev, Mark van Schilfgaarde, and Takao Kotani. All-electron self-consistent GW approximation: Application to Si, MnO, and NiO. *Phys. Rev. Lett.*, 93:126406, 2004.

[93] Manuel Grumet, Peitao Liu, Merzuk Kaltak, Ji ří Klimeš, and Georg Kresse. Beyond the quasiparticle approximation: Fully self-consistent GW calculations. *Phys. Rev. B*, 98:155143, 2018.

[94] G. Strinati. Effects of dynamical screening on resonances at inner-shell thresholds in semiconductors. *Phys. Rev. B*, 29:5718–5726, 1984.

[95] Michael Rohlfing and Steven G. Louie. Electron-hole excitations and optical spectra from first principles. *Phys. Rev. B*, 62:4927–4944, 2000.

[96] Stefano Baroni, Stefano de Gironcoli, Andrea Dal Corso, and Paolo Giannozzi. Phonons and related crystal properties from density-functional perturbation theory. *Rev. Mod. Phys.*, 73:515–562, 2001.

[97] Xiaobo Chen, Shaohua Shen, Liejin Guo, and Samuel S. Mao. Semiconductor-based photocatalytic hydrogen generation. *Chemical Reviews*, 110:6503–6570, 2010.

[98] Chuncheng Chen, Wanhong Ma, and Jincai Zhao. Semiconductor-mediated photodegradation of pollutants under visible-light irradiation. *Chem. Soc. Rev.*, 39:4206–4219, 2010.

[99] Akihiko Kudo and Yugo Miseki. Heterogeneous photocatalyst materials for water splitting. *Chem. Soc. Rev.*, 38:253–278, 2009.

[100] Anna Kubacka, Marcos Fernández-García, and Gerardo Colón. Advanced nanoarchitectures for solar photocatalytic applications. *Chemical Reviews*, 112:1555–1614, 2012.

[101] Maidhily Manikandan, Toyokazu Tanabe, Peng Li, Shigenori Ueda, Gubbala V. Ramesh, Rajesh Kodiyath, Junjie Wang, Toru Hara, Arivuoli Dakshanamoorthy, Shinsuke Ishihara, Katsuhiko Ariga, Jinhua Ye, Naoto Umezawa, and Hideki Abe. Photocatalytic

water splitting under visible light by mixed-valence Sn_3O_4. *ACS Applied Materials & Interfaces*, 6:3790–3793, 2014.

[102] Pei Zhao, Yan Liang, Yandong Ma, Baibiao Huang, and Ying Dai. Janus chromium dichalcogenide monolayers with low carrier recombination for photocatalytic overall water-splitting under infrared light. *The Journal of Physical Chemistry C*, 123:4186–4192, 2019.

[103] Kazunari Domen, Akihiko Kudo, Takaharu Onishi, Nobuhiro Kosugi, and Haruo Kuroda. Photocatalytic decomposition of water into hydrogen and oxygen over nickel(ii) oxide-strontium titanate ($SrTiO_3$) powder. 1. structure of the catalysts. *The Journal of Physical Chemistry*, 90:292–295, 1986.

[104] S. Ahuja and T.R.N. Kutty. Nanoparticles of $SrTiO_3$ prepared by gel to crystallite conversion and their photocatalytic activity in the mineralization of phenol. *Journal of Photochemistry and Photobiology A: Chemistry*, 97:99 – 107, 1996.

[105] Katsuya Iwashina and Akihiko Kudo. Rh-doped $SrTiO_3$ photocatalyst electrode showing cathodic photocurrent for water splitting under visible-light irradiation. *Journal of the American Chemical Society*, 133:13272–13275, 2011.

[106] Qian Zhang, Yu Huang, Lifeng Xu, Jun-ji Cao, Wingkei Ho, and Shun Cheng Lee. Visible-light-active plasmonic Ag-$SrTiO_3$ nanocomposites for the degradation of no in air with high selectivity. *ACS Applied Materials & Interfaces*, 8:4165–4174, 2016.

[107] Ryo Niishiro, Shumpei Tanaka, and Akihiko Kudo. Hydrothermal-synthesized $SrTiO_3$ photocatalyst codoped with rhodium and antimony with visible-light response for sacrificial H_2 and O_2 evolution and application to overall water splitting. *Applied Catalysis B: Environmental*, 150-151:187 – 196, 2014.

[108] Huaqiao Tan, Zhao Zhao, Wan-bin Zhu, Eric N. Coker, Binsong Li, Min Zheng, Weixing Yu, Hongyou Fan, and Zaicheng Sun. Oxygen vacancy enhanced photocatalytic activity of pervoskite $SrTiO_3$. *ACS Applied Materials & Interfaces*, 6:19184–19190, 2014.

[109] Kelvin H. L. Zhang, Rui Wu, Fengzai Tang, Weiwei Li, Freddy E. Oropeza, Liang Qiao, Vlado K. Lazarov, Yingge Du, David J. Payne, Judith L. MacManus-Driscoll,

and Mark G. Blamire. Electronic structure and band alignment at the NiO and $SrTiO_3$ p-n heterojunctions. *ACS Applied Materials & Interfaces*, 9:26549–26555, 2017.

[110] Ryoko Konta, Tatsuya Ishii, Hideki Kato, and Akihiko Kudo. Photocatalytic activities of noble metal ion doped $SrTiO_3$ under visible light irradiation. *The Journal of Physical Chemistry B*, 108:8992–8995, 2004.

[111] Hsin-Chieh Chen, Chao-Wei Huang, Jeffrey C. S. Wu, and Shiang-Tai Lin. Theoretical investigation of the metal-doped $SrTiO_3$ photocatalysts for water splitting. *The Journal of Physical Chemistry C*, 116:7897–7903, 2012.

[112] Peng Liu, Jawad Nisar, Biswarup Pathak, and Rajeev Ahuja. Hybrid density functional study on $SrTiO_3$ for visible light photocatalysis. *International Journal of Hydrogen Energy*, 37:11611 – 11617, 2012.

[113] Yating Guo, Xiaowei Qiu, Hao Dong, and Xin Zhou. Trends in non-metal doping of the $SrTiO_3$ surface: a hybrid density functional study. *Phys. Chem. Chem. Phys.*, 17:21611–21621, 2015.

[114] Pakpoom Reunchan, Shuxin Ouyang, Naoto Umezawa, Hua Xu, Yuanjian Zhang, and Jinhua Ye. Theoretical design of highly active $SrTiO_3$-based photocatalysts by a codoping scheme towards solar energy utilization for hydrogen production. *J. Mater. Chem. A*, 1:4221–4227, 2013.

[115] Shuxin Ouyang, Hua Tong, Naoto Umezawa, Junyu Cao, Peng Li, Yingpu Bi, Yuanjian Zhang, and Jinhua Ye. Surface-alkalinization-induced enhancement of photocatalytic H_2 evolution over $SrTiO_3$-based photocatalysts. *Journal of the American Chemical Society*, 134:1974–1977, 2012.

[116] Ryan B. Comes, Peter V. Sushko, Steve M. Heald, Robert J. Colby, Mark E. Bowden, and Scott A. Chambers. Band-gap reduction and dopant interaction in epitaxial La,Cr Co-doped $SrTiO_3$ thin films. *Chemistry of Materials*, 26:7073–7082, 2014.

[117] Masahiro Miyauchi, Minoru Takashio, and Hiroki Tobimatsu. Photocatalytic activity of $SrTiO_3$ codoped with nitrogen and lanthanum under visible light illumination. *Langmuir*, 20:232–236, 2004.

[118] Wei Chen, Heng Liu, Xiying Li, Shuang Liu, Li Gao, Liqun Mao, Zeyun Fan, Wenfeng Shangguan, Wenjian Fang, and Yongsheng Liu. Polymerizable complex synthesis of $SrTiO_3$:(Cr/Ta) photocatalysts to improve photocatalytic water splitting activity under visible light. *Applied Catalysis B: Environmental*, 192:145 – 151, 2016.

[119] Ryo Niishiro, Hideki Kato, and Akihiko Kudo. Nickel and either tantalum or niobium-codoped TiO_2 and $SrTiO_3$ photocatalysts with visible-light response for H_2 or O_2 evolution from aqueous solutions. *Phys. Chem. Chem. Phys.*, 7:2241–2245, 2005.

[120] He Yu, Shuxin Ouyang, Shicheng Yan, Zhaosheng Li, Tao Yu, and Zhigang Zou. Sol–gel hydrothermal synthesis of visible-light-driven Cr-doped $SrTiO_3$ for efficient hydrogen production. *J. Mater. Chem.*, 21:11347–11351, 2011.

[121] S. Kawasaki, K. Nakatsuji, J. Yoshinobu, F. Komori, R. Takahashi, M. Lippmaa, K. Mase, and A. Kudo. Epitaxial Rh-doped $SrTiO_3$ thin film photocathode for water splitting under visible light irradiation. *Applied Physics Letters*, 101:033910, 2012.

[122] Wei Wei, Ying Dai, Meng Guo, Lin Yu, and Baibiao Huang. Density functional characterization of the electronic structure and optical properties of N-doped, La-doped, and N/La-codoped $SrTiO_3$. *The Journal of Physical Chemistry C*, 113:15046–15050, 2009.

[123] Wei Wei, Ying Dai, Meng Guo, Lin Yu, Hao Jin, Shenghao Han, and Baibiao Huang. Codoping synergistic effects in N-doped $SrTiO_3$ for higher energy conversion efficiency. *Phys. Chem. Chem. Phys.*, 12:7612–7619, 2010.

[124] Yanqin Gai, Jingbo Li, Shu-Shen Li, Jian-Bai Xia, and Su-Huai Wei. Design of narrow-gap TiO_2: A passivated codoping approach for enhanced photoelectrochemical activity. *Phys. Rev. Lett.*, 102:036402, 2009.

[125] Brindaban Modak and Swapan K. Ghosh. Role of f in improving the photocatalytic activity of Rh-doped $SrTiO_3$. *The Journal of Physical Chemistry C*, 119:7215–7224, 2015.

[126] Brindaban Modak and Swapan K. Ghosh. Enhancement of visible light photocatalytic activity of $SrTiO_3$: A hybrid density functional study. *The Journal of Physical Chemistry C*, 119:23503–23514, 2015.

[127] Tangui Le Bahers and Kazuhiro Takanabe. Combined theoretical and experimental characterizations of semiconductors for photoelectrocatalytic applications. *Journal of Photochemistry and Photobiology C: Photochemistry Reviews*, 40:212–233, 2019.

[128] Michael G. Walter, Emily L. Warren, James R. McKone, Shannon W. Boettcher, Qixi Mi, Elizabeth A. Santori, and Nathan S. Lewis. Solar water splitting cells. *Chemical Reviews*, 110:6446–6473, 2010.

[129] Vladan Stevanović, Stephan Lany, David S. Ginley, Willam Tumas, and Alex Zunger. Assessing capability of semiconductors to split water using ionization potentials and electron affinities only. *Phys. Chem. Chem. Phys.*, 16:3706–3714, 2014.

[130] Y. Y. Mi, S. J. Wang, J. W. Chai, J. S. Pan, C. H. A. Huan, Y. P. Feng, and C. K. Ong. Effect of nitrogen doping on optical properties and electronic structures of $SrTiO_3$ films. *Applied Physics Letters*, 89:231922, 2006.

[131] Tao Sun and Ming Lu. Modification of $SrTiO_3$ surface by nitrogen ion bombardment for enhanced photocatalysis. *Applied Surface Science*, 274:176 – 180, 2013.

[132] C M Liu, X T Zu, and W L Zhou. Photoluminescence of nitrogen doped $SrTiO_3$. *Journal of Physics D: Applied Physics*, 40:7318–7322, 2007.

[133] Alexander Tkach, Paula M. Vilarinho, and Andrei L. Kholkin. Structure–microstructure–dielectric tunability relationship in Mn-doped strontium titanate ceramics. *Acta Materialia*, 53:5061 – 5069, 2005.

[134] Hao Yang, Paul G. Kotula, Yukio Sato, Miaofang Chi, Yuichi Ikuhara, and Nigel D. Browning. Segregation of Mn^{2+} dopants as interstitials in $SrTiO_3$ grain boundaries. *Materials Research Letters*, 2:16–22, 2014.

[135] Cristiana Di Valentin, Emanuele Finazzi, Gianfranco Pacchioni, Annabella Selloni, Stefano Livraghi, Maria Cristina Paganini, and Elio Giamello. N-doped TiO_2: Theory and experiment. *Chemical Physics*, 339:44 – 56, 2007.

[136] Cristiana Di Valentin, Gianfranco Pacchioni, and Annabella Selloni. Theory of carbon doping of titanium dioxide. *Chemistry of Materials*, 17:6656–6665, 2005.

[137] Amrita Bhattacharya and Saswata Bhattacharya. Unraveling the role of vacancies in the potentially promising thermoelectric clathrates $Ba_8Zn_xGe_{46-x-y}\square_y$. *Phys. Rev. B*, 94:094305, 2016.

[138] Pooja Basera, Shikha Saini, Ekta Arora, Arunima Singh, Manish Kumar, and Saswata Bhattacharya. Stability of non-metal dopants to tune the photo-absorption of TiO_2 at realistic temperatures and oxygen partial pressures: A hybrid dft study. *Scientific Reports*, 9:1–13, 2019.

[139] Mark S. Hybertsen and Steven G. Louie. First-principles theory of quasiparticles: Calculation of band gaps in semiconductors and insulators. *Phys. Rev. Lett.*, 55:1418–1421, 1985.

[140] G. Kresse and J. Furthmüller. Efficiency of ab-initio total energy calculations for metals and semiconductors using a plane-wave basis set. *Computational Materials Science*, 6:15 – 50, 1996.

[141] G. Kresse and D. Joubert. From ultrasoft pseudopotentials to the projector augmented-wave method. *Phys. Rev. B*, 59:1758–1775, 1999.

[142] P. E. Blöchl. Projector augmented-wave method. *Phys. Rev. B*, 50:17953–17979, 1994.

[143] K. van Benthem, C. Elsässer, and R. H. French. Bulk electronic structure of $SrTiO_3$: Experiment and theory. *Journal of Applied Physics*, 90:6156–6164, 2001.

[144] Saswata Bhattacharya, Sergey V Levchenko, Luca M Ghiringhelli, and Matthias Scheffler. Efficient ab initio schemes for finding thermodynamically stable and metastable atomic structures: benchmark of cascade genetic algorithms. *New Journal of Physics*, 16:123016, 2014.

[145] Amrita Bhattacharya and Saswata Bhattacharya. Exploring N-rich phases in Li_xN_y clusters for hydrogen storage at nanoscale. *The Journal of Physical Chemistry Letters*, 6:3726–3730, 2015.

[146] Ekta Arora, Shikha Saini, Pooja Basera, Manish Kumar, Arunima Singh, and Saswata Bhattacharya. Elucidating the role of temperature and pressure to the thermodynamic stability of charged defects in complex metal-hydrides: A case study of $NaAlH_4$. *The Journal of Physical Chemistry C*, 123:62–69, 2019.

[147] Jinshu Wang, Shu Yin, Masakazu Komatsu, Qiwu Zhang, Fumio Saito, and Tsugio Sato. Preparation and characterization of nitrogen doped $SrTiO_3$ photocatalyst. *Journal of Photochemistry and Photobiology A: Chemistry*, 165:149 – 156, 2004.

[148] Jingbo Li, Su-Huai Wei, Shu-Shen Li, and Jian-Bai Xia. Design of shallow acceptors in ZnO: First-principles band-structure calculations. *Phys. Rev. B*, 74:081201, 2006.

[149] Manuel Cardona. Optical properties and band structure of $SrTiO_3$ and $BaTiO_3$. *Phys. Rev.*, 140:A651–A655, 1965.

[150] M. M. Fadlallah, M. F. Shibl, T. J. H. Vlugt, and U. Schwingenschlögl. Theoretical study on cation codoped $SrTiO_3$ photocatalysts for water splitting. *J. Mater. Chem. A*, 6:24342–24349, 2018.

[151] Yong Xu and Martin A. A. Schoonen. The absolute energy positions of conduction and valence bands of selected semiconducting minerals. *American Mineralogist*, 85:543–556, 2000.

[152] A. Janotti, D. Steiauf, and C. G. Van de Walle. Strain effects on the electronic structure of $SrTiO_3$: Toward high electron mobilities. *Phys. Rev. B*, 84:201304, 2011.

[153] M. Marques, L. K. Teles, V. Anjos, L. M. R. Scolfaro, J. R. Leite, V. N. Freire, G. A. Farias, and E. F. da Silva. Full-relativistic calculations of the $SrTiO_3$ carrier effective masses and complex dielectric function. *Applied Physics Letters*, 82:3074–3076, 2003.

[154] Wei Ku, Tom Berlijn, and Chi-Cheng Lee. Unfolding first-principles band structures. *Phys. Rev. Lett.*, 104:216401, 2010.

[155] Voicu Popescu and Alex Zunger. Extracting E versus $\vec{k}$ effective band structure from supercell calculations on alloys and impurities. *Phys. Rev. B*, 85:085201, 2012.

[156] Karthik Krishnaswamy, Burak Himmetoglu, Youngho Kang, Anderson Janotti, and Chris G Van de Walle. First-principles analysis of electron transport in $BaSnO_3$. *Physical Review B*, 95:205202, 2017.

[157] Qian Wang and Kazunari Domen. Particulate photocatalysts for light-driven water splitting: Mechanisms, challenges, and design strategies. *Chemical Reviews*, 120:919–985, 2020.

[158] Dakota E McCoy, Teresa Feo, Todd Alan Harvey, and Richard O Prum. Structural absorption by barbule microstructures of super black bird of paradise feathers. *Nature Communications*, 9:1–8, 2018.

[159] Jie Li, Hao Li, Guangming Zhan, and Lizhi Zhang. Solar water splitting and nitrogen fixation with layered bismuth oxyhalides. *Accounts of Chemical Research*, 50:112–121, 2017.

[160] Yuting Wang, Changhong Wang, Mengyang Li, Yifu Yu, and Bin Zhang. Nitrate electroreduction: mechanism insight, in situ characterization, performance evaluation, and challenges. *Chem. Soc. Rev.*, 50:6720–6733, 2021.

[161] Xingzhu Chen, Neng Li, Zhouzhou Kong, Wee-Jun Ong, and Xiujian Zhao. Photocatalytic fixation of nitrogen to ammonia: state-of-the-art advancements and future prospects. *Mater. Horiz.*, 5:9–27, 2018.

[162] Ashish Kumar, Ajay Kumar, and Venkata Krishnan. Perovskite oxide based materials for energy and environment-oriented photocatalysis. *ACS Catalysis*, 10:10253–10315, 2020.

[163] Akira Fujishima and Kenichi Honda. Electrochemical photolysis of water at a semiconductor electrode. *Nature*, 238:37–38, 1972.

[164] Xiangye Liu, Guilian Zhu, Xin Wang, Xiaotao Yuan, Tianquan Lin, and Fuqiang Huang. Progress in black titania: A new material for advanced photocatalysis. *Advanced Energy Materials*, 6:1600452, 2016.

[165] Qiongzhi Gao, Fangyuan Si, Shengsen Zhang, Yueping Fang, Xiaobo Chen, and Siyuan Yang. Hydrogenated F-doped TiO_2 for photocatalytic hydrogen evolution and pollutant degradation. *International Journal of Hydrogen Energy*, 44:8011–8019, 2019.

[166] Nitish Roy, Norihiro Suzuki, Chiaki Terashima, and Akira Fujishima. Recent improvements in the production of solar fuels: From CO_2 reduction to water splitting and artificial photosynthesis. *Bulletin of the Chemical Society of Japan*, 92:178–192, 2019.

[167] Junwei Fu, Kexin Jiang, Xiaoqing Qiu, Jiaguo Yu, and Min Liu. Product selectivity of photocatalytic CO_2 reduction reactions. *Materials Today*, 32:222–243, 2020.

[168] Kazuhiko Maeda and Thomas E. Mallouk. Two-dimensional metal oxide nanosheets as building blocks for artificial photosynthetic assemblies. *Bulletin of the Chemical Society of Japan*, 92:38–54, 2019.

[169] Guowei Li, Graeme R. Blake, and Thomas T. M. Palstra. Vacancies in functional materials for clean energy storage and harvesting: the perfect imperfection. *Chem. Soc. Rev.*, 46:1693–1706, 2017.

[170] Ashish Kumar and Venkata Krishnan. Vacancy engineering in semiconductor photocatalysts: Implications in hydrogen evolution and nitrogen fixation applications. *Advanced Functional Materials*, 31:2009807, 2021.

[171] Yajun Zhang, Zhongfei Xu, Guiyu Li, Xiaojuan Huang, Weichang Hao, and Yingpu Bi. Direct observation of oxygen vacancy self-healing on TiO_2 photocatalysts for solar water splitting. *Angewandte Chemie International Edition*, 58:14229–14233, 2019.

[172] Guoqiang Zhang, Xun Yang, Chuanxin He, Peixin Zhang, and Hongwei Mi. Constructing a tunable defect structure in TiO_2 for photocatalytic nitrogen fixation. *J. Mater. Chem. A*, 8:334–341, 2020.

[173] Balaji Sambandam, Robin Jude Vimal Michael, and Periakaruppan T. Manoharan. Oxygen vacancies and intense luminescence in manganese loaded ZnO microflowers for visible light water splitting. *Nanoscale*, 7:13935–13942, 2015.

[174] Dapeng Wu, Rui Wang, Can Yang, Yipeng An, Hai Lu, Hongju Wang, Kun Cao, Zhiyong Gao, Wenchao Zhang, Fang Xu, and Kai Jiang. Br doped porous bismuth oxychloride micro-sheets with rich oxygen vacancies and dominating {0 0 1} facets for enhanced nitrogen photo-fixation performances. *Journal of Colloid and Interface Science*, 556:111–119, 2019.

[175] Xiaolan Xue, Renpeng Chen, Hongwei Chen, Yi Hu, Qingqing Ding, Ziteng Liu, Lianbo Ma, Guoyin Zhu, Wenjun Zhang, Qian Yu, Jie Liu, Jing Ma, and Zhong Jin. Oxygen vacancy engineering promoted photocatalytic ammonia synthesis on ultrathin two-dimensional bismuth oxybromide nanosheets. *Nano Letters*, 18:7372–7377, 2018.

[176] Tianpeng Yu, Zunhang Lv, Kaihang Wang, Kaili Sun, Xin Liu, Guixue Wang, Luhua Jiang, and Guangwen Xie. Constructing $SrTiO_3$-T/CdZnS heterostructure with tunable

oxygen vacancies for solar-light-driven photocatalytic hydrogen evolution. *Journal of Power Sources*, 438:227014, 2019.

[177] Jinmeng Cai, Ang Cao, Jingjing Huang, Wenfeng Jin, Jing Zhang, Zheng Jiang, and Xingang Li. Understanding oxygen vacancies in disorder-engineered surface and subsurface of $CaTiO_3$ nanosheets on photocatalytic hydrogen evolution. *Applied Catalysis B: Environmental*, 267:118378, 2020.

[178] Hao Li, Chengliang Mao, Huan Shang, Zhiping Yang, Zhihui Ai, and Lizhi Zhang. New opportunities for efficient N_2 fixation by nanosheet photocatalysts. *Nanoscale*, 10:15429–15435, 2018.

[179] Chengliang Mao, Jiaxian Wang, Yunjie Zou, Hao Li, Guangming Zhan, Jie Li, Jincai Zhao, and Lizhi Zhang. Anion (O, N, C, and S) vacancies promoted photocatalytic nitrogen fixation. *Green Chem.*, 21:2852–2867, 2019.

[180] Ashish Kumar, Vempuluru Navakoteswara Rao, Ajay Kumar, Aamir Mushtaq, Lalita Sharma, Aditi Halder, Suman Kalyan Pal, Muthukonda Venkatakrishnan Shankar, and Venkata Krishnan. Three-dimensional carbonaceous aerogels embedded with Rh-$SrTiO_3$ for enhanced hydrogen evolution triggered by efficient charge transfer and light absorption. *ACS Applied Energy Materials*, 3:12134–12147, 2020.

[181] Ashish Kumar, Vempuluru Navakoteswara Rao, Ajay Kumar, Muthukonda Venkatakrishnan Shankar, and Venkata Krishnan. Interplay between mesocrystals of $CaTiO_3$ and edge sulfur atom enriched MoS_2 on reduced graphene oxide nanosheets: Enhanced photocatalytic performance under sunlight irradiation. *ChemPhotoChem*, 4:427–444, 2020.

[182] Guoqiang Zhang, Wenshuai Jiang, Shixin Hua, Haifeng Zhao, Ligong Zhang, and Zaicheng Sun. Constructing bulk defective perovskite $SrTiO_3$ nanocubes for high performance photocatalysts. *Nanoscale*, 8:16963–16968, 2016.

[183] Shikha Saini, Pooja Basera, Manish Kumar, Preeti Bhumla, and Saswata Bhattacharya. Metastability triggered reactivity in clusters at realistic conditions: a case study of N-doped $(TiO_2)_n$ for photocatalysis. *Journal of Physics: Materials*, 4:015001, 2020.

[184] Run Shi, Geoffrey I.N. Waterhouse, and Tierui Zhang. Recent progress in photocatalytic CO_2 reduction over perovskite oxides. *Solar RRL*, 1:1700126, 2017.

[185] Shengtao Chen, Dong Liu, and Tianyou Peng. Fundamentals and recent progress of photocatalytic nitrogen-fixation reaction over semiconductors. *Solar RRL*, 5:2000487, 2021.

[186] Michael M. Lee, Joël Teuscher, Tsutomu Miyasaka, Takurou N. Murakami, and Henry J. Snaith. Efficient hybrid solar cells based on meso-superstructured organometal halide perovskites. *Science*, 338:643–647, 2012.

[187] Christian Wehrenfennig, Giles E. Eperon, Michael B. Johnston, Henry J. Snaith, and Laura M. Herz. High charge carrier mobilities and lifetimes in organolead trihalide perovskites. *Advanced Materials*, 26:1584–1589, 2014.

[188] Tom J. Savenije, Carlito S. Ponseca, Lucas Kunneman, Mohamed Abdellah, Kaibo Zheng, Yuxi Tian, Qiushi Zhu, Sophie E. Canton, Ivan G. Scheblykin, Tonu Pullerits, Arkady Yartsev, and Villy Sundström. Thermally activated exciton dissociation and recombination control the carrier dynamics in organometal halide perovskite. *The Journal of Physical Chemistry Letters*, 5:2189–2194, 2014.

[189] Joseph S. Manser, Jeffrey A. Christians, and Prashant V. Kamat. Intriguing optoelectronic properties of metal halide perovskites. *Chemical Reviews*, 116:12956–13008, 2016.

[190] K. Xerxes Steirer, Philip Schulz, Glenn Teeter, Vladan Stevanovic, Mengjin Yang, Kai Zhu, and Joseph J. Berry. Defect tolerance in methylammonium lead triiodide perovskite. *ACS Energy Letters*, 1:360–366, 2016.

[191] Hairen Tan, Fanglin Che, Mingyang Wei, Yicheng Zhao, Makhsud I Saidaminov, Petar Todorović, Danny Broberg, Grant Walters, Furui Tan, Taotao Zhuang, et al. Dipolar cations confer defect tolerance in wide-bandgap metal halide perovskites. *Nature Communications*, 9:3100, 2018.

[192] Julian Burschka, Norman Pellet, Soo-Jin Moon, Robin Humphry-Baker, Peng Gao, Mohammad K Nazeeruddin, and Michael Grätzel. Sequential deposition as a route to high-performance perovskite-sensitized solar cells. *Nature*, 499:316, 2013.

[193] Rafael S. Sanchez, Victoria Gonzalez-Pedro, Jin-Wook Lee, Nam-Gyu Park, Yong Soo Kang, Ivan Mora-Sero, and Juan Bisquert. Slow dynamic processes in lead halide per-

ovskite solar cells. characteristic times and hysteresis. *The Journal of Physical Chemistry Letters*, 5:2357–2363, 2014.

[194] Guangru Li, Zhi-Kuang Tan, Dawei Di, May Ling Lai, Lang Jiang, Jonathan Hua-Wei Lim, Richard H. Friend, and Neil C. Greenham. Efficient light-emitting diodes based on nanocrystalline perovskite in a dielectric polymer matrix. *Nano Letters*, 15:2640–2644, 2015.

[195] Natalia Yantara, Saikat Bhaumik, Fei Yan, Dharani Sabba, Herlina A. Dewi, Nripan Mathews, Pablo P. Boix, Hilmi Volkan Demir, and Subodh Mhaisalkar. Inorganic halide perovskites for efficient light-emitting diodes. *The Journal of Physical Chemistry Letters*, 6:4360–4364, 2015.

[196] Felix Deschler, Michael Price, Sandeep Pathak, Lina E. Klintberg, David-Dominik Jarausch, Ruben Higler, Sven Hüttner, Tomas Leijtens, Samuel D. Stranks, Henry J. Snaith, Mete Atatüre, Richard T. Phillips, and Richard H. Friend. High photoluminescence efficiency and optically pumped lasing in solution-processed mixed halide perovskite semiconductors. *The Journal of Physical Chemistry Letters*, 5:1421–1426, 2014.

[197] Guichuan Xing, Nripan Mathews, Swee Sien Lim, Natalia Yantara, Xinfeng Liu, Dharani Sabba, Michael Grätzel, Subodh Mhaisalkar, and Tze Chien Sum. Low-temperature solution-processed wavelength-tunable perovskites for lasing. *Nature Materials*, 13:476, 2014.

[198] Xiaoming Li, Dejian Yu, Jun Chen, Yue Wang, Fei Cao, Yi Wei, Ye Wu, Lin Wang, Ying Zhu, Zhiguo Sun, Jianping Ji, Yalong Shen, Handong Sun, and Haibo Zeng. Constructing fast carrier tracks into flexible perovskite photodetectors to greatly improve responsivity. *ACS Nano*, 11:2015–2023, 2017.

[199] Chunxiong Bao, Jie Yang, Sai Bai, Weidong Xu, Zhibo Yan, Qingyu Xu, Junming Liu, Wenjing Zhang, and Feng Gao. High performance and stable all-inorganic metal halide perovskite-based photodetectors for optical communication applications. *Advanced Materials*, 30:1803422, 2018.

[200] Wan-Jian Yin, Ji-Hui Yang, Joongoo Kang, Yanfa Yan, and Su-Huai Wei. Halide perovskite materials for solar cells: A theoretical review. *J. Mater. Chem. A*, 3:8926–8942, 2015.

[201] Bayrammurad Saparov, Feng Hong, Jon-Paul Sun, Hsin-Sheng Duan, Weiwei Meng, Samuel Cameron, Ian G. Hill, Yanfa Yan, and David B. Mitzi. Thin-film preparation and characterization of $Cs_3Sb_2I_9$: A lead-free layered perovskite semiconductor. *Chemistry of Materials*, 27:5622–5632, 2015.

[202] Alex M. Ganose, Christopher N. Savory, and David O. Scanlon. Beyond methylammonium lead iodide: Prospects for the emergent field of ns^2 containing solar absorbers. *Chem. Commun.*, 53:20–44, 2017.

[203] Abhishek Swarnkar, Wasim J. Mir, and Angshuman Nag. Can b-site doping or alloying improve thermal- and phase-stability of all-inorganic $CsPbX_3$ (X = Cl, Br, I) perovskites? *ACS Energy Letters*, 3:286–289, 2018.

[204] Sabine Körbel, Miguel A. L. Marques, and Silvana Botti. Stability and electronic properties of new inorganic perovskites from high-throughput ab initio calculations. *J. Mater. Chem. C*, 4:3157–3167, 2016.

[205] T. Jesper Jacobsson, Meysam Pazoki, Anders Hagfeldt, and Tomas Edvinsson. Goldschmidt's rules and strontium replacement in lead halogen perovskite solar cells: Theory and preliminary experiments on $CH_3NH_3SrI_3$. *The Journal of Physical Chemistry C*, 119:25673–25683, 2015.

[206] Akash Kumar, K. R. Balasubramaniam, Jiban Kangsabanik, Vikram, and Aftab Alam. Crystal structure, stability, and optoelectronic properties of the organic-inorganic wide-band-gap perovskite $\mathrm{CH_3NH_3BaI_3}$: Candidate for transparent conductor applications. *Phys. Rev. B*, 94:180105, 2016.

[207] Tom C. Jellicoe, Johannes M. Richter, Hugh F. J. Glass, Maxim Tabachnyk, Ryan Brady, Siân E. Dutton, Akshay Rao, Richard H. Friend, Dan Credgington, Neil C. Greenham, and Marcus L. Böhm. Synthesis and optical properties of lead-free cesium tin halide perovskite nanocrystals. *Journal of the American Chemical Society*, 138:2941–2944, 2016.

[208] Abhishek Swarnkar, Vikash Kumar Ravi, and Angshuman Nag. Beyond colloidal cesium lead halide perovskite nanocrystals: Analogous metal halides and doping. *ACS Energy Letters*, 2:1089–1098, 2017.

[209] Hai-Chen Wang, Paul Pistor, Miguel A. L. Marques, and Silvana Botti. Double perovskites as p-type conducting transparent semiconductors: a high-throughput search. *J. Mater. Chem. A*, 7:14705–14711, 2019.

[210] Yao Cai, Wei Xie, Yin Ting Teng, P. C. Harikesh, Biplab Ghosh, Patrick Huck, Kristin A. Persson, Nripan Mathews, Subodh G. Mhaisalkar, Matthew Sherburne, and Mark Asta. High-throughput computational study of halide double perovskite inorganic compounds. *Chemistry of Materials*, 31:5392–5401, 2019.

[211] Qingde Sun, Wan-Jian Yin, and Su-Huai Wei. Searching for stable perovskite solar cell materials using materials genome techniques and high-throughput calculations. *J. Mater. Chem. C*, 8:12012–12035, 2020.

[212] George Volonakis, Marina R. Filip, Amir Abbas Haghighirad, Nobuya Sakai, Bernard Wenger, Henry J. Snaith, and Feliciano Giustino. Lead-free halide double perovskites via heterovalent substitution of noble metals. *The Journal of Physical Chemistry Letters*, 7:1254–1259, 2016.

[213] Marina R. Filip, Samuel Hillman, Amir Abbas Haghighirad, Henry J. Snaith, and Feliciano Giustino. Band gaps of the lead-free halide double perovskites $Cs_2BiAgCl_6$ and $Cs_2BiAgBr_6$ from theory and experiment. *The Journal of Physical Chemistry Letters*, 7:2579–2585, 2016.

[214] Jun Zhou, Zhiguo Xia, Maxim S. Molokeev, Xiuwen Zhang, Dongsheng Peng, and Quanlin Liu. Composition design, optical gap and stability investigations of lead-free halide double perovskite $Cs_2AgInCl_6$. *J. Mater. Chem. A*, 5:15031–15037, 2017.

[215] Federico Locardi, Matilde Cirignano, Dmitry Baranov, Zhiya Dang, Mirko Prato, Filippo Drago, Maurizio Ferretti, Valerio Pinchetti, Marco Fanciulli, Sergio Brovelli, Luca De Trizio, and Liberato Manna. Colloidal synthesis of double perovskite $Cs_2AgInCl_6$ and Mn-doped $Cs_2AgInCl_6$ nanocrystals. *Journal of the American Chemical Society*, 140:12989–12995, 2018.

[216] Nila Nandha K. and Angshuman Nag. Synthesis and luminescence of Mn-doped $Cs_2AgInCl_6$ double perovskites. *Chem. Commun.*, 54:5205–5208, 2018.

[217] Ying Liu, Yuyu Jing, Jing Zhao, Quanlin Liu, and Zhiguo Xia. Design optimization of lead-free perovskite $Cs_2AgInCl_6$:Bi nanocrystals with 11.4% photoluminescence quantum yield. *Chemistry of Materials*, 31:3333–3339, 2019.

[218] Debjit Manna, Tapan Kumar Das, and Aswani Yella. Tunable and stable white light emission in Bi^{3+}-alloyed $Cs_2AgInCl_6$ double perovskite nanocrystals. *Chemistry of Materials*, 31:10063–10070, 2019.

[219] Habibul Arfin, Jagjit Kaur, Tariq Sheikh, Sudip Chakraborty, and Angshuman Nag. Bi^{3+}-Er^{3+} and Bi^{3+}-Yb^{3+} codoped $Cs_2AgInCl_6$ double perovskite near-infrared emitters. *Angewandte Chemie International Edition*, 59:11307–11311, 2020.

[220] Zewen Xiao, Ke-Zhao Du, Weiwei Meng, David B. Mitzi, and Yanfa Yan. Chemical origin of the stability difference between copper(I)- and silver(I)-based halide double perovskites. *Angewandte Chemie International Edition*, 56:12107–12111, 2017.

[221] Alexandre Tkatchenko and Matthias Scheffler. Accurate molecular van der waals interactions from ground-state electron density and free-atom reference data. *Phys. Rev. Lett.*, 102:073005, 2009.

[222] Raman Singh Lamba, Pooja Basera, Saswata Bhattacharya, and Sameer Sapra. Band gap engineering in $Cs_2(Na_xAg_{1-x})BiCl_6$ double perovskite nanocrystals. *The Journal of Physical Chemistry Letters*, 10:5173–5181, 2019.

[223] W. Travis, E. N. K. Glover, H. Bronstein, D. O. Scanlon, and R. G. Palgrave. On the application of the tolerance factor to inorganic and hybrid halide perovskites: A revised system. *Chem. Sci.*, 7:4548–4556, 2016.

[224] R. D. Shannon. Revised effective ionic radii and systematic studies of interatomic distances in halides and chalcogenides. *Acta Crystallographica Section A*, 32:751–767, 1976.

[225] Pooja Basera, Manish Kumar, Shikha Saini, and Saswata Bhattacharya. Reducing lead toxicity in the methylammonium lead halide $\mathrm{MAPbI_3}$: Why Sn substitution should be preferred to Pb vacancy for optimum solar cell efficiency. *Phys. Rev. B*, 101:054108, 2020.

[226] Manish Kumar, Pooja Basera, Shikha Saini, and Saswata Bhattacharya. Role of defects in photocatalytic water splitting: Monodoped vs codoped $SrTiO_3$. *The Journal of Physical Chemistry C*, 124:10272–10279, 2020.

[227] Christopher J. Bartel, Jacob M. Clary, Christopher Sutton, Derek Vigil-Fowler, Bryan R. Goldsmith, Aaron M. Holder, and Charles B. Musgrave. Inorganic halide double perovskites with optoelectronic properties modulated by sublattice mixing. *Journal of the American Chemical Society*, 142:5135–5145, 2020.

[228] Xin-Gang Zhao, Dongwen Yang, Ji-Chang Ren, Yuanhui Sun, Zewen Xiao, and Lijun Zhang. Rational design of halide double perovskites for optoelectronic applications. *Joule*, 2:1662 – 1673, 2018.

[229] T. Thao Tran, Jessica R. Panella, Juan R. Chamorro, Jennifer R. Morey, and Tyrel M. McQueen. Designing indirect-direct bandgap transitions in double perovskites. *Mater. Horiz.*, 4:688–693, 2017.

[230] Jiban Kangsabanik, Supriti Ghorui, M. Aslam, and Aftab Alam. Optoelectronic properties and defect physics of lead-free photovoltaic absorbers $\mathrm{Cs_2Au^IAu^{III}}X_6$ $(X = \mathrm{I, Br})$. *Phys. Rev. Applied*, 13:014005, 2020.

[231] Dongwen Yang, Wenmei Ming, Hongliang Shi, Lijun Zhang, and Mao-Hua Du. Fast diffusion of native defects and impurities in perovskite solar cell material $CH_3NH_3PbI_3$. *Chemistry of Materials*, 28:4349–4357, 2016.

[232] Abhishek Swarnkar, Wasim J. Mir, Rayan Chakraborty, Metikoti Jagadeeswararao, Tariq Sheikh, and Angshuman Nag. Are chalcogenide perovskites an emerging class of semiconductors for optoelectronic properties and solar cell? *Chemistry of Materials*, 31:565–575, 2019.

[233] Aslihan Babayigit, Anitha Ethirajan, Marc Muller, and Bert Conings. Toxicity of organometal halide perovskite solar cells. *Nature Materials*, 15:247–251, 2016.

[234] Yi-Yang Sun, Michael L. Agiorgousis, Peihong Zhang, and Shengbai Zhang. Chalcogenide perovskites for photovoltaics. *Nano Letters*, 15:581–585, 2015.

[235] Weiwei Meng, Bayrammurad Saparov, Feng Hong, Jianbo Wang, David B. Mitzi, and Yanfa Yan. Alloying and defect control within chalcogenide perovskites for optimized photovoltaic application. *Chemistry of Materials*, 28:821–829, 2016.

[236] Korina Kuhar, Andrea Crovetto, Mohnish Pandey, Kristian S. Thygesen, Brian Seger, Peter C. K. Vesborg, Ole Hansen, Ib Chorkendorff, and Karsten W. Jacobsen. Sulfide perovskites for solar energy conversion applications: Computational screening and synthesis of the selected compound $\mathrm{LaYS_3}$. *Energy Environ. Sci.*, 10:2579–2593, 2017.

[237] Nathalie Vonrüti and Ulrich Aschauer. Band-gap engineering in $\mathrm{AB(O}_x\mathrm{S}_{1-x})_3$ perovskite oxysulfides: a route to strongly polar materials for photocatalytic water splitting. *J. Mater. Chem. A*, 7:15741–15748, 2019.

[238] Henry Igwebuike Eya, Esidor Ntsoenzok, and Nelson Y. Dzade. First–principles investigation of the structural, elastic, electronic, and optical properties of $\alpha-$ and $\beta-\mathrm{SrZrS_3}$: Implications for photovoltaic applications. *Materials*, 13, 2020.

[239] Wei Li, Shanyuan Niu, Boyang Zhao, Ralf Haiges, Zhiqiang Zhang, Jayakanth Ravichandran, and Anderson Janotti. Band gap evolution in Ruddlesden-Popper phases. *Phys. Rev. Materials*, 3:101601, 2019.

[240] Corrado Comparotto, Alexandra Davydova, Tove Ericson, Lars Riekehr, Marcos V. Moro, Tomas Kubart, and Jonathan Scragg. Chalcogenide perovskite $\mathrm{BaZrS_3}$: Thin film growth by sputtering and rapid thermal processing. *ACS Applied Energy Materials*, 3:2762–2770, 2020.

[241] Xiucheng Wei, Haolei Hui, Samanthe Perera, Aaron Sheng, David F. Watson, Yi-Yang Sun, Quanxi Jia, Shengbai Zhang, and Hao Zeng. Ti-alloying of $\mathrm{BaZrS_3}$ chalcogenide perovskite for photovoltaics. *ACS Omega*, 5:18579–18583, 2020.

[242] Vikash Kumar Ravi, Seong Hoon Yu, Parikshit Kumar Rajput, Chandrani Nayak, Dibyendu Bhattacharyya, Dae Sung Chung, and Angshuman Nag. Colloidal $\mathrm{BaZrS_3}$ chalcogenide perovskite nanocrystals for thin film device fabrication. *Nanoscale*, 13:1616–1623, 2021.

[243] Kota Hanzawa, Soshi Iimura, Hidenori Hiramatsu, and Hideo Hosono. Material design of green-light-emitting semiconductors: Perovskite-type sulfide $SrHfS_3$. *Journal of the American Chemical Society*, 141:5343–5349, 2019.

[244] Yukinori Nishigaki, Takayuki Nagai, Mitsutoshi Nishiwaki, Takuma Aizawa, Masayuki Kozawa, Kota Hanzawa, Yoshitsune Kato, Hitoshi Sai, Hidenori Hiramatsu, Hideo Hosono, and Hiroyuki Fujiwara. Extraordinary strong band-edge absorption in distorted chalcogenide perovskites. *Solar RRL*, 4:1900555, 2020.

[245] Liping Yu and Alex Zunger. Identification of potential photovoltaic absorbers based on first-principles spectroscopic screening of materials. *Phys. Rev. Lett.*, 108:068701, 2012.

[246] Alex M Ganose, Adam J Jackson, and David O Scanlon. sumo: Command-line tools for plotting and analysis of periodic ab initio calculations. *Journal of Open Source Software*, 3:717, 2018.

[247] Peitao Liu, Bongjae Kim, Xing-Qiu Chen, D. D. Sarma, Georg Kresse, and Cesare Franchini. Relativistic GW+BSE study of the optical properties of Ruddlesden-Popper iridates. *Phys. Rev. Materials*, 2:075003, 2018.

[248] Maurizia Palummo, Eduardo Berrios, Daniele Varsano, and Giacomo Giorgi. Optical properties of lead-free double perovskites by ab initio excited-state methods. *ACS Energy Letters*, 5:457–463, 2020.

[249] Hiroki Kawai, Giacomo Giorgi, Andrea Marini, and Koichi Yamashita. The mechanism of slow hot-hole cooling in lead-iodide perovskite: First-principles calculation on carrier lifetime from electron–phonon interaction. *Nano Letters*, 15:3103–3108, 2015.

[250] Manish Jain, James R. Chelikowsky, and Steven G. Louie. Reliability of hybrid functionals in predicting band gaps. *Phys. Rev. Lett.*, 107:216806, 2011.

[251] Tathagata Biswas, Pramod Ravindra, Eashwer Athresh, Rajeev Ranjan, Sushobhan Avasthi, and Manish Jain. Optical properties of $Zn_2Mo_3O_8$: Combination of theoretical and experimental study. *The Journal of Physical Chemistry C*, 121:24766–24773, 2017.

[252] Giacomo Giorgi, Koichi Yamashita, and Maurizia Palummo. Two-dimensional optical excitations in the mixed-valence $\mathrm{Cs_2Au_2I_6}$ fully inorganic double perovskite. *J. Mater. Chem. C*, 6:10197–10201, 2018.

[253] Pooja Basera, Arunima Singh, Deepika Gill, and Saswata Bhattacharya. Capturing excitonic effects in lead iodide perovskites from many-body perturbation theory. *arXiv preprint arXiv:2008.03381*, 2020.

[254] Laura M. Herz. How lattice dynamics moderate the electronic properties of metal-halide perovskites. *The Journal of Physical Chemistry Letters*, 9:6853–6863, 2018.

[255] Menno Bokdam, Tobias Sander, Alessandro Stroppa, Silvia Picozzi, D D Sarma, Cesare Franchini, and Georg Kresse. Role of polar phonons in the photo excited state of metal halide perovskites. *Scientific Reports*, 6:1–8, 2016.

[256] Stephen Filippone, Boyang Zhao, Shanyuan Niu, Nathan Z. Koocher, Daniel Silevitch, Ignasi Fina, James M. Rondinelli, Jayakanth Ravichandran, and R. Jaramillo. Discovery of highly polarizable semiconductors $\mathrm{BaZrS_3}$ and $\mathrm{Ba_3Zr_2S_7}$. *Phys. Rev. Materials*, 4:091601, 2020.

[257] Michael Sendner, Pabitra K. Nayak, David A. Egger, Sebastian Beck, Christian Müller, Bernd Epding, Wolfgang Kowalsky, Leeor Kronik, Henry J. Snaith, Annemarie Pucci, and Robert Lovrinčić. Optical phonons in methylammonium lead halide perovskites and implications for charge transport. *Mater. Horiz.*, 3:613–620, 2016.

[258] Jarvist Moore Frost. Calculating polaron mobility in halide perovskites. *Phys. Rev. B*, 96:195202, 2017.

[259] Robert W. Hellwarth and Ivan Biaggio. Mobility of an electron in a multimode polar lattice. *Phys. Rev. B*, 60:299–307, 1999.

[260] Cesare Franchini, Michele Reticcioli, Martin Setvin, and Ulrike Diebold. Polarons in materials. *Nature Reviews Materials*, pages 1–27, 2021.

[261] A python3 implementation of the spectroscopic limited maximum efficiency (SLME) analysis of solar absorbers. https://github.com/ldwillia/SL3ME. accessed: January 12, 2021.

[262] William Shockley and Hans J. Queisser. Detailed balance limit of efficiency of p-n junction solar cells. *Journal of Applied Physics*, 32:510–519, 1961.

Manish Kumar

Visiting Scholar

Institut für Physik and IRIS Adlershof, Humboldt-Universität zu Berlin
Zum Großen Windkanal 2, D-12489 Berlin, Germany
✉ *manish.kumar@physik.hu-berlin.de*

Profile & Research Interests

Manish Kumar presently is a visiting scholar in the institute of physics of Humboldt-Universität zu Berlin. He works in inter-disciplinary areas of condensed matter physics with broad research interest in first principles-based simulation of designing new materials and understanding their properties using state-of-the-art density functional theory (DFT) and beyond approaches. He is involved in predicting properties of various advanced energy materials (having applications in solar cell, photocatalysis, semiconducting devices, battery materials, etc.) by integrating different level of theories starting from DFT to highly sophisticated quantum chemistry methods (viz., GW, BSE, model-BSE, DFPT etc.). In order to capture the effect at finite temperature to the configurational entropy he employs *ab initio* atomistic thermodynamics (harmonic approximation) approach. Most of the materials he designs have significant impact in materials science.

Experience

April 2022 – Present **Visiting Scholar**, *Institute of Physics of Humboldt-Universität zu Berlin*.

Education

July 2017 – March 2022 **Ph.D.**, *Indian Institute of Technology Delhi, New Delhi*.
Mr. Kumar did his Ph.D. under supervision of Prof. Saswata Bhattacharya on the topic of "Understanding Defects and Excited-State Properties in Perovskites from Many-Body Perturbation Theory". Course work grade: 9.25

July 2015 – July 2017 **M.Sc. Physics**, *Kirori Mal College, University of Delhi, New Delhi*.
Specialization: Electronics. First Class with 76.65%. College Rank: 1

July 2012 – July 2015 **B.Sc. (H) Physics**, *Kirori Mal College, University of Delhi, New Delhi*.
First Class with 91.14%. College Rank: 1

Expertise & Technical Skills

Methods	Ground state electronic structure calculations: DFT and beyond DFT, Excited state calculations: GW, BSE, model-BSE, DFPT, phonopy, *ab initio* atomistic thermodynamics
Programming	Python, C++, C, MATLAB
OS and software	Unix, Linux, Windows, Xmgrace, Gnuplot, Materials Studio, p4vasp, Jmol, Vesta, VMD, LaTeX
Codes	VASP, FHI-AIMS, CASTEP, Quantum ESPRESSO, exciting, YAMBO
Languages	English, Hindi
Miscellaneous	Academic research, teaching, coding, using materials data repositories, learning and publishing.

Awards & Academic Recognitions

1. Reviewer in Scientific Journals: J. Phys. Mater., J. Phys. D: Appl. Phys., J. Appl. Phys., Phys. Scr., Mater. Res. Express
2. Nominated for the Graduate Award in Theoretical Chemistry sponsored by The Journal of Physical Chemistry, 2021
3. CSIR Travel Grant by CSIR, India in 2020 to participate in APS March Meeting

4. Nominated for the Ken Hass Outstanding Student Paper Award, endowed and administered by the APS Forum on Industrial and Applied Physics (FIAP), 2020
5. CSIR Research Fellowship for Ph.D. from CSIR, India from 2017-2022
6. Academic Award and Dr. N. Subramanyam Award for 1^{st} rank in M.Sc. Physics
7. Meritorious Award for academic excellence in B.Sc. (H) and M.Sc. Physics
8. Academic Award, Dr. N. S. Khare Award and Dr. N Subramanyam Award for 1^{st} rank in B.Sc. (H) Physics
9. Certificate of Merit for being among the top 0.1% candidates of Delhi Senior School Certificate Examination 2012 in Computer Science from CBSE, Class 12^{th}, 2012
10. Certificate of Merit for 1^{st} rank in Class 12^{th}, Rajkiya Pratibha Vikas Vidyalaya, Civil lines, New Delhi, India
11. Appreciation Award for Science Open Merit Test, 2009

Publications

1. S. Sheoran, **M. Kumar**, P. Bhumla, and S. Bhattacharya, "Rashba spin splitting and anomalous spin textures in the bulk ferroelectric oxide perovskite KIO_3", Materials Advances **3**, 4170 (2022).
2. M. Jain, P. Bhumla, **M. Kumar**, and S. Bhattacharya, "Lead-free alloyed double perovskites: An emerging class of materials for optoelectronic applications", The Journal of Physical Chemistry C **126**, 6753 (2022).
3. A. Kumar, **M. Kumar**, V. N. Rao, M. V. Shankar, S. Bhattacharya, and V. Krishnan, "Unraveling the structural and morphological stability of oxygen vacancy engineered leaf-templated $CaTiO_3$ towards photocatalytic H_2 evolution and N_2 fixation reactions", Journal of Materials Chemistry A **9**, 17006 (2021).
4. **M. Kumar***, A. Singh, D. Gill, and S. Bhattacharya, "Optoelectronic properties of chalcogenide perovskites by many-body perturbation theory", The Journal of Physical Chemistry Letters **12**, 5301 (2021).
5. K. M. Dehury, P. K. Kanaujia, M. Adnan, **M. Kumar**, S. Bhattacharya, and G. V. Prakash, "Structure-dependent (non)linear optical excitons in primary cyclic ammonium ($C_nH_{2n-1}NH_2$; $n = 3 - 8$)-based inorganic-organic hybrid semiconductor series", The Journal of Physical Chemistry C **125**, 6821 (2021).
6. D. Gill, P. Bhumla, **M. Kumar**, and S. Bhattacharya, "High-throughput screening to modulate electronic and optical properties of alloyed $Cs_2AgBiCl_6$ for enhanced solar cell efficiency", Journal of Physics Materials **4**, 025005 (2021).
7. **M. Kumar***, M. Jain, A. Singh, and S. Bhattacharya, "Sublattice mixing in $Cs_2AgInCl_6$ for enhanced optical properties from first-principles", Applied Physics Letters **118**, 021901 (2021).
8. P. Bhumla, **M. Kumar**, and S. Bhattacharya, "Theoretical insights into C–H bond activation of methane by transition metal clusters: The role of anharmonic effects", Nanoscale Advances **3**, 575 (2021).
9. S. Saini, P. Basera, **M. Kumar**, P. Bhumla, and S. Bhattacharya, "Metastability triggered reactivity in clusters at realistic conditions: A case study of N-doped $(TiO_2)_n$ for photocatalysis", Journal of Physics Materials **4**, 015001 (2020).
10. **M. Kumar***, P. Basera, S. Saini, and S. Bhattacharya, "Theoretical insights of codoping to modulate electronic structure of TiO_2 and $SrTiO_3$ for enhanced photocatalytic efficiency", Scientific Reports **10**, 15372 (2020).
11. G. Bahuguna, I. Mondal, M. Verma, **M. Kumar**, S. Bhattacharya, R. Gupta, and G. U. Kulkarni, "Innovative approach to photo-chemiresistive sensing technology: Surface-fluorinated SnO_2 for VOC detection", ACS Applied Materials & Interfaces **12**, 37320 (2020).
12. D. Gill, **M. Kumar**, P. Basera, and S. Bhattacharya, "Understanding the ionic diffusivity in (meta)stable (un)doped solid state electrolyte from first-principles: A case study of LISICON", The Journal of Physical Chemistry C **124**, 17485 (2020).

13. M. Jain, A. Singh, P. Basera, **M. Kumar**, and S. Bhattacharya, "Understanding the role of Sn-substitution and Pb-$\square$ in enhancing the stability of $CH(NH_2)_2Pb_{1-X-Y}Sn_X\square_YBr_3$: A hybrid density functional approach", Journal of Materials Chemistry C **8**, 10362 (2020).
14. **M. Kumar***, P. Basera, S. Saini, and S. Bhattacharya, "Role of defects in photocatalytic water splitting: Monodoped vs codoped $SrTiO_3$", The Journal of Physical Chemistry C **124**, 10272 (2020).
15. P. Basera, **M. Kumar**, S. Saini, and S. Bhattacharya, "Reducing lead toxicity in the methylammonium lead halide $MAPbI_3$: Why Sn substitution should be preferred to Pb vacancy for optimum solar cell efficiency", Physical Review B **101**, 054108 (2020).
16. A. Singh, P. Basera, S. Saini, **M. Kumar**, and S. Bhattacharya, "Importance of many-body dispersion in the stability of vacancies and antisites in free-standing monolayer of MoS_2 from first-principles approaches", The Journal of Physical Chemistry C **124**, 1390 (2020).
17. P. Basera, S. Saini, E. Arora, A. Singh, **M. Kumar**, and S. Bhattacharya, "Stability of non-metal dopants to tune the photo-absorption of TiO_2 at realistic temperatures and oxygen partial pressures: A hybrid DFT study", Scientific Reports **9**, 11427 (2019).
18. E. Arora, S. Saini, P. Basera, **M. Kumar**, A. Singh, and S. Bhattacharya, "Elucidating the role of temperature and pressure to the thermodynamic stability of charged defects in complex metal-hydrides: A case study of $NaAlH_4$", The Journal of Physical Chemistry C **123**, 62 (2019).

Conferences Attended

1. DAE Symposium on Current Trends in Theoretical Chemistry (CTTC-2020), September 23-25, 2021, at virtual platform. (Poster Presentation)
2. MAX/CECAM Virtual School on Electronic Excitations in Solids and Nanostructures using the Yambo Code, April 8-9 and 15-16, 2021, at virtual platform. (Poster Presentation)
3. APS March Meeting 2021, March 15-19, at virtual platform. (Oral Presentation)
4. Young Investigator Meet on Quantum Condensed Matter Theory (YIMQCMT-2020), December 15-18, 2020, at virtual platform. (Oral Presentation)
5. 4th Departmental Symposium on Advances in Physics, December 1-3, 2020, at Indian Institute of Technology Delhi, India. (Oral Presentation)
6. On-line Workshop on Excited Charge Dynamics in Semiconductors, September 28-30, 2020, at virtual platform, ICTP. (Poster Presentation)
7. Modern Approaches in Chemistry and Biology-2020 (MACB-2020), February 18-20, 2020, at JNCASR, Bengaluru, India. (Poster Presentation)
8. Second Indian Materials Conclave & 31st Annual General Meeting of Materials Research Society of India (MRSI), February 11-14, 2020, at CSIR-Central Glass & Ceramic Research Institute (CSIR-CGCRI), Kolkata, India. (Poster Presentation)
9. 3rd Departmental Symposium on Advances in Physics, April 6-7, 2019, at Indian Institute of Technology Delhi, India. (Poster Presentation)
10. Workshop and Symposium on Advanced Simulation Methods: DFT, MD and Beyond (ASM2019), March 6-10, 2019, at Indian Institute of Technology Delhi, India. (Poster Presentation)
11. International Workshop on Nano/Micro 2D-3D Fabrication, Manufacturing of Electronic Biomedical Devices & Applications (IWNEBD-2018), 31st October to 2nd November 2018, at Indian Institute of Technology Mandi, Himachal Pradesh, India. (Poster Presentation)

References

1. **Prof. Claudia Draxl**
   Professor
   Institut für Physik and IRIS Adlershof
   Humboldt-Universität zu Berlin
   Zum Großen Windkanal 2, D-12489 Berlin, Germany
   Tel: +49 30 2093 66363
   Email: claudia.draxl@physik.hu-berlin.de

2. **Prof. Saswata Bhattacharya**
   Associate Professor
   Department of Physics
   Indian Institute of Technology Delhi
   Hauz Khas, New Delhi 110016, India
   Tel: +91-11-2659-1359
   Email: saswata@physics.iitd.ac.in

3. **Prof. Amrita Bhattacharya**
   Associate Professor
   Department of Metallurgical Engineering and Materials Science
   Indian Institute of Technology Bombay
   Powai, Mumbai 400076, Maharashtra, India
   Tel: +91-22-2576-7620
   Email: b_amrita@iitb.ac.in

4. **Prof. Venkata Krishnan**
   Associate Professor
   School of Basic Sciences
   Indian Institute of Technology Mandi
   Kamand, Mandi 175005, Himachal Pradesh, India
   Tel: +91-190-526-7065
   Email: vkn@iitmandi.ac.in